Diplomarbeit

Correlated NN-Interactions and Phenomenological Corrections for Nuclear Structure Calculations

(Revised Edition)

Heiko Hergert

Januar 2004

In liebevollem Andenken an
Adelheid Hergert
(1935 — 1998)

Contents

Introduction

Stating the nuclear many-body problem is deceptively simple - "calculate the properties of a complex nucleus consisting of Z protons and N neutrons from the nuclear interaction". As with most simple statements in physics, the solution of the corresponding problem proves to be difficult.

There are two major problems we have to face when we want to treat the nucleus in quantum mechanics. First, it consists of too many particles to solve the Schrödinger equation exactly. Second, the nuclear force has a very rich and complex operator structure, and the constraints imposed by experimental observations are not strong enough to discern between different models. Low-energy data, like phase shifts obtained from the analysis of nucleon-nucleon scattering, only depend on the *on-shell properties* of the interaction, so models with considerable off-shell differences will reproduce them equally well. In nuclei or nuclear matter, on the other hand, only the total four-momentum is conserved, hence many interactions will be between half-on-shell or off-shell nucleons, and therefore the various models arrive at different predictions. A well-known manifestation is the *Coester line* in nuclear matter calculations, where practically all employed nucleon-nucleon interactions lead to different results for the nuclear matter saturation point. This would be helpful to decide which model is correct, if there was not the problem that (at least in nonrelativistic calculations, see the review [1]) all predictions are well apart from the values derived from experimental observations.

Quantum Chromodynamics (QCD) has been established as the microscopic theory of the strong force, describing the interaction between quarks by the exchange of gluons. On a conceptual level, nucleons are the relevant degrees of freedom in the low energy regime, and the forces that bind them together in a nucleus are residual in nature, i.e., the structure of these interactions is very involved. Furthermore, aside from the sheer number of particles involved, there are two inter-related properties of QCD which effectively prevent us from tackling the derivation of these residual forces — quark confinement and the asymptotic freedom of the theory, i.e., the breakdown of perturbative treatments at the low energy scales relevant for nuclear physics.

In the past decade, there has been considerable effort to make contact between nuclear physics and QCD in the framework of effective field theories (EFTs). Work undertaken along this direction has recently produced a very promising nucleon-nucleon potential derived from chiral perturbation theory (χPT) [2].

Parallel to the theoretical efforts of the past decades, several so-called realistic potential models were developed. Starting from varying degrees of theoretical development like meson theory or simple invariance considerations, the current generation of these interactions describes nucleon-nucleon scattering data and deuteron properties with very

high precision. The good description of low-energy observables comes at a price, however — all high-precision models have typically $30 - 50$ free parameters which are used to fit the experimental data. Nevertheless, these potentials provide a good starting point for nuclear structure calculations, for which a host of powerful techniques like Green's Function Monte Carlo (GFMC) have been developed over the years. The sheer computational effort has thus far limited these calculations to nuclei with $A \leq 12$ [3].

Methods used in nuclear structure calculations have to cope with two important properties of the realistic nucleon-nucleon interactions — the existence of a repulsive core, and tensor forces. Unfortunately, this rules out the use of standard mean-field approaches, because the Slater determinants used in Hartree-Fock and similar schemes cannot model the correlations induced by these effects. In order to employ the realistic NN-potentials in mean-field calculations, the Unitary Correlation Operator Method (UCOM) has been developed [4, 5, 6, 7], which yields good results with relatively low computational effort.

A recent development from the application of renormalization group (RG) techniques to the realistic nucleon-nucleon interactions is the $V_{\text{low-k}}$ potential [8], which represents the NN-interaction in the low-momentum regime. Since the treatment of central and tensor correlations by means of UCOM amounts to a separation of momentum scales, the two methods are conceptually alike and give very similar results, although there is no one-to-one correspondence.

The correlated interactions constructed by applying unitary correlation operators to realistic interactions contain three- and higher many-nucleon forces, which are (presently) neglected in order to implement the correlated potentials in many-body calculations. One of the main issues addressed in this work is the construction and discussion of several phenomenological two-nucleon corrections to replace these missing many-nucleon contributions.

In chapter 1, realistic NN potentials are reviewed, with emphasis on the Argonne [9] and Bonn potentials [10, 11, 12], which are used for nuclear structure calculations in the present work, and the recent chiral potential model of Entem and Machleidt [2].

Chapter 2 introduces the unitary correlation operator method (UCOM). It is shown how unitary correlation operators provide a way to introduce central and tensor correlations into simple many-body model states of Slater determinants, making it possible to combine a computationally affordable model space with realistic NN interactions.

Fermionic Molecular Dynamics (FMD) [13, 14], the model used for the nuclear structure calculations, is summarized in Chapter 3. The violation of symmetries in mean-field models is also discussed, considering translational and rotational invariance as examples. The restoration of the latter is achieved by angular momentum projection techniques [15], which are described in detail.

Central and tensor correlation operators for the Argonne V18 and Bonn-A potentials are presented in Chapter 4, along with the correlated interactions themselves. Several modifications, both on a global and a nucleus-by-nucleus basis, are constructed to improve the agreement of the groundstate properties of nuclei up to $A = 60$ with experimental data.

The final versions of the modified interactions are subsequently used to perform nuclear structure calculations for selected nuclei in Chapter 5. The impact of the modifications on the density distributions and spectra is critically examined.

Chapter 6 summarizes the results of this work, and ends with an outlook.

Appendix A lists important UCOM formulas for reference. Calculations of basic correlated operators are performed in detail, to illustrate the method. Appendix B serves as a reference for the partial-wave analysis of the NN interactions, in particular the derivation of matrix elements between angular momentum eigenstates in $(LS)J$ coupling, and the decomposition of Cartesian tensor operators into irreducible components. In Appendices C and D, we provide the parameters of the correlators and the parametrizations of the correlated interactions for use with the FMD code. Finally, Appendix E summarizes the notation used for vectors, operators and coordinates, as well as the conventions employed for, e.g., Clebsch-Gordan coefficients and common functions.

Chapter 1

Realistic Nucleon-Nucleon Potentials

1.1 A Brief Historical Overview

Chadwicks discovery of the neutron in 1932 [16] marks the birth of nuclear physics, and the problem of determining the force responsible for binding the nuclei has been at the center of the field ever since. The first rather fundamental attempt to explain the nature of the nuclear force was Yukawa's *meson theory*, published in 1935, and reformulated in the framework of quantum field theory (QFT) two years later.

In the following years, several authors considered other meson fields in addition to Yukawa's scalar particle, leading to the so-called *mixed-meson theories*, which produced force models with rich operator structures. However, most physicists at the time believed that the fundamental nuclear force would in the end turn out to be given by some simple law, just as for the Coulomb force and gravitation. Experiment would prove them wrong – over the years, it became clear that no simple model would be able to explain the observed phenomena.

When the pion was finally found in cosmic rays in 1947 and shortly thereafter in the Berkeley cyclotron lab, Yukawa was awarded the Nobel prize in 1949. The discovery of the strongly interacting meson motivated theoretical efforts to describe the nuclear force by the pion alone, treating it as *the* quantum of the strong interaction in analogy to the photon in Quantum Electrodynamics (QED). While the one-pion exchange (OPE) became experimentally well-established as the long-range part of the nuclear force, the two-pion exchange, considered to be the source of an intermediate attractive part, evolved very much in the other direction, producing calculations which deviated from experiment by orders of magnitude.

During the 1950s, another line of research was begun, though, which had far more modest goals, and proved more successful - it was the attempt to give a simple phenomenological description of the nuclear potential, with data from NN scattering experiments being its basis. Such a model can be used as input for nuclear structure calculations, and serve as a reference point for comparisons with models founded entirely on theory. The most general form of a nonrelativistic potential can be derived from invariance considerations (e.g., Galilei-invariance). Using a set of such invariant

operators, Gammel and Thaler constructed the first quantitative NN potential ever, which may well be considered the ancestor of today's realistic phenomenological potentials. The Gammel-Thaler potential introduced a *hard core* region at small distances to account for the sign change of the $^1S_0$ phase shift at laboratory energies above $250\,\mathrm{MeV}$. Improved phenomenological potentials were constructed in the following years, most notable among them Reid's hard- and soft-core models, one of which became the most frequently used potential in nuclear structure calculations in the 1970s.

The attempt to model the nuclear force as a pion-exchange QFT, on the other hand, was considered a failure in the 1960s, for reasons which are clear nowadays — the crucial impact of chiral symmetry on pion dynamics was not known at the time. In light of the phenomenological experience with the nucleon-nucleon interaction, Breit and others revived theories using additional mesons which had been shown to predict these features. The subsequent discovery of heavy mesons like the ρ in Brookhaven and the ω in Berkeley, both in 1961, sparked new developments, the first of which were the so-called one-boson exchange (OBE) models. These models are based on Yukawa's theory, but in addition they take advantage of the observation that groups of mesons are correlated due to the strong interaction between them. Uncorrelated multi-pion exchanges were neglected altogether, creating a certain unease in their application. Nevertheless, OBE models are preferable for pragmatic reasons – OBE evaluation is straightforward, and the NN data can be described reasonably well with very few parameters, i.e., meson-nucleon couplings and vertex cutoffs, which therefore acquire, at least in principle, a physical meaning.

Work to derive the nuclear force proceeded along the lines of dispersion and field theory, and accidentally, most of it was done in two European capitals, Paris and Bonn, the results being the Paris potential ([17] and Sect. 1.5.1), published in 1980, and the Bonn full model ([10] and Sect. 1.2), published in 1987.

The Paris and Bonn potentials, along with the meson-theoretic Nijmegen potential (Sect. 1.5.2) and a series of phenomenological interactions constructed by the Argonne (Urbana and Argonne series, see Sect. 1.3) group, came to be known as the "realistic potentials" in the 1990s. They describe phase shifts and other low energy observables with high precision, and are therefore considered good starting points for nuclear structure calculations. However, even nuclear many-body calculations combining these interactions with the most powerful techniques like the quasi-exact Green's Function Monte Carlo (GFMC) method show a shortcoming of these models — their inherent lack of genuine three- or higher many-nucleon forces, due to their construction from phase shift data, i.e., two-nucleon scattering. This issue remains unresolved to the present day — several models for $3N$-forces have been proposed and employed in calculations, but their free parameters are ultimately not much more than additional fit parameters. A way to address this and other problems of the realistic potentials would be the derivation of the NN-interaction, including many-nucleon-forces, from first principles.

Nowadays, QCD has been established as the microscopic theory of the strong interaction. The force responsible for binding a nucleus together is a mere residual effect of the more fundamental quark-gluon interactions, and for this reason, the chance of ever deriving it directly from QCD are considerably slim. The problem is exacerbated by the non-perturbative character of QCD at low energies. Although some QCD-inspired theories like the Skyrmion or constituent quark cluster models were developed, they are at

heart still phenomenological like the meson theories since they are modeled after QCD, not derived from it. In addition, only the quantitative features of the nuclear force are predicted correctly, while the qualitative results are poor – hence they are the exact opposite of the high-precision potentials, which are partly based on phenomenology but yield good results.

1.2 The Bonn Model and Derived Potentials

The *full Bonn model* [10] is a field-theoretic meson-exchange model for the nucleon-nucleon interaction. Starting from a Lagrangian which contains nucleons, mesons (see below) and the Δ-isobar, the Bonn group evaluated a wide range of diagrams in time-ordered perturbation theory (as is usual in many-body physics), from one-boson exchanges to 3π- and 4π-diagrams with and without intermediate isobars. The Bonn model exhibits sensitive cancellations between different types of diagrams, and the 3π and 4π contributions decrease in size in a way that indicates convergence of the perturbation series. Several of the small effects are dropped in the process of constructing potentials since it involves further approximations and, of course, fitting to data.

The model includes six mesons below $1\,\mathrm{GeV}$: π, η, σ' (2π-s-wave resonance), ρ, ω, δ. Other mesons of similar mass are dropped either because of their strange-quark content, which means that their coupling to the nucleon is suppressed by the *Okubo-Zweig-Iizuka (OZI) rule*, or because their range would be below the vertex cutoff ranges employed to account for the extended substructure of the hadrons. The Lagrangian thus contains three types of basic couplings, for pseudoscalar, scalar, and vector mesons, respectively:

$$\mathcal{L}_{NNps} = g_{ps}\overline{\psi}i\gamma^5\psi\varphi_{(ps)}\,, \tag{1.1}$$

$$\mathcal{L}_{NNs} = g_s\overline{\psi}\psi\varphi_s\,, \tag{1.2}$$

$$\mathcal{L}_{NNv} = g_v\overline{\psi}\gamma_\mu\psi\varphi_v^\mu + \frac{f_v}{4m_v}\overline{\psi}\sigma_{\mu\nu}\psi(\partial^\mu\varphi_v^\nu - \partial^\nu\varphi_v^\mu)\,. \tag{1.3}$$

In the case of isovector mesons – π, ρ, δ – the replacement

$$\varphi_\alpha \longrightarrow \boldsymbol{\tau} \cdot \boldsymbol{\varphi}_\alpha \tag{1.4}$$

has to be made.

Alternative to the *pseudoscalar* coupling of Eq. (1.1), the *pseudovector* coupling

$$\mathcal{L}_{NNps} = \frac{f_{ps}}{m_{ps}}\overline{\psi}\gamma^5\gamma^\mu\psi\partial_\mu\varphi_{(ps)}\,, \quad f_{ps} = \frac{m_{ps}}{2m_N}g_{ps}\,, \tag{1.5}$$

can be employed for the pseudoscalar mesons π and η. In fact, in π-N scattering a dominant p-wave (i.e., vector) contribution is found. In relativistic calculations, (1.1) is found to produce unphysically high antinucleon contributions, while (1.5) gives more realistic results. Another noteworthy point is the appearance of the pseudovector coupling as an effective coupling due to chiral invariance (see Sect. 1.4). Both couplings reduce to the same nonrelativistic expressions.

OBE, 2π-exchange, and π-ρ-exchange contributions are calculated from these interaction Lagrangians and Δ-nucleon-meson terms, with the additional use of a monopole

or dipole vertex form factor to regulate the amplitudes at short ranges:

$$F_\alpha(\boldsymbol{q}^2) = \left(\frac{\Lambda_\alpha^2 - m_\alpha^2}{\Lambda_\alpha^2 + \boldsymbol{q}^2} \right)^{n_\alpha} . \tag{1.6}$$

A general OBE Feynman amplitude in the center-of-mass system of the interacting nucleons reads

$$-i\overline{v}_\alpha(k',k) = \overline{u}_1(\boldsymbol{k}')\Gamma_1^{(\alpha)}u_1(\boldsymbol{k})P_\alpha(k',k)\overline{u}_2(-\boldsymbol{k}')\Gamma_2^{(\alpha)}u_2(-\boldsymbol{k}) , \tag{1.7}$$

where P_α and $\Gamma^{(\alpha)}$ denote the corresponding meson propagators and vertices, respectively, and $\boldsymbol{k}$ and $\boldsymbol{k}'$ denote the initial and final relative momenta. The OBE potential is then defined by

$$v(\boldsymbol{k}',\boldsymbol{k}) = \sqrt{\frac{m_N}{E}}\sqrt{\frac{m_N}{E'}} \sum_\alpha \overline{v}_\alpha(\boldsymbol{k}',\boldsymbol{k})F_\alpha^2(\boldsymbol{k}'-\boldsymbol{k};\Lambda_\alpha) , \tag{1.8}$$

where the sum runs over all mesons, E and E' are the initial and final energies of the nucleons, and m_N denotes the nucleon mass. The square-root factors are included to allow the application of reduction schemes like the *Blankenbecler-Sugar method* [18], which recast the four-dimensional Bethe-Salpeter equation into the form of the Lippmann-Schwinger equation and hence make it possible to use these relativistic potential expressions in a consistent way in nonrelativistic nuclear structure and scattering calculations.

Starting from the full model, the Bonn group has constructed several OBE potentials, both in momentum (OBEPQ) and configuration space (OBEPR) [11]. Of particular interest to this work are the two configuration space potentials, Bonn-A and -B. In order to outline their derivation (and for later use), consider the one-pion exchange amplitude

$$\begin{aligned}\overline{v}_\pi(\boldsymbol{k}',\boldsymbol{k}) = &-\frac{g_\pi^2}{4m_N^2}\frac{(E'+m_N)(E+m_N)}{(\boldsymbol{k}'-\boldsymbol{k})^2+m_\pi^2}\left(\frac{\boldsymbol{\sigma}_1\cdot\boldsymbol{k}'}{E'+m_N} - \frac{\boldsymbol{\sigma}_1\cdot\boldsymbol{k}}{E+m_N} \right) \\ &\times \left(\frac{\boldsymbol{\sigma}_2\cdot\boldsymbol{k}'}{E'+m_N} - \frac{\boldsymbol{\sigma}_2\cdot\boldsymbol{k}}{E+m_N} \right)\end{aligned} \tag{1.9}$$

(notation as in Eq. (1.8)). Note that (1.9) (as well as the other OBE amplitudes derived from Eq. (1.7)) is a *nonlocal* expression, since Fourier transformation into configuration space will yield functions of r and r', the relative positions of the incoming and outgoing nucleons, respectively, and the energy-dependent square root factors create additional nonlocality. Thus, if one wants to construct a local potential, which is technically easier to use in coordinate space calculations, further approximations are necessary.

The standard approach is to use the *on-shell approximation*, i.e., set $E' = E$ in the spinors and square root factors, and subsequently expand them in terms of the momenta

$$\boldsymbol{q} = \boldsymbol{k}' - \boldsymbol{k} \quad \text{and} \quad \boldsymbol{p} = \frac{1}{2}(\boldsymbol{k}' + \boldsymbol{k}) . \tag{1.10}$$

By keeping the lowest order terms, nonlocality enters the r-space potential through $\boldsymbol{p}^2$ and $\boldsymbol{q} \times \boldsymbol{p}$, the former providing Δ, the latter angular momentum terms after Fourier transformation. This scheme yields the OPE amplitude

$$v_\pi^{(\text{loc})}(\boldsymbol{q}) = -\frac{g_\pi^2}{4m_N^2}\frac{(\boldsymbol{\sigma}_1\cdot\boldsymbol{q})(\boldsymbol{\sigma}_2\cdot\boldsymbol{q})}{\boldsymbol{q}^2+m_\pi^2} , \tag{1.11}$$

where the index (loc) indicates that the amplitude has been localized, as it only depends on one momentum. Subsequent Fourier transformation yields

$$v_\pi^{(loc)}(\boldsymbol{r}) = \frac{g_\pi^2}{4\pi}\frac{1}{3}\left(\frac{m_\pi}{2m_N}\right)^2\left[\left(m_\pi\mathcal{Y}(m_\pi r) - \frac{4\pi}{m_\pi^2}\delta^3(\boldsymbol{r})\right)\boldsymbol{\sigma}_1\cdot\boldsymbol{\sigma}_2 \right.$$
$$\left. + m_\pi\mathcal{Z}(m_\pi r)\mathrm{s}_{12}\right] \tag{1.12}$$

where

$$\mathrm{s}_{12} \equiv 3(\boldsymbol{\sigma}_1\cdot\hat{\mathbf{r}})(\boldsymbol{\sigma}_2\cdot\hat{\mathbf{r}}) - \boldsymbol{\sigma}_1\cdot\boldsymbol{\sigma}_2 \tag{1.13}$$

is the *tensor operator*, and the *Yukawa functions* are defined by

$$\mathcal{Y}(x) \equiv \frac{e^{-x}}{x} \quad\text{and}\quad \mathcal{Z}(x) \equiv \left(1 + \frac{3}{x} + \frac{3}{x^2}\right)\mathcal{Y}(x). \tag{1.14}$$

This is the familiar *local OPE potential*, which coincides with the result one would obtain by using the *static limit* $E' \approx E \approx m_N$. Upon inspection, it turns out that the various approximations substantially enhance the off-shell contributions of the tensor force [12]. Thus, nuclear structure or nuclear matter calculations, which depend on the off-shell properties of the interaction, will significantly differ from results obtained with local potentials if the Bonn interaction is used in form of the amplitudes (1.7). Once all OBE amplitudes have been treated with the described approximation scheme, the general structure of the OBEPR potentials reads

$$\mathrm{v} = \sum_{S,T}v_{ST}^c(\mathrm{r})\,\Pi_{ST} + \sum_{S,T}\frac{1}{2}\left(v_{ST}^p(\mathrm{r})\mathbf{p}^2 + \mathbf{p}^2 v_{ST}^p(\mathrm{r})\right)\Pi_{ST}$$
$$+ \sum_T v_T^t(\mathrm{r})\,\mathrm{s}_{12}\,\Pi_T + \sum_T v_T^{ls}(\mathrm{r})\,\mathbf{l}\cdot\mathbf{s}\,\Pi_T, \tag{1.15}$$

where $\mathbf{l}\cdot\mathbf{s}$ is the spin-orbit operator, and Π_T and Π_{ST} are projection operators on the T and ST-channels (cf. Appendix E), respectively. The radial dependencies of the interaction are given by superpositions of Yukawa functions and their derivatives, as contributed by each meson.

Multimeson and σ' exchanges are accounted for by the introduction of two fictitious σ mesons, one for each isospin channel. Their properties are used as the 'main' degrees of freedom for a data fit — generally, one will aim to reproduce the predictions of the full model by adjusting them. The potential keeps the five other mesons from the full model, each associated with three parameters — a mass, a coupling constant, and the value of the cutoff for the vertex form factor (setting $n_\alpha = 1$ in (1.6)). The five 'real' meson masses and the pion coupling are held fixed, so there is a total of 15 parameters used to fit phase shift data; their values are listed in Tab. 1.1.

The Bonn-A potential will be used for calculations in this work, because it has a weaker tensor force than Bonn-B and is therefore considered a better starting point for the handling of tensor correlations in the UCOM framework described in Chapter 2.

The newest member of the Bonn family of interactions is the high-precision CD-Bonn potential [12]. Aside from accounting for changes in coupling constants, most
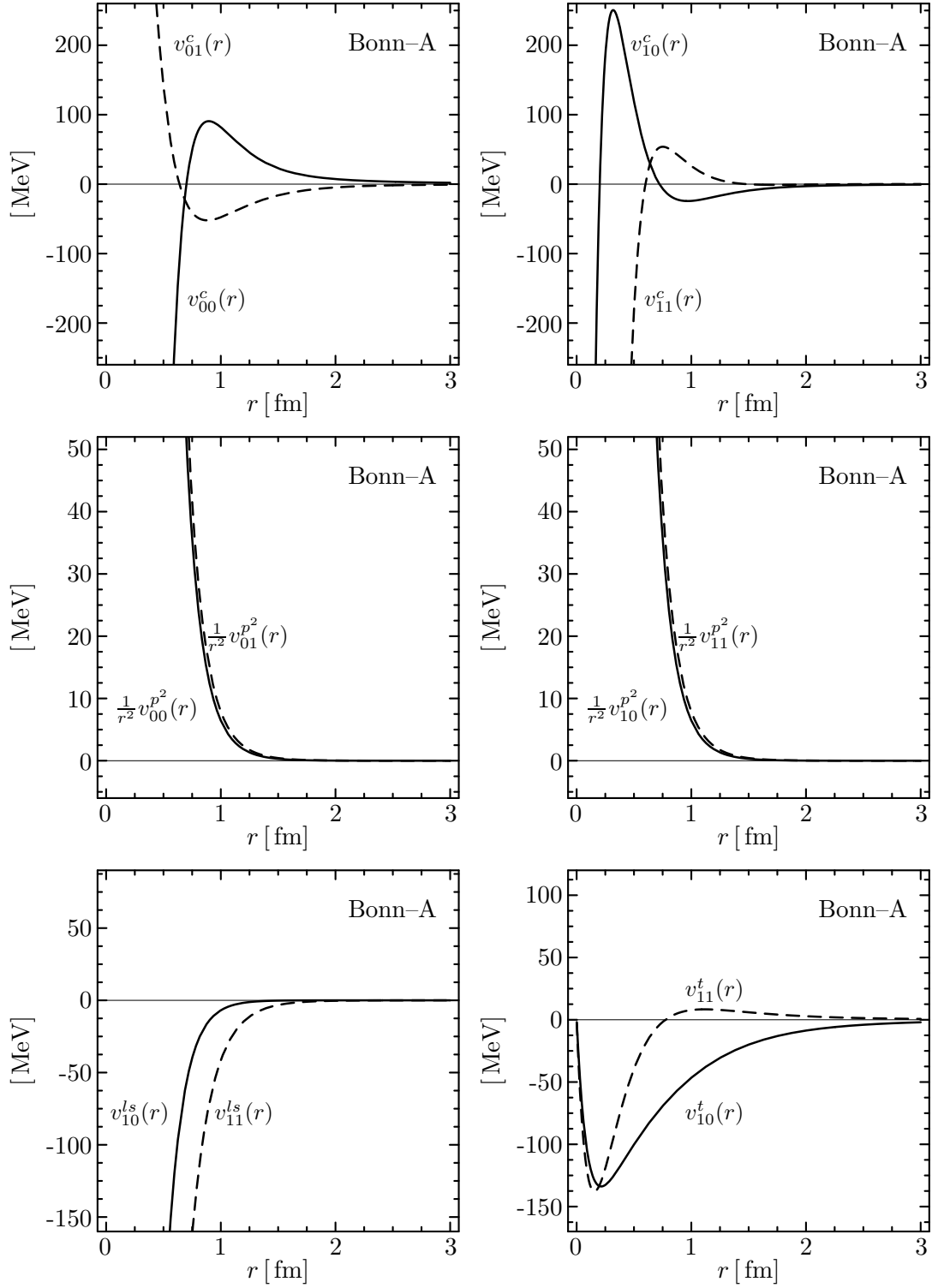
Figure 1.1: Radial dependencies of the Bonn-A configuration space potential. The momentum-dependent potential has been weighted by $1/r^2$ for better comparison with the l^2-part of AV18 (see Fig. 1.3).

	$m\,[\,\mathrm{MeV}\,]$	Bonn-A		Bonn-B	
		$g^2/4\pi$	$\Lambda\,[\,\mathrm{GeV}\,]$	$g^2/4\pi$	$\Lambda\,[\,\mathrm{GeV}\,]$
π	138.03	14.9	1.3	14.9	2.0
η	548.8	2.0	1.5	0.	–
ρ	769.0	1.2	1.2	1.7	1.1
ω	782.6	25.0	1.4	29.0	1.3
δ	983.0	2.742	2.0	6.729	2.0
$\sigma_{T=1}$	550.0	8.7171	2.0	8.8322	1.4
$\sigma_{T=0}$	710 / 700	17.6205	2.0	16.0707	2.0

Table 1.1: Parameters of the configuration space Bonn-A and -B potentials ([11]). The tensor/vector coupling ratios are held at $f_\rho/g_\rho = 6.1$ and $f_\omega/g_\omega = 0.0$. Bonn-A uses 710 MeV for the $\sigma_{T=0}$ mass, Bonn-B 700 MeV.

notably g_π, over the years, it is also the first Bonn potential taking *charge independence breaking* (CIB) and *charge symmetry breaking* (CSB) into account in order to improve the agreement with experimental data. Formally, this means that

$$\big[\mathrm{v}, \mathbf{t}\big] \neq 0 \quad \text{and/or} \quad \big[\mathrm{v}, e^{i\pi \mathrm{t}_2}\big] \neq 0\,, \tag{1.16}$$

i.e., the interaction is no longer invariant under general rotations (CIB) or rotations by π around the 2-axis (CSB) in isospin space. The main causes are the pion and neutron-proton mass differences, or, from a more fundamental point of view, the mass difference between the u and d quarks. Multimeson exchanges like 2π and $\pi\rho$ lead to significant CIB and CSB effects, too. Since the fits of the older Bonn potentials indicate that a vanishing coupling for the η meson is favorable (see Tab. 1.1), the new model drops it completely, just like the δ meson, whose contribution was found to be very small. CD-Bonn's excellent agreement with experimental phase shifts is achieved by refitting the σ mesons in each partial wave, increasing the amount of free parameters to 43 and turning it into an essentially phenomenological potential. Unfortunately, no 'official' non-relativistic description is available, and the partial wave representation prevents its use with the FMD basis underlying our existing computer programs, because the FMD states are no angular momentum eigenstates (see Chapter 3). In nuclear structure calculations, CD-Bonn is supplemented by a refined electromagnetic interaction developed by the Nijmegen group for their phase-shift analysis [19], including one- and two-photon Coulomb terms, the Darwin-Foldy term (see e.g., [20]) as a first order relativistic correction, vacuum polarization, and a magnetic dipole-dipole interaction.

1.3 The Argonne Interactions

The Argonne V18 potential is the latest in a series of local potentials constructed by the Argonne group, its predecessors being the Urbana V14 and Argonne V14 interactions [21]. AV18 consists of three main parts – the local coordinate space OPE potential familiar from the discussion of the Bonn model in Sect. 1.2, a phenomenological parametrization of the intermediate- and short-range part of the NN interaction, and

ST(NN)	Type	$I\,[\mathrm{MeV}]$	$P\,[\mathrm{MeV}]$	$Q\,[\mathrm{MeV}]$	$R\,[\mathrm{MeV}]$
01(pp)	c	-11.27028	3346.6874	1859.5627*	0
01(np)	c	-10.66788	3126.5542	1746.4298*	0
01(nn)	c	-11.27028	3342.7664	1857.4367*	0
01	l^2	0.12472	16.7780	9.0972*	0
00	c	-2.09971	1204.4301	511.9380*	0
	l^2	-0.31452	217.4559	117.9063*	0
11(pp)	c	-7.62701	1815.4920	969.3863*	1847.8059
11(np)	c	-7.62701	1813.5315	966.2483*	1847.8059
11(nn)	c	-7.62701	1811.5710	967.2603*	1847.8059
11	l^2	0.06709	342.0669	185.4713*	-615.2339
	t	1.07985	0	-190.0949	-811.2040
	ls	-0.62697	-570.5571	-309.3605*	819.1222
	$(ls)^2$	0.74129	9.3418	5.0652*	-376.4384
10	c	-8.62770	2605.2682	1459.6345*	441.9733
	l^2	-0.13201	253.4350	137.4144*	-1.0076
	t	1.485601	0	-1126.8359	370.1324
	ls	0.10180	86.0658	46.6655*	-356.5175
	$(ls)^2$	0.07357	-217.5791	-117.9731*	18.3935

Table 1.2: AV18 short-range potential parameters. The asterisk denotes that the value was computed by Eq. (1.22) and not fit. The parameters of the Woods-Saxon function are held at $r_0 = 0.5$ fm and $a_0 = 0.2$ fm, the cutoff is always $c = 2.1$ fm^{-2}.

the electromagnetic interaction of the Nijmegen group:

$$\mathrm{v} = \mathrm{v}_\pi + \mathrm{v}_{\mathrm{sr}} + \mathrm{v}_{\mathrm{em}}\,. \tag{1.17}$$

Charge-independence breaking (CIB) is taken into account by distinguishing between the charged and neutral pion exchanges as well as nn, pp and np scattering. As a caveat, one should note that the Bonn and Argonne groups use slightly different definitions of the pion decay constant f^2 (cf. Eq. (1.5)):

$$f^{2(\mathrm{AV18})} = 0.075 \iff \frac{f_\pi^{2(\mathrm{B\text{-}A})}}{4\pi} = \frac{g_\pi^2}{4\pi}\frac{m_\pi^2}{4m_N^2}\,. \tag{1.18}$$

Instead of the dipole form factors used in the Bonn model, the AV18 potential is regulated by multiplying the Yukawa functions $\mathcal{Y}$ and $\mathcal{Z}$ (Eq. (1.14)) with exponential form factors:

$$f_{\mathcal{Y}}(r) = 1 - e^{-cr^2} \quad \text{and} \quad f_{\mathcal{Z}}(r) = \left(1 - e^{-cr^2}\right)^2\,. \tag{1.19}$$

The radial dependencies of the phenomenological part are parametrized by

$$v^i_{STM_T}(r) = I^i_{STM_T}\mathcal{Z}^2(\mu r)f_{\mathcal{Z}}^2(r) + \left[P^i_{STM_T} + \mu r Q^i_{STM_T} + (\mu r)^2 R^i_{STM_T}\right]W(r)\,, \tag{1.20}$$

where i runs over the different operator types ($c, t, l^2, ls, (ls)^2$), M_T denotes the isospin projection, μ is the average of the pion masses, and

$$W(r) = \left[1 + e^{(r-r_0)/a}\right]^{-1} \tag{1.21}$$
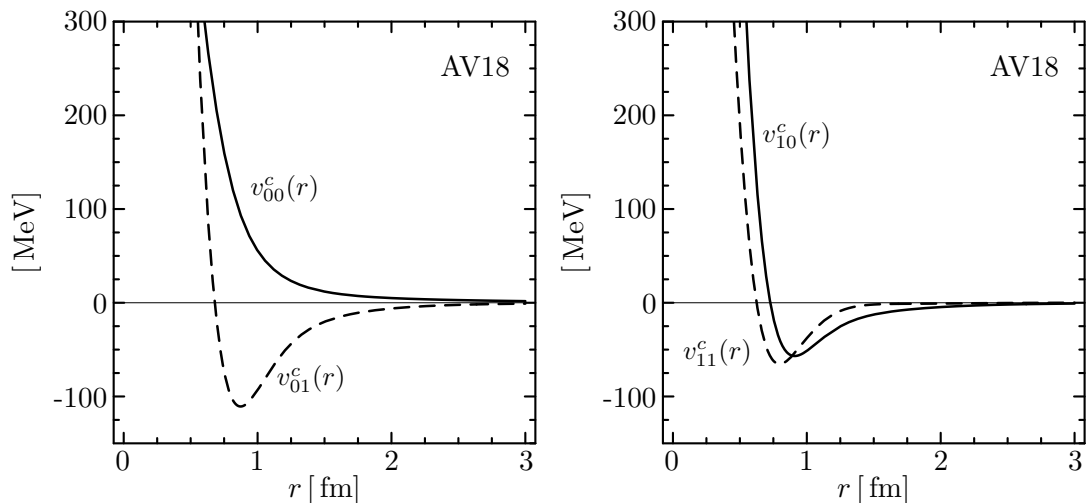
Figure 1.2: Radial dependencies of the AV18 potential. Depicted is the central part of AV18, projected onto the four ST-channels.

is a *Woods-Saxon* function providing the short-range core. With the imposition of the additional regularization conditions

$$v^t_{STM_T}(r = 0) = 0 \quad \text{and} \quad \left.\frac{\partial v^{i\neq t}_{STM_T}}{\partial r}\right|_{r=0} = 0 \,, \tag{1.22}$$

a total of 40 nonzero intermediate- and short-range parameters $I^i_{STM_T}, P^i_{STM_T}, Q^i_{STM_T}$, and $R^i_{STM_T}$ remain. Their values are listed in Tab. 1.2.

The potential given in (STM_T)-channels can be projected onto 18 operators, thus giving AV18 its name. For this work, however, we will prefer working with the ST-projected potential. As shown in Tab. 1.2, charge dependence (CD) and charge asymmetry (CA) in the phenomenological part of the potential are caused by the splitting of the central potential in the $T = 1$ channel only, while the OPE part contributes CIB effects both to the $T = 1$ central and tensor parts. The charge-dependent part of AV18 is then given by

$$\begin{aligned}
\mathrm{v}^{CD}_{ST} = &\frac{1}{6}\left[\frac{1}{2}(v^c_{S1,pp}(\mathrm{r}) + v^c_{S1,nn}(\mathrm{r})) - v^c_{S1,np}(\mathrm{r})\right]\mathrm{t}_{12} \\
&+ \frac{1}{6}\left[\frac{1}{2}(v^t_{S1,pp}(\mathrm{r}) + v^t_{S1,nn}(\mathrm{r})) - v^t_{S1,np}(\mathrm{r})\right]\mathrm{s}_{12}\mathrm{t}_{12}\,,
\end{aligned} \tag{1.23}$$

where the isotensor operator

$$\mathrm{t}_{12} \equiv 3\tau_{z,1}\tau_{z,2} - \boldsymbol{\tau}_1 \cdot \boldsymbol{\tau}_2 \tag{1.24}$$

has been introduced, and for the charge-asymmetric part one finds

$$\mathrm{v}^{CA}_{ST} = \frac{1}{4}(v^c_{S1,pp}(\mathrm{r}) - v^c_{S1,nn}(\mathrm{r}))(\tau_{z,1} + \tau_{z,2})\,. \tag{1.25}$$
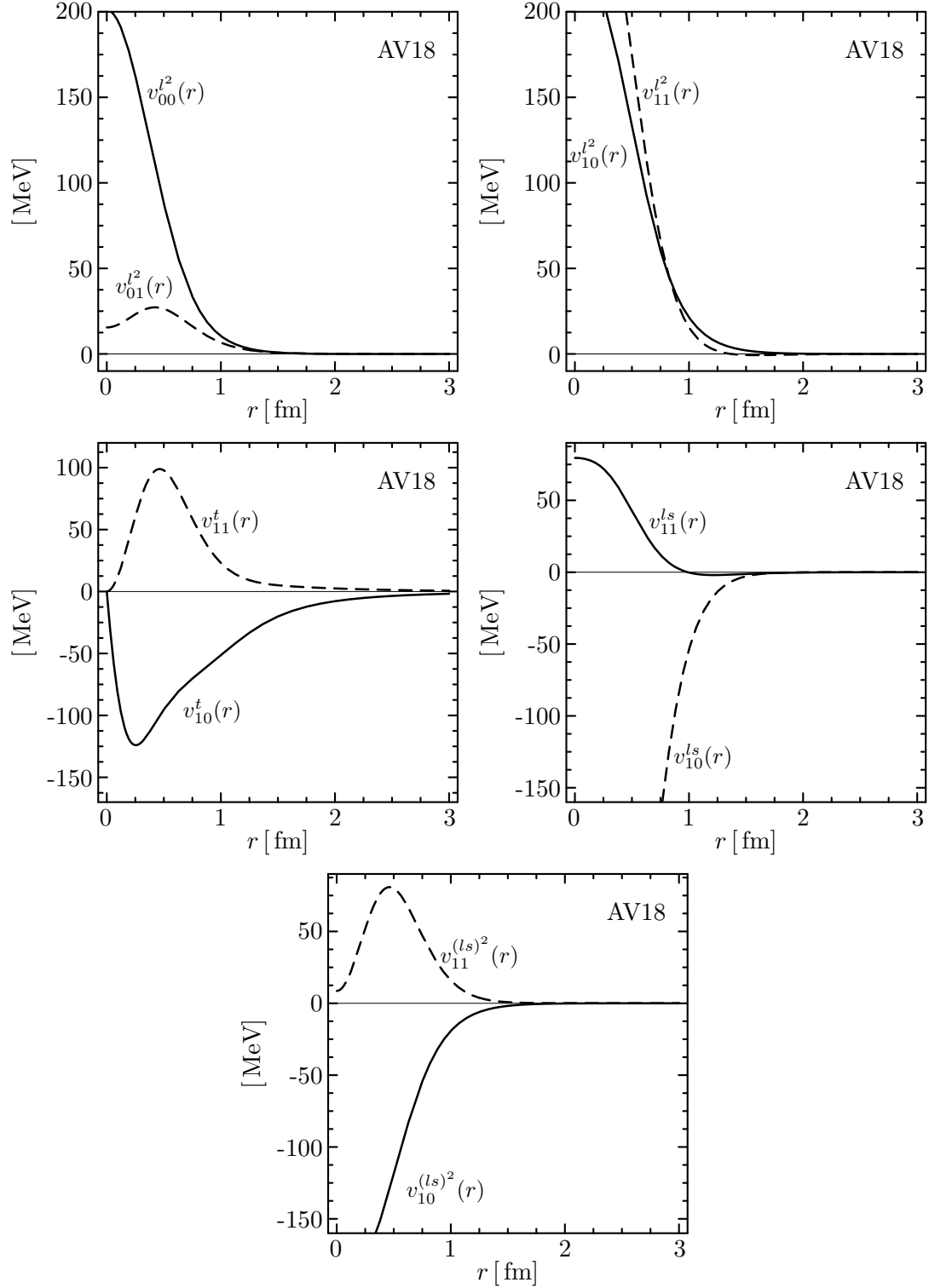
Figure 1.3: Radial dependencies of the AV18 potential (cont.). Depicted are the tensor, angular momentum, spin-orbit, and quadratic spin-orbit parts of AV18 in the four ST-channels.

The charge-independent part of AV18 reads

$$v = \sum_{ST} v_{ST}^{c,CI}(r)\,\Pi_{ST} + \sum_{T} v_{1T}^{t,CI}(r)\,s_{12}\Pi_{1T} + \sum_{ST} v_{ST}^{l^2}(r)\,\mathbf{l}^2\Pi_{ST}$$
$$+ \sum_{T} v_{1T}^{ls}(r)\,\mathbf{l}\cdot\mathbf{s}\,\Pi_{1T} + \sum_{T} v_{1T}^{(ls)^2}(r)\,(\mathbf{l}\cdot\mathbf{s})^2\,\Pi_{1T}\,, \tag{1.26}$$

where

$$v_{ST}^{i,CI}(r) = \begin{cases} \frac{1}{3}\left(v_{S1,pp}^{i}(r) + v_{S1,nn}^{i}(r) + v_{S1,np}^{i}(r)\right) & \text{for } T = 1 \\ v_{ST}^{i}(r) & \text{for } T = 0 \end{cases} \tag{1.27}$$

with $i = c, t$. The radial dependencies in the four ST-channels are plotted by interaction type in Figs. 1.2 and 1.3.

1.4 The Chiral NN Potential

Recent years have seen efforts to make contact between QCD and low-energy nuclear physics by means of effective field theories (EFTs). The notion of an *effective* theory suggests that the theory is not *fundamental*, but it is considered very likely nowadays that all quantum field theories, including the supposedly fundamental standard model, are just low-energy approximations of some 'higher' theory. Underlying these considerations is the recognition of distinct energy scales in nature, each having their characteristic degrees of freedom. Once higher energy or, equivalently, smaller distance scales are probed, new degrees of freedom become relevant, e.g., the quark substructure of hadrons in scattering experiments. In the same manner, a transition to lower energy scales leads to a "freezing out" of some degrees of freedom which become irrelevant.

Weinberg showed that the most general Lagrangian consistent with the symmetries of the underlying theory needs to be considered in order to construct an EFT [22, 23]. This will ensure that one obtains the most general possible S-matrix consistent with these symmetries, analyticity, (perturbative) unitarity, and the cluster decomposition principle, and therefore the correct low-energy limit of the underlying theory. Further assumptions, especially regarding the renormalizability of the theory, are to be avoided — this does not pose a problem, since the EFT is only defined up to a certain energy scale.

Naturally, one can think of infinitely many consistent interaction terms for the effective Lagrangian, so a scheme to identify the relevant terms is required. Applying the basic concept of EFTs, interaction terms are classified by powers of (p/Λ), where p is a four-momentum typical for the interaction, and Λ is the scale beyond which the effective theory is not valid any more. With such a *power counting scheme* at hand, one can now perform perturbative calculations with a finite number of interaction terms. As an example, consider the description of a weak interaction process by Fermi's theory (cf. Fig. 1.4). It is applicable as long as the involved four-momenta are small in comparison to the W-boson mass m_W, one of the mediators of the weak interaction in the Standard Model. In these cases, the denominator of the W-boson propagator can be approximated,

$$\frac{1}{p^2 - m_W^2 + i\varepsilon} \approx \frac{1}{m_W^2}\,, \tag{1.28}$$
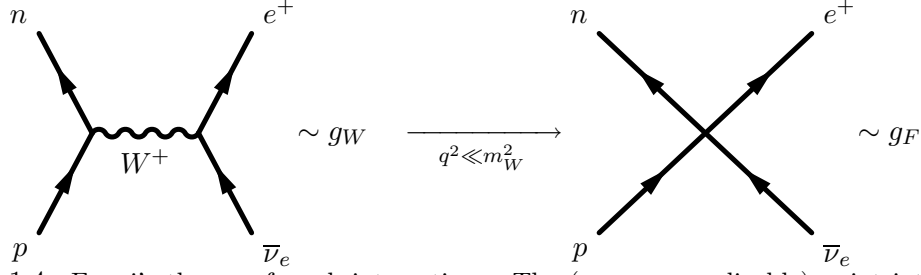
Figure 1.4: Fermi's theory of weak interactions. The (non-renormalizable) point interaction of fermion fields (right) can be understood as a low-energy limit of a standard model process mediated by W^+ exchange (left). q^2 denotes the four-momentum transfer between proton and neutron, m_W is the W-boson mass, and g_W and g_F are the weak and Fermi coupling constants, respectively.

and one obtains an effective point interaction of fermion fields. The 'effect' of the W-boson is contained in the effective coupling constant,

$$g_F \sim \frac{g_W}{m_W^2} . \tag{1.29}$$

Once the four-momenta and m_W become comparable in size, the propagator starts to *resonate*, and Fermi's theory breaks down since the dynamics of the W are no longer negligible[1].

In the case of QCD, the transition from the 'fundamental' to the effective level happens through the spontaneous breakdown of chiral symmetry. For chiral symmetry between three quark flavors — u, d, and s — the breakdown of $SU(3)_L \times SU(3)_R$ to $SU(3)_V$ reduces the number of symmetry generators by $3^2 - 1 = 8$, and one expects eight pseudoscalar Goldstone bosons, which can be identified with the lightest mesons — $\pi^0, \pi^\pm, K^0, \overline{K}^0, K^\pm$, and η. Their non-zero masses [24] are attributed to the approximative nature of the chiral symmetry, which is explicitly broken by the non-vanishing quark masses. Since the u and d masses are very small, and $m_u \approx m_d \ll m_s$, the approximation is better for a two-flavor chiral symmetry with only the pions as Goldstone bosons.

The effective field theory describing the chiral dynamics of hadrons at low energies is known as *chiral perturbation theory* (χPT) [25]. It is applicable up to the scale Λ_χ, which is usually taken to be the mass of the ρ-meson, $m_\rho \approx 770 \, \text{MeV}$ [24], since ρ is the lightest meson *not* identifiable as a Goldstone boson associated with chiral symmetry breaking. As Λ_χ is approached, the ρ-propagator becomes resonant, and the meson's dynamics have to be taken into account explicitly. This is essentially the same situation as for Fermi's weak interaction theory and the W-boson.

In order to treat the NN-system in χPT, one has to overcome one further obstacle: obviously, the nucleon mass m_N is not small compared to Λ_χ, which leads to inconvenient interdependencies between tree and loop graphs of all orders [25]. The solution is to take a non-relativistic limit by further expanding in terms of $1/m_N$, i.e., the nucleons are treated as quasi-static sources of pion fields. This approach is known as the *heavy baryon* formulation of chiral perturbation theory, HBχPT. Within this framework, the

---

[1]One usually speaks of "new physics" coming into play.

effective Lagrangian reads

$$\mathcal{L}_{\text{eff}} = \mathcal{L}_{\pi\pi}^{(2)} + \hat{\mathcal{L}}_{\pi N}^{(1)} + \hat{\mathcal{L}}_{\pi N}^{(2)} + \hat{\mathcal{L}}_{\pi N}^{(3)} + \dots, \tag{1.30}$$

where the superscript refers to the so-called *chiral dimension* or *chiral order*, i.e., the number of derivatives (from the pseudovector pion couplings, cf. Sect. 1.2) or pion mass insertions, and the hat on $\hat{\mathcal{L}}_{\pi N}$ implies a heavy baryon 'projection'.

At leading order, the relativistic $\pi\pi$ Lagrangian is given by

$$\mathcal{L}_{\pi\pi}^{(2)} = \frac{f_\pi^2}{4} \text{tr}[\partial^\mu U \partial_\mu U^\dagger + m_\pi^2(U + U^\dagger)], \tag{1.31}$$

where m_π and f_π are the pion mass and decay constant in the *chiral limit* of vanishing quark masses, respectively, and the matrix-valued field U collects the pions

$$U = 1 + \frac{i}{f_\pi}\boldsymbol{\tau} \cdot \boldsymbol{\pi} - \frac{1}{2f_\pi^2}\boldsymbol{\pi}^2 - \frac{i\alpha}{f_\pi^3}(\boldsymbol{\tau} \cdot \boldsymbol{\pi})^3 + \frac{8\alpha - 1}{8f_\pi^4}\boldsymbol{\pi}^4 + \dots. \tag{1.32}$$

Here, the notation $\boldsymbol{\pi}$ indicates that the pion is an isovector particle. The factor α appearing in the expansion of U is arbitrary, which makes it necessary to group diagrams involving three- or four-pion vertices together so that the α-dependencies cancel.

At chiral dimension 1 and in lowest order in $1/m_N$, the πN Lagrangian reads

$$\begin{aligned} \hat{\mathcal{L}}_{\pi N}^{(1)} &= \overline{N}\left(D_0 - \frac{g_A}{2}\boldsymbol{\sigma} \cdot \boldsymbol{u}\right)N \\ &= \overline{N}\left(i\partial_0 - \frac{1}{4f_\pi^2}\boldsymbol{\tau} \cdot (\boldsymbol{\pi} \times \partial_0 \boldsymbol{\pi}) - \frac{g_A}{2f_\pi}\boldsymbol{\tau} \cdot (\boldsymbol{\sigma} \cdot \boldsymbol{\nabla})\boldsymbol{\pi}\right)N + \dots, \end{aligned} \tag{1.33}$$

where the spatial components of

$$u_\mu = -\frac{1}{f_\pi}\boldsymbol{\tau} \cdot \partial_\mu \boldsymbol{\pi} + \dots \tag{1.34}$$

and the 0-component of the covariant derivative

$$D_\mu = \partial_\mu + \frac{i}{4f_\pi^2}\boldsymbol{\tau} \cdot (\boldsymbol{\pi} \times \partial_0 \boldsymbol{\pi}) + \dots \tag{1.35}$$

have been inserted. In the HB formulation, the nucleon field operators N describe the spin in Pauli (two-component) instead of Dirac spinors, and they also contain Pauli spinors describing the isospin.

The HB-projected πN Lagrangian of chiral dimension 2 can be split into two distinct parts [26, 27],

$$\hat{\mathcal{L}}_{\pi N}^{(2)} = \hat{\mathcal{L}}_{\pi N, \text{fix}}^{(2)} + \hat{\mathcal{L}}_{\pi N, \text{ct}}^{(2)}, \tag{1.36}$$

where the 'fixed' part

$$\hat{\mathcal{L}}_{\pi N, \text{fix}}^{(2)} = \overline{N}\left(\frac{1}{2m_N}\boldsymbol{D} \cdot \boldsymbol{D} + i\frac{g_A}{4m_N}\{\boldsymbol{\sigma} \cdot \boldsymbol{D}, u_0\}\right)N \tag{1.37}$$

is entirely generated by the heavy baryon expansion of $\mathcal{L}_{\pi N}^{(1)}$ and does not contain any new free parameters, while the second part,

$$\hat{\mathcal{L}}_{\pi N,\text{ct}}^{(2)} = \overline{N}\bigg(2c_1 m_\pi^2 (U + U^\dagger) + \bigg(c_2 - \frac{g_A^2}{8m_N}\bigg)u_0^2 + $$
$$c_3 u_\mu u^\mu + \frac{i}{2}\bigg(c_4 + \frac{1}{4m_N}\bigg)\boldsymbol{\sigma}\cdot(\boldsymbol{u}\times\boldsymbol{u})\bigg)N\,, \tag{1.38}$$

contributes new πN interactions which depend on the *low energy constants* (LECs) c_1 to c_4. The latter need to be determined by fits to experimental data (e.g., pion-nucleon scattering).

The HB-projected Lagrangian at chiral dimension 3 can formally be written as

$$\hat{\mathcal{L}}_{\pi N}^{(3)} = \sum_{i=1}^{23}\hat{d}_i\overline{N}\hat{O}_i^{(3)}N + \hat{\mathcal{L}}_{\pi N,\text{fix}}^{(3)}\,, \tag{1.39}$$

where the $\hat{d}_i$ are a new set of LECs, and $\hat{\mathcal{L}}_{\pi N,\text{fix}}^{(3)}$ is again completely fixed by the HB-formalism. The number of LECs has increased notably while advancing from chiral dimension 2 to 3, which is a general trend for all EFTs. At chiral dimension 4, the relativistic and HB-projected Lagrangians already feature 118 linear independent LECs [26].

For NN scattering, only 4 linear independent terms of $\hat{\mathcal{L}}^{(3)}$ are important, for which the values of the corresponding $\hat{d}_i$ can be determined from fits of πN scattering data, for example. Aside from the discussed $\pi\pi$ and πN Lagrangians, there is also a Lagrangian containing contact terms, which arise in any EFT. In the present case, these contact interactions are between the (static) nucleons:

$$\mathcal{L}_{\overline{N}N} = \mathcal{L}_{\overline{N}N}^{(0)} + \mathcal{L}_{\overline{N}N}^{(2)} + \mathcal{L}_{\overline{N}N}^{(4)} + \dots\,, \tag{1.40}$$

where

$$\mathcal{L}_{\overline{N}N}^{(0)} = \frac{1}{2}C_S\overline{N}N\overline{N}N + \frac{1}{2}C_T\overline{N}\boldsymbol{\sigma}N\cdot\overline{N}\boldsymbol{\sigma}N\,, \tag{1.41}$$

with undetermined coefficients C_S and C_T. Similarly, the higher order $\mathcal{L}^{(\nu)}$ consist of $\overline{N}ON$ bilinears and their products, where O are operators constructed from σ-matrices and gradients[2].

Contact Lagrangians with odd chiral dimensions ν are not allowed, since their vertices would sport odd numbers of nucleon three-momenta, which is forbidden by parity invariance. For the same reason, the πN contacts in $\mathcal{L}^{(1)}$ and $\mathcal{L}^{(3)}$ can only contribute at the loop level, since the tree level contributions would violate parity, too.

The two contact terms of order $(Q/\Lambda_\chi)^0$ (see Eq. (1.41)), seven of order $(Q/\Lambda_\chi)^2$, and fifteen of order $(Q/\Lambda_\chi)^4$ all contribute to the NN-potential at order 4, aside from one- and two-pion exchange. Here, Q denotes either a pion four-momentum, a pion mass, or a nucleon *three*-momentum. The potential terms are regulated by multiplying them with a cutoff

$$\exp\left[-\left(\frac{p}{\Lambda}\right)^{2n} - \left(\frac{p'}{\Lambda}\right)^{2n}\right]\,, \tag{1.42}$$

---

[2]The $\boldsymbol{\sigma}$ structures arise in the non-relativistic limit of the Dirac matrices $1, \gamma^\mu, \sigma^{\mu\nu}, \gamma^5\gamma^\mu, \gamma^5$.

where $\Lambda = 0.5\,\text{GeV}$, and $p = |\boldsymbol{p}|$ and $p' = |\boldsymbol{p}'|$ are the moduli of the initial and final nucleon three-momenta in the center-of-mass system. The powers $2n$ are chosen such as to prevent the regulators from contributing at the order $(Q/\Lambda_\chi)^\nu$ of the terms they multiply.

The 24 contact terms and two charge dependent contact terms arising from the inclusion of isospin violation at next-to-leading order (denoted NLØ, [28]) are the main fit parameters of the recently published chiral potential by Entem and Machleidt [2]. In addition, they have taken the three LECs c_2, c_3, and c_4 to be semi-free, hence raising the amount of parameters to a total of 29. Aside from providing a phase shift fit which rivals the quality of the AV18 potential (which uses 40 parameters), the chiral potential has the additional attractive aspect that it contains well-defined three-nucleon forces [25]. Generally, three- and many-nucleon forces arise from multi-pion exchange in χPT, hence they are well-defined at each order ν.

1.5 Other Models

1.5.1 Dispersion Theory - the Paris Potential

When the field-theoretic program aiming to build a 'fundamental' microscopic theory around the pion failed in the 1950s, some physicists embarked on a different theoretical route, known as *dispersion theory*. In contrast to quantum field theory with its problems of renormalization, convergence and the very definition of a potential, dispersion theory drops Lagrangians, Hamiltonians and potentials altogether in order to deal with directly observable quantities only, e.g., scattering amplitudes, form factors, etc., in a non-perturbative way. Its principal framework is based on three assumptions (see e.g., [29]): *causality*, *unitarity*, and *crossing symmetry*. From (micro-)causality, one derives the analytic properties of a scattering amplitude, whose pole structure encodes information about particle masses and couplings. Furthermore, analytic continuation of the scattering amplitude establishes crossing symmetry, i.e., it links amplitudes of processes like

$$p \longrightarrow n + e^+ + \nu_e \qquad \text{and} \qquad p + \overline{\nu}_e \longrightarrow n + e^+\,, \qquad (1.43)$$

which differ by the replacement of particles and antiparticles with their counterparts in the incoming or outgoing channel. The unitarity of the S-matrix implies the *optical theorem* [29, 30], and thus relates the imaginary part of a scattering amplitude to the total cross section for a process.

A dispersion relation for a scattering amplitude f is usually given in the form

$$\text{Re}\, f(s) = \frac{1}{\pi}\mathcal{P}\int\limits_0^\infty ds'\, \frac{\text{Im}\, f(s')}{s' - s}\,, \qquad (1.44)$$

where s is some energy, e.g., the total energy in the center-of-mass system (as suggested by the use of the Mandelstam nomenclature). Then the identity

$$\frac{1}{s' - s - i\epsilon} = \mathcal{P}\frac{1}{s' - s} + i\pi\delta(s' - s) \qquad (1.45)$$

implies that the full amplitude is given by

$$f(s) = \frac{1}{\pi} \int\limits_0^\infty ds' \, \frac{\mathrm{Im}\, f(s')}{s' - s - i\epsilon} \, . \tag{1.46}$$

Usually, the imaginary part of $f(s)$ (e.g., a total cross section) is not known at large energies, but this knowledge is needed to describe the behavior at low s. The influence of the high-s region can be lessened by means of *subtractions*, e.g., one considers $(f(s) - f(0))/s$ instead of $f(s)$ and finds

$$f(s) = f(0) + \frac{s}{\pi} \int\limits_0^\infty \frac{ds'}{s'} \, \frac{\mathrm{Im}\, f(s')}{s' - s - i\epsilon} \, , \tag{1.47}$$

or generally

$$f(s) = R(s) + \frac{P(s)}{4\pi^2} \int\limits_0^\infty \frac{ds'}{P(s')} \, \frac{\mathrm{Im}\, f(s')}{s' - s - i\epsilon} \, , \tag{1.48}$$

where $P(s)$ and $R(s)$ are polynomials whose coefficients will be determined by normalization conditions imposed by either theory or experiment. The high energy region is suppressed by the factor $1/P(s)$ in Eq. (1.45). The method of subtractions is particularly important if $|f(s)|$ does not vanish in the limit $s \to \infty$, since this would cause non-vanishing contributions from the arcs of the contour integrals used to derive Eq. (1.45) in the first place. From a modern point of view, this procedure is reminiscent of renormalization and EFT techniques ([31, 30, 23]), and indeed, if dispersion relations are applied in EFTs, the coefficients of the polynomials, also called *subtraction constants*, are closely related to the parameters of effective Lagrangians [32].

The appeal of dispersion relations arises from the fact that Feynman diagrams have the same analytic structure as the amplitude they contribute to, and can therefore be rewritten as (subtracted) dispersion relations. In this way, one can extract the predictions of the theory without going through the calculation of sets of Feynman diagrams, which usually involves applying complicated regularization and renormalization techniques to deal with the divergences of each graph. Furthermore, $\mathrm{Im}\, f(s)$ is often known experimentally — think of the total scattering cross section, for example — and can therefore be considered an 'exact' or 'ideal' input.

Work along the dispersion theory line ultimately culminated in the final version of the Paris potential in 1980 [17]. It includes one-pion exchange, correlated and uncorrelated two-pion exchange, and ω-exchange contributions derived from dispersion theory as well as a phenomenological soft core. In configuration space, the potential is given by

$$\begin{aligned}
v = {} & \sum_{S,T} v_{ST}^c(\mathrm{r})\, \Pi_{ST} + \sum_{S,T} \left[\frac{\mathbf{p}^2}{m_N} v_{ST}^{p^2} + v_{ST}^{p^2} \frac{\mathbf{p}^2}{m_N} \right] \Pi_{ST} + \sum_T v_T^t(\mathrm{r})\, \mathrm{s}_{12}\, \Pi_T \\
& + \sum_T v_T^{ls}(\mathrm{r})\, \mathbf{l} \cdot \mathbf{s}\, \Pi_T + \sum_T v_T^q(\mathrm{r})\, \mathrm{q}_{12}\, \Pi_T \, ,
\end{aligned} \tag{1.49}$$

where the *quadratic spin-orbit tensor* q_{12} has been introduced:

$$q_{12} \equiv \frac{1}{2}((\boldsymbol{\sigma}_1 \cdot \mathbf{l})(\boldsymbol{\sigma}_2 \cdot \mathbf{l}) + (\boldsymbol{\sigma}_2 \cdot \mathbf{l})(\boldsymbol{\sigma}_1 \cdot \mathbf{l})) = (\boldsymbol{\sigma}_1 \cdot \mathbf{l})(\boldsymbol{\sigma}_2 \cdot \mathbf{l}) = \mathbf{l} \cdot \mathbf{s} - \mathbf{l}^2 + 2(\mathbf{l} \cdot \mathbf{s})^2 . \quad (1.50)$$

q_{12} arises from the decomposition of $(\mathbf{l} \cdot \mathbf{s})^2$ into irreducible tensor operators, for which a slightly different prescription will be employed in this work (cf. Sect. 4.1.2 and Appendix B).

The parametrized Paris potential presented in [17] fits the 14 radial dependencies in Eq. (1.49) with superpositions of Yukawa functions:

$$v_{ST}^i(r) = \sum_{j=1}^{12} g_{STj} \mathcal{Y}(\mu_{Tj}r) , \quad i = c, p^2 , \quad (1.51a)$$

$$v_T^{ls}(r) = \sum_{j=1}^{11} g_{Tj} \mathcal{Y}'(\mu_{Tj}r) , \quad (1.51b)$$

$$v_T^t(r) = \sum_{j=1}^{11} g_{Tj} \mathcal{Z}(\mu_{Tj}r) , \quad (1.51c)$$

$$v_T^q(r) = \sum_{j=1}^{11} g_{Tj} \left(\frac{1}{\mu_{Tj}r}\right)^2 \mathcal{Z}(\mu_{Tj}r) . \quad (1.51d)$$

The range parameters μ_j are held fixed, hence the 164 strengths g_j are fit parameters. They are constrained further by at least 22 additional conditions, depending on the required degree of accuracy. In the literature, $60 - 80$ parameters are assumed to be free (cf. [33]), as opposed to 12 parameters of the original dispersion theoretic potential [34].

1.5.2 The Nijmegen Potentials

The Nijmegen group has constructed several models over the past decades. Nijmegen-78 and the updated Nijmegen-93 [35] are derived from meson theory in a similar fashion like the Bonn potentials introduced in Sect. 1.2. There are differences in the choice of included particles — in addition to the π, η, σ' (also called ϵ), ρ, ω, and δ (also called a_0) these are the η', $S^*(975)$, and $\phi(1020)$ mesons, respectively. Furthermore, contributions of several Regge trajectories are taken into account (see e.g., [36]). In spite of this considerably large amount of particles, the total number of the Nijmegen-93's free parameters is only 15, and thus comparable to the Bonn models. Charge dependence enters the potential by taking the pion-mass splitting into account for the OPE part. The cooordinate-space potential reads (cf. (1.49))

$$\mathbf{v} = \sum_{S,T} v_{ST}^c(\mathbf{r}) \, \Pi_{ST} + \sum_{S,T} v_{ST}^s(\mathbf{r}) \, \boldsymbol{\sigma}_1 \cdot \boldsymbol{\sigma}_2 \, \Pi_{ST} + \sum_T v_T^t(\mathbf{r}) \, \mathbf{s}_{12} \, \Pi_T$$
$$+ \sum_T v_T^{ls}(\mathbf{r}) \, \mathbf{l} \cdot \mathbf{s} \, \Pi_T + \sum_T v_T^q(\mathbf{r}) \, q_{12} \, \Pi_T + \sum_T v_T^a(\mathbf{r}) \, a_{12} \, \Pi_T , \quad (1.52)$$

with q_{12} as defined in (1.50), and the so-called *antisymmetric spin-orbit operator* a_{12}

$$a_{12} \equiv \frac{1}{2}(\boldsymbol{\sigma}_1 - \boldsymbol{\sigma}_2) \cdot \mathbf{l}, \quad (1.53)$$

	PWA93	Nijm I	Nijm II	Reid93	Nijm93	AV18	CD-Bonn
type	nl	nl	l	l	nl	l	nl
n_{par}	39	41	47	50	15	40	43
pp	1.00	1.00	1.00	1.00	1.78	1.10	1.00
np	0.99	1.05	1.04	1.04	1.93	1.08	1.03
NN	0.99	1.03	1.03	1.03	1.87	1.09	1.02

Table 1.3: Comparison of χ^2/datum of CD-Bonn (Ref. [12]), AV18 (Ref. [9]), the Nijmegen potentials (Ref. [35]) and the Nijmegen PWA for the reproduction of the pp, np, and full Nijmegen databases [19] ($E_{\mathrm{lab}} \leq 350$ MeV). In addition, the number of parameters n_{par} and the character of the potential (l local, nl nonlocal) are shown.

which is not symmetric under particle exchange and can therefore not contribute in identical-particle scattering.

A comparison shows that the fit quality of the Nijmegen-93 potential is not considerably better than that of the Paris or Bonn potentials (see Sect. 1.6). In order to describe scattering data with a level of accuracy comparable to their own phase shift analysis [19], the Nijmegen group constructed both a local and a nonlocal potential, named Nijmegen-I & -II. These potentials take charge-dependence and charge symmetry breaking into account, and are refitted in every partial wave, similar to the CD-Bonn potential. The amount of free parameters therefore increases to 41 and 47, respectively.

In the spirit of Reid's construction of his famous soft-core potential [37], an updated version was developed and fit to the Nijmegen phase shift data. This Reid-93 potential has 50 free parameters.

1.6   A Comparison

The various potentials introduced in the previous sections describe the phase shifts of pp- and np-scattering with χ^2/datum ≈ 2.0 or better. Models which draw most of their parameters from theory — Bonn and Nijmegen-93 — are found at the upper limit of this range. Unfortunately, these potentials have never been applied to the same database, so a direct comparison is impossible. For the Bonn full model, Machleidt and Li found a χ^2/datum of 1.80 for 3228 NN data below 300 MeV [33]; values for the OBEPR potentials could not be found, but are expected to be slightly worse than those achieved for the full model due to the approximations necessary for their derivation. The Nijmegen-93 potential reproduces the full Nijmegen set of $E_{\mathrm{lab}} \leq 350$ MeV data (NN93) with χ^2/datum= 1.87 (see Tab. 1.3). The Paris group quotes the values 1.99 for pp- and 2.17 for np-scattering, using 913- and 2239-point databases at laboratory energies lower than 350 MeV, respectively for the parametrized potential (cf. Sect. 1.5.1, [17]).

The current high-precision potentials manage a χ^2/datum close to the perfect value 1.0. As mentioned before, this good description comes at the cost of introducing many fit parameters, i.e., the models are essentially *phenomenological* in nature despite the theoretical background some of them possess. In Tab. 1.3, the description of the NN93 database by these potentials is compared. Local and nonlocal potentials describe the

database	# of data	χ^2/datum		
		PWA93	CD-Bonn	AV18
1992 pp	1787	1.00	1.00	1.10
post-1992 pp	1145	1.24	1.03	1.74
1999 pp	2932	1.09	1.01	1.35
1992 np	2514	0.99	1.03	1.08
post-1992 np	544	0.99	0.99	1.02
1999 np	3058	0.99	1.02	1.07
1992 NN	4301	0.99	1.02	1.09
1999 NN	5990	1.04	1.02	1.21

Table 1.4: Comparison of χ^2/datum of CD-Bonn, AV18 and the Nijmegen PWA for the reproduction of the Nijmegen ('1992 data') and extended databases ('post-1992')at $E_{\mathrm{lab}} \leq 350$ MeV, as discussed in [12]. Data taken from Refs. [19], [9] and [12].

	# of data	NLO	NNLO	N^{3}LO	AV18
pp	2057	80.1	35.4	1.50	1.38
np	2402	36.2	10.1	1.10	1.04

Table 1.5: χ^2/datum for the reproduction of the 1999 NN database [12] below 290 MeV by χPT potentials of increasing order (cf. [2] and references therein) and the AV18 potential (Ref. [9]).

phase shifts equally well. Looking at the post-1999 data shown in Tab. 1.4, one finds that the uniformity encountered in the description of the NN93 database breaks down. The pp data shows a significant increase of χ^2/datum for both the Nijmegen partial-wave analysis (PWA) and the AV18 potential, caused primarily by their problems with describing new high-quality pp spin correlation data. Since the Nijmegen-I and -II as well as the Reid93 potentials are essentially equivalent to the PWA, their χ^2/datum increases, too.

Clearly, as both the local AV18 and the nonlocal Nijmegen PWA exhibit this discrepancy, the different character of these types of potentials cannot be the sole cause, which is made more evident by noting that the nonlocal CD-Bonn is able to describe the new data just as well as the NN93 set. In fact, the Unitary Correlation Operator Method (UCOM) introduced in Chapter 2 proves that one can always shift potential strength between interaction terms, local or nonlocal, without affecting the phase shifts at all.

As a possible source of the discrepancy in the pp-data description, one other difference remains — the treatment of the charge dependence and the breaking of charge symmetry. AV18 and the Nijmegen potentials and PWA use the same charge-dependent OPE part; the former introduces CSB only in its phenomenological central part (see Tab. 1.2), while the latter take no CSB into account at all. Contributions from multimeson exchanges are included in neither of the two models, but they *are* part of the full Bonn model (see Sect. 1.2). As described in [12], the σ mesons are tuned to reproduce the effects of the multimeson exchanges on the phase shifts once the transition to the

OBE picture is made.

With the recent development of the N^{3}LO chiral potential (see Sect. 1.4), this particular branch has made an encouraging step forward. As can be seen in Tab. 1.5, the new chiral potential is able to reproduce the 1999 pp and np data below 290 MeV discussed in [12] with a χ^2/datum comparable to the AV18 potential, while using only 29 parameters compared to the 40 employed by the latter. In addition, the fit model represented by the contact terms of the N^{3}LO potential is more systematic than the rather phenomenological choice of operators of AV18 (see e.g., [31]).

Chapter 2

The Unitary Correlation Operator Method

2.1 Basic Concepts

The aim of the Unitary Correlation Operator Method (UCOM) [4, 5, 6, 7] is the conjoining of realistic nuclear interactions with simple many-body states used, e.g., in mean field or shell model calculations. All realistic NN interactions have two properties which cause problems when they are used with simple many-body states in a naive fashion: the repulsive central core and the strong tensor force.

In order to describe a many-body system with central and tensor correlations between pairs of nucleons, the base states would have to provide the necessary degrees of freedom. The relative distances r_{mn} and total spin S_{mn} of all possible pairs (m, n) have to be encoded in the states. These degrees of freedom are needed to properly account for the strong suppression of the two-nucleon wavefunctions at distances below the core radius (Sect. 2.2), and the correlations between their total spin and relative distance (Sect. 2.3) due to the tensor force. Suited states would be rather complicated superpositions of partial wave states (see Appendix B), for example.

The *single* Slater determinants used in mean field models, on the other hand, depend on the position and spin of *single particles only*. The suppression of their two-body densities at ranges inside the core is weaker than for proper eigenstates of the relative distance operator, which causes very large or even divergent interaction energies. In addition, important binding energy contributions from the tensor force are missing, since the Slater determinants cannot reproduce the alignment between the spins and relative distances well. To remedy this shortcoming, the correlations are introduced into the many-body states by means of unitary correlation operators, which provide the necessary degrees of freedom in a systematic fashion.

One chooses to construct *unitary* correlation operators in order to preserve the norm of the states they are applied to. The unitarity also facilitates the switching between the two viewpoints which can be taken while pursuing this approach: one can either apply the correlation operator to the states of a specified simple model space, mapping it onto a new one which has the proper degrees of freedom to describe correlations, i.e.,

$$\left| \widetilde{\Psi} \right\rangle = \mathrm{C} \left| \Psi \right\rangle, \tag{2.1}$$

or perform a similarity transformation of the operators and evaluate them in a simple
model space:

$$\widetilde{O} = C^\dagger O C \,. \tag{2.2}$$

The tilde is used to denote correlated states and operators throughout this work (cf.
Appendix E). Expectation values and matrix elements do not depend on the way the
correlations are introduced, since

$$\langle\, \Phi \,|\, C^\dagger O C \,|\, \Psi \,\rangle = \langle\, \widetilde{\Phi} \,|\, O \,|\, \widetilde{\Psi} \,\rangle = \langle\, \Phi \,|\, \widetilde{O} \,|\, \Psi \,\rangle \,. \tag{2.3}$$

2.1.1   The Generator

Any unitary operator has the form

$$C = \exp(-iG)\,, \tag{2.4}$$

where G is the hermitian generator of the transformation it represents on the Hilbert
space of states. At this stage, one is already able to make some requirements concerning
the form of the generator. The aim is to handle *two-body* correlations, hence G will be a
two-body operator; in order to describe genuine three-body correlations, a corresponding
three-body generator would be required. Another prerequisite is the preservation of
the symmetries of the original Hamiltonian. In the case of the nonrelativistic NN
interaction, this implies invariance under the transformations belonging to the Galilei
group. G can then only depend on the relative coordinate and momentum of two
nucleons due to translation and boost invariance, respectively. In addition, rotational
invariance implies that G is a scalar operator, i.e., it transforms under the scalar ($j = 0$)
representation of the rotation group[1]. The most general generator G consistent with
the discussed symmetries is therefore

$$G = \sum_{i<j} g(\mathbf{r}_{ij}, \mathbf{q}_{ij}, \boldsymbol{\sigma}_i, \boldsymbol{\sigma}_j, \boldsymbol{\tau}_i, \boldsymbol{\tau}_j)\,, \tag{2.5}$$

where the indices i and j run over all particles in the space where G is to be defined.
One formally distinguishes between the two-body operator g, defined in a two-body
space, and the many-body operator G, defined on the A-body space (cf. Appendix E).

The final requirement will be that G obeys the *cluster decomposition principle*
(CDP), which states that observables of *separate subsystems* do not affect each other.
This implies that the correlation operator can be decomposed into a direct product of
correlation operators acting on the separate subsystems, i.e., particle clusters

$$C_A \longrightarrow C_n \otimes C_{A-n}\,. \tag{2.6}$$

A very nice discussion of the CDP, which also deals with the case of interactions of
infinite range, can be found in [29].

---

[1]Note that rotations are generated by the *total angular momentum operator*, which implies that even
though the 'tensor' operator s_{12} mixes orbital angular momenta, it is an irreducible tensor operator of
rank 0, too; see Appendix B.

2.1.2 Spin-Isospin Dependence

It is common practice to project the nuclear interaction on the four ST-channels, because certain parts of it do not contribute in all of them. The tensor and spin-orbit terms, in particular, have nonzero expectation values only in the $S = 1$ channels. In the case of a charge-independent, i.e., isoscalar NN interaction or negligible charge-independence breaking effects the ST channels remain (at least approximately) unmixed, and the ansatz

$$\mathrm{g} = \sum_{ST} \mathrm{g}_{ST} \Pi_{ST} \tag{2.7}$$

can be used for the generators in two-body space. Due to the property

$$\Pi_{ST} \Pi_{S'T'} = \Pi_{ST} \delta_{SS'} \delta_{TT'} \,, \tag{2.8}$$

the projection operators factor out of the exponential used to define the unitary correlation operator:

$$\mathrm{c} = \exp(-i\mathrm{g}) = \sum_{ST} \exp\left(-i\mathrm{g}_{ST}\right) \Pi_{ST} \,. \tag{2.9}$$

This implies

$$\widetilde{\mathrm{v}} = \mathrm{c}^\dagger \mathrm{vc} = \sum_{ST} \exp\left(i\mathrm{g}_{ST}\right) \mathrm{v}_{ST} \exp\left(-i\mathrm{g}_{ST}\right) \Pi_{ST} \,, \tag{2.10}$$

i.e., the correlations in the different ST-channels decouple, and the correlators for each channel can be determined independently.

2.1.3 Cluster Expansion

The correlation operator is defined as the exponential of the generator G discussed in the previous sections, implying that C is *not* a two-body operator due to the generation of operators with increasing particle number by repeated application of G. Consider many-body calculations in a Hilbert space with fixed particle number A, denoted $\mathcal{H}_A$. Owing to the cluster decomposition principle, the representation of a correlated operator will then be given by

$$\widetilde{\mathrm{O}} = \mathrm{C}^\dagger \mathrm{OC} = \sum_{i=1}^A \widetilde{\mathrm{O}}^{[i]} \,, \tag{2.11}$$

where $\widetilde{\mathrm{O}}^{[i]}$ denotes an *irreducible* i-particle operator. The $\widetilde{\mathrm{O}}^{[i]}$ are defined recursively:

$$\widetilde{\mathrm{O}}^{[1]} = \sum_{k,k'} \left\langle k \right| \mathrm{C}^\dagger \mathrm{OC} \left| k' \right\rangle \mathrm{a}_k^\dagger \mathrm{a}_{k'} = \sum_{k,k'} \left\langle k \right| \mathrm{O} \left| k' \right\rangle \mathrm{a}_k^\dagger \mathrm{a}_{k'} \,, \tag{2.12}$$

$$\widetilde{\mathrm{O}}^{[n]} = \frac{1}{(n!)^2} \sum_{\substack{k_1 \ldots k_n \\ k'_1 \ldots k'_n}} {}_a\left\langle k_1 \ldots k_n \right| \mathrm{C}^\dagger \mathrm{OC} - \sum_i^{n-1} \widetilde{\mathrm{O}}^{[i]} \left| k'_1, \ldots, k'_n \right\rangle_a$$
$$\times \mathrm{a}_{k_1}^\dagger \ldots \mathrm{a}_{k_n}^\dagger \mathrm{a}_{k'_n} \ldots \mathrm{a}_{k'_1} \,, \tag{2.13}$$

where $n \leq A$,

$$\left| k_1, \ldots, k_n \right\rangle_a = \mathrm{a}_{k_1}^\dagger \ldots \mathrm{a}_{k_n}^\dagger \left| \emptyset \right\rangle, \quad \mathrm{a}_{k_i} \left| \emptyset \right\rangle = 0, \tag{2.14}$$

and the index a affixed to the kets and bras implies antisymmetrization.

For practical applications, one would like to restrict the calculations to the second cluster order, since the third order contributions are already very involved. This approximation will be justified if the density of the system and the range of the correlators are sufficiently small. Otherwise, the probability to find more than two particles simultaneously inside the correlation volume increases, and the higher orders of the cluster expansion become non-negligible. The notation

$$\left[\mathrm{C}^\dagger \mathrm{O} \mathrm{C} \right]^{C2} = \widetilde{\mathrm{O}}^{[1]} + \widetilde{\mathrm{O}}^{[2]} \tag{2.15}$$

is introduced to indicate that the two-body approximation has been applied.

Two remarks are in order regarding the two-body approximation. First, a convenient way to study the correlations in the nucleus is provided by the one- and two-body density matrices:

$$\rho^{(1)}(q_1, q_1') \equiv \left\langle \Phi \right| \Psi^\dagger(q_1) \Psi(q_1') \left| \Phi \right\rangle, \tag{2.16}$$

$$\rho^{(2)}(q_1, q_2; q_1', q_2') \equiv \left\langle \Phi \right| \Psi^\dagger(q_1) \Psi^\dagger(q_2) \Psi(q_2') \Psi(q_1') \left| \Phi \right\rangle, \tag{2.17}$$

where $\Psi(q)$ and $\Psi^\dagger(q)$ are the usual field annihilation and creation operators[2], and the short hand notation $q_i = (\boldsymbol{x}_i, m_{s,i}, m_{t,i})$ was introduced. By using the *Wick theorem*, it is easy to prove the following *reduction formula*:

$$\int dq_2 \, \rho^{(2)}(q_1, q_2; q_1', q_2) = (A - 1)\rho^{(1)}(q_1, q_1'), \tag{2.18}$$

where the 'integration' over q implies integration over $\boldsymbol{x}$ and summation over m_s and m_t. The correlated density matrices

$$\widetilde{\rho}^{(1)}(q_1, q_1') = \left\langle \Phi \right| \mathrm{C}^\dagger \Psi^\dagger(q_1) \Psi(q_1') \mathrm{C} \left| \Phi \right\rangle = \sum_{n=1}^{A} \left\langle \Phi \right| \left[\mathrm{C}^\dagger \Psi^\dagger(q_1) \Psi(q_1') \mathrm{C} \right]^{[n]} \left| \Phi \right\rangle \tag{2.19}$$

and

$$\begin{aligned}
\widetilde{\rho}^{(2)}(q_1, q_2; q_1', q_2') &= \left\langle \Phi \right| \mathrm{C}^\dagger \Psi^\dagger(q_1) \Psi^\dagger(q_2) \Psi(q_2') \Psi(q_1') \mathrm{C} \left| \Phi \right\rangle \\
&= \sum_{n=2}^{A} \left\langle \phi \right| \left[\mathrm{C}^\dagger \Psi^\dagger(q_1) \Psi^\dagger(q_2) \Psi(q_2') \Psi(q_1') \mathrm{C} \right]^{[n]} \left| \phi \right\rangle
\end{aligned} \tag{2.20}$$

still satisfy the reduction formula, but *this will no longer be the case if the two-body approximation is applied*! However, in those cases when the truncation is justified, (2.18) will be a good approximation for the truncated correlated densities.

The second remark concerns the use of two-body approximated Hamiltonians in variational calculations. *Ritz' variational principle* [20] implies that, for a given trial state $\left| \Psi \right\rangle$, the inequality

$$\frac{\left\langle \Psi \right| \mathrm{H} \left| \Psi \right\rangle}{\left\langle \Psi | \Psi \right\rangle} \geq E_0 \tag{2.21}$$

---

[2]To avoid confusion, the many-body state will be called $\left| \Phi \right\rangle$ whenever field operators appear in a formula.
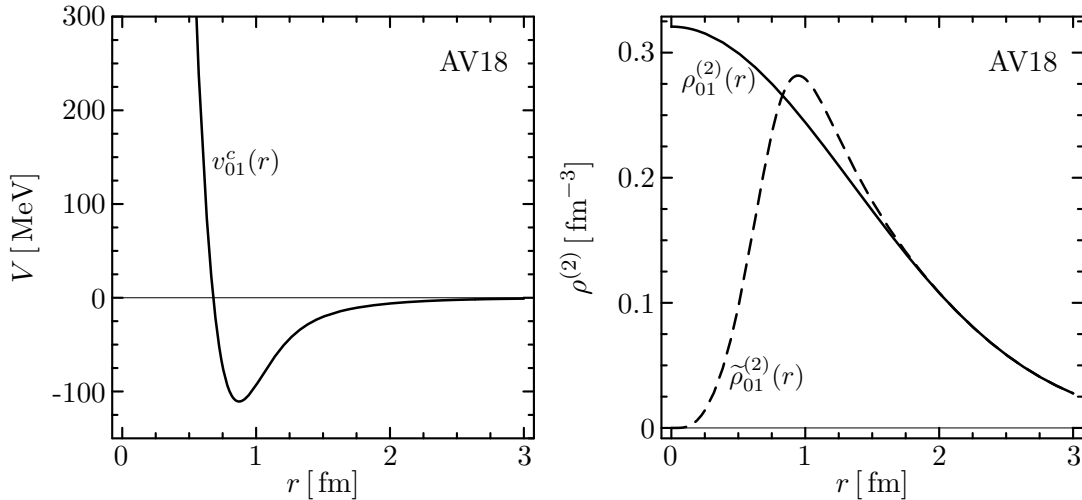
Figure 2.1: Correlation hole in the ^{4}He two-body density. The AV18 potential in the ST=01 channel is plotted on the left. The right figure shows the uncorrelated and correlated two-body densities obtained for a $L = 0$ ^{4}He harmonic oscillator shell model trial state [6, 38] which reproduces the experimental charge radius $r_{cms} = 1.6758$ fm.

holds, implying that the true groundstate energy E_0 is a rigorous lower bound to the expectation value of the Hamiltonian. This is no longer the case if the truncated Hamiltonian $\widetilde{\mathrm{H}}^{C2}$ is used due to cancellations between energy contributions of the different cluster orders.

2.2 Central Correlations

Let us have a look at the two-body density matrix (2.17). We introduce center-of-mass coordinates for the nucleons, assuming an average mass for protons and neutrons (cf. Appendix E),

$$\boldsymbol{x}_{\mathrm{cm}} = \frac{1}{2}(\boldsymbol{x}_1 + \boldsymbol{x}_2) \quad \text{and} \quad \boldsymbol{r} = \boldsymbol{x}_1 - \boldsymbol{x}_2 \,, \tag{2.22}$$

and couple their spins and isospins. Subsequent integration over $\boldsymbol{x}_{\mathrm{cm}}$ yields

$$\rho^{(2)}_{SM_S,TM_T}(\boldsymbol{r}) = \sum_{m_{s,1},m_{s,2}} \sum_{m_{t,1},m_{t,2}} \big\langle \tfrac{1}{2}m_{s,1}\tfrac{1}{2}m_{s,2}\big|SM_S\big\rangle \big\langle \tfrac{1}{2}m_{t,1}\tfrac{1}{2}m_{t,2}\big|TM_T\big\rangle$$
$$\times \int d^3 x_{\mathrm{cm}}\, \rho^{(2)}_{m_{s,1}m_{t,1};m_{s,2}m_{t,2}}(\boldsymbol{x}_{\mathrm{cm}} + \tfrac{\boldsymbol{r}}{2}, \boldsymbol{x}_{\mathrm{cm}} - \tfrac{\boldsymbol{r}}{2}; \boldsymbol{x}_{\mathrm{cm}} + \tfrac{\boldsymbol{r}}{2}, \boldsymbol{x}_{\mathrm{cm}} - \tfrac{\boldsymbol{r}}{2}) \tag{2.23}$$

for the probability of finding two nucleons with spin and isospin orientations M_S and M_T in the ST-channel at a relative distance $\boldsymbol{r}$. Since the NN interaction is rotationally invariant and (approximately) charge-independent, it is unnecessary to distinguish between M_S and M_T components when the two-body densities are studied.

For illustrative purposes, consider the Argonne V18 potential in the $ST = 01$ channel (see Sect. 1.3), and a trial state with relative angular momentum $L = 0$. By doing so, one only needs to consider the central part of the interaction, since the tensor- and
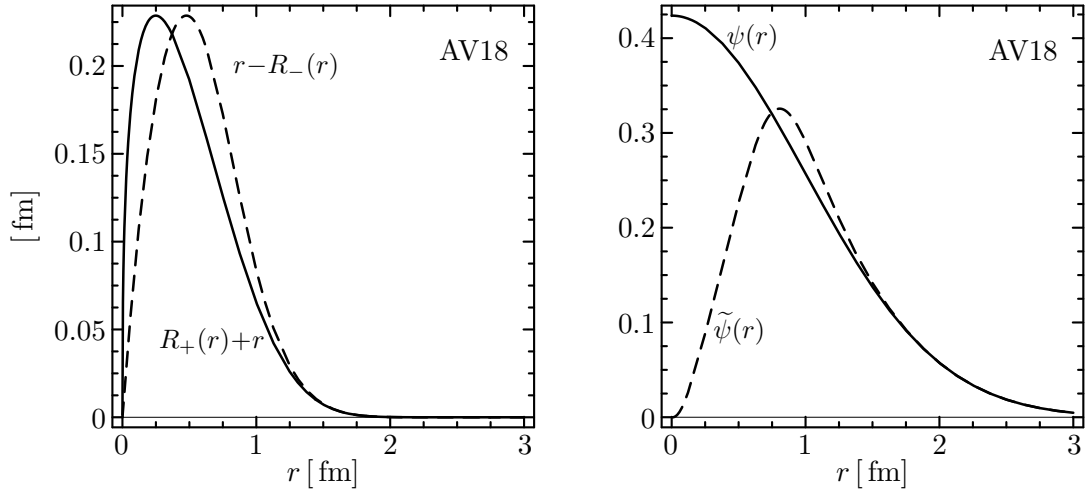
Figure 2.2: Left: central correlation functions $R_+(r) - r$ (solid) and $r - R_-(r)$ (dashed) for the AV18 potential in the $ST = 10$ channel (cf. Tab. C.1). Right: Action of the corresponding central correlator on a three-dimensional Gaussian wavefunction (cf. [6]).

spin-orbit terms only contribute in $S = 1$ channels, and the l^2-potential is obviously zero. AV18 has the same strong repulsive core as all realistic potentials. As can be seen in Fig. 2.1, this leads to a correlation hole at short distances in the two-body density. Mean-field model states cannot reproduce this strong suppression and therefore lead to non-vanishing probabilities to find nucleons within the core, which in turn result in unphysically high or even infinite energies.

In order to induce a short-range correlation hole in the model state, one needs to construct an operator which shifts the nucleons out of the range of the core region. Since this shift has to occur in the radial direction, along the relative distance vector $\boldsymbol{r}$ of the two nucleons, the obvious choice is to use the radial momentum operator

$$\mathrm{p}_r = \frac{1}{2}\left(\mathbf{p} \cdot \hat{\mathbf{r}} + \hat{\mathbf{r}} \cdot \mathbf{p}\right) \tag{2.24}$$

(see Sect. A.1) to construct the generator g_r. The strength of the shift will be modeled by an r-dependent function $s(r)$, because the shift needs to be strong for relative distances smaller than the core radius, and at large distances no shift is needed at all. A suitable hermitian generator is therefore given by

$$\mathrm{g}_r \equiv \frac{1}{2}\left(\mathrm{p}_r s(\mathrm{r}) + s(\mathrm{r})\mathrm{p}_r\right) = s(\mathrm{r})\mathrm{p}_r - \frac{i}{2}s'(\mathrm{r})\,. \tag{2.25}$$

Applying the unitary correlation operator constructed from (2.25) to a nucleon-pair wavefunction in coordinate space, one finds

$$\left\langle \boldsymbol{x}_{cm}, \boldsymbol{r}\,\middle|\, \mathrm{c}\,\middle|\, \phi\,\right\rangle = \mathcal{R}_-(r)\left\langle \boldsymbol{x}_{\mathrm{cm}}, \boldsymbol{R}_-(\boldsymbol{r})\middle|\phi\,\right\rangle \tag{2.26}$$

and

$$\left\langle \boldsymbol{x}_{cm}, \boldsymbol{r}\,\middle|\, \mathrm{c}^\dagger\,\middle|\, \phi\,\right\rangle = \mathcal{R}_+(r)\left\langle \boldsymbol{x}_{\mathrm{cm}}, \boldsymbol{R}_+(\boldsymbol{r})\middle|\phi\,\right\rangle, \tag{2.27}$$

where

$$\boldsymbol{R}_{\pm}\boldsymbol{r} = R_{\pm}(r)\hat{\boldsymbol{r}} \quad \text{and} \quad \mathcal{R}_{\pm}(r) = \frac{R_{\pm}(r)}{r}\sqrt{R'_{\pm}(r)}\,. \tag{2.28}$$

The functions $R_{\pm}(r)$ will be referred to as *(UCOM) correlation functions.* They are mutually inverse:

$$R_{\pm}[R_{\mp}(r)] = r\,. \tag{2.29}$$

The functions $\mathcal{R}_{\pm}(r)$ provide a metric factor which preserves the norm of the wavefunction and thus, together with the inversion properties of the $R_{\pm}(r)$, reflects the unitarity of the transformation generated by g_r. The correlation functions are connected to the shift function $s(r)$ by the integral equation

$$\int_r^{R_{\pm}(r)} \frac{d\xi}{s(\xi)} = \pm 1\,, \tag{2.30}$$

which implies

$$R_{\pm}(r) \approx r \pm s(r) \tag{2.31}$$

for a weakly r-dependent $s(r)$, i.e., $s(r)$ can be interpreted as the distance of the radial shift of two nucleons at a relative distance r in this approximation. In practical calculations, it is technically advantageous to use the correlation functions to completely specify the behavior of a central correlation operator; in fact, the notion central correlator is used synonymously for both the function and the operator.

2.3 Tensor Correlations

Aside from the strongly repulsive core, all realistic NN potentials share another property — a strong tensor force, which primarily originates from one-pion exchange as outlined in Chapter 1. The tensor force induces strong correlations between the relative spatial orientation of a nucleon pair and the orientation of the nucleons' spins in the $S = 1$ channels, while the $S = 0$ channels remain unaffected due to the vanishing matrix elements of the total spin operator (cf. Appendix B).

The dipole-dipole interaction of two magnets is a simple classical analogy (see Fig. 2.3): the interaction has the same structure as s_{12} if $\boldsymbol{\sigma}_i$ is understood as the classical magnetic dipole moment vector for the moment. If the interaction is attractive, magnets with parallel magnetic moments $\boldsymbol{\sigma}_i$ align themselves such that the relative orientation $\boldsymbol{r}$ and $\boldsymbol{\sigma}_i$ are parallel, too, in order to lower the system's energy. Likewise, for magnets with antiparallel magnetic moments, the energetically preferred configuration is achieved by having the relative distance vector $\boldsymbol{r}$ being perpendicular to the $\boldsymbol{\sigma}_i$.

The deuteron is the paradigm of the influence of the tensor force in a nucleus. In relative coordinates and using the $(LS)J$-coupling, its exact ground state is given by

$$\big|\hat{\psi}^d; 1M\big\rangle = \big|\hat{\psi}_0^d, (01)1M\big\rangle + \big|\hat{\psi}_2^d, (21)1M\big\rangle\,, \tag{2.32}$$

where

$$\big\langle r\big|\hat{\psi}_{L=0,2}^d\big\rangle = \hat{\psi}_{L=0,2}^d(r) \tag{2.33}$$

denote the radial wavefunctions in the $^3S_1$ and $^3D_1$ partial waves, respectively, and the omitted isospin quantum numbers are fixed to $T = 0, M_T = 0$ by the asymmetry

$$V \sim - \left(3(\boldsymbol{\sigma}_1 \cdot \hat{\boldsymbol{r}})(\boldsymbol{\sigma}_2 \cdot \hat{\boldsymbol{r}}) - \boldsymbol{\sigma}_1 \cdot \boldsymbol{\sigma}_2 \right)$$
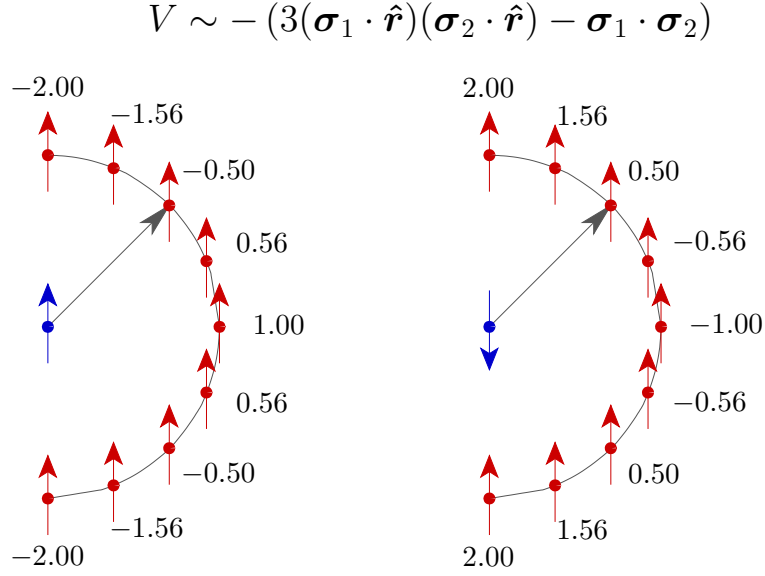
Figure 2.3: Classical analogy to the tensor interaction between parallel (left) and antiparallel spins (right): shown are the values of the 'classical' tensor structure corresponding to s_{12}. $\boldsymbol{\sigma}_i$ is to be understood as a classical vector describing, e.g., a magnetic dipole moment. An overall factor of (-1) has been introduced to reflect the attractive nature of the interaction.

of the full state. The $\hat{\psi}^d_L(r)$ can be obtained by solving the coupled system of radial Schrödinger equations numerically. Fig. 2.4 shows $\hat{\psi}^d_0(r)$ and $\hat{\psi}^d_2(r)$ for the AV18 and the Bonn-A interactions. The action of the tensor force is evident in the mixing of the two partial waves, because the tensor operator s_{12} is of rank 2 in coordinate space and does therefore not conserve L in nucleon-nucleon interactions.

Fig. 2.5 displays the exact deuteron two-body density projected on the spin triplet,

$$\hat{\rho}^{(2)}_{1M_S}(\boldsymbol{r}) = \frac{1}{3} \sum_{M=-1}^{1} \left| \langle \, \boldsymbol{r}; S = 1, M_S | \hat{\psi}_d; J = 1M \, \rangle \right|^2 , \qquad (2.34)$$

averaged over all possible spatial orientations. The hole due to the central correlations is clearly visible, as is the interplay between the spatial alignment and the spin of the nucleons. The shapes one finds for the density distributions are as expected from the classical analogy: nucleon pairs with parallel spins, $M_S = \pm 1$, are primarily located around the poles of a sphere whose z-direction is defined by the spin-polarization axis, and likewise the nucleon pairs with antiparallel spin, $M_S = 0$, are found in its equatorial region.

In order to construct a unitary tensor correlation operator c_Ω, T. Neff started from the following ansatz for an implicitly centrally correlated deuteron ground state (see [6, 7]):

$$\left| \psi_d; 1M \, \right\rangle = \left| \psi^d_0(01)1M \, \right\rangle, \quad \langle \, r | \psi^d_0 \, \rangle = \psi^d_0(r) . \qquad (2.35)$$

The tensor correlator has to map this $L = 0$ state onto the exact solution (2.32),

$$\left| \hat{\psi}_d; 1M \, \right\rangle = c_\Omega \left| \psi_d; 1M \, \right\rangle = \exp(-i g_\Omega) \left| \psi_d; 1M \, \right\rangle, \qquad (2.36)$$
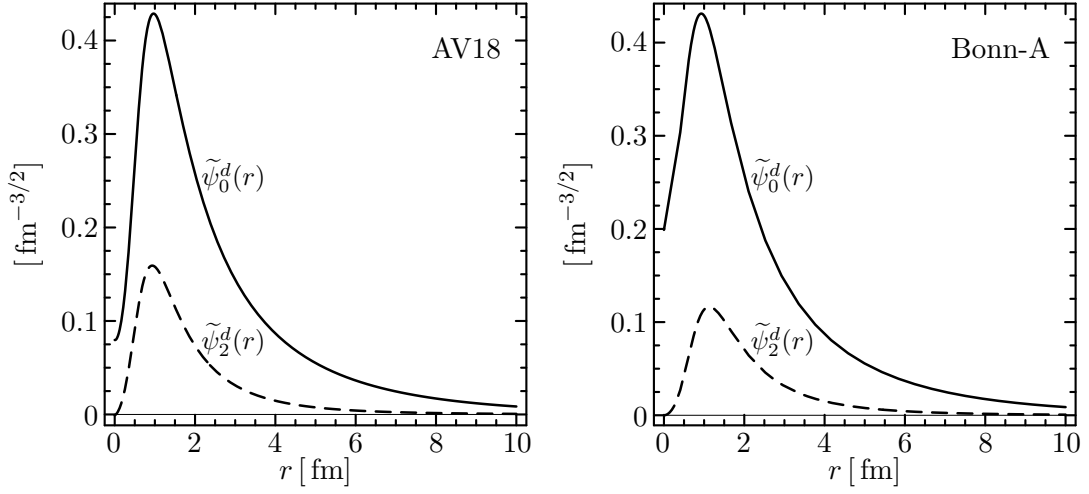
Figure 2.4: Exact deuteron wave functions $\hat{\psi}^d_{L=0,2}(r)$ for the AV18 (left) and Bonn-A potential (right). Note that AV18 has a larger $^3D_1$-wave admixture than Bonn-A. In addition, the correlation hole is larger for AV18 because its central core is stronger (cf. Figs. 1.1, 1.2, 1.3, and Ref. [6]).

i.e., the $L = 2$ admixture is entirely generated by c_Ω. This implies that the generator g_Ω has to be of rank 2 in coordinate space. By the general requirements formulated in Sect. 2.1.1, one can conclude that it has to be a rank 2 tensor in two-body spin space, too, because this is the only way both parts can be coupled to a scalar operator of rank 0 under the full rotation group. There is only one such operator in two-body spin space (see Appendix B):

$$s^{(2)}_q = \left\{ s^{(1)} s^{(1)} \right\}^{(2)}_q , \quad \text{where} \quad s^{(1)}_q = \frac{1}{2} \left(\sigma^{(1)} \otimes \mathbb{1} + \mathbb{1} \otimes \sigma^{(1)} \right) . \tag{2.37}$$

Note that the same reasoning is true for the tensor operator s_{12}, and therefore g_Ω will have a similar structure. In coordinate space, the shifts generated by g_Ω are required to be perpendicular to the radial shifts generated by g_r in order to decouple the actions of the central and tensor correlation operators as much as possible. As shown by T. Neff in [6, 7], this can be achieved by using the so-called *orbital momentum operator*

$$\mathbf{p}_\Omega = \frac{1}{2r}(\mathbf{l} \times \hat{\mathbf{r}} - \hat{\mathbf{r}} \times \mathbf{l}) \tag{2.38}$$

(see Sect. A.1) to construct the hermitian tensor operator

$$s_{12}(\mathbf{r}, \mathbf{p}_\Omega) = \frac{3}{2} \left((\boldsymbol{\sigma}_1 \cdot \mathbf{r})(\boldsymbol{\sigma}_2 \cdot \mathbf{p}_\Omega) + (\boldsymbol{\sigma}_1 \cdot \mathbf{p}_\Omega)(\boldsymbol{\sigma}_2 \cdot \mathbf{r}) - (\boldsymbol{\sigma}_1 \cdot \boldsymbol{\sigma}_2)(\mathbf{r} \cdot \mathbf{p}_\Omega + \mathbf{p}_\Omega \cdot \mathbf{r}) \right), \tag{2.39}$$

and from this the generator

$$g_\Omega = \vartheta(\mathrm{r}) s_{12}(\mathbf{r}, \mathbf{p}_\Omega) . \tag{2.40}$$

That g_Ω does not shift the relative wavefunction radially can easily be seen from the properties of $\mathbf{p}_\Omega$ and $\mathbf{r}$, which both commute with arbitrary functions of r. The tensor

$$S = 1, M_S = 0 \qquad\qquad\qquad S = 1, M_S = \pm 1$$
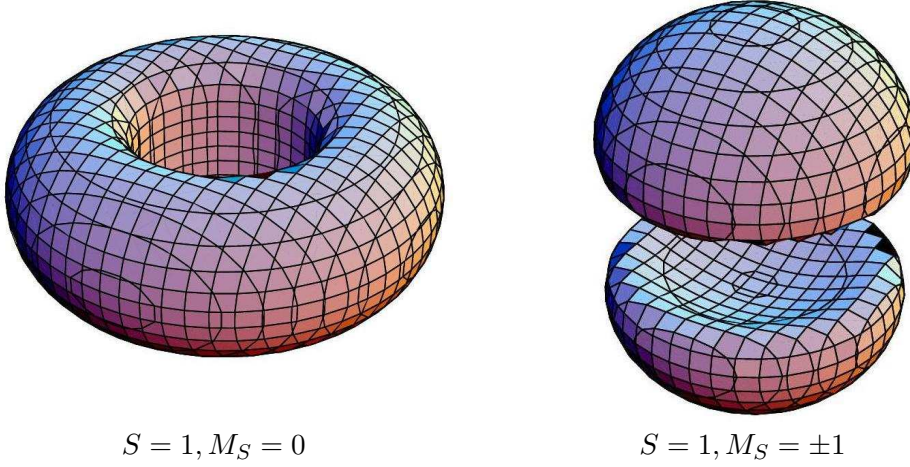
Figure 2.5: Isodensity surfaces at $\hat{\rho}^{(2)}_{1M_S} = 0.005$ fm^{-3} for the deuteron, calculated for the AV18 potential (cf. [6]).

correlation function $\vartheta(r)$ can be used to adjust the strength of the correlator, and as a tensor correlation operator is completely specified by $\vartheta(r)$, the term tensor correlator is used synonymously for both.

The action of the tensor correlator on angular momentum eigenstates like the ones in (2.36) can be derived using its matrix elements. Using the *Wigner-Eckart theorem* (B.38), one finds

$$\big\langle\, (L'S')J'M' \big|\, \mathrm{s}_{12}(\mathbf{r}, \mathbf{p}_\Omega)\, \big|(LS)JM \,\big\rangle =$$
$$\delta_{JJ'}\delta_{MM'}\delta_{SS'}\frac{\big\langle\, (L'S)J \big|\big|\, \mathrm{s}_{12}(\mathbf{r}, \mathbf{p}_\Omega)\, \big|\big|(LS)J \,\big\rangle}{\sqrt{2J+1}}\,, \qquad (2.41)$$

where the reduced matrix element is given by

$$\big\langle\, (L'S)J \big|\big|\, \mathrm{s}_{12}(\mathbf{r}, \mathbf{p}_\Omega)\, \big|\big|(LS)J \,\big\rangle =$$
$$3i\sqrt{J(J+1)}\sqrt{2J+1}\delta_{S1}(\delta_{L',J+1}\delta_{L,J-1} - \delta_{L',J-1}\delta_{L,J+1})\,; \qquad (2.42)$$

the second square root factor is common to all scalar operators and cancels the corresponding factor in the Wigner-Eckart theorem for the conventions employed in this work. The derivation of the matrix elements is outlined in Appendix B, and the non-vanishing ones for the lowest angular momenta J are listed in Tab. B.2. The resulting 2×2-matrix in each J-subspace can be simply exponentiated, and one finds

$$\mathrm{c}_\Omega \big|(J \mp 1, 1)JM \,\big\rangle =$$
$$\cos\left(\theta^{(J)}(\mathrm{r})\right) \big|(J \mp 1, 1)JM \,\big\rangle \pm \sin\left(\theta^{(J)}(\mathrm{r})\right) \big|(J \pm 1, 1)JM \,\big\rangle\,, \qquad (2.43)$$

where the shorthand notation

$$\theta^{(J)}(\mathrm{r}) \equiv 3\sqrt{J(J+1)}\vartheta(\mathrm{r}) \qquad (2.44)$$

has been introduced. For all other states, the tensor correlator reduces to the identity operator.

Using these results, Eq. (2.36) can be evaluated further:

$$
\begin{aligned}
\langle\, r\,|\, \mathrm{c}_\Omega\, |\,\psi_d; 1M\,\rangle = {} & \\
& \psi_0^d(r)\left[\cos\left(3\sqrt{2}\vartheta^d(r)\right)\,|(01)1M\,\rangle + \sin\left(3\sqrt{2}\vartheta^d(r)\right)\,|(21)1M\,\rangle\right].
\end{aligned}
\tag{2.45}
$$

By comparison with the exact deuteron solution (2.32), one can identify

$$
\hat{\psi}_0^d(r) = \psi_0^d(r)\cos\left(3\sqrt{2}\vartheta^d(r)\right) \quad\text{and}\quad \hat{\psi}_2^d(r) = \psi_0^d(r)\sin\left(3\sqrt{2}\vartheta^d(r)\right).
\tag{2.46}
$$

Dividing these equations yields

$$
\frac{\hat{\psi}_2^d(r)}{\hat{\psi}_0^d(r)} = \tan\left(3\sqrt{2}\vartheta^d(r)\right)
\tag{2.47}
$$

and the deuteron tensor correlation function $\vartheta^d(r)$ is obtained directly from the exact deuteron solution:

$$
\vartheta^d(r) = \frac{1}{3\sqrt{2}}\arctan\frac{\hat{\psi}_2^d(r)}{\hat{\psi}_0^d(r)}.
\tag{2.48}
$$

The $\vartheta^d(r)$ are plotted in Fig. 2.6 for the AV18 and Bonn-A interactions, together with the D-wave ground state admixtures for comparison. Since the deuteron trial state (2.35) did not have any $L = 2$ admixtures at all, these entire wavefunctions have to be generated by the tensor correlator, and this manifests itself in the very long range of the tensor correlation functions. The corresponding tensor correlator will induce notable many-nucleon correlations when applied in a many-body system, which in turn implies that the truncation of the cluster expansion after the two-body order ceases to be a good approximation. In order to avoid this problem, the low-momentum/long-range part of $\Delta L = 2$ admixtures should be present in the states of an aptly chosen model space, so that c_Ω can be restricted to short ranges.

2.4 Correlated Operators

In applications, it is more convenient to work with correlated operators than with correlated states, in particular once many-body calculations in a mean-field basis are performed. The correlated Hamiltonian at second cluster order is given by

$$
\widetilde{\mathrm{H}}^{C2} = \widetilde{\mathrm{T}}^{[1]} + \widetilde{\mathrm{T}}^{[2]} + \widetilde{\mathrm{V}}^{[2]} = \sum_i \widetilde{\mathrm{t}}_i^{[1]} + \sum_{i<j}\widetilde{\mathrm{t}}_{ij}^{[2]} + \sum_{i<j}\widetilde{\mathrm{v}}_{ij}^{[2]},
\tag{2.49}
$$

where the indices run over all nucleons and $\mathrm{o}_{i_1,\dots,i_k}^{[k]}$ denotes an irreducible k-body operator. The explicit construction of $\widetilde{\mathrm{t}}_i^{[1]}, \widetilde{\mathrm{t}}_{ij}^{[2]}$, and $\widetilde{\mathrm{v}}_{ij}^{[2]}$ is the aim of the present section.
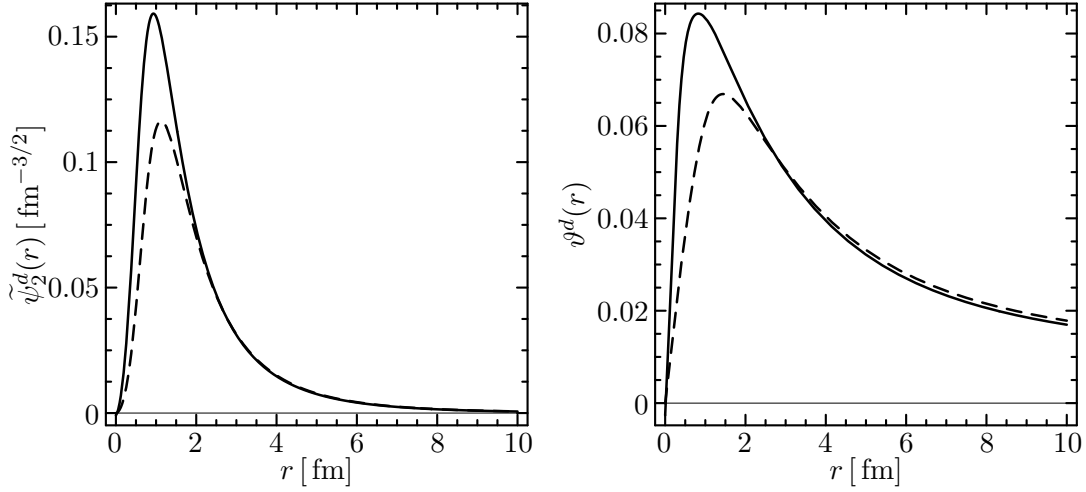
Figure 2.6: Deuteron correlation functions: shown are again the $^3D_1$ admixtures to the deuteron groundstate (left), and the deuteron correlation functions $\vartheta^d(r)$ for the AV18 (solid) and Bonn-A interactions (dashed) (cf. [6]).

2.4.1   Central Correlations

In two-body space, the correlated kinetic energy consists of a one- and a two-body operator. The one-body operator is identical to the uncorrelated kinetic energy because g_r is a two-body operator and $c = \exp(-ig_r)$ therefore only contains two-body and higher terms aside from the unit operator:

$$\widetilde{t}^{[1]} = c_r^\dagger t^{[1]} c_r = t^{[1]} \,. \tag{2.50}$$

The two-body kinetic energy is best evaluated in the center-of-mass system. In terms of the relative and total momentum operators

$$\mathbf{p}_{\text{rel}} = \frac{1}{2}(\mathbf{p}_1 - \mathbf{p}_2) \quad \text{and} \quad \mathbf{p}_{\text{cm}} = \mathbf{p}_1 + \mathbf{p}_2 \,, \tag{2.51}$$

the kinetic energies of relative and center-of-mass motion are

$$t_{\text{rel}} = \frac{\mathbf{p}_{\text{rel}}^2}{m_N} \quad \text{and} \quad t_{\text{cm}} = \frac{\mathbf{p}_{\text{cm}}^2}{4m_N} \,, \tag{2.52}$$

where the same average mass m_N was assumed for protons and neutrons. The orbital angular momentum will also be needed; it is easily verified that

$$\mathbf{l}_1 + \mathbf{l}_2 = \mathbf{l}_{\text{cm}} + \mathbf{l}_{\text{rel}} \,, \tag{2.53}$$

where

$$\mathbf{l}_{\text{rel}} = \mathbf{r} \times \mathbf{p}_{\text{rel}} \quad \text{and} \quad \mathbf{l}_{\text{cm}} = \mathbf{x}_{\text{cm}} \times \mathbf{p}_{\text{cm}} \,. \tag{2.54}$$

The center-of-mass kinetic energy is unaffected by the correlator, since it only acts on the relative coordinate. The kinetic energy of the relative motion can be decomposed into a radial and an angular part:

$$t = t_r + t_\Omega = \frac{p_r^2}{m_N} + \frac{\mathbf{l}^2}{m_N \, r^2} \,. \tag{2.55}$$
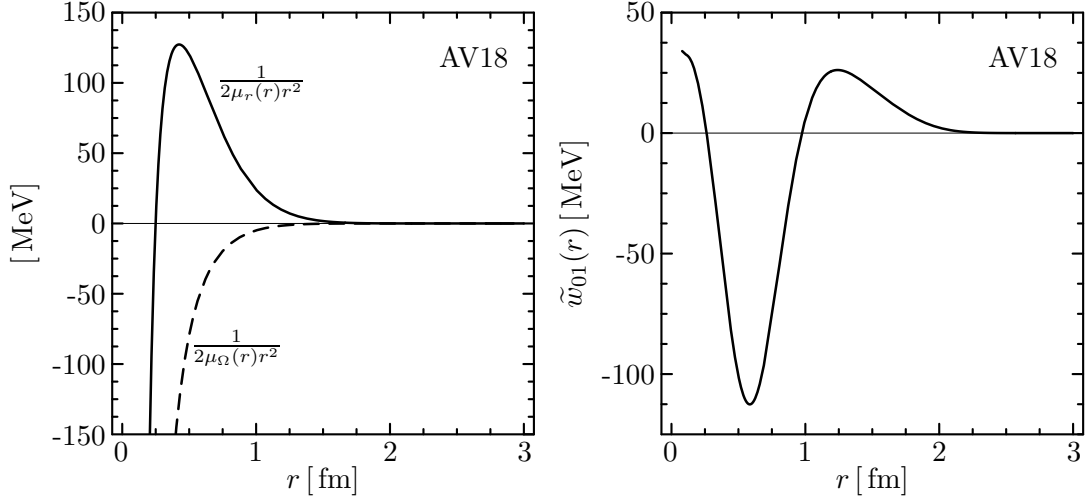
Figure 2.7: Centrally correlated kinetic energy (cf. [6]): shown are the inverse radial and angular masses, divided by r^2 for better comparison with other energies (left), and the local potential $\widetilde{w}_{01}$ (right), obtained with the AV18 central correlator min in the $ST = 01$ channel (cf. Tab. C.1).

Since one will mostly be dealing with relative motion, the subscript 'rel' on momenta, angular momenta, and kinetic energies is dropped from this point on. Using Eq. (2.13), one finds the expression

$$\widetilde{t}_r^{[2]} = c_r^\dagger t_r c_r - t_r = \frac{1}{2} \left(p_r^2 \frac{1}{2\widetilde{\mu}_r(r)} + \frac{1}{2\widetilde{\mu}_r(r)} p_r^2 \right) + \widetilde{w}(r) \tag{2.56}$$

for the correlated radial part of the kinetic energy, where

$$\frac{1}{2\widetilde{\mu}_r(r)} = \frac{1}{m_N} \left(\frac{1}{[R_+'(r)]^2} - 1 \right) \tag{2.57}$$

will be referred to as a *correlated radial mass*, and

$$\widetilde{w}(r) = \frac{1}{m_N} \left(\frac{7 R_+''(r)^2}{4 R_+'(r)^4} - \frac{R_+'''(r)}{2 R_+'(r)^3} \right) \tag{2.58}$$

is an additional local potential term. Applying the correlator to the angular part of the correlated kinetic energy yields

$$\widetilde{t}_\Omega^{[2]} = c_r^\dagger t_\Omega c_r - t_\Omega = \frac{1}{2\widetilde{\mu}_\Omega(r)} \frac{l^2}{r^2} , \tag{2.59}$$

where the *correlated angular mass* is defined by

$$\frac{1}{2\widetilde{\mu}_\Omega(r)} = \frac{1}{m_N} \left(\frac{r^2}{R_+^2(r)} - 1 \right) . \tag{2.60}$$

Note that the $-\frac{1}{m_N}$-terms in the correlated masses result from the subtraction of the uncorrelated kinetic energies. The correlated masses and the additional central potential are displayed in Fig. 2.7.
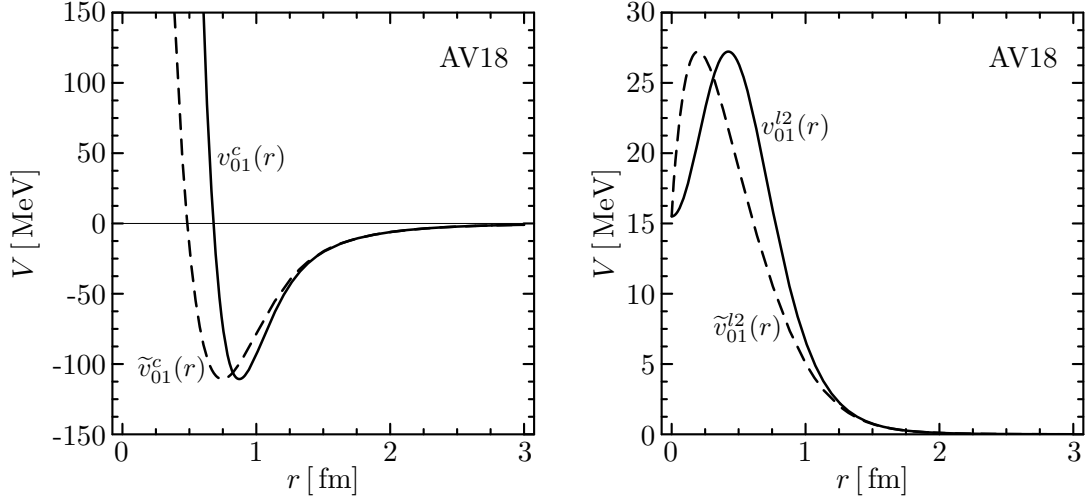
Figure 2.8: Centrally correlated potential components of the AV18 interaction in the $ST = 01$ channel. The only contributions in this channel come from the central (left) and l^2 potential (right).

Since the radial momentum operator commutes with most of the interaction operators,

$$\left[\mathrm{p}_r, \mathrm{o}_i\right] = 0, \quad \mathrm{o}_i \in \left\{\mathbb{1}, \mathrm{s}_{12}, \mathbf{l}^2, \mathbf{l} \cdot \mathbf{s}, (\mathbf{l} \cdot \mathbf{s})^2\right\}, \tag{2.61}$$

application of the central correlator simply transforms the radial dependence of the potential term (see Fig. 2.8):

$$\widetilde{\mathrm{v}}^i = \mathrm{c}_r^\dagger \mathrm{v}^i \mathrm{c}_r = v^i(R_+(\mathrm{r}))\mathrm{o}_i. \tag{2.62}$$

The only exceptions are momentum-dependent terms like the v^{p^2} occurring in the Bonn-A potential. Similar to the kinetic energy, it is useful to decompose this term into a radial and an angular part:

$$\mathrm{v}^{p^2} = \frac{1}{2}\left(\mathbf{p}^2 v^{p^2}(\mathrm{r}) + v^{p^2}(\mathrm{r})\mathbf{p}^2\right) = \frac{1}{2}\left(\mathrm{p}_r^2 v^{p^2}(\mathrm{r}) + v^{p^2}(\mathrm{r})\mathrm{p}_r^2\right) + \frac{v^{p^2}(\mathrm{r})}{\mathrm{r}^2}\mathbf{l}^2. \tag{2.63}$$

The application of the central correlator then yields a correlated potential which is similar to the correlated kinetic energy, with some additional terms arising due to the non-vanishing commutator of p_r and $v^{p^2}(\mathrm{r})$:

$$\begin{aligned}
\widetilde{\mathrm{v}}^{p^2} = \mathrm{c}_r^\dagger \mathrm{v}^{p^2} \mathrm{c}_r =& \frac{1}{2}\left(\mathrm{p}_r^2 \frac{v^{p^2}(R_+(\mathrm{r}))}{[R_+'(\mathrm{r})]^2} + \frac{v^{p^2}(R_+(\mathrm{r}))}{[R_+'(\mathrm{r})]^2}\mathrm{p}_r^2\right) \\
&+ v^{p^2}(R_+(\mathrm{r}))\left(\frac{7[R_+''(\mathrm{r})]^2}{4[R_+'(\mathrm{r})]^4} - \frac{R_+'''(\mathrm{r})}{2[R_+'(\mathrm{r})]^3}\right) - v^{p^2\prime}(R_+(\mathrm{r}))\frac{R_+''(\mathrm{r})}{[R_+'(\mathrm{r})]^2} \quad (2.64) \\
&+ \frac{v^{p^2}(R_+(\mathrm{r}))}{R_+^2(\mathrm{r})}\mathbf{l}^2.
\end{aligned}$$

2.4.2 Central and Tensor Correlations Combined

The unitarity of the correlation operators comes in handy once they are applied to interaction operators in order to construct fully correlated potentials. Formally, a correlated two-body operator is now

$$\widetilde{o} = c_r^\dagger c_\Omega^\dagger o c_\Omega c_r \,. \tag{2.65}$$

As with the wavefunctions, $\widetilde{o}$ now denotes a *fully correlated* operator. Exploiting the unitarity, one can write

$$c_r^\dagger c_\Omega^\dagger o c_\Omega c_r = \left(c_r^\dagger c_\Omega^\dagger c_r \right) \left(c_r^\dagger o c_r \right) \left(c_r^\dagger c_\Omega c_r \right)$$

$$= \left(c_r^\dagger c_\Omega c_r \right)^\dagger \left(c_r^\dagger o c_r \right) \left(c_r^\dagger c_\Omega c_r \right) \,. \tag{2.66}$$

The centrally correlated tensor correlator can be calculated easily, because g_r commutes with $s_{12}(\mathbf{r}, \mathbf{p}_\Omega)$:

$$c_r^\dagger c_\Omega c_r = c_r^\dagger \exp\left(-i\vartheta(\mathrm{r}) s_{12}(\mathbf{r}, \mathbf{p}_\Omega) \right) c_r = \exp\left(-i\vartheta\left(R_+(\mathrm{r}) \right) s_{12}(\mathbf{r}, \mathbf{p}_\Omega) \right) \,. \tag{2.67}$$

At this point, one can again proceed along two different lines, by either applying centrally correlated operators in tensor-correlated states, or constructing fully correlated operators. The latter will require further approximations beside the ones already made, and therefore the decision between the two approaches will be made depending on the specific problem at hand.

Centrally Correlated Operators in Tensor-Correlated $(LS)J$-States

This approach extends the examination of the tensor-correlated deuteron state in Sect. 2.3 by including the central correlations in an explicit fashion, i.e., by inspecting the matrix elements of $c_r^\dagger c_\Omega c_r$. Only reduced matrix elements are given below. Since all operators occurring in NN interactions as well as the correlators are scalar operators, the angular momentum projection enters the full matrix element only in terms of $\delta_{MM'}$. For brevity, let us introduce

$$\left((LS)J \,\middle|\middle|\, o \,\middle|\middle|\, (LS)J \right) = \frac{\left\langle (LS)J \,\middle|\middle|\, o \,\middle|\middle|\, (LS)J \right\rangle}{\sqrt{2J+1}} \tag{2.68}$$

(cf. Appendix B). The isospin T is fixed by requiring the state's antisymmetry, and M_T is omitted, not accounting for charge-independence breaking at this point. Eq. (2.43) implies that the only nontrivial matrix elements of $c_r^\dagger c_\Omega c_r$ will be between states with $L = J \pm 1$ and $L' = J \pm 1$. Some of the diagonal matrix elements were already presented in [6].

The fully correlated radial part of the two-body kinetic energy has the diagonal and off-diagonal matrix elements

$$\left((J \pm 1, 1)J \,\middle|\middle|\, \widetilde{t}_r^{[2]} \,\middle|\middle|\, (J \pm 1, 1)J \right) = \left((J \pm 1, 1)J \,\middle|\middle|\, c_r^\dagger c_\Omega^\dagger t_r c_\Omega c_r - t_r \,\middle|\middle|\, (J \pm 1, 1)J \right)$$

$$= \frac{1}{2} \left(p_r^2 \frac{1}{2\widetilde{\mu}_r(\mathrm{r})} + \frac{1}{2\widetilde{\mu}_r(\mathrm{r})} p_r^2 \right) + \frac{1}{m_N} \left(3\sqrt{J(J+1)}\, \vartheta'(R_+(\mathrm{r})) \right)^2 + \widetilde{w}(\mathrm{r}) \,. \tag{2.69}$$

and

$$
\begin{aligned}
\left((J\mp 1,1)J\middle|\middle|\,\widetilde{\mathrm{t}}^{[2]}_r\,\middle|\middle|(J\pm 1,1)J\right) &= \left((J\mp 1,1)1\middle|\middle|\,\mathrm{c}^\dagger_r\mathrm{c}^\dagger_\Omega\mathrm{t}_r\mathrm{c}_\Omega\mathrm{c}_r - \mathrm{t}_r\,\middle|\middle|(J\pm 1,1)1\right) \\
&= \pm 3i\sqrt{J(J+1)}\left[\mathrm{p}_r\frac{\vartheta'(R_+(\mathrm{r}))}{mR'_+(\mathrm{r})} + \frac{\vartheta'(R_+(\mathrm{r}))}{mR'_+(\mathrm{r})}\mathrm{p}_r\right].
\end{aligned}
\tag{2.70}
$$

The tensor correlations contribute an additional potential term reminiscent of centrifugal potentials due to the radial dependence of $\vartheta(r)$. $\widetilde{\mu}(r)$ and $\widetilde{w}(r)$ are unchanged from Eqs. (2.57) and (2.58).

The mixing of different orbital angular momenta leads to the following expressions for the fully correlated angular part of the kinetic two-body energy:

$$
\begin{aligned}
\left((J\mp 1,1)J\middle|\middle|\,\widetilde{\mathrm{t}}^{[2]}_\Omega\,\middle|\middle|(J\mp 1,1)J\right) &= \left((J\mp 1,1)J\middle|\middle|\,\mathrm{c}^\dagger_r\mathrm{c}^\dagger_\Omega\mathrm{t}_\Omega\mathrm{c}_\Omega\mathrm{c}_r - \mathrm{t}_\Omega\,\middle|\middle|(J\mp 1,1)J\right) \\
&= \frac{1}{m_N R^2_+(\mathrm{r})}\Big[\cos^2\left(\theta^{(J)}(R_+(\mathrm{r}))\right)\left((J\mp 1,1)J\middle|\middle|\,\mathbf{l}^2\,\middle|\middle|(J\mp 1,1)J\right) \\
&\qquad + \sin^2\left(\theta^{(J)}(R_+(\mathrm{r}))\right)\left((J\pm 1,1)J\middle|\middle|\,\mathbf{l}^2\,\middle|\middle|(J\pm 1,1)J\right)\Big] \\
&\quad - \frac{1}{m_N\mathrm{r}^2}\left((J\mp 1,1)J\middle|\middle|\,\mathbf{l}^2\,\middle|\middle|(J\mp 1,1)J\right).
\end{aligned}
\tag{2.71}
$$

The expressions for the momentum-dependent interaction are very similar. After decomposing v^{p^2} into radial and angular parts, we find the diagonal matrix element

$$
\begin{aligned}
\left((J\mp 1,1)J\middle|\middle|\,\widetilde{\mathrm{v}}^{p^2}_r\,\middle|\middle|(J\mp 1,1)J\right) &= \left((J\mp 1,1)J\middle|\middle|\,\mathrm{c}^\dagger_r\mathrm{c}^\dagger_\Omega\mathrm{v}^{p^2}_r\mathrm{c}_\Omega\mathrm{c}_r\,\middle|\middle|(J\mp 1,1)J\right) \\
&= \mathrm{c}^\dagger_r\mathrm{v}^{p^2}_r\mathrm{c}_r + v^{p^2}(R_+(\mathrm{r}))\left(3\sqrt{J(J+1)}\,\vartheta'(R_+(\mathrm{r}))\right)^2
\end{aligned}
\tag{2.72}
$$

for the radial part, where $\mathrm{c}^\dagger_r\mathrm{v}^{p^2}_r\mathrm{c}_r$ is just the centrally correlated radial part of Eq. (2.64). In addition, we have non-vanishing off-diagonal matrix elements:

$$
\begin{aligned}
\left((J\mp 1,1)J\middle|\middle|\,\widetilde{\mathrm{v}}^{p^2}_r\,\middle|\middle|(J\pm 1,1)J\right) &= \left((J\mp 1,1)J\middle|\middle|\,\mathrm{c}^\dagger_r\mathrm{c}^\dagger_\Omega\mathrm{v}^{p^2}_r\mathrm{c}_\Omega\mathrm{c}_r\,\middle|\middle|(J\pm 1,1)J\right) \\
&= \pm 3i\sqrt{J(J+1)}\left[\mathrm{p}_r\frac{v^{p^2}(R_+(\mathrm{r}))\vartheta'(R_+(\mathrm{r}))}{R'_+(\mathrm{r})} + \frac{v^{p^2}(R_+(\mathrm{r}))\vartheta'(R_+(\mathrm{r}))}{R'_+(\mathrm{r})}\mathrm{p}_r\right].
\end{aligned}
\tag{2.73}
$$

The correlated angular part of the potential is diagonal:

$$
\begin{aligned}
\left((J\mp 1,1)J\middle|\middle|\,\widetilde{\mathrm{v}}^{p^2}_\Omega\,\middle|\middle|(J\mp 1,1)J\right) &= \left((J\mp 1,1)J\middle|\middle|\,\mathrm{c}^\dagger_r\mathrm{c}^\dagger_\Omega\mathrm{v}^{p^2}_\Omega\mathrm{c}_\Omega\mathrm{c}_r\,\middle|\middle|(J\mp 1,1)J\right) \\
&= \frac{v^{p^2}(R_+(\mathrm{r}))}{R^2_+(\mathrm{r})}\Big[\cos^2\left(\theta^{(J)}(R_+(\mathrm{r}))\right)\left((J\mp 1,1)J\middle|\middle|\,\mathbf{l}^2\,\middle|\middle|(J\mp 1,1)J\right) \\
&\qquad + \sin^2\left(\theta^{(J)}(R_+(\mathrm{r}))\right)\left((J\pm 1,1)J\middle|\middle|\,\mathbf{l}^2\,\middle|\middle|(J\pm 1,1)J\right)\Big].
\end{aligned}
\tag{2.74}
$$

The central components of the interaction are not affected by tensor correlations,

$$
\left((J\mp 1,1)J\middle|\middle|\,\mathrm{c}^\dagger_r\mathrm{c}^\dagger_\Omega\mathrm{v}^c\mathrm{c}_\Omega\mathrm{c}_r\,\middle|\middle|(J\mp 1,1)J\right) = v^c(R_+(\mathrm{r})),
\tag{2.75}
$$

and since the l^2-potential is almost identical to $v_\Omega^{p^2}$, we can read off

$$
\begin{aligned}
((J \mp 1, 1)J || \, \widetilde{v}^{l^2} \, || (J \mp 1, 1)J) &= ((J \mp 1, 1)J || \, c_r^\dagger c_\Omega^\dagger v_\Omega^{l^2} c_\Omega c_r \, || (J \mp 1, 1)J) \\
&= v^{l^2}(R_+(\mathrm{r})) \Big[\cos^2 \Big(\theta^{(J)} \left(R_+(\mathrm{r}) \right) \Big) ((J \mp 1, 1)J || \, \mathbf{l}^2 \, || (J \mp 1, 1)J) \\
&\quad + \sin^2 \Big(\theta^{(J)} \left(R_+(\mathrm{r}) \right) \Big) ((J \pm 1, 1)J || \, \mathbf{l}^2 \, || (J \pm 1, 1)J) \Big] .
\end{aligned}
\tag{2.76}
$$

The correlated spin-orbit interaction is diagonal, too, and so we find

$$
\begin{aligned}
((J \mp 1, 1)J || \, \widetilde{v}^{ls} \, || (J \mp 1, 1)J) &= ((J \mp 1, 1)J || \, c_r^\dagger c_\Omega^\dagger v_\Omega^{ls} c_\Omega c_r \, || (J \mp 1, 1)J) \\
&= v^{ls}(R_+(\mathrm{r})) \Big[\cos^2 \Big(\theta^{(J)} \left(R_+(\mathrm{r}) \right) \Big) ((J \mp 1, 1)J || \, \mathbf{l} \cdot \mathbf{s} \, || (J \mp 1, 1)J) \\
&\quad + \sin^2 \Big(\theta^{(J)} \left(R_+(\mathrm{r}) \right) \Big) ((J \pm 1, 1)J || \, \mathbf{l} \cdot \mathbf{s} \, || (J \pm 1, 1)J) \Big] .
\end{aligned}
\tag{2.77}
$$

The tensor interaction naturally has both diagonal and off-diagonal contributions:

$$
\begin{aligned}
((J \mp 1, 1)J || \, \widetilde{v}^{t} \, || (J \mp 1, 1)J) &= ((J \mp 1, 1)J || \, c_r^\dagger c_\Omega^\dagger v_\Omega^{t} c_\Omega c_r \, || (J \mp 1, 1)J) \\
&= v^{t}(R_+(\mathrm{r})) \Big[\cos^2 \Big(\theta^{(J)} \left(R_+(\mathrm{r}) \right) \Big) ((J \mp 1, 1)J || \, s_{12} \, || (J \mp 1, 1)J) \\
&\quad \pm 2 \cos \Big(\theta^{(J)} \left(R_+(\mathrm{r}) \right) \Big) \sin \Big(\theta^{(J)} \left(R_+(\mathrm{r}) \right) \Big) ((J \mp 1, 1)J || \, s_{12} \, || (J \pm 1, 1)J) \\
&\quad + \sin^2 \Big(\theta^{(J)} \left(R_+(\mathrm{r}) \right) \Big) ((J \pm 1, 1)J || \, s_{12} \, || (J \pm 1, 1)J) \Big]
\end{aligned}
\tag{2.78}
$$

and

$$
\begin{aligned}
((J \mp 1, 1)J || \, \widetilde{v}^{t} \, || (J \pm 1, 1)J) &= ((J \mp 1, 1)J || \, c_r^\dagger c_\Omega^\dagger v_\Omega^{t} c_\Omega c_r \, || (J \pm 1, 1)J) \\
&= v^{t}(R_+(\mathrm{r})) \Big[\cos^2 \Big(\theta^{(J)} \left(R_+(\mathrm{r}) \right) \Big) ((J \mp 1, 1)J || \, s_{12} \, || (J \pm 1, 1)J) \\
&\quad - \sin^2 \Big(\theta^{(J)} \left(R_+(\mathrm{r}) \right) \Big) ((J \pm 1, 1)J || \, s_{12} \, || (J \mp 1, 1)J) \Big] ,
\end{aligned}
\tag{2.79}
$$

where we have used that s_{12} is not just hermitian, but even symmetric (see Tabs. B.1 and B.2).

Centrally and Tensor-Correlated Operators

A general tensor-correlated operator

$$
c_\Omega^\dagger \mathrm{o} c_\Omega = e^{i g_\Omega} \, \mathrm{o} \, e^{-i g_\Omega}
\tag{2.80}
$$

can be calculated by using the Baker-Campbell-Hausdorff formula,

$$
e^{i g_\Omega} \mathrm{o} e^{-i g_\Omega} = \mathrm{o} + i \big[g_\Omega, \mathrm{o} \big] + \frac{i^2}{2} \big[g_\Omega, [g_\Omega, \mathrm{o}] \big] + \ldots \equiv e^{\mathrm{L}_\Omega} \mathrm{o} ,
\tag{2.81}
$$

where the super-operator

$$
\mathrm{L}_\Omega \equiv i \big[g_\Omega, \circ \big]
\tag{2.82}
$$

has been introduced. For r and p_r, the series (2.81) terminates,

$$
c_\Omega^\dagger \mathrm{r} c_\Omega = \mathrm{r}
\tag{2.83}
$$

and

$$c_\Omega^\dagger p_r c_\Omega = p_r - \vartheta'(r) s_{12}(\mathbf{r}, \mathbf{p}_\Omega)\,. \tag{2.84}$$

The latter implies

$$\begin{aligned}
c_\Omega^\dagger p_r^2 c_\Omega =& p_r^2 - \left(p_r \vartheta'(r) + \vartheta'(r) p_r\right) s_{12}(\mathbf{r}, \mathbf{p}_\Omega) + \vartheta'(r)^2 s_{12}(\mathbf{r}, \mathbf{p}_\Omega)^2 \\
=& p_r^2 - \left(p_r \vartheta'(r) + \vartheta'(r) p_r\right) s_{12}(\mathbf{r}, \mathbf{p}_\Omega) \\
& + \vartheta'(r)^2 \Big((18 + 6\mathbf{l}^2)\Pi_1 + \frac{45}{2}\mathbf{l}\cdot\mathbf{s} + \frac{3}{2} s_{12}(\mathbf{l},\mathbf{l})\Big)\,,
\end{aligned} \tag{2.85}$$

where the decomposition formula (B.29) was used in the last line. Unfortunately, these are the only simple cases, because the algebraic relations between $s_{12}(\mathbf{r}, \mathbf{p}_\Omega)$ and the 'non-radial' parts of the interaction, like $\mathbf{l}^2$ or $\mathbf{l}\cdot\mathbf{s}$, generate increasing powers of angular momentum and tensor operators, e.g.,

$$\left[s_{12}(\mathbf{r}, \mathbf{p}_\Omega), \mathbf{l}\cdot\mathbf{s}\right] = -i\left(2r^2 s_{12}(\mathbf{p}_\Omega, \mathbf{p}_\Omega) + s_{12}(\mathbf{l},\mathbf{l}) - \frac{1}{2} s_{12}\right) \equiv -i\bar{s}_{12}(\mathbf{p}_\Omega, \mathbf{p}_\Omega)\,, \tag{2.86}$$

where

$$s_{12}(\mathbf{l},\mathbf{l}) \equiv 3(\boldsymbol{\sigma}_1\cdot\mathbf{l})(\boldsymbol{\sigma}_2\cdot\mathbf{l}) - (\boldsymbol{\sigma}_1\cdot\boldsymbol{\sigma}_2)\mathbf{l}^2 \tag{2.87}$$

and

$$s_{12}(\mathbf{p}_\Omega, \mathbf{p}_\Omega) \equiv 3(\boldsymbol{\sigma}_1\cdot\mathbf{p}_\Omega)(\boldsymbol{\sigma}_2\cdot\mathbf{p}_\Omega) - (\boldsymbol{\sigma}_1\cdot\boldsymbol{\sigma}_2)\mathbf{p}_\Omega^2 \tag{2.88}$$

(see Sect. B.4 for a complete listing). In order to use fully correlated operators in practical calculations, the series needs to be truncated at a certain order of angular momentum.

T. Neff suggests a truncation after third order in angular momentum [6], which causes only a 0.005 MeV deviation in the deuteron binding energy, originating from the omission of new central interaction terms generated at higher orders of the Baker-Campbell-Hausdorff series (cf. Sect. B.4). For heavier nuclei, the approximation can still be justified, because the terms generated by the correlator are short-ranged. Thus, their effects are small due to the suppression of the two-nucleon wavefunctions by the centrifugal barrier. Applying this truncation scheme, the correlated interaction can be expressed in terms of the operators

$$\mathcal{B} = \left\{\mathbb{1}, \mathbf{l}^2, \mathbf{l}\cdot\mathbf{s}, s_{12}, s_{12}(\mathbf{l},\mathbf{l}), \bar{s}_{12}(\mathbf{p}_\Omega, \mathbf{p}_\Omega), \mathbf{l}^2\mathbf{l}\cdot\mathbf{s}, \left(\mathbf{l}^2\bar{s}_{12}(\mathbf{p}_\Omega, \mathbf{p}_\Omega)\right)_h\right\}\,, \tag{2.89}$$

where the subscript h on the last operator indicates hermitization, i. e.,

$$\left(\mathbf{l}^2\bar{s}_{12}(\mathbf{p}_\Omega, \mathbf{p}_\Omega)\right)_h \equiv \frac{1}{2}(\mathbf{l}^2\bar{s}_{12}(\mathbf{p}_\Omega, \mathbf{p}_\Omega) + \bar{s}_{12}(\mathbf{p}_\Omega, \mathbf{p}_\Omega)\mathbf{l}^2)\,. \tag{2.90}$$

The set $\mathcal{B}$ spans a space of 'super-potential vectors', $\mathcal{P}$, whose components are the radial dependencies of the corresponding interaction terms. On this space, L_Ω is represented

by the matrix

$$
L_\Omega = i\vartheta(\mathrm{r})\Pi_{S=1}
\begin{pmatrix}
0 & 0 & 0 & -24 & 0 & 108 & 0 & 324 \\
0 & 0 & 0 & 0 & 0 & 96 & 0 & 600 \\
0 & 0 & 0 & -18 & 0 & 153 & 0 & 477 \\
0 & 0 & 0 & 3 & 0 & 0 & 0 & 0 \\
0 & 0 & 0 & 0 & 0 & 15 & 0 & 51 \\
0 & 2 & -1 & 0 & 7 & 0 & -3 & 0 \\
0 & 0 & 0 & 0 & 0 & 36 & 0 & 477 \\
0 & 0 & 0 & 0 & 0 & 0 & -1 & 0
\end{pmatrix},
\tag{2.91}
$$

which only needs to be exponentiated in order to obtain the correlated interaction, including the angular part of the correlated kinetic energy, too, which can be readily expressed in the basis $\mathcal{B}$. The projection operator $\Pi_{S=1}$ ensures that the tensor correlator only acts on the $S = 1$ central and $\mathbf{l}^2$-potentials. All other operators only give nonzero contributions to the $S = 1$ channels anyway. Note that all operators of $\mathcal{B}$ commute with $\Pi_{S=1}$.

The calculation method can be extended to include the correlated radial kinetic energy and radial-momentum-dependent interaction terms by embedding $\mathcal{P}$ in a larger space with the basis

$$
\begin{aligned}
\bar{\mathcal{B}} = \{\, & (\mathrm{p}_r^2)_h, \mathbb{1}, \mathbf{l}^2, \mathbf{l} \cdot \mathbf{s}, \mathrm{s}_{12}, \mathrm{s}_{12}(\mathbf{l},\mathbf{l}), \\
& \bar{\mathrm{s}}_{12}(\mathbf{p}_\Omega, \mathbf{p}_\Omega), \mathbf{l}^2\mathbf{l}\cdot\mathbf{s}, \left(\mathbf{l}^2\bar{\mathrm{s}}_{12}(\mathbf{p}_\Omega,\mathbf{p}_\Omega)\right)_h, (\mathrm{p}_r\mathrm{s}_{12}(\mathbf{r},\mathbf{p}_\Omega))_h \,\},
\end{aligned}
\tag{2.92}
$$

To take care of the non-commutativity of p_r and $v^i(\mathrm{r})$, the subscripts on $(\mathrm{p}_r^2)_h$ and $(\mathrm{p}_r\mathrm{s}_{12}(\mathbf{r},\mathbf{p}_\Omega))_h$ are used to indicate hermitization, i.e., super-potential vectors which have these components are to be understood in the sense of

$$
\left(v(\mathrm{r}), 0, 0, 0, 0, 0, 0, 0, 0, 0\right)^T \iff \frac{1}{2}\left(\mathrm{p}_r^2 v(\mathrm{r}) + v(\mathrm{r})\mathrm{p}_r^2\right)
\tag{2.93}
$$

and

$$
\left(0, 0, 0, 0, 0, 0, 0, 0, 0, v(\mathrm{r})\right)^T \iff \frac{1}{2}\left(\mathrm{p}_r v(\mathrm{r}) + v(\mathrm{r})\mathrm{p}_r\right)\mathrm{s}_{12}(\mathbf{r}, \mathbf{p}_\Omega).
\tag{2.94}
$$

In the enlarged space $\bar{\mathcal{P}}$, one has

$$
\bar{L}_\Omega = i\vartheta(\mathrm{r})\Pi_{S=1}
\begin{pmatrix}
0 & 0 & 0 & 0 & 0 & 0 & 0 & 0 & 0 & 0 \\
0 & 0 & 0 & 0 & -24 & 0 & 108 & 0 & 324 & 0 \\
0 & 0 & 0 & 0 & 0 & 0 & 96 & 0 & 600 & 0 \\
0 & 0 & 0 & 0 & -18 & 0 & 153 & 0 & 477 & 0 \\
0 & 0 & 0 & 0 & 3 & 0 & 0 & 0 & 0 & 0 \\
0 & 0 & 0 & 0 & 0 & 0 & 15 & 0 & 51 & 0 \\
0 & 0 & 2 & -1 & 0 & 7 & 0 & -3 & 0 & 0 \\
0 & 0 & 0 & 0 & 0 & 0 & 36 & 0 & 477 & 0 \\
0 & 0 & 0 & 0 & 0 & 0 & 0 & -1 & 0 & 0 \\
0 & 0 & 0 & 0 & 0 & 0 & 0 & 0 & 0 & 0
\end{pmatrix},
\tag{2.95}
$$

and the tensor-correlated interaction is given by the super-potential vector

$$\widetilde{\mathcal{V}} = (\mathrm{K}_\Omega + \exp \bar{\mathrm{L}}_\Omega)\mathcal{H} - \mathcal{T}\,, \tag{2.96}$$

where

$$\mathrm{K}_\Omega = \Pi_1 \begin{pmatrix} 0 & 0 & 0 & 0 & 0 & 0 & 0 & 0 & 0 & 0 \\ 18\vartheta'(\mathrm{r})^2 & 0 & 0 & 0 & 0 & 0 & 0 & 0 & 0 & 0 \\ 6\vartheta'(\mathrm{r})^2 & 0 & 0 & 0 & 0 & 0 & 0 & 0 & 0 & 0 \\ \frac{45}{2}\vartheta'(\mathrm{r})^2 & 0 & 0 & 0 & 0 & 0 & 0 & 0 & 0 & 0 \\ 0 & 0 & 0 & 0 & 0 & 0 & 0 & 0 & 0 & 0 \\ \frac{45}{2}\vartheta'(\mathrm{r})^2 & 0 & 0 & 0 & 0 & 0 & 0 & 0 & 0 & 0 \\ 0 & 0 & 0 & 0 & 0 & 0 & 0 & 0 & 0 & 0 \\ 0 & 0 & 0 & 0 & 0 & 0 & 0 & 0 & 0 & 0 \\ 0 & 0 & 0 & 0 & 0 & 0 & 0 & 0 & 0 & 0 \\ -2\vartheta'(\mathrm{r}) & 0 & 0 & 0 & 0 & 0 & 0 & 0 & 0 & 0 \end{pmatrix} \tag{2.97}$$

represents the first and second order contributions[3] to the correlated radial kinetic energy (see Eq. (2.85)), and $\mathcal{H}$ and

$$\mathcal{T} = \left(\frac{1}{m}, 0, \frac{1}{m\mathrm{r}^2}, 0, 0, 0, 0, 0, 0, 0 \right) \tag{2.98}$$

are the Hamiltonian and the kinetic energy in the super-potential vector representation, respectively. By applying the central correlator to $\widetilde{\mathcal{V}}$, the fully correlated interaction is obtained.

2.5   Determination of Correlators

After the discussion of the central and tensor correlators in the preceding sections, the task of actually determining the central and tensor correlation functions remains. In Refs. [5] and [6] two general concepts to achieve this goal have been discussed in detail: minimizing the energy of a specific trial state, and mapping the uncorrelated onto exact two-body eigenstates of the Hamiltonian, similar to the treatment of the deuteron in Sect. 2.3. The results obtained with both methods are very similar in most cases, but the mapping methods can produce comparably long-ranged correlation functions, like the tensor correlation function $\vartheta^d(r)$ constructed from the deuteron wavefunctions, or $R_+(r)$ for purely repulsive ST-channels. This puts the two-body approximation in question, so we will only use correlators obtained from energy minimization for many-body calculations in this work.

In principle, the ideal procedure would be to consider the energy expectation value as a functional of the correlation functions,

$$E[R_+, \vartheta] = \frac{\left\langle \Psi \right| \widetilde{\mathrm{H}}^{C2}[R_+, \vartheta] \left| \Psi \right\rangle}{\left\langle \Psi \middle| \Psi \right\rangle} = \frac{\left\langle \Psi \right| \left[\mathrm{C}_r^\dagger[R_+]\mathrm{C}_\Omega^\dagger[\vartheta]\mathrm{H}\mathrm{C}_\Omega[\vartheta]\mathrm{C}_r[R_+] \right]^{C2} \left| \Psi \right\rangle}{\left\langle \Psi \middle| \Psi \right\rangle}, \tag{2.99}$$

---

[3]The zeroth order contributions are due to the identity operator in $\bar{\mathcal{P}}$, which is included in the exponential of $\bar{\mathrm{L}}_\Omega$.

and determine optimal correlation functions for a given many-body trial state by varia-
tion. In practice, of course, one uses parametrizations for $R_+(r)$ and $\vartheta(r)$, and minimizes
the energy of a given trial state by varying their parameters, typically 4-5. Furthermore,
it is assumed that the parameters of the central and tensor correlators can be deter-
mined separately as they act on different domains. One could now determine 'optimal'
correlation functions for every possible nucleus, but this was found to be unnecessary,
because correlators optimized for 'heavier' nuclei are practically identical to the ones
obtained by minimizing the energy of the two-nucleon system [6]. The parameters of
the employed correlation functions are listed in Appendix C. ^{4}He-optimized correlators
are included for comparison, but not used in calculations.

2.6 Renormalization Aspects of the UCOM Approach

The introduction of correlation operators decouples the energy scales of the realistic
interactions — the correlation operator models the high-momentum/short-distance be-
havior, i.e., the short-range repulsion by the core and the admixing of higher angular
momenta by the tensor force, while the low-momentum/long-range behavior is specified
by the many-body state. In this sense, UCOM has a lot in common with renormalization
techniques, like those used by the Stony Brook group to construct the low-momentum
potential $V_{\text{low-k}}$ [39, 8]. However, there is no one-to-one correspondence: the UCOM
approach ensures the equivalence of the full on-shell T-matrices of the uncorrelated and
correlated interactions by using similarity transformations of finite range, i.e.,

$$\mathrm{c}^\dagger T \mathrm{c} \quad \xrightarrow[r\to\infty, k\to 0]{} \quad T \tag{2.100}$$

as the relative distance r becomes large or the relative three-momentum k approaches
zero. $V_{\text{low-k}}$, on the other hand, is derived by *demanding* the equivalence of the half-
on-shell T-matrices before and after the projection onto states with momenta below a
cutoff Λ,

$$T_{\text{low-k}}(k', k; k^2) \stackrel{!}{=} T(k', k; k^2), \tag{2.101}$$

which is the minimal condition to ensure phase shift equivalence. The notation k^2 in
the argument indicates that k is the three-momentum of the on-shell nucleon. Since the
phase-shifts are observables, they should not depend on Λ, and therefore $T(k', k; k^2)$
is required to be cutoff-independent. In this way, a flow equation for the potential is
obtained:

$$\frac{dT(k', k; k^2)}{d\Lambda} = 0 \quad \Longrightarrow \quad \frac{dV_{\text{low-k}}}{d\Lambda} = \frac{2}{\pi} \frac{V_{\text{low-k}}(k', \Lambda) T(\Lambda, k; \Lambda^2)}{1 - (k/\Lambda)^2}, \tag{2.102}$$

where conventional scattering units have been used, i.e., $\hbar^2/m_N = \hbar = c = 1$.

It was shown in [6] that the matrix elements of the correlated Bonn-A and AV18
interactions almost coincide in the $^1S_0$ and $^3S_1$ partial waves (see Fig. 2.9), similar to
what one observes for the $V_{\text{low-k}}$ matrix elements derived from Bonn-A and AV18 [8].
Thus, the unitary correlation operator method, just as the $V_{\text{low-k}}$ approach, extracts the
low-energy part of the input interactions in the studied partial waves.
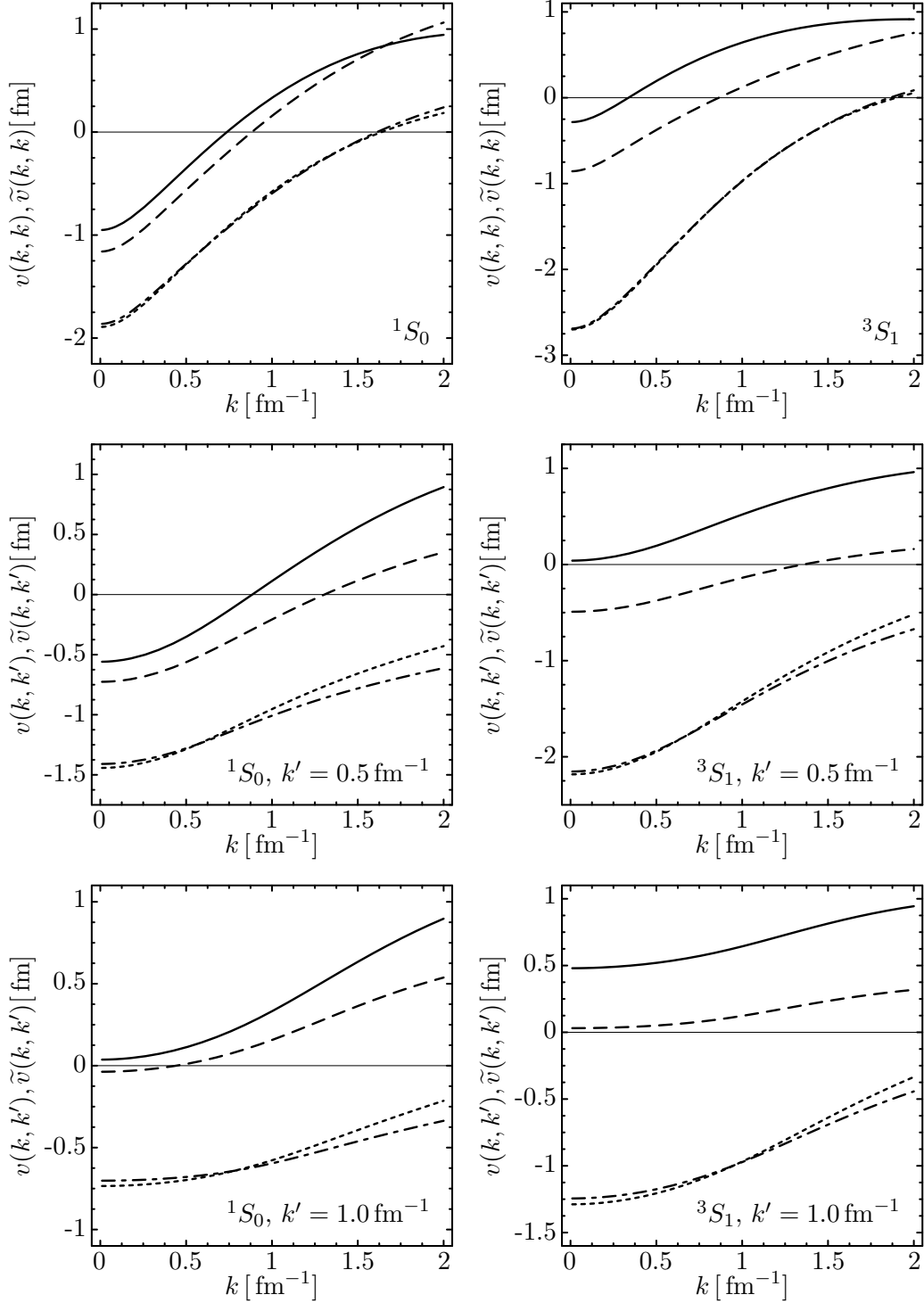
Figure 2.9: Diagonal and off-diagonal momentum space matrix elements of AV18 (———) and Bonn-A (— — —), as well as the correlated AV18 (-------) and Bonn-A (-·—-·-). The central correlator min ($ST = 01$) is used in the $^1S_0$ partial wave, and the central correlator and tensor correlators min and min^γ ($ST = 10$) in the $^3S_1$ partial wave (parameters cf. Appendix C). Scattering units $\hbar^2/m_N = \hbar = c = 1$ are used, hence $v(k,k)$ and $\widetilde{v}(k,k')$ are in units of fm.

Chapter 3

Fermionic Molecular Dynamics (FMD)

Nuclear structure calculations are performed in the mean-field model of Fermionic Molecular Dynamics (FMD) [13, 14]. Originally, it was developed to describe heavy ion reactions in the low and intermediate energy regimes, below the particle production threshold. It uses antisymmetrized Gaussian many-body states, whose dynamics are governed by a time-dependent variational principle. The FMD states are found to be very flexible — they can reproduce the familiar harmonic oscillator shell model states just as well as model states with complex intrinsic structures, like multipole deformations and clustering, so it is well-suited for our purposes.

3.1 The FMD Model

3.1.1 Single-Particle States

In coordinate space, FMD single particle states are represented by Gaussians

$$\left\langle \boldsymbol{x} \middle| a, \boldsymbol{b} \right\rangle = \exp\left(-\frac{(\boldsymbol{x} - \boldsymbol{b})^2}{2a} \right) , \tag{3.1}$$

where a is the complex width of the wave packet, and $\boldsymbol{b} = \boldsymbol{\rho} + ia\boldsymbol{\pi}$ combines its mean position and momentum:

$$\boldsymbol{\rho} = \frac{\left\langle a, \boldsymbol{b} \middle| \mathbf{x} \middle| a, \boldsymbol{b} \right\rangle}{\left\langle a, \boldsymbol{b} \middle| a, \boldsymbol{b} \right\rangle} \quad \text{and} \quad \boldsymbol{\pi} = \frac{\left\langle a, \boldsymbol{b} \middle| \mathbf{p} \middle| a, \boldsymbol{b} \right\rangle}{\left\langle a, \boldsymbol{b} \middle| a, \boldsymbol{b} \right\rangle} . \tag{3.2}$$

The variances in coordinate and momentum space are determined by the real and imaginary parts of the width parameter:

$$\frac{3}{2} \frac{|a|^2}{\operatorname{Re} a} = \frac{\left\langle a, \boldsymbol{b} \middle| (\mathbf{x} - \boldsymbol{\rho})^2 \middle| a, \boldsymbol{b} \right\rangle}{\left\langle a, \boldsymbol{b} \middle| a, \boldsymbol{b} \right\rangle} \quad \text{and} \quad \frac{3}{2} \frac{1}{\operatorname{Re} a} = \frac{\left\langle a, \boldsymbol{b} \middle| (\mathbf{p} - \boldsymbol{\pi})^2 \middle| a, \boldsymbol{b} \right\rangle}{\left\langle a, \boldsymbol{b} \middle| a, \boldsymbol{b} \right\rangle} . \tag{3.3}$$

The spin can be parametrized either by the projection on the quantization axis (i.e., spin up or down) or by a complex spinor allowing arbitrary directions. The isospin is

given by its projection, fixing the nucleon to be either a proton or a neutron:

$$\left|q_k\right\rangle = \left|a_k, \boldsymbol{b}_k\right\rangle \otimes \left|m_{s,k}\right\rangle \otimes \left|m_{t,k}\right\rangle \tag{3.4}$$

$$\left|q_k\right\rangle = \left|a_k, \boldsymbol{b}_k\right\rangle \otimes \left|\chi_k\right\rangle \otimes \left|m_{t,k}\right\rangle . \tag{3.5}$$

In some cases, we use superpositions of Gaussians to describe single-particle states:

$$\left|q_k\right\rangle = \sum_j c_{k,j} \left|q_{k,j}\right\rangle . \tag{3.6}$$

This increased flexibility of the single-particle state is particularly important to model the exponentially decaying neutron or proton density of halo nuclei.

3.1.2   Many-Body States

General uncorrelated many-body states will be Slater determinants of the single-particle states introduced in the previous section, i.e.,

$$\left|Q\right\rangle = \mathcal{A}\left(\left|q_1\right\rangle \otimes \ldots \otimes \left|q_A\right\rangle\right) , \tag{3.7}$$

where $\mathcal{A}$ denotes the antisymmetrization operator. Depending on whether we use one or two Gaussians for the single-nucleon states, the many-body states will be referred to as *single* and *double Gaussian* trial states, respectively.

A correlated many-body state can be defined by

$$\left|\widetilde{Q}\right\rangle = \mathrm{C}_\Omega \mathrm{C}_r \left|Q\right\rangle , \tag{3.8}$$

but in computations one always evaluates the expectation values of correlated operators in uncorrelated states, using the two-body approximation:

$$\frac{\left\langle\widetilde{Q}\right| \mathrm{O} \left|\widetilde{Q}\right\rangle}{\left\langle\widetilde{Q}|\widetilde{Q}\right\rangle} \stackrel{C2}{=} \frac{\left\langle Q\right| \left[\mathrm{C}_r^\dagger \mathrm{C}_\Omega^\dagger \mathrm{O} \mathrm{C}_\Omega \mathrm{C}_r\right]^{C2} \left|Q\right\rangle}{\left\langle Q|Q\right\rangle} \tag{3.9}$$

3.1.3   Matrix Elements

Since the FMD single-particle states do not form an orthogonal basis, this non-orthogonality has to be accounted for in the evaluation of matrix elements. The overlap between two single-particle states defines the *overlap matrix* n and its inverse o:

$$n_{kl} \equiv \left\langle q_k|q_l\right\rangle , \quad \mathrm{o} \equiv \mathrm{n}^{-1} . \tag{3.10}$$

Using these definitions, the expectation values of one- and two-body operators become

$$\frac{\left\langle Q\right| \mathrm{A}^{[1]} \left|Q\right\rangle}{\left\langle Q|Q\right\rangle} = \sum_{kl} \left\langle q_k\right| \mathrm{a}^{[1]} \left|q_l\right\rangle o_{lk} \tag{3.11}$$

and

$$\begin{aligned} \frac{\left\langle Q\right| \mathrm{A}^{[2]} \left|Q\right\rangle}{\left\langle Q|Q\right\rangle} &= \frac{1}{2} \sum_{klmn} {}_a\left\langle q_k, q_l\right| \mathrm{a}^{[2]} \left|q_m, q_n\right\rangle_a o_{mk} o_{nl} \\ &= \frac{1}{2} \sum_{klmn} \left\langle q_k, q_l\right| \mathrm{a}^{[2]} \left|q_m, q_n\right\rangle (o_{mk} o_{nl} - o_{nk} o_{ml}) , \end{aligned} \tag{3.12}$$

respectively.

3.1.4 Interactions

With the abbreviations

$$\lambda_{kl} = \frac{1}{a_k^* + a_l}\,, \tag{3.13}$$

$$\alpha_{kl} = \lambda_{kl} a_k^* a_l\,, \tag{3.14}$$

$$\boldsymbol{\pi}_{kl} = i\lambda_{kl}(\boldsymbol{b}_k^* - \boldsymbol{b}_l)\,, \tag{3.15}$$

$$\boldsymbol{\rho}_{kl} = \lambda_{kl}(a_l\boldsymbol{b}_k^* + a_k^*\boldsymbol{b}_l)\,, \tag{3.16}$$

the overlap between FMD single-particle states in coordinate space is

$$R_{kl} \equiv \big\langle\, a_k, \boldsymbol{b}_k \big| a_l, \boldsymbol{b}_l \,\big\rangle = (2\pi\alpha_{kl})^{3/2} \exp\left(\frac{\boldsymbol{\pi}_{kl}^2}{2\lambda_{kl}}\right)\,. \tag{3.17}$$

A calculation of the one-body part of the correlated kinetic energy now yields

$$\big\langle\, a_k, \boldsymbol{b}_k \big| \mathrm{t} \big| a_l, \boldsymbol{b}_l \,\big\rangle = \frac{1}{2m_N}(3\lambda_{kl} + \boldsymbol{\pi}_{kl}^2)R_{kl}\,; \tag{3.18}$$

recall that this is identical to the uncorrelated kinetic energy.

For use with the FMD program code, the radial functions of the correlated interaction are fitted to desired accuracy by a linear superposition of Gaussians (see Sect. D.2). All matrix elements can then be expressed by analytical expressions, and one does not need to evaluate integrals numerically. As an instructive example, consider the spin-orbit interaction:

$$\mathrm{v}^{ls} = \sum_i \gamma_i \exp\left(-\frac{\mathrm{r}^2}{2\kappa_i}\right) (\mathbf{r} \times \mathbf{p}) \cdot \mathbf{S}\,. \tag{3.19}$$

Its matrix elements can then be calculated by means of

$$\begin{aligned}
v_{klmn}^{ls} &= \big\langle\, a_k\boldsymbol{b}_k\chi_k, a_l\boldsymbol{b}_l\chi_l \big| \mathrm{v}^{ls} \big| a_m\boldsymbol{b}_m\chi_m, a_n\boldsymbol{b}_n\chi_n \,\big\rangle \\
&= R_{km}R_{ln}(\boldsymbol{\rho}_{klmn} \times \boldsymbol{\pi}_{klmn}) \cdot \boldsymbol{S}_{klmn} \\
&\quad \times \sum_i \gamma_i \left(\frac{\kappa_i}{\alpha_{klmn} + \kappa_i}\right)^{5/2} \exp\left(-\frac{\boldsymbol{\rho}_{klmn}^2}{2(\alpha_{klmn} + \kappa_i)}\right)\,,
\end{aligned} \tag{3.20}$$

where

$$\alpha_{klmn} = \alpha_{km} + \alpha_{ln}\,, \quad \boldsymbol{\rho}_{klmn} = \boldsymbol{\rho}_{km} - \boldsymbol{\rho}_{ln}\,, \quad \boldsymbol{\pi}_{klmn} = \frac{1}{2}(\boldsymbol{\pi}_{km} - \boldsymbol{\pi}_{ln})\,, \tag{3.21}$$

and $\boldsymbol{S}_{klmn}$ is the matrix element of the spin operator (cf. [40]). $\boldsymbol{\rho}_{klmn}$ and $\boldsymbol{\pi}_{klmn}$ can be interpreted as the matrix elements of the relative distance and momentum operators of the interacting nucleons, and α_{klmn} as the width of the wave packets in the relative coordinate.

3.2 Mean-Field Models and Symmetry

Exact many-body Hamiltonians are usually invariant under several symmetry groups. Unfortunately, we run into serious problems if we consider systems with many particles and strong correlations, because the simple mean-field states which are preferable to describe such systems often violate these symmetries. Consider a product of plane wave states, for example — such a state preserves the translational invariance of the system, but is obviously ill-suited to describe cluster effects, since it is extended over all space. The FMD states, on the other hand, reproduce intrinsic deformations very well, but they are localized in space, and therefore they violate translational invariance. Furthermore, they are no angular momentum eigenstates either, i.e., they also violate rotational symmetry. The methods used to restore the broken symmetries in order to obtain the symmetry-invariant physical ground state are outlined in this section. A detailed discussion of the subject can be found in [41].

3.2.1 Center-of-Mass Motion

Consider the translationally invariant A-body Hamiltonian

$$\mathrm{H}(\mathbf{x}_i) = \sum_i \frac{\mathbf{p}_i^2}{2m_N} + \sum_{i<j} v(\mathbf{r}_{ij}), \quad \mathbf{r}_{ij} = \mathbf{x}_i - \mathbf{x}_j. \tag{3.22}$$

We can introduce collective and intrinsic coordinates by transforming to the center-of-mass system,

$$\boldsymbol{x}_{\mathrm{cm}} = \frac{1}{A}\sum_i \boldsymbol{x}_i, \quad \boldsymbol{x}_i' = \boldsymbol{x}_i - \boldsymbol{x}_{\mathrm{cm}}, \quad \boldsymbol{r}_{ij}' = \boldsymbol{r}_{ij}. \tag{3.23}$$

This implies that the intrinsic coordinates $\boldsymbol{x}_i'$ are functions of a set of $3A-3$ internal coordinates ξ_ν, since we have to conserve the overall number of degrees of freedom; thus,

$$\boldsymbol{x}_i' = \boldsymbol{x}_i'(\xi_1, \ldots, \xi_{3A-3}), \tag{3.24}$$

and we have the constraints

$$\sum_i \boldsymbol{x}_i'(\xi_\nu) = 0. \tag{3.25}$$

The transformed Hamiltonian has the general structure

$$\mathrm{H}(\mathbf{x}_{\mathrm{cm}}, \xi_\nu) = \mathrm{H}_{\mathrm{coll}}(\mathbf{x}_{\mathrm{cm}}) + \mathrm{H}_{\mathrm{intr}}(\xi_\nu) + \mathrm{H}_{\mathrm{coupl}}(\mathbf{x}_{\mathrm{cm}}, \xi_\nu). \tag{3.26}$$

We could now solve the eigenvalue problem of the transformed Hamiltonian, but this quickly becomes very complicated due to complex, often nonlinear dependencies between the ξ_ν and the $\boldsymbol{x}_i$, even if the coupling term vanishes due to symmetries or is small enough to be treated perturbatively.

In order to facilitate calculations, one wants to retain a 'simple' structure for the intrinsic Hamiltonian. To this end, the method of *redundant variables* was developed (see [41] and references to the original literature therein). We embed the A-body Hilbert

space $\mathcal{H}_A$ represented in the single-particle coordinates $\boldsymbol{x}_1, \dots, \boldsymbol{x}_A$ into a larger space $\bar{\mathcal{H}}_A$ by

$$
\begin{aligned}
\boldsymbol{x}_i =& \boldsymbol{x}_i(\boldsymbol{x}'_1, \dots, \boldsymbol{x}'_A, \boldsymbol{x}_{\mathrm{cm}}), \quad i = 1, \dots, A, \\
g_i =& g_i(\boldsymbol{x}'_1, \dots, \boldsymbol{x}'_A, \boldsymbol{x}_{\mathrm{cm}}), \quad i = 1, \dots, 3,
\end{aligned}
\tag{3.27}
$$

where the $\boldsymbol{x}'_i$ are cms-coordinates as above, and the redundant variables $g_1, \dots, g_3$ contain the constraints. The physical submanifold of $\bar{\mathcal{H}}_A$ is characterized by the vanishing of these unphysical degrees of freedom, i.e.,

$$
g_1 = g_2 = g_3 = 0. \tag{3.28}
$$

Using the same notation as above, we have

$$
\boldsymbol{x}_i = \boldsymbol{x}'_i + \boldsymbol{x}_{\mathrm{cm}}, \quad \boldsymbol{g} = \frac{1}{A} \sum_j \boldsymbol{x}'_j \tag{3.29}
$$

or

$$
\boldsymbol{x}'_i = \boldsymbol{x}_i - \frac{1}{A} \sum_j \boldsymbol{x}_j + \boldsymbol{g}, \quad \boldsymbol{x}_{\mathrm{cm}} = \frac{1}{A} \sum_j \boldsymbol{x}_j - \boldsymbol{g}. \tag{3.30}
$$

The derivatives are then given by $(a, b = 1, 2, 3)$

$$
\begin{aligned}
\frac{\partial}{\partial x_{i,a}} =& \sum_b \frac{\partial x_{\mathrm{cm},b}}{\partial x_{i,a}} \frac{\partial}{\partial x_{\mathrm{cm},b}} + \sum_{k,b} \frac{\partial x'_{k,b}}{\partial x_{i,a}} \frac{\partial}{\partial x'_{k,b}} \\
=& \frac{1}{A} \frac{\partial}{\partial x_{\mathrm{cm},a}} + \sum_{k,b} (\delta_{ik} - \frac{1}{A} \sum_j \delta_{jk}) \delta_{ab} \frac{\partial}{\partial x'_{k,b}} \\
=& \frac{1}{A} \frac{\partial}{\partial x_{\mathrm{cm},a}} + \frac{\partial}{\partial x'_{i,a}} - \frac{1}{A} \sum_j \frac{\partial}{\partial x'_{j,a}},
\end{aligned}
\tag{3.31}
$$

where one has to remember that g_i and $x_{i,a}$ are independent variables in the expanded space. Thus, one finds the following transformation for the momenta:

$$
\mathbf{p}_i = \frac{1}{A} \mathbf{p}_{\mathrm{cm}} + \mathbf{p}'_i - \frac{1}{A} \sum_j \mathbf{p}'_j, \tag{3.32}
$$

where $\mathbf{p}'_i$ is the canonical conjugate to $\mathbf{x}'_i$. Using

$$
\begin{aligned}
\sum_i \left(\frac{1}{A} \mathbf{p}_{\mathrm{cm}} + \mathbf{p}'_i - \frac{1}{A} \sum_j \mathbf{p}'_j \right)^2 =& \\
= \sum_i & \left[\frac{1}{A^2} \mathbf{p}_{\mathrm{cm}}^2 + \mathbf{p}'^2_i + \frac{2}{A} \mathbf{p}_{\mathrm{cm}} \cdot \mathbf{p}'_i - \frac{2}{A^2} \sum_j \mathbf{p}_{\mathrm{cm}} \cdot \mathbf{p}'_j - \frac{2}{A} \sum_j \mathbf{p}'_i \cdot \mathbf{p}'_j + \frac{1}{A^2} \sum_{j,k} \mathbf{p}'_j \cdot \mathbf{p}'_k \right] \\
= \frac{1}{A} & \mathbf{p}_{\mathrm{cm}}^2 + \sum_i \mathbf{p}'^2_i + \frac{2}{A} \left(\sum_i \mathbf{p}_{\mathrm{cm}} \cdot \mathbf{p}'_i - \sum_j \mathbf{p}_{\mathrm{cm}} \cdot \mathbf{p}'_j \right) - \frac{2}{A} \left(\sum_{i,j} \mathbf{p}'_i \cdot \mathbf{p}'_j - \sum_{j,k} \mathbf{p}'_j \cdot \mathbf{p}'_k \right) \\
= \frac{1}{A} & \mathbf{p}_{\mathrm{cm}}^2 + \sum_i \mathbf{p}'^2_i - \frac{1}{A} \sum_{i,j} \mathbf{p}'_i \cdot \mathbf{p}'_j,
\end{aligned}
\tag{3.33}
$$

the Hamiltonian now takes the form

$$H = \frac{\mathbf{p}_{cm}^2}{2Am_N} + \sum_i \frac{\mathbf{p}_i'^2}{2m_N} + \sum_{i<j} v(\mathbf{r}_{ij}') - \frac{1}{2Am_N} \sum_{i,j} \mathbf{p}_i' \mathbf{p}_j' \,, \tag{3.34}$$

which does not change at all if one considers the physical submanifold $\boldsymbol{g} = 0$. We also see that the coupling term present in the general Hamiltonian (3.26) vanishes, owing to translational invariance. The collective part is given by the kinetic energy of the center-of-mass motion, and therefore its eigenstates are plane waves. Thus, a general eigenstate of H decouples into an intrinsic and a collective part,

$$\big| \Psi \big\rangle = \big| \boldsymbol{k} \big\rangle_{cm} \times \big| \Phi \big\rangle_{intr}, \tag{3.35}$$

so we need not worry about translation invariance if we treat the intrinsic Hamiltonian with mean-field techniques, as we only have to multiply the mean-field state with a plane wave to obtain the physical ground state. The intrinsic Hamiltonian

$$H_{intr} = \sum_i \frac{\mathbf{p}_i'^2}{2m_N} + V - \frac{1}{2Am_N} \left(\sum_i \mathbf{p}_i' \right)^2 \equiv H' - T_{cm}' \tag{3.36}$$

is similar to the original one, with the exception that the kinetic energy of the center-of-mass motion in the *intrinsic system* is subtracted. The reason for this becomes a little clearer if one separates the NN-interaction in the intrinsic system in a shell model potential and a residual part — there are *spurious solutions* from the center-of-mass motion, which correspond to the movement of the nucleus as a whole in the potential. These unphysical solutions mix with the physical ones, and therefore one needs to correct for their contributions to the total energy etc.[1] In the special case of a harmonic oscillator potential, the center-of-mass motion and the single-particle motion can be separated by means of a *Talmi transformation* ([38, 6]).

3.2.2   Angular Momentum Projection

Whenever a state is a superposition of different angular momentum eigenstates, rotational symmetry is violated. The restoration of rotational symmetry by means of the method of redundant variables, as discussed in the previous section, proves to be very problematic in this case — the search for a suitable transformation to the intrinsically deformed system remains an open problem, in part due to the non-Abelian character of the rotation group. The supposedly obvious choice, using the principal axes of the inertial tensor as the basis for the intrinsic system, unfortunately leads to a strong coupling term in the decomposition of the Hamiltonian analogous to (3.26) (see e.g. [42]). Naturally, the eigenvalue problem becomes rather complex, so one has to resort to different techniques. This is where angular momentum projection (AMP) comes into play, a special case of a *generator-coordinate method* [41, 43].

The arbitrariness in the orientation of the symmetry-violating wavefunction is removed by integrating over all allowed orientations:

$$\big| \Psi \big\rangle = \int d\Omega \, f(\Omega) R(\Omega) \big| \Phi \big\rangle \,, \quad \Omega = (\alpha, \beta, \gamma) \,, \tag{3.37}$$

---

[1]There would be no mixing in an exact treatment, see [41].

where $\left|\Phi\right\rangle$ is the deformed many-body state, e.g., from a mean-field calculation, Ω is a set of Euler angles corresponding to a given rotation, and

$$\mathrm{R}(\Omega) = e^{-i\alpha\mathrm{J}_z}e^{-i\beta\mathrm{J}_y}e^{-i\gamma\mathrm{J}_z} \,. \tag{3.38}$$

The integration in Eq. (3.37) is understood to run over the whole parameter space of the rotation group $SU(2)$, using the corresponding invariant *Haar measure* (see e.g. [44])

$$d\Omega = \sin\beta d\alpha d\beta d\gamma \,. \tag{3.39}$$

In order to obtain angular momentum eigenstates $\left|\Psi^{JM}\right\rangle$, the weight function in Eq. (3.37) is expanded in terms of the *Wigner D-functions*

$$D_{KM}^J(\Omega) = \left\langle\,JK\right|\mathrm{R}(\Omega)\left|JM\,\right\rangle \,. \tag{3.40}$$

Eq. (3.37) yields

$$\left|\Psi^{JM}\right\rangle = \frac{2J+1}{8\pi^2}\sum_K g_K^J \int d\Omega D_{MK}^{J*}(\Omega)\mathrm{R}(\Omega)\left|\Phi\,\right\rangle \equiv \sum_K g_K^J\mathrm{P}_{MK}^J\left|\Phi\,\right\rangle, \tag{3.41}$$

where $\mathrm{P}_{MK}^J\left|\Phi\,\right\rangle$ defines a generalized projection operator with the properties

$$\mathrm{P}_{MK}^J = \sum_\nu \left|\nu JM\,\right\rangle\!\left\langle\,\nu JK\right| \,, \tag{3.42a}$$

$$\left(\mathrm{P}_{MK}^J\right)^\dagger = \mathrm{P}_{KM}^J \,, \tag{3.42b}$$

$$\mathrm{P}_{MK}^J\mathrm{P}_{M'K'}^{J'} = \delta_{JJ'}\delta_{KM'}\mathrm{P}_{MK'}^J \,. \tag{3.42c}$$

ν in Eq. (3.42a) is understood as a collective index for all non-rotational quantum numbers. If $\left|\Phi\,\right\rangle$ is decomposed into eigenstates of J_z,

$$\left|\Phi\,\right\rangle = \sum_K \left|\Phi_K\,\right\rangle, \quad \mathrm{J}_z\left|\Phi_K\,\right\rangle = K\left|\Phi_K\,\right\rangle \tag{3.43}$$

Eq. (3.42a) implies that

$$\mathrm{P}_{MK}^J\left|\Phi\,\right\rangle = \mathrm{P}_{MK}^J\sum_{K'}\left|\Phi_{K'}\,\right\rangle = \sum_{\nu,K'}\left|\nu JM\,\right\rangle\!\left\langle\,\nu JK\right|\Phi_{K'}\,\right\rangle, \tag{3.44}$$

i.e., the projector transforms the K-component into a simultaneous eigenstate of $\mathbf{J}^2$ and J_z with eigenvalues J and M, and annihilates all components of $\left|\Phi\,\right\rangle$ for which $K \neq K'$.

The energy of the projected state is now given by

$$E^{JM} = E^J = \frac{\left\langle\,\Psi^{JM}\right|\mathrm{H}\left|\Psi^{JM}\,\right\rangle}{\left\langle\,\Psi^{JM}\right|\Psi^{JM}\,\right\rangle} = \frac{\sum\limits_{KK'}g_K^{J*}g_{K'}^J h_{KK'}^J}{\sum\limits_{KK'}g_K^{J*}g_{K'}^J n_{KK'}^J} \,, \tag{3.45}$$

where

$$h_{KK'}^J \equiv \left\langle\,\Phi\right|\mathrm{HP}_{KK'}^J\left|\Phi\,\right\rangle, \tag{3.46a}$$

$$n_{KK'}^J \equiv \left\langle\,\Phi\right|\mathrm{P}_{KK'}^J\left|\Phi\,\right\rangle. \tag{3.46b}$$

Naturally, E^J is independent of M due to the restored rotational invariance. The coefficients g_K^J are obtained by solving the *Hill-Wheeler equations*

$$\sum_{K'} h_{KK'}^J g_{K'} = E^J \sum_{K'} n_{KK'}^J g_{K'} \,, \tag{3.47}$$

which constitute a generalized eigenvalue problem. Solving it corresponds to a diagonalization of H in the space spanned by the non-orthogonal states $\mathrm{P}_{MK}^J \left| \Phi \right\rangle$.

Variation Before and After the Projection

Up to this point, the symmetry-violating wavefunction $\left| \Phi \right\rangle$ has not been specified. In our technical framework, we want to derive it from a FMD variational calculation, which allows two possible ways to proceed:

(i) *Projection after variation (PAV)*. $\left| \Phi \right\rangle$ is determined by requiring the functional

$$E[\Phi] = \frac{\left\langle \Phi \right| \mathrm{H} - \mathrm{T_{cm}} \left| \Phi \right\rangle}{\left\langle \Phi | \Phi \right\rangle} \tag{3.48}$$

to be minimal. The variation needs to be performed only once, but we technically violate the variational principle, since we do not vary the projected wavefunction, and we do not account for possible changes of the self-consistent mean-field within the rotational bands.

(ii) *Variation after projection (VAP)*. The proper variational principle

$$E[\Psi^J] = \frac{\left\langle \Psi^J \right| \mathrm{H} - \mathrm{T_{cm}} \left| \Psi^J \right\rangle}{\left\langle \Psi^J | \Psi^J \right\rangle} = \text{minimal} \tag{3.49}$$

is used, i.e., the projected energy $\mathrm{P}^J(\mathrm{H} - \mathrm{T_{cm}})\mathrm{P}^J$ is minimized within the space of FMD states $\left| \Phi \right\rangle$. This method is preferable, but greatly increases the computational effort, since many off-diagonal many-body matrix elements have to be calculated repeatedly in order to perform the integration over the Euler angles in (3.41) when the parameters of the FMD state $\left| \Phi \right\rangle$ are varied. In addition, the variation has to be done for each angular momentum J separately.

Since the present work is more concerned with the correlated interactions rather than detailed structure studies of specific isotopes, we will be content with the results of PAV calculations for the time being.

A Note on the Implementation: The Zaremba-Conroy-Wolfsberg (ZCW) Method

From the definition (3.41) of the projection operator P_{MK}^J, it is obvious that numerical calculations of the energy and other observables require three-dimensional integrations. Nowadays, numerical integrations rely on Monte-Carlo techniques, but in early implementation stages of the AMP program, the discretization of the angular integrals for random Euler angles (α, β, γ) lead to convergence problems and unsatisfying results,

most likely because the dimension of the integral is not large enough to make the statistical error of the Monte-Carlo method sufficiently small [45].

The solution to these problems was the use of a nonrandom method for integration, originally proposed independently by Zaremba and Conroy, and later refined by Wolfsberg and co-workers [46]. They showed that it is possible to find nonrandom optimal angles, which are ideal sampling points for integrands with uniformly convergent[2] Fourier series (see, e.g., [44]). Using them improves the convergence of the integration algorithm and reduces the error of the result, which is of order $O(1/N)$ for a one-dimensional integration, as opposed to the statistical error $O(1/\sqrt{N})$ of the Monte Carlo method.

---

[2] *Uniform convergence* means that the partial sums of the Fourier series converge to the true function for arbitrary function arguments.

Chapter 4

Correlated Interactions and Corrections

4.1 Correlated Interactions

With the unitary correlation operator method at hand, one can now construct correlated versions of the realistic potentials introduced in Chapter 1.

4.1.1 Correlators for Argonne V18 and Bonn-A

The central and tensor correlators used for the AV18 and Bonn-A interactions are shown in Figs. 4.2 and 4.3, respectively. The parameters of the correlation functions can be found in Appendix C; they were determined in [6] by an energy minimization as described in Sect. 2.5. A comparison shows that the central and tensor correlators for the Argonne interaction tend to be stronger than those for the Bonn-A OBEPR potential. This is not surprising, since it was already noted in Sect. 2.3 that AV18 has a stronger tensor force than Bonn-A, which causes a larger $^3D_1$-wave admixture to the deuteron groundstate wavefunction (see Fig. 4.1). However, both potentials are constructed to reproduce the same low-energy observables, and hence they give the same deuteron binding energies. In order to achieve this, the gain in binding energy provided by AV18's stronger tensor force has to be balanced by an increase in the repulsion generated by its core.

The tensor correlators displayed in Fig. 4.3 are long-ranged compared to the central correlators, hence one obtains a rather large correlation volume. Since the importance of higher cluster orders increases with the probability to find more than two nucleons inside the correlation volume, this raises concerns regarding the validity of the two-body approximation (cf. Sect. 2.1.3). The $ST = 11$ channel proves to be unproblematic due to the small values of the corresponding correlation functions, but in the $ST = 10$ channel, one encounters a similar situation as with the exact deuteron tensor correlator, which was found to be of very long range in Sect. 2.3. To ensure the validity of the two-body approximation, its range is restricted by minimizing the energy under the
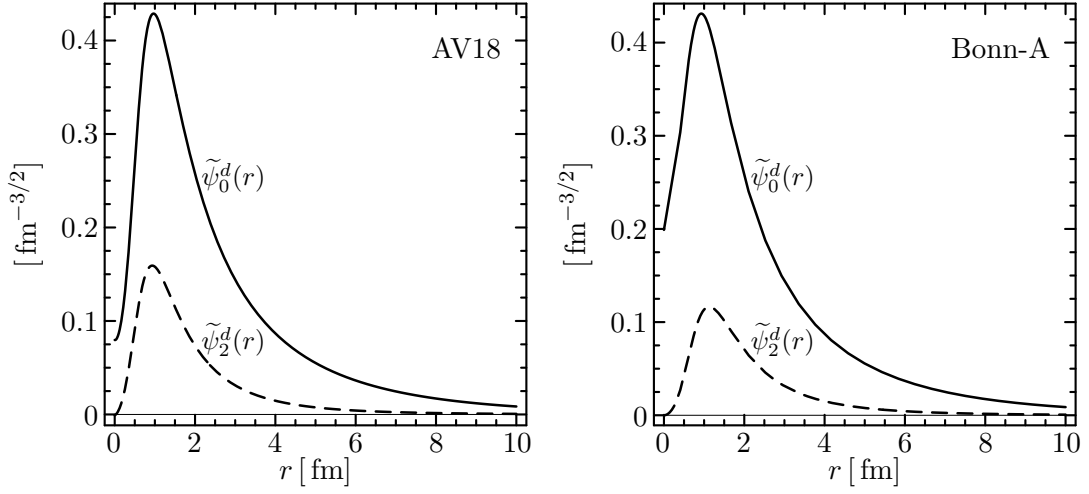
Figure 4.1: Deuteron wave functions $\widetilde{\psi}^d_{L=0,2}(r)$ for the AV18 (left) and Bonn-A potential (right) (cf. Ref. [6]).

following constraints:

$$\int dr\, r^2\, \vartheta(r) \overset{!}{=} \begin{cases} 0.1 \text{ fm}^3 & \alpha \\ 0.2 \text{ fm}^3 & \beta \\ 0.5 \text{ fm}^3 & \gamma \end{cases}. \tag{4.1}$$

In this way, the tensor correlators denoted min^α, min^β, and min^γ are obtained.

4.1.2 Correlated Interactions in Coordinate Space

In Figs. 4.4 to 4.6, we display the radial dependencies of the correlated AV18 and Bonn-A OBEPR interactions in the $ST = 10$ channel. The interactions are given in terms of the operators

$$\{ \left(\mathrm{p}_r^2\right)_h, \mathbb{1}, \mathbf{l}^2, \mathbf{l}\cdot\mathbf{s}, \mathrm{s}_{12}, \mathrm{s}_{12}(\mathbf{l},\mathbf{l}), \bar{\mathrm{s}}_{12}(\mathbf{p}_\Omega, \mathbf{p}_\Omega), \\ \mathbf{l}^2\mathbf{l}\cdot\mathbf{s}, \left(\mathbf{l}^2\bar{\mathrm{s}}_{12}(\mathbf{p}_\Omega, \mathbf{p}_\Omega)\right)_h, \left(\mathrm{p}_r\mathrm{s}_{12}(\mathbf{r}, \mathbf{p}_\Omega)\right)_h \}, \tag{4.2}$$

(cf. Sect. 2.4), where the subscript h indicates hermitization. The correspondence between the radial dependencies and the operators is obvious in most cases; the tensor operators are denoted

$$
\begin{array}{llll}
t : & \mathrm{s}_{12} & trp : & \mathrm{s}_{12}(\mathbf{r}, \mathbf{p}_\Omega) \\
tll : & \mathrm{s}_{12}(\mathbf{l},\mathbf{l}) & tpp : & \bar{\mathrm{s}}_{12}(\mathbf{p}_\Omega, \mathbf{p}_\Omega)
\end{array}
$$

when they are referred to in superscripts. It should also be noted that we will use the notation $\widetilde{\mathrm{v}}$ for the *whole* correlated interaction from now on, including the two-body contributions from the kinetic energy (cf. Chapter 2).

The quadratic spin-orbit operator $(\mathbf{l}\cdot\mathbf{s})^2$ occurring in the AV18 interaction has been decomposed into irreducible components,

$$(\mathbf{l}\cdot\mathbf{s})^2 = \frac{2}{3}\mathbf{l}^2\Pi_1 - \frac{1}{2}\mathbf{l}\cdot\mathbf{s} + \frac{1}{6}\mathrm{s}_{12}(\mathbf{l},\mathbf{l}), \tag{4.3}$$
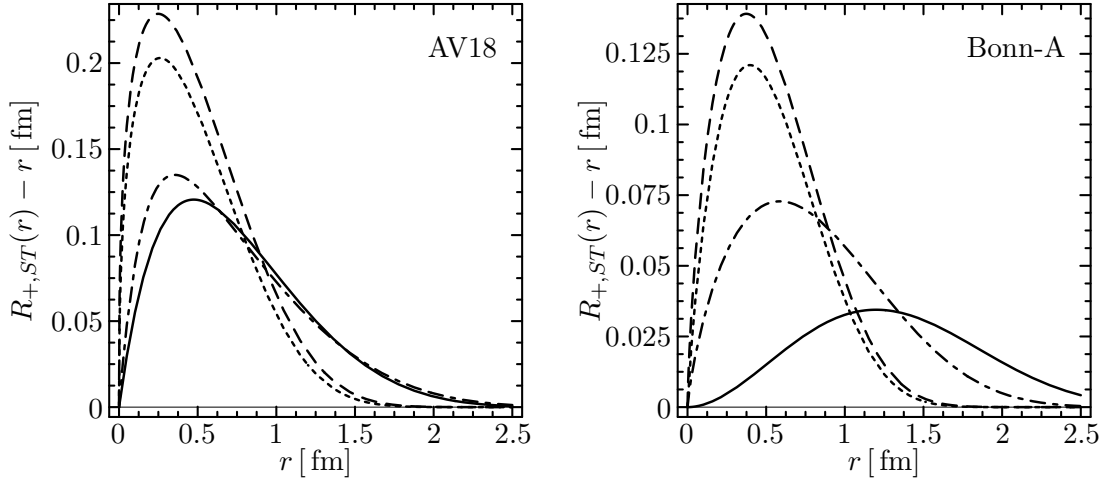
Figure 4.2: Central correlators for the AV18 (left) and Bonn-A OBEPR (right) interactions (cf. Tabs. C.1, C.3 and Ref. [6]): depicted is the correlator min^α in the $ST = 00$ channel (———), as well as the correlators min in the channels 01 (— — —), 10 (· · · · · · · ·), 11 (—·—·—).
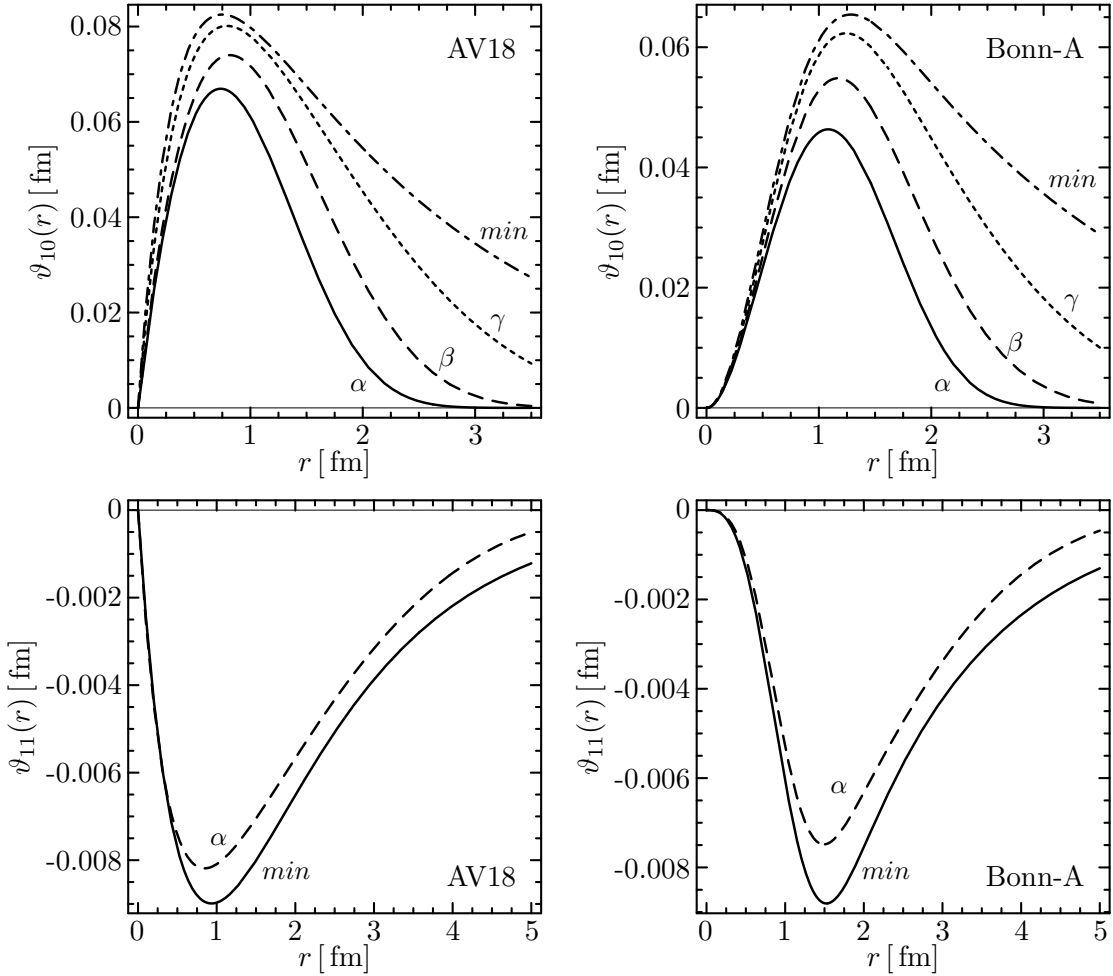
Figure 4.3: Tensor correlators for the AV18 (left) and Bonn-A OBEPR (right) interactions (cf. Tabs. C.2, C.4 and Ref. [6]). Greek letters denote min^α, min^β, and min^γ.

and AV18's charge-asymmetric and charge-dependent components (cf. Sect. 1.3, Eqs. (1.23) and (1.25)) have been dropped, since they have only a small impact on the bulk properties of the nuclei. Only the plots for the tensor correlator min^α are shown, since the overall structure of the radial dependencies is virtually identical for min^β and min^γ (cf. [6]).

The repulsive central core of AV18 is reduced in range by the central correlator, and additional attraction is generated by the tensor correlator. In the case of Bonn-A, the combined effects of the central and tensor correlator render the central part completely attractive. The contributions from the correlated kinetic energy give AV18 a radial-momentum-dependent potential, whose radial dependency is the correlated radial mass introduced in Sect. 2.4, and make the l^2-potential strongly attractive. The effects are less dramatic for Bonn-A, which had strong momentum-dependent parts to begin with. These parts are slightly weakened at small distances, but their overall range is increased by contributions from the correlated kinetic energy. The spin-orbit interaction of AV18 is shifted to shorter ranges and obtains a slightly attractive part, while it is merely 'washed out' in the case of Bonn-A. The minimum of the tensor interaction is shifted to smaller distances for both potentials — in the case of AV18, however, its strength is slightly reduced, while it remains unchanged for Bonn-A. The uncorrelated AV18 has a $s_{12}(\mathbf{l}, \mathbf{l})$-potential from the decomposition of the quadratic spin-orbit potential, which is weakened considerably by the correlators.

This covers the range of 'basic' interaction terms, which are present in one or both of the uncorrelated potentials. All other contributions are generated by the correlation procedure. Note that the radial dependencies of these terms are all very short-ranged, as we had already mentioned in the general discussion of the coordinate-space representations of the correlated interaction in Sect. 2.4. In addition, they only contribute for nonzero orbital angular momenta and remain *finite*, hence they are negligible in comparison to the centrifugal barrier. To obtain a numerical estimate, consider the centrifugal barrier acting in a state with relative orbital angular momentum $L = 1$:

$$\left\langle\, t_\Omega\,\right\rangle_{L=1} = \frac{L(L+1)\hbar c}{m_N r^2} \approx \frac{83\,\mathrm{MeV}\,\mathrm{fm}^2}{r^2}\,, \tag{4.4}$$

i.e., its strength ranges from $166\,\mathrm{MeV}$ at $r = 0.5\,\mathrm{fm}$ to $830\,\mathrm{MeV}$ at $0.1\,\mathrm{fm}$, whereas Figs. 4.5 and 4.6 show that the omitted interaction terms are more than an order of magnitude smaller at these distances.

4.1.3 Correlated Interactions for the FMD model

Since the FMD code uses a Gaussian parametrization of interaction matrix elements, it is technically advantageous to represent p_r and $\mathbf{l}^2$ interaction terms symmetrically in terms of radial derivatives and gradients,

$$\left(r\frac{\overleftarrow{\partial}}{\partial r}\right)\frac{1}{r}\widetilde{v}^{p_r^2}(r)\frac{1}{r}\left(\frac{\overrightarrow{\partial}}{\partial r}r\right),\qquad \overleftarrow{\boldsymbol{\nabla}}\,\widetilde{v}^{p^2}(r)\,\overrightarrow{\boldsymbol{\nabla}}\,, \tag{4.5}$$
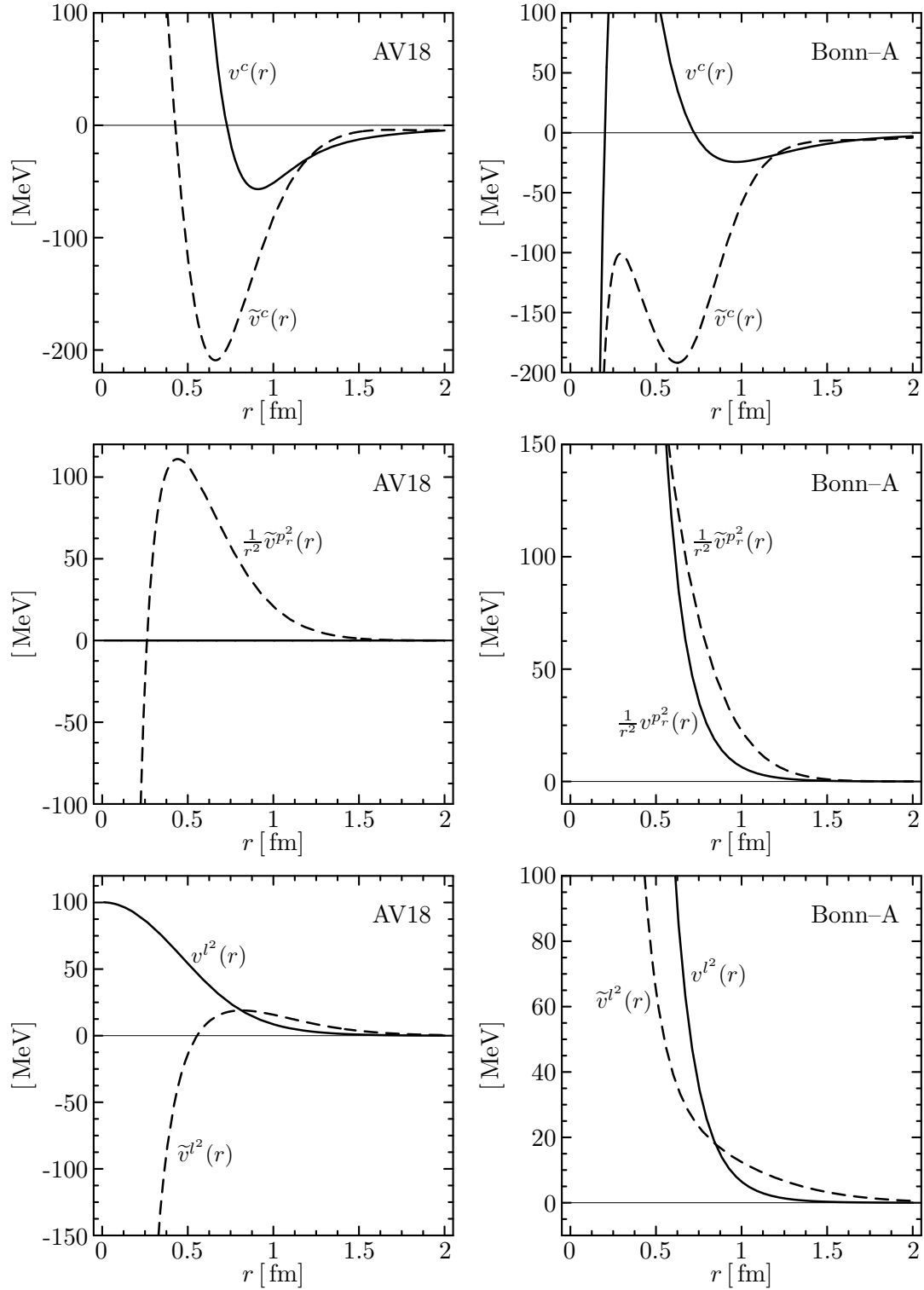
Figure 4.4: Radial dependencies of the AV18 and Bonn-A OBEPR interactions ($———$) in the $ST = 10$ channel, using the central and tensor correlators min and min^{α}, respectively. The uncorrelated interactions are shown for comparison ($———$).
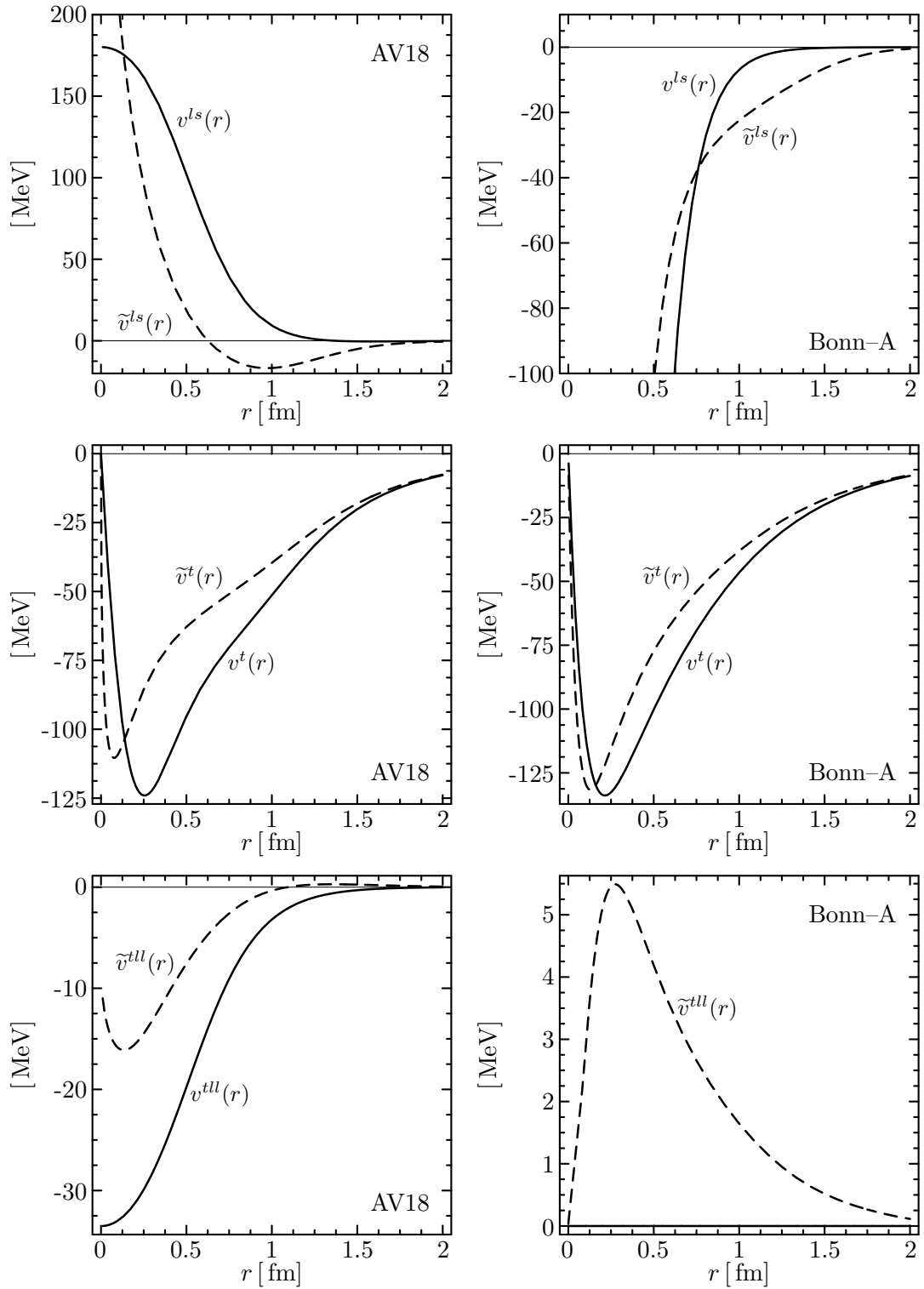
Figure 4.5: (cont.) Radial dependencies of the AV18 and Bonn-A OBEPR interactions ($---$) in the $ST = 10$ channel, using the central and tensor correlators min and min^α, respectively. The uncorrelated interactions are shown for comparison (———).
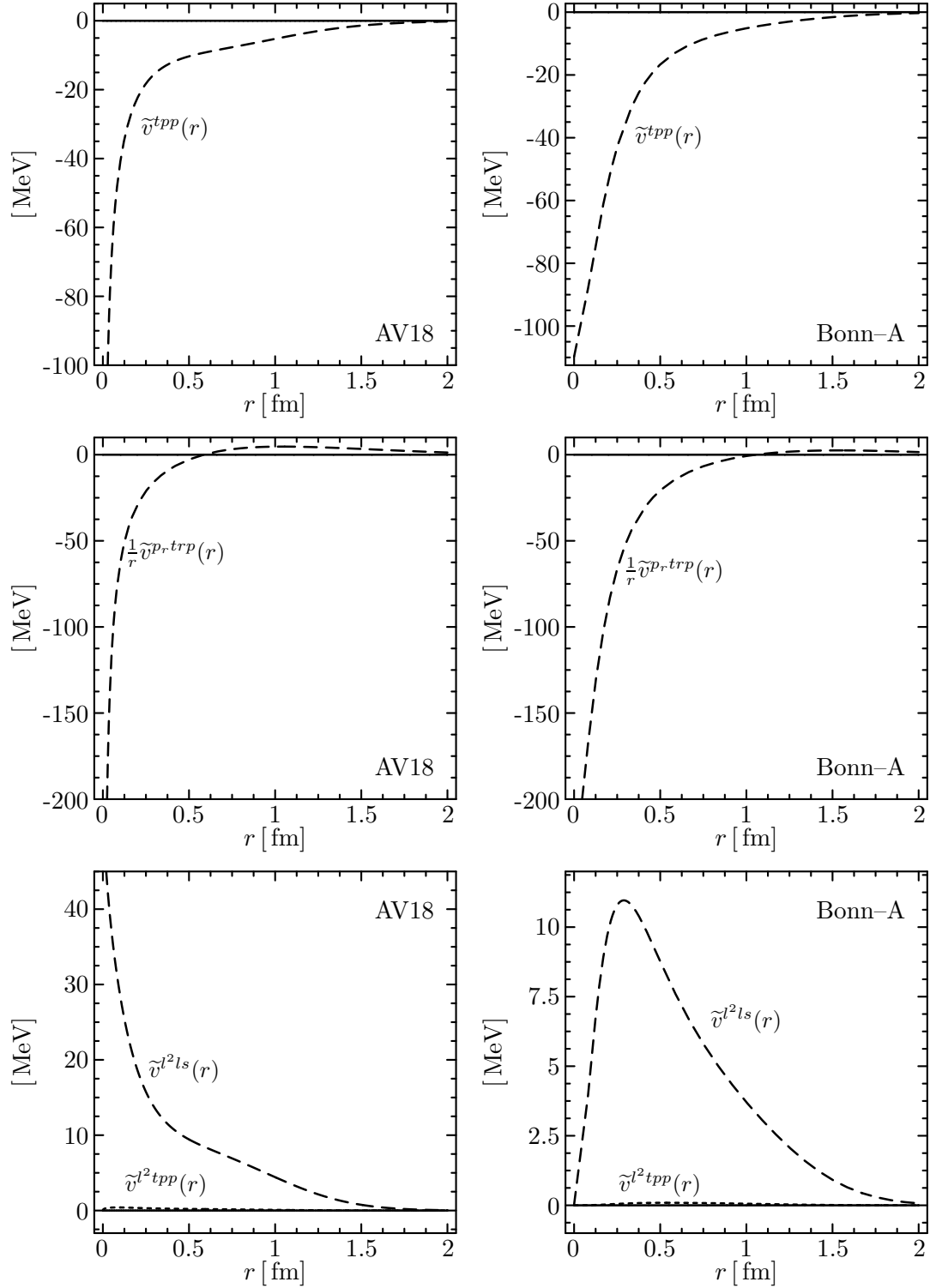
Figure 4.6: (cont.) Radial dependencies of the AV18 and Bonn-A OBEPR interactions ($-\,-\,-$) in the $ST = 10$ channel, using the central and tensor correlators min and min^{α}, respectively. The uncorrelated interactions are shown for comparison (------).

where the arrows indicate the direction in which the derivative acts. Using Eq. (A.17), we obtain what we refer to as the *FMD form* of these terms,

$$\frac{1}{2}\left(\mathrm{p}_r^2\,\widetilde{v}^{p_r^2}(\mathrm{r}) + \widetilde{v}^{p_r^2}(\mathrm{r})\mathrm{p}_r^2\right) = \mathrm{p}_r\widetilde{v}^{p_r^2}(\mathrm{r})\mathrm{p}_r - \frac{1}{2}\widetilde{v}^{p_r^2\prime\prime}(\mathrm{r}) - \frac{\widetilde{v}^{p_r^2\prime}(\mathrm{r})}{\mathrm{r}} \tag{4.6a}$$

$$\widetilde{v}^{l^2}(\mathrm{r})\,\mathbf{l}^2 = \frac{1}{2}\left(\mathbf{p}^2\,\mathrm{r}^2\,\widetilde{v}^{l^2}(\mathrm{r}) + \mathrm{r}^2\,\widetilde{v}^{l^2}(\mathrm{r})\,\mathbf{p}^2\right) - \frac{1}{2}\left(\mathrm{p}_r^2\,\mathrm{r}^2\,\widetilde{v}^{l^2}(\mathrm{r}) + \mathrm{r}^2\,\widetilde{v}^{l^2}(\mathrm{r})\,\mathrm{p}_r^2\right)$$

$$= \mathbf{p}\,\mathrm{r}^2\,\widetilde{v}^{l^2}(\mathrm{r})\,\mathbf{p} - \mathrm{p}_r\,\mathrm{r}^2\,\widetilde{v}^{l^2}(\mathrm{r})\,\mathrm{p}_r \tag{4.6b}$$

where the $\widetilde{v}^i(r)$ are the radial dependencies of the correlated interaction, i.e., the two-body part of the correlated Hamiltonian, with respect to the operators (4.2).

From Eqs. 4.6, the following radial dependencies for the FMD interactions are obtained:

$$\widetilde{v}_{\mathrm{FMD}}^c(r) = \widetilde{v}^c(r) - \frac{1}{2r}\frac{\partial^2}{\partial r^2}(r\,\widetilde{v}^{p_r^2}(r))\,, \tag{4.7a}$$

$$\widetilde{v}_{\mathrm{FMD}}^{p_r^2}(r) = \widetilde{v}^{p_r^2}(r) - r^2\,\widetilde{v}^{l^2}(r)\,, \tag{4.7b}$$

$$\widetilde{v}_{\mathrm{FMD}}^{p^2}(r) = r^2\,\widetilde{v}^{l^2}(r)\,. \tag{4.7c}$$

The higher order tensor and orbital angular momentum interactions are omitted, since their contributions can be neglected for the reasons discussed in the previous section. We *do* keep the $L = 1$ contribution of $\mathbf{l}^2\mathbf{l}\cdot\mathbf{s}$, however, by adding it to the spin-orbit interaction:

$$\widetilde{v}_{\mathrm{FMD}}^{ls}(r) = \widetilde{v}^{ls}(r) + 2\widetilde{v}^{l^2ls}(r), \quad (\langle\,L=1\,|\,\mathbf{l}^2\,|\,L=1\,\rangle = 2)\,. \tag{4.8}$$

We will drop the subscript FMD from now on, since we will only discuss FMD interactions in the remainder of this chapter.

Furthermore, we drop the residual tensor interaction $\widetilde{v}^t$, since it only gives very small contributions — typically less than 0.1% — in FMD calculations [6, 45]. This can be understood as a consequence of the vanishing directional average of the tensor operator,

$$\int d\Omega\,[3(\boldsymbol{\sigma}_1\cdot\hat{\mathbf{r}})(\boldsymbol{\sigma}_1\cdot\hat{\mathbf{r}}) - \boldsymbol{\sigma}_1\cdot\boldsymbol{\sigma}_2] = 0\,, \tag{4.9}$$

and the averaging nature of the mean-field itself. Given the tendency towards the formation of energetically favorable α-clusters, we can then understand the small contributions arising for non-spherical nuclei as residual effects due to

- $\alpha - \alpha$ interactions, e.g., spin polarization,

- small deformations of the α due to the Coulomb force, and

- interactions with nucleons not bound in an α-cluster, whose density distribution is concentrated at ranges affected only by the weak large distance tail of the correlated tensor interaction.

The parametrized correlated interactions, used for calculations with the FMD programs in the present work, are listed in Appendix D. We will refer to these FMD interactions as AV18α, Bonn-Aα, and Bonn-Aγ for the remainder of this work.
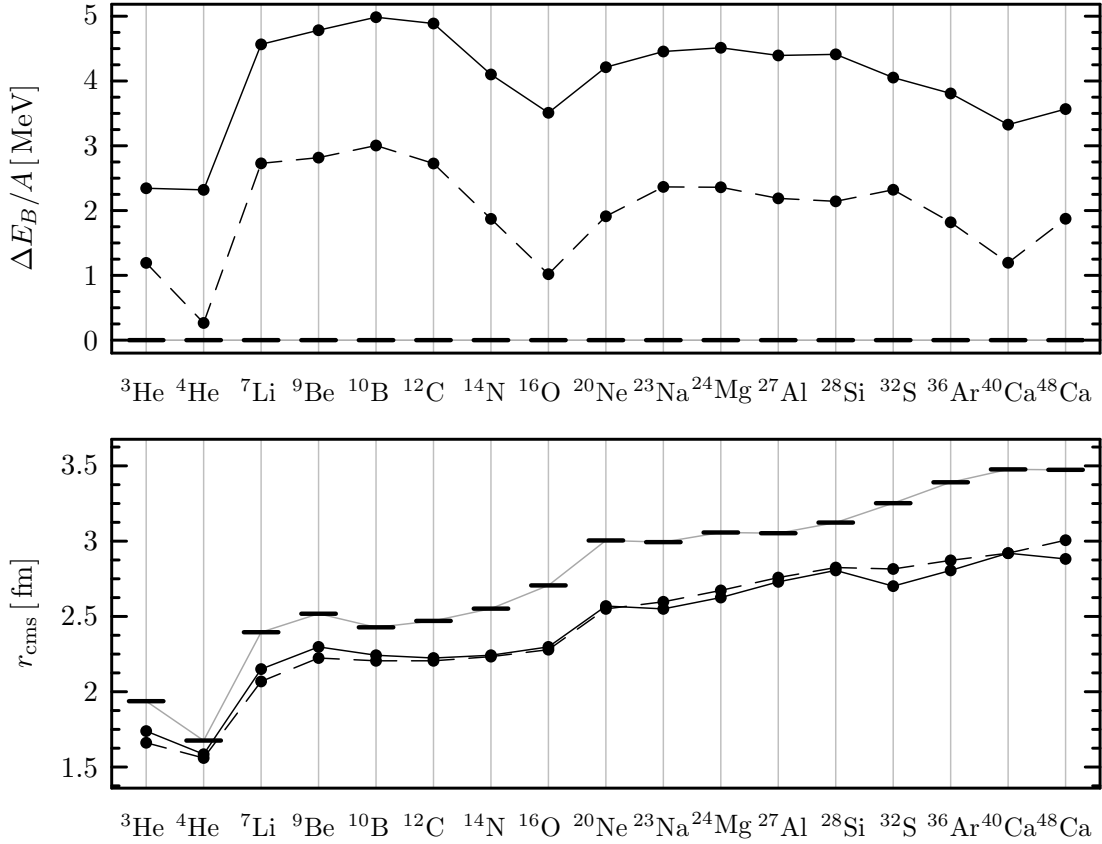
Figure 4.7: Binding energy deviations and root-mean-square charge radii calculated with Bonn-$A\alpha$ (———) and Bonn-$A\gamma$ (– – –) compared to experimental values (bars).

4.1.4 Groundstate Properties of Selected Isotopes

In Fig. 4.7, we compare the binding energies and root-mean-square charge radii of several stable isotopes, calculated using Bonn-$A\alpha$ and -γ, with experimental data. All experimental binding energies and charge radii referenced in this work have been taken from [47] and [48], respectively. The results from FMD variational calculations were obtained using single-Gaussian trial states with free spin (cf. Chapter 3), which are the default choice for all calculations in this chapter unless noted otherwise. Since r_p, the rms-charge radius of the proton, is of the same order of magnitude as the nuclear radii and interaction ranges, we have to include it when we compare our results to experimental charge radii:

$$r_{\mathrm{cms}} = \sqrt{\left\langle r_{\mathrm{ms},p}^2 \right\rangle + r_p^2}, \quad r_p = 0.862 \text{ fm}. \tag{4.10}$$

Here, $\left\langle r_{\mathrm{ms},p}^2 \right\rangle$ denotes the mean-square radius of the proton distribution, and the numerical value for r_p is taken from [49][1].

---

[1]The determination of r_p from $e-p$-scattering is dated, but in reasonal agreement with the currently recommended value $r_p = 0.870 \pm 0.008|_{ex} \pm 0.006|_{th}$ fm [24]. Modern methods to determine r_p focus on measurements and calculations of the Lamb shift.
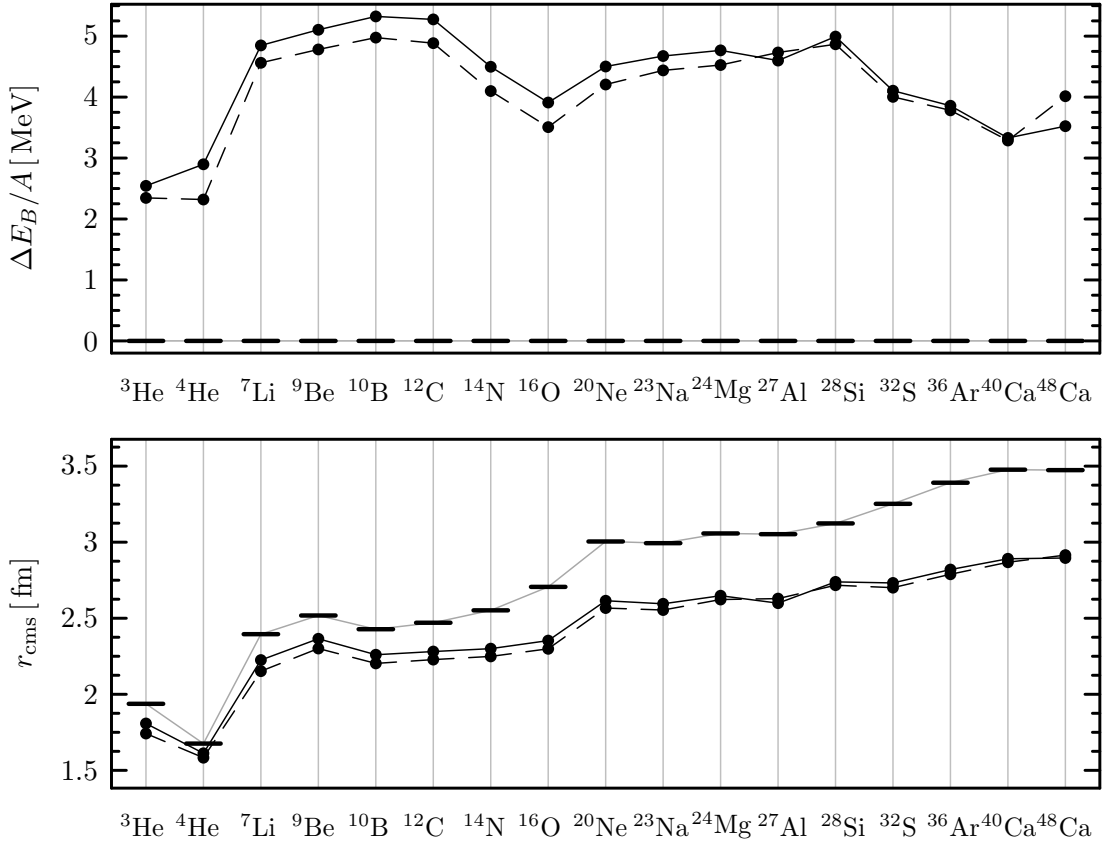
Figure 4.8: Binding energy deviations and root-mean-square charge radii calculated with AV18α (———) and Bonn-Aα (— — —) compared to experimental values (bars).

Examining our results, we find that the binding energies of most nuclei are too low, and the radii are too small at the same time. The binding energies obtained with Bonn-Aγ are in better agreement with experiment, but due to the rather large range of the tensor correlator min^γ, we have to worry about the validity of the two-body approximation (cf. Sect. 4.1.1). The root-mean-square charge radii r_{cms} are almost identical for both interactions, which illustrates that the difference in the tensor correlators affects primarily the strength of the interaction's radial dependencies rather than its structure, i.e., the location of the energy minima. In addition, the trends of the $\Delta E_B/A$-curves are very similar and the binding energies differ only by an almost constant shift.

From looking at Fig. 4.8, in which the groundstate results obtained with the AV18α interaction are compared to those of Bonn-Aα, it is evident that we cannot obtain major improvements of our results by switching to another interaction, at least not one that is phase-shift equivalent to Bonn-A. A comparison of AV18γ and Bonn-Aγ yields the same picture. The reason for the similitude of the results becomes apparent when the correlated interactions are examined in momentum space — as indicated in Sect. 2.6, the diagonal and off-diagonal matrix elements of the correlated Bonn-A and AV18 interactions are practically identical at laboratory energies below 300 MeV. Thus, all interactions between on-shell and/or off-shell nucleons inside the nucleus are essentially
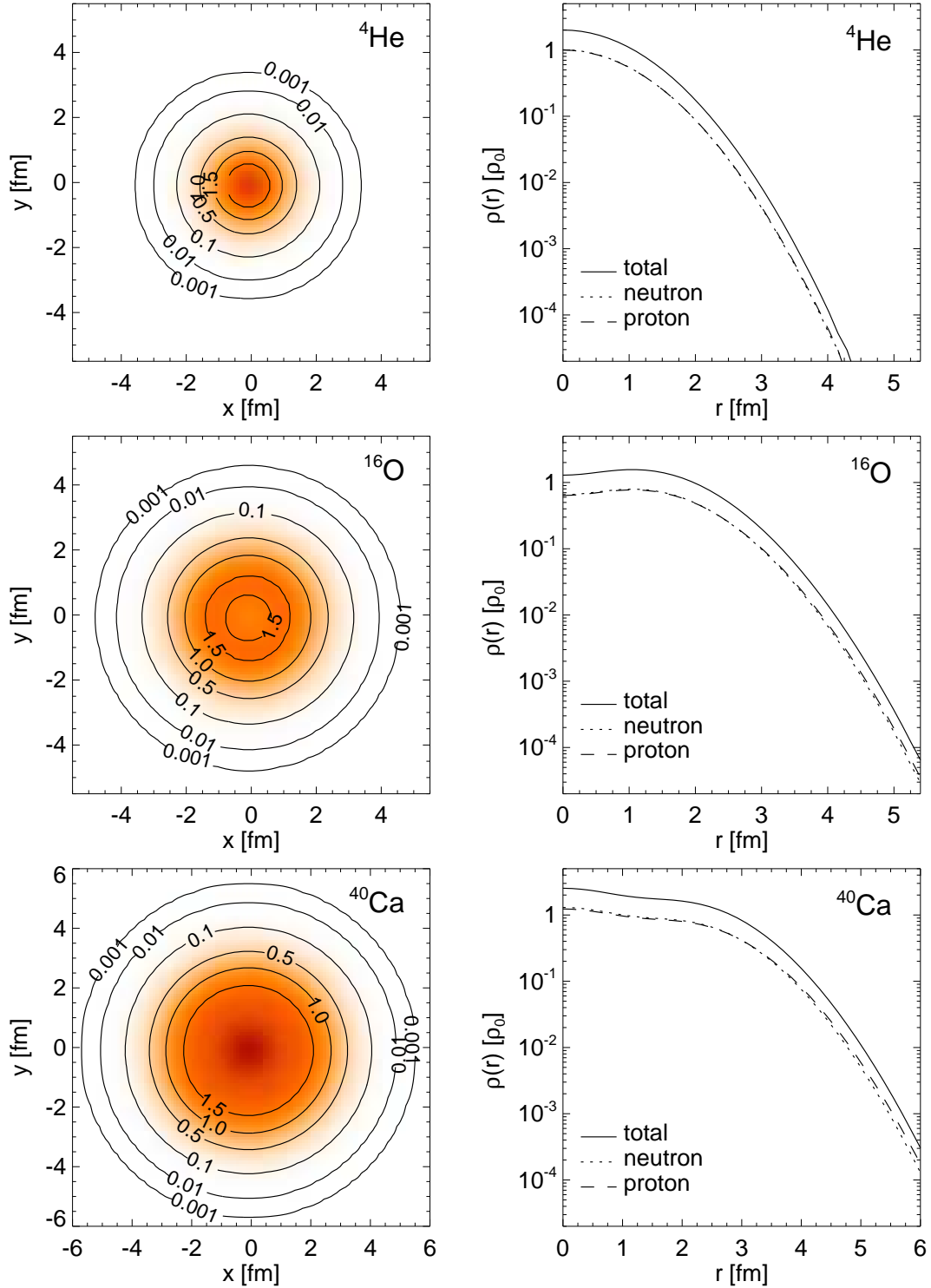
Figure 4.9: Intrinsic one-body density distributions of the lightest doubly magic nuclei, calculated with the AV18α interaction. Shown are density cuts in the xy-plane along with iso-density contours (left) and radial density distributions (right) in units of the nuclear matter density $\rho_0 = 0.17 \text{ fm}^{-3}$.
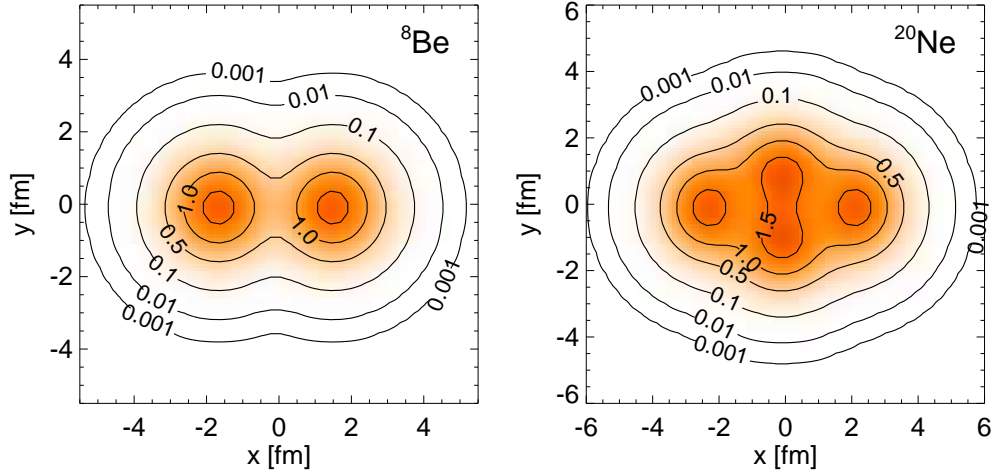
Figure 4.10: Intrinsic one-body densities and radial density distributions of ^{8}Be and ^{20}Ne, calculated using AV18α. Contours are in units of ρ_0.
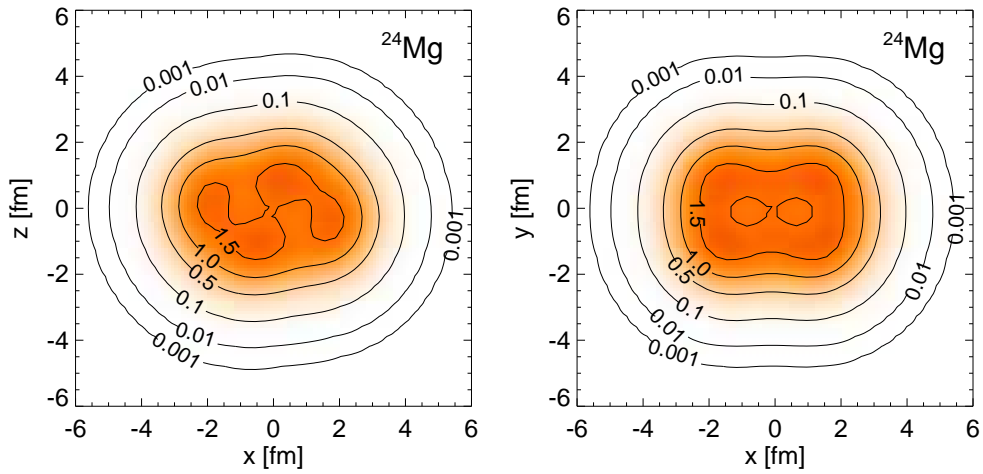
Figure 4.11: Intrinsic one-body density of ^{24}Mg, calculated with the AV18α interaction.
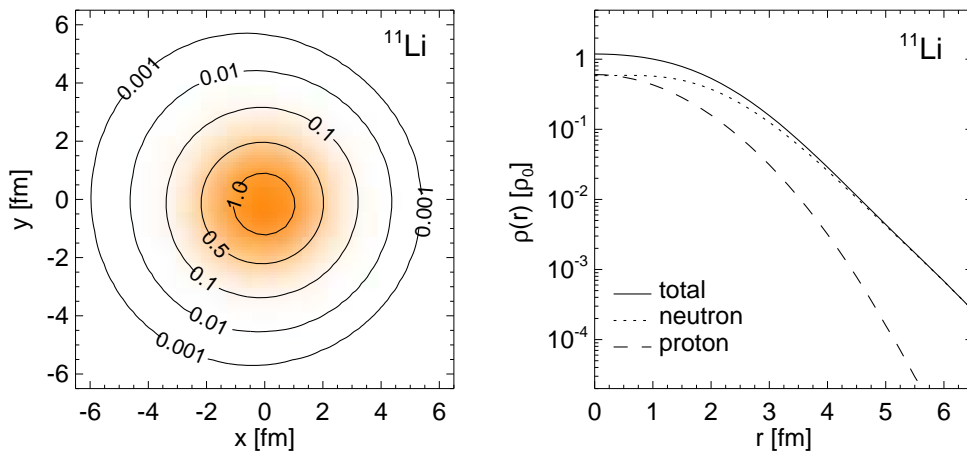
Figure 4.12: Intrinsic one-body density and radial density distribution of the halo nucleus ^{11}Li, calculated using a double Gaussian trial state. Contours are in units of ρ_0.

due to the same potential, and in turn, the results for the groundstate properties are identical.

In order to demonstrate the flexibility of the combined UCOM- and FMD-framework (and complement existing results for the Bonn-Aγ interaction presented in [6]), we show density cuts for magic and non-magic nuclei in Figs. 4.9 to 4.12, calculated with the AV18α interaction. The doubly magic nuclei ^{4}He, ^{16}O, and ^{40}Ca show the radially symmetric density distributions one would expect from the shell model.

For more complex nuclei, we find distinct clustering effects, in particular multi-α structures for even-even $N = Z$ nuclei like ^{8}Be, ^{20}Ne, and ^{24}Mg. Since these results show that the formation of α-clusters is very common in light nuclei, we obtain a first set of candidate configurations for multi-configuration mixing calculations of other isotopes. In fact, recent calculations [45, 50] indicate that even the magic ^{16}O might have a considerable admixture of a 4α-tetrahedron configuration to its groundstate, allowing it to gain several MeVs of binding energy after angular momentum projection, and possibly explaining why its experimental charge radius, $r_{\mathrm{cms}} = 2.7061$ fm, is slightly larger than that of ^{17}O ($r_{\mathrm{cms}} = 2.6975$ fm).

Fig. 4.12 shows the one-body density and radial density distribution of ^{11}Li. The variational calculation using a double-Gaussian trial state is able to describe the neutron halo, as evidenced by the extended tail of the radial neutron density distribution.

When compared to the Bonn-Aγ results of [6], the density distributions show only minor differences — they extend slightly further for the AV18α interaction. These findings illustrate both the similarity of the correlated Bonn-A and AV18 interactions and the similar structure of the α- and γ-correlated interactions' radial dependencies.

4.2　Phenomenological Corrections

The results of Sect. 4.1.4 illustrate that the correlated interactions are a good starting point for nuclear structure calculations, but evidently, something is still missing from the picture. During their derivation, we made the following approximations:

- truncation of the cluster expansion after the second order (*two-body approximation*),

- restriction of the correlator ranges through constraints on the correlation volume (cf. Sect. 4.1.1),

- truncation of the Baker-Campbell-Hausdorff series for the tensor-correlated interaction, and

- omission of higher order tensor and angular momentum operators.

The error due to the third and fourth approximations has been checked and found to be negligibly small for the deuteron (see Sect. 2.4 and Ref. [6]). While there will be some accumulation with increasing mass number, the centrifugal barrier becomes increasingly important, too. As discussed earlier, the omitted interaction terms will therefore be suppressed anyway.

The situation is far less clear for the two-body approximation. Results for centrally correlated interactions in [4, 5] showed how higher cluster orders, although small in

comparison to two-body contributions, can nevertheless have a significant influence on the binding energy of a nucleus. The total binding energy E_B is the result of cancellations between the positive kinetic energy and the negative correlated NN interaction, which are typically an order of magnitude larger than E_B itself. Thus, the omitted contributions from the higher cluster orders are one of the primary causes for differences between the calculated and the experimental binding energies.

In a related manner, we restricted the correlation volume of the $ST = 10$ tensor correlators to ensure the validity of the two-body approximation in the first place. However, the exact deuteron tensor correlator derived in Sect. 2.3 shows that the two-nucleon system actually *requires* long-ranged tensor correlations, whether we can deal with them in calculations or not. The restriction of the tensor correlator ranges prevents the system from becoming 'perfectly' correlated, and important contributions to the binding energies are missing.

The third major cause is the omission of *genuine three-nucleon and higher many-nucleon forces*, which cannot be determined from two-nucleon-scattering data and are therefore not included in the uncorrelated AV18 and Bonn-A interactions in the first place. As mentioned in Chapter 1, the results of quasi-exact Green's Function Monte Carlo (GFMC) performed by the Argonne group [51, 52, 53, 3] show that three-nucleon forces *must* be included to obtain better agreement with experiment. Many phenomenological $3N$-forces have been employed in calculations, but their parameters are reduced to mere fit degrees of freedom in the end. There is hope that the chiral potential (cf. Sect. 1.4) with its well-defined $3N$ forces provides a way to overcome these problems.

These three sources of error,

- the omission of higher cluster orders,

- the imperfect correlations due to the restricted tensor correlator range, and

- the lack of genuine three- and many-nucleon forces,

necessitate the introduction of corrections in order to achieve agreement between calculation results and experimental data.

The evaluation of higher cluster orders is in principle only a problem of the calculational effort, both in the derivation of their terms and their evaluation in numerical calculations. For the many-nucleon forces, on the other hand, we first need to have a consistent, well-defined model, e.g., the chiral potential, which must then be examined in order to construct genuine n-body correlation operators. Afterwards, the whole program of Chapter 2 would have to be carried out for all of these new correlators.

These calculations are very involved, and the implementation of these effects in the FMD code will greatly increase the computational effort: in a nucleus of mass number A, the number of possible nucleon pairs and triplets are given by

$$\binom{A}{2} = \frac{1}{2}A(A-1) = \mathcal{O}(A^2) \quad \text{and} \quad \binom{A}{3} = \frac{1}{6}A(A-1)(A-2) = \mathcal{O}(A^3), \quad (4.11)$$

which implies that the numerical effort for the calculation of two- and three-body matrix elements scales with A^4 and A^6. Therefore, we relegate the introduction of three-body correlations and three-body forces to a later time, and examine ways to simulate their

effects by effective two-body corrections, whose parameters we will determine by fitting experimental data.

The symmetries of the NN interaction — invariance under the Galilei algebra, isospin transformations, as well as the parity and time-reversal operations — restrict the structure of the correction, but still leave us with an infinite number of consistent terms. Since we truncated the expansion of the tensor-correlated interaction after terms of third order in angular momentum, it would be contradictory to use terms of higher orders in $\mathbf{l}$ at this point, which limits the possible choices. In light of the discussion in Sect. 4.1.3, it does not make sense to use $\mathbf{l}$-operators other than $\mathbf{l}^2$ and $\mathbf{l} \cdot \mathbf{s}$ at all, unless the radial potential function of the correction were large enough to compete with the centrifugal barrier. One could hardly speak of a correction in this case. The tensor operators contained in the correlated interaction,

$$\mathrm{s}_{12}, \mathrm{s}_{12}(\mathbf{l}, \mathbf{l}), \mathrm{s}_{12}(\mathbf{r}, \mathbf{p}_\Omega), \overline{\mathrm{s}}_{12}(\mathbf{p}_\Omega, \mathbf{p}_\Omega), \mathrm{s}_{12}(\mathbf{r}, \mathbf{p}_\Omega) \,, \tag{4.12}$$

cover most ways to construct $\mathrm{s}_{12}(\mathbf{a}, \mathbf{b})$ operators (aside from using $\mathbf{p}$), and since they are all negligible according to our previous discussions, we do not consider them either. Higher powers of these operators can always be decomposed into products of the basic irreducible terms and angular momentum polynomials (cf. Appendix B), and are therefore no suitable choices for correction terms. Thus, we are left with the operators

$$\mathrm{p}_r^2, \mathbf{p}^2, \mathbb{1}, \mathbf{l} \cdot \mathbf{s} \,, \tag{4.13}$$

which make up the correlated interactions in the FMD picture.

Owing to the similarity of the results obtained for the various correlated interactions in Sect. 4.1.4, it is sufficient to study the modifications for a single correlated interaction only. Optimized versions for the other interactions can be obtained by a readjustment of the corrections' parameters.

4.2.1   Central and Momentum-Dependent Corrections

Looking at the binding energies and charge radii displayed in Figs. 4.7 and 4.8, the first choice for a correction would be the addition of an attractive term to the central part of the correlated interaction. Using a Gaussian radial dependency, we have

$$\widetilde{v}_{\mathrm{mod}}^c(r) = \widetilde{v}^c(r) + \gamma^c \exp\left(-\frac{r^2}{2\kappa^c}\right) \,, \quad \gamma < 0 \,. \tag{4.14}$$

Choosing the Bonn-Aγ interaction as a test candidate, since its binding energies agree better with experimental data, we immediately find that $\widetilde{v}_{\mathrm{mod}}^c(r)$ causes severe over-binding of the 'heavier' nuclei around the Calcium region if we tune the parameters γ^c and κ^c in order to reproduce the binding energy of ^{4}He. Naturally, the already too small radii decrease even further. A solution to this problem is the addition of a short-ranged repulsive interaction. Since the over-binding grows worse with increasing nucleon number, we choose to add a repulsive term to the momentum-dependent part of Bonn-Aγ,

$$\widetilde{v}_{\mathrm{mod}}^{p^2}(r) = \widetilde{v}^{p^2}(r) + \gamma^{p^2} \exp\left(-\frac{r^2}{2\kappa^{p^2}}\right) \,, \quad \gamma > 0 \,, \tag{4.15}$$
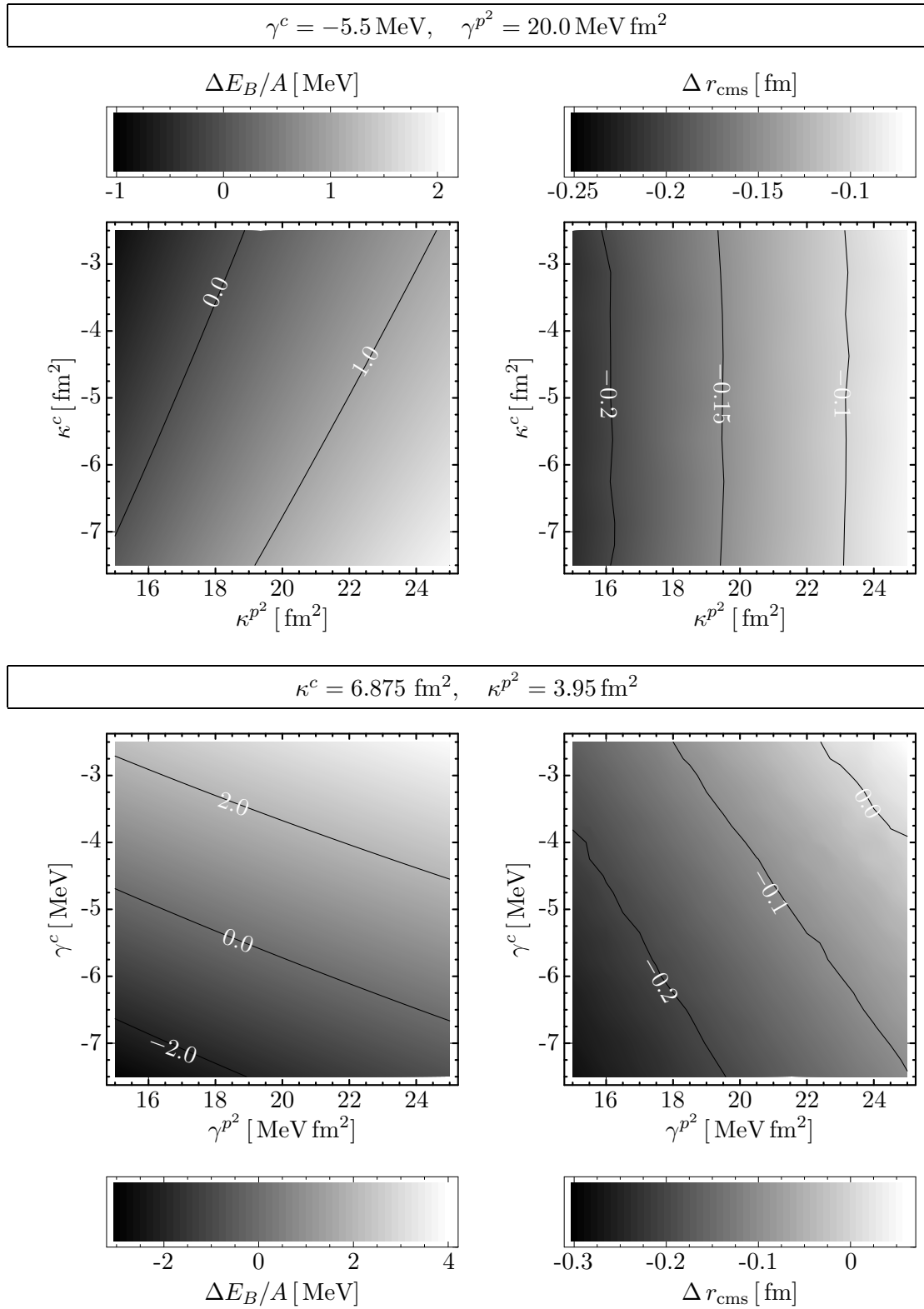
Figure 4.13: $\Delta E_B/A$ and Δr_{cms} of ^{16}O for the Bonn-Aγ interaction and $ST = 10$ corrections with varying parameters.

rather than just the p_r^2-part, which increases the repulsive effect on the binding energies of the heavier nuclei through the $\mathbf{l}^2$-term in

$$\mathbf{p}\widetilde{v}^{p^2}(\mathrm{r})\mathbf{p} = \mathrm{p}_r\widetilde{v}^{p^2}(\mathrm{r})\mathrm{p}_r + \widetilde{v}^{p^2}(\mathrm{r})\mathbf{l}^2 \ . \tag{4.16}$$

$ST = 10$ corrections

The spin and isospin spaces provide sufficient freedom to antisymmetrize a state of four nucleons, hence we can assume that the coordinate space wavefunction will be symmetric. Comparison with the harmonic oscillator shell model backs this assumption, since neutrons and protons occupy the respective s-shells. Thus, in order to fit the properties of ^{4}He, we only need to introduce a correction to the even channels.

As we discussed in Sect. 4.1.1, the $ST = 10$ channel contains strong contributions from the correlated tensor interaction, depending on the size and range of the corresponding tensor correlators. Thus, the $ST = 10$ channel is more likely to be the source of deviations from experimental data than the 01-channel, either due to non-negligible many-body correlations, which we would expect for the correlator min^γ, or the 'severe' restriction of the correlation range in case of min^α. For this reason, we introduce a $ST = 10$ correction consisting of the aforementioned attractive local and repulsive momentum-dependent central parts, and tune its parameters — $\gamma^c, \kappa^c, \gamma^{p^2}$, and κ^{p^2} — to fit the binding energies and root-mean-square charge radii of the doubly magic nuclei ^{4}He, ^{16}O, and ^{40}Ca. We keep an eye on the groundstate properties of the doubly-magic ^{48}Ca, too, but do not use them as input for fitting.

Fig. 4.13 illustrates how the the binding energy and root-mean-square charge radius of ^{16}O change with the parameters of the correction. The behavior of the binding energy is as expected — if the κ^i are held fixed (lower plot), increasing the strength of the attractive central part will increase the binding energy, increasing the strength of the repulsive part decreases it again, and vice versa. The same situation occurs if the γ^i are fixed and the ranges are varied (upper part). The behavior of the charge radius proves to be more interesting. While a change of the γ^i at fixed κ^i produces the same trends as for the binding energy, the charge radii appear to be almost insensitive to a change of κ^c for fixed γ^i (upper right plot). We can explain this by inspecting the modified radial dependencies displayed in Fig. 4.14: the location of the central interaction's minimum at $r \approx 1.2$ fm will only change notably for large γ^c and short ranges κ^c, for which the slope of the Gaussians changes strongly across the location of the minimum. If κ^c is large, the Gaussian is rather flat, and only the energy of the minimum will be shifted upward or downward, depending on γ^c. Since the momentum-dependent interaction is purely repulsive, increasing its range κ^{p^2} will evidently be the primary cause for shifts of the overall energy minimum to larger r. Under this aspect, it is sensible to fix the value of κ^{p^2} first, e.g., by fitting a selected charge radius.

Mathematically, we can fit either two of the three doubly magic nuclei perfectly with our modification's four parameters. However, if ^{16}O and ^{40}Ca are fit, ^{4}He becomes under-bound, and tuning the correction to ^{4}He and ^{16}O gives bad results for ^{40}Ca and the 'constraint' ^{48}Ca. Nevertheless, we *can* obtain a very good simultaneous description of ^{4}He and ^{40}Ca, and get reasonable results for ^{16}O and ^{48}Ca (see Fig. 4.15). The parameters of the corresponding correction, denoted Bonn-Aγ + st10, are listed in Tab. 4.2 at the end of the section, and the modified radial dependencies are displayed in Fig.
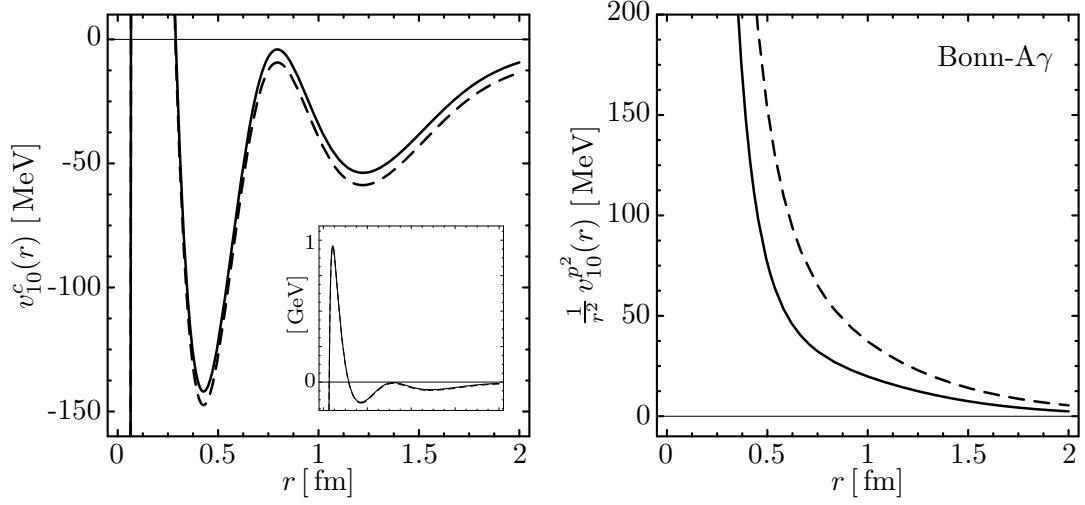
Figure 4.14: Modified radial dependencies of Bonn-Aγ + st10 interaction ($---$) (cf. 4.2), in comparison with Bonn-Aγ (———). Note that both interactions are represented in the FMD form.
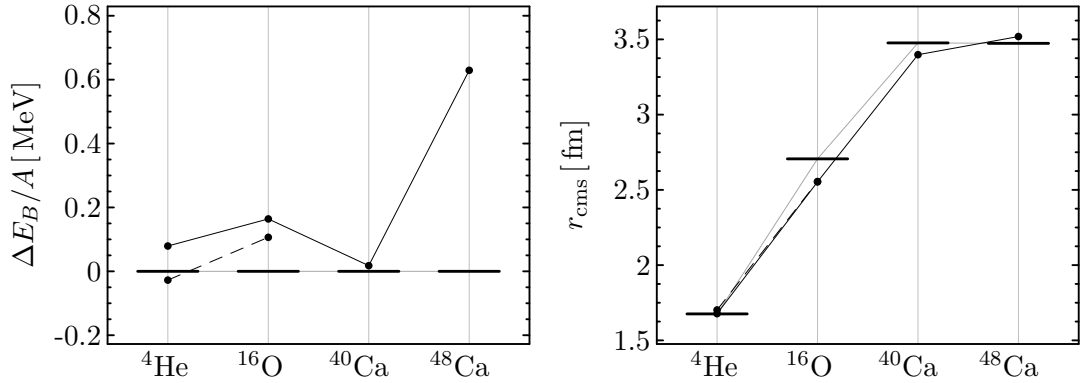
Figure 4.15: Binding energy deviations and rms charge radii for the lightest doubly magic nuclei, calculated for Bonn-Aγ + st10, using single Gaussian states with free spin (———) and double Gaussian states with fixed spin ($---$).

4.14. The 'curve' of the charge radii has a dent at ^{16}O, while the results for the other doubly magic nuclei agree fairly well with experiment. In a similar fashion, ^{16}O is still under-bound by about 0.1 MeV per nucleon, which results in a characteristic triangular arc in the $\Delta E_B/A$ plot. As already mentioned in Sect. 4.1.4, these deviations, in particular the increased r_{cms} when compared to the neighboring isotopes and predictions for closed shell nuclei, are indications of a 4α-tetrahedron admixture to the groundstate, which increases the charge radius towards the experimental value, and leads to a larger groundstate binding energy after angular momentum projection.

The results obtained with the $ST = 10$ correction do not change notably if we shift some or all of its strength to the $ST = 01$ channel, i.e., if we use potentials of the form

$$\mathrm{v}_{ee}^i(\varepsilon) \equiv \mathrm{v}^i \left(\varepsilon \Pi_{10} + (1 - \varepsilon)\Pi_{01} \right) , \quad i = c, p^2 , \tag{4.17}$$

where the index ee indicates a shift between the even channels. To illustrate this

Nucleus	ST				# of NN-pairs
	00	01	10	11	
^{4}He	–	3	3	–	6
^{16}O	6	30	30	54	120
^{40}Ca	45	165	165	405	780

Table 4.1: Multiplicities of the four ST-channels in the doubly magic nuclei.

insensitivity, the binding energy deviations and charge radii of the Carbon and Calcium isotopes are displayed in Fig. 4.16, for $\varepsilon = 0.5, 0.75$, and 1.0.

Given the differences in the radial dependencies of the even channels (see Fig. 4.17), these findings are surprising, but they underline that the radii are primarily determined by the location of the minima in the central part. If they are not dislocated notably, the radii do not change. The insensitivity also implies that both even channels occur with roughly the same multiplicities in the studied isotopes, since an unweighted shift would otherwise create serious over- or under-binding. They can be estimated by comparison with, e.g., the harmonic oscillator shell model: we only need to couple the quantum numbers of a nucleon pair occupying given single-particle states, and explicitly count the pairs which contribute to the different ST-channels. For the doubly magic nuclei, we find the values listed in Tab. 4.1, which back our assumption.

Even-Odd Corrections

The isotope chains presented in Fig. 4.16 also show that there is still considerable room for improvement. Since we are now aware that corrections to the even channels are practically equivalent for the mass range under consideration, the obvious choice is to introduce correction terms in the odd channels. If we add both a local and a momentum-dependent Gaussian central correction restricted to the $ST = 11$ channel, we would ideally need to determine all parameters of the correction — two strengths and two ranges for each channel — by a simultaneous variation. In practice, this means that the number of parameter sets which have to be checked becomes unfeasibly high, since the calculational effort is of order N^8, where N is the number of possible values for each of the parameters, and we would need to perform a minimization of each fit nucleus — at least four, so that we can obtain a conclusive fit of eight nuclear properties — for every possible parameter set.

In order to reduce the computation time, we need to fix some of the parameters to reasonable values, preferably in a way that will retain the good results for ^{40}Ca. As we have discussed above, ^{4}He will not be affected by a $ST = 11$ correction, since its nucleons are coupled to even-channel pairs, so an $ST = 10$ part which gives a good fit of the Helium data is chosen as the starting point. Two methods have been chosen to proceed:

(i) The parameters $\gamma_{11}^c, \gamma_{11}^{p^2}, \kappa_{11}^c$, and $\kappa_{11}^{p^2}$ are varied freely to improve the agreement of the ^{16}O results with experimental data. As Fig. 4.18 illustrates for two sample
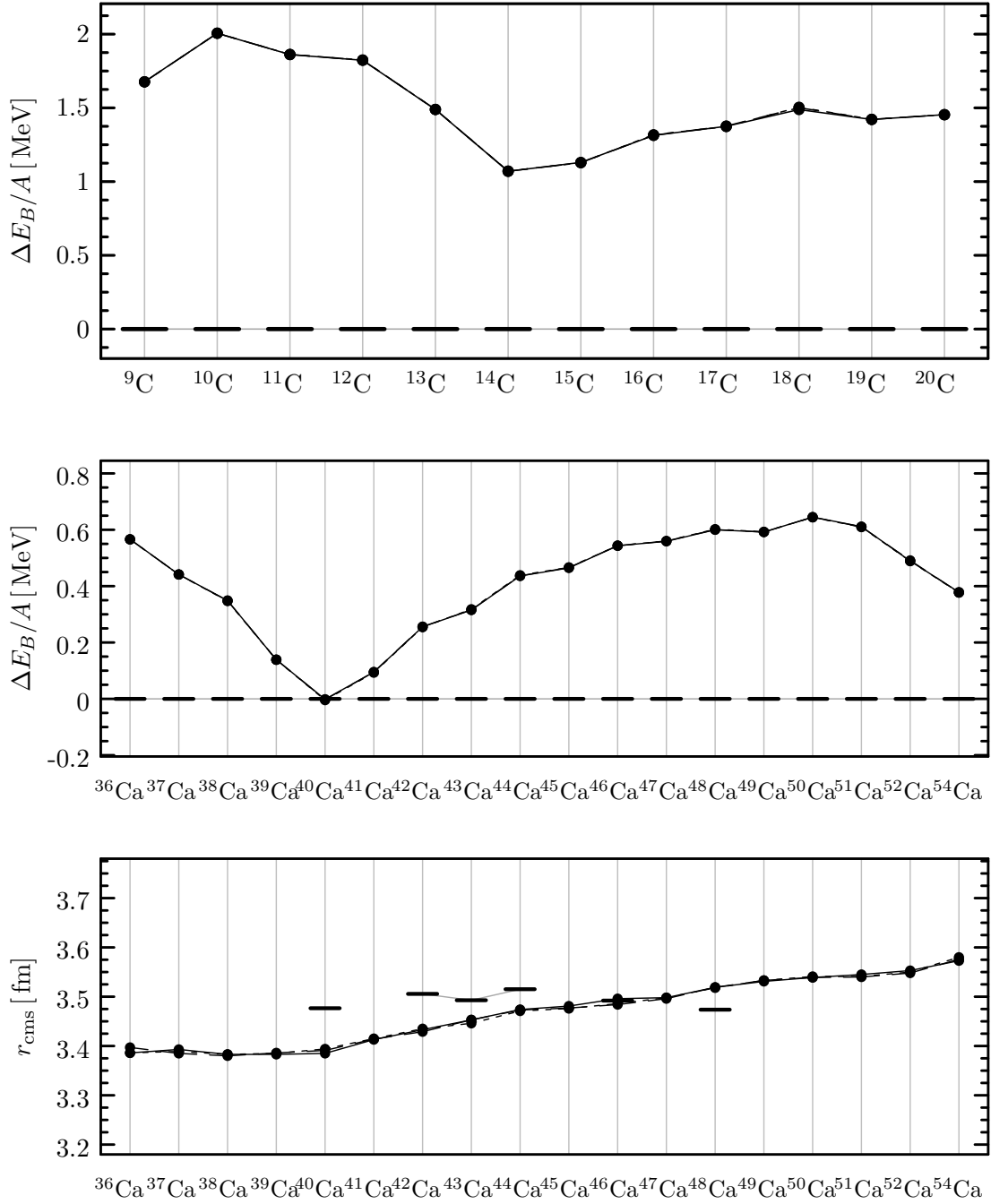
Figure 4.16: Shift between the $ST = 10$ and $ST = 01$ channels for the Bonn-Aγ + st10 interaction. Shown are $\Delta E_B/A$ and r_{cms} for Carbon and Calcium isotopes, for $\varepsilon = 0.5$ (———), 0.75 (— — —), and 1.0 (·—·—·) . The results are almost indistinguishable.
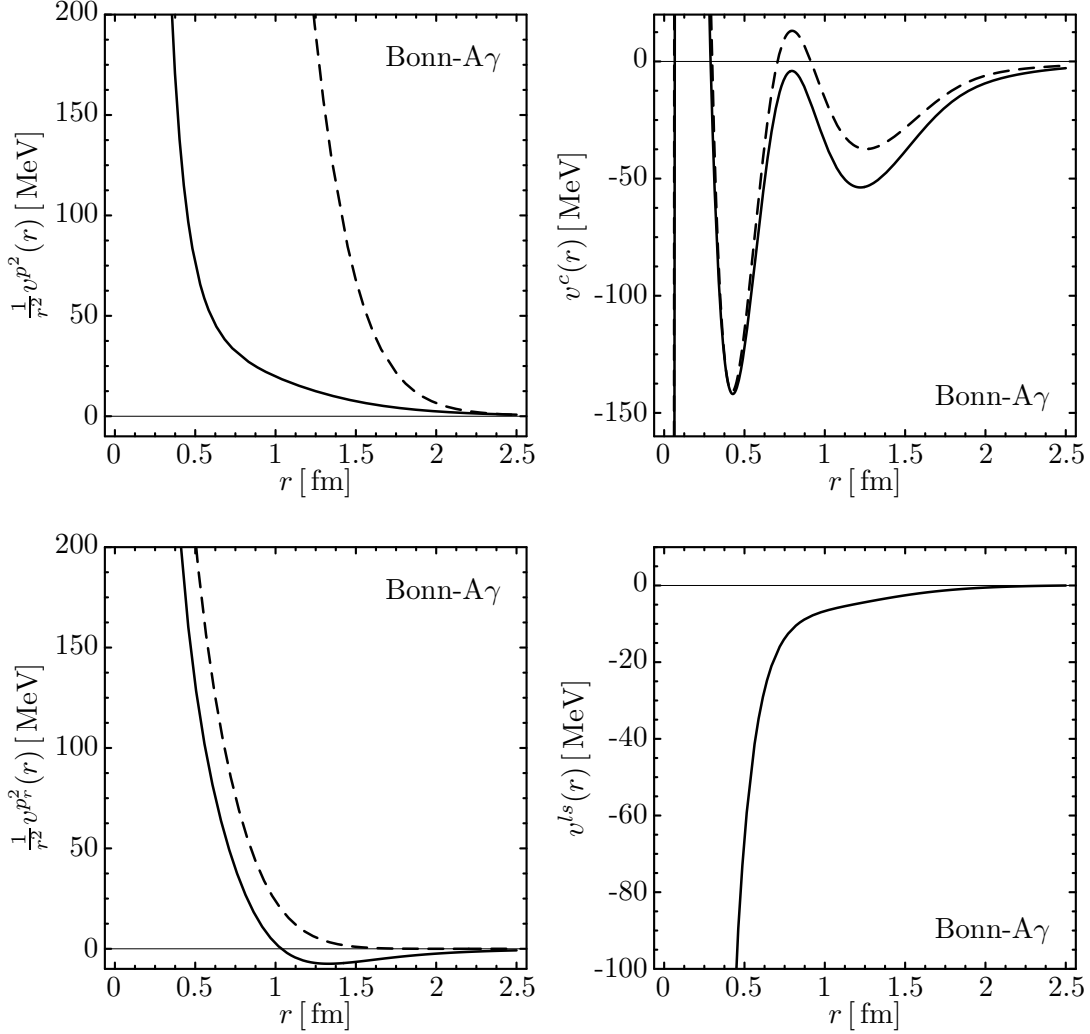
Figure 4.17:   Radial dependencies of Bonn-Aγ in the $ST = 10$ (———) and $ST = 01$ ($---$) channels.

corrections,

$$
\begin{aligned}
\gamma^c_{11} &= -8.353 \text{ MeV}\,, & \kappa^c_{11} &= 3.0 \text{ fm}^2\,, \\
\gamma^{p^2}_{11} &= 20.587 \text{ MeV fm}^2\,, & \kappa^{p^2}_{11} &= 2.0 \text{ fm}^2\,,
\end{aligned}
\tag{vI}
$$

and

$$
\begin{aligned}
\gamma^c_{11} &= -2.644 \text{ MeV}\,, & \kappa^c_{11} &= 6.0 \text{ fm}^2\,, \\
\gamma^{p^2}_{11} &= 9.170 \text{ MeV fm}^2\,, & \kappa^{p^2}_{11} &= 3.0 \text{ fm}^2\,,
\end{aligned}
\tag{vII}
$$

this comes at the price of worse results for ^{40}Ca. Graphically speaking, varying the parameters corresponds to 'rotating' the $\Delta E_B/A$- and r_{cms}-curves around the 'hub' ^{4}He without deforming them notably. Varying all four $ST = 11$ parameters simultaneously still requires a computational effort of order N^4 and hence limits the use of this method.
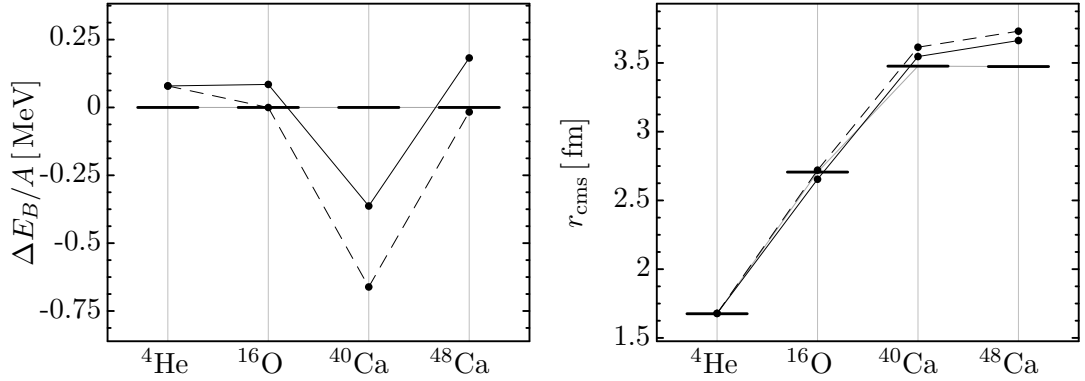
Figure 4.18: Binding energy deviations and rms charge radii for selected doubly magic nuclei, calculated for Bonn-Aγ + st10 + 11-vI (——) and -vII (– – –).

(ii) As an alternative approach, we use the ansatz

$$\mathrm{v}_{eo}^i(\varepsilon) = \mathrm{v}^i\left((1-\varepsilon)\Pi_{10} + \varepsilon\Pi_{11}\right), \quad i = c, p^2, \tag{4.18}$$

where the index eo now indicates a mixing of even and odd channels. The ranges κ^c and κ^{p^2} are held fixed at their values from the pure $ST = 10$ correction, which reduces the free parameters to ε, γ^c, and γ^{p^2}. To hold the ^{4}He properties fixed, we further require that the $ST = 10$ correction is reproduced independently of ε, i.e.,

$$\gamma^c \overset{!}{=} \frac{\gamma_{10}^c}{1-\varepsilon}, \tag{4.19a}$$

$$\gamma^{p^2} \overset{!}{=} \frac{\gamma_{10}^{p^2}}{1-\varepsilon}. \tag{4.19b}$$

The altered radial dependencies in the $ST = 11$ channel are displayed in Fig. 4.19, alongside with $\Delta E_B/A$ and r_{cms} of our selected doubly magic nuclei (Fig. 4.20) for $\varepsilon = 0, 0.2$, and 0.5. We observe that an increase of ε increases the difference between the $\Delta E_B/A$ of ^{16}O and ^{40}Ca, which is caused by the different relative weight of the channels in these nuclei,

$$^{16}\mathrm{O}: \quad \frac{n_{11}}{n_{10}} = \frac{54}{30} = 1.8, \qquad ^{40}\mathrm{Ca}: \quad \frac{n_{11}}{n_{10}} = \frac{405}{165} = 2.455, \tag{4.20}$$

(cf. Tab. 4.1). The $ST = 11$ correction is repulsive at short ranges, hence ^{16}O becomes increasingly under-bound, while it is attractive at intermediate and long ranges, causing the over-binding of ^{40}Ca. The charge radii (except for ^{4}He) increase with ε due to the additional repulsion generated by $v_{11}^{p^2}(r)$ first, but move back towards the values of the pure $ST = 10$ correction as we approach $\varepsilon = 0.5$. Thus, the attractive local central part becomes strong enough to outweigh the repulsion and concentrates the two-body densities in the region of the minimum at $r \approx 2\,\mathrm{fm}$.
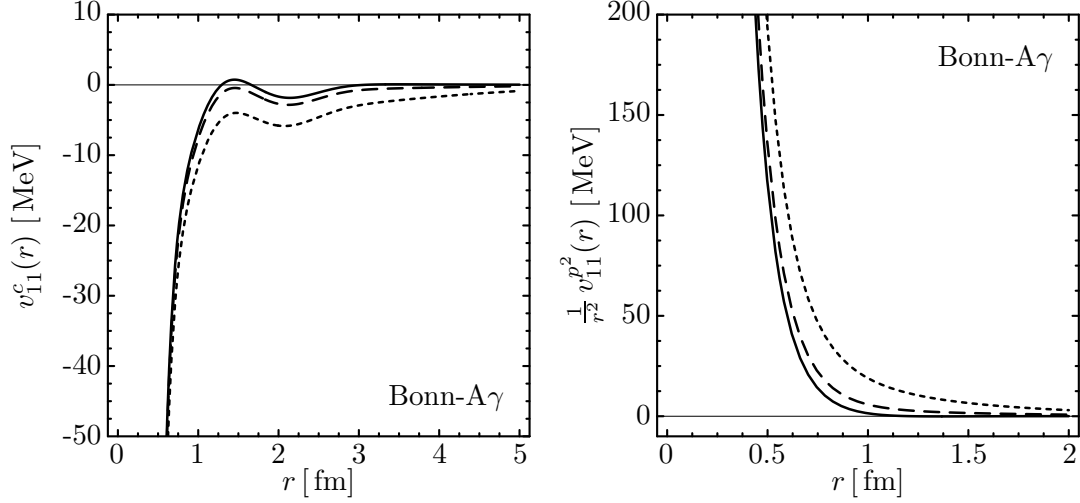
Figure 4.19: Radial dependencies of Bonn-Aγ + st10 + 11-ε, for $\varepsilon = 0$ (———) (unmodified $ST = 11$ channel), 0.2 (— — —), and 0.5 (-------).
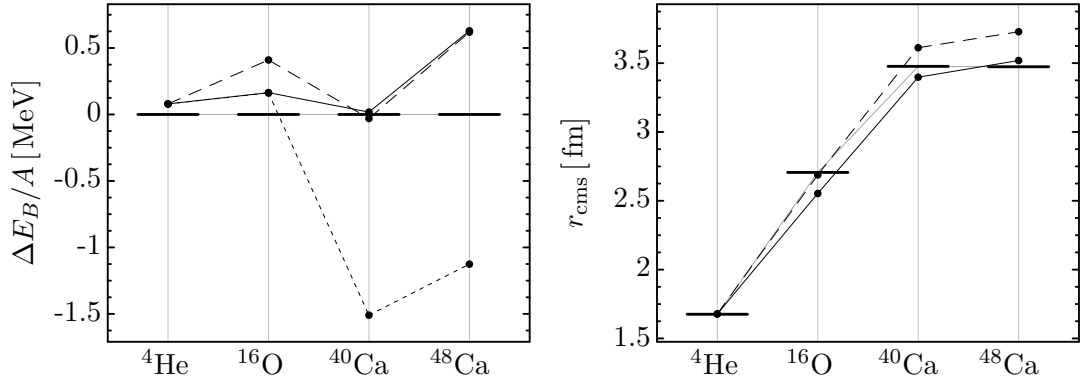
Figure 4.20: Binding energy deviations and rms charge radii for selected doubly magic nuclei, calculated for Bonn-Aγ + st10 + 11-ε with $\varepsilon = 0$ (———)($ST = 10$ correction), 0.2 (— — —), and 0.5 (-------).

min$^\alpha$ vs. min$^\gamma$

As we have discussed in Sect. 4.1 and at the beginning of the present section, the long range and large correlation volume of the tensor correlator min^γ give serious cause for concern regarding the validity of the two-body approximation: its range is almost 4 fm (see Fig. 4.3), which is about twice as large as the mean distance of the nucleons inside the nucleus. Hence, there is a high probability to find three nucleons inside the correlation volume simultaneously, and the three-nucleon correlations become large. The range of min^α, on the other hand, is only about 2 fm, and therefore comparable to the nucleon mean distance, hence we expect that only two nucleons will be inside the correlation volume most of the time, i.e., the two-body approximation is good. However, min^α also lacks binding energy contributions due to its restricted range, as indicated before.

This lack of binding energy actually works to our advantage if we use Bonn-Aα as the
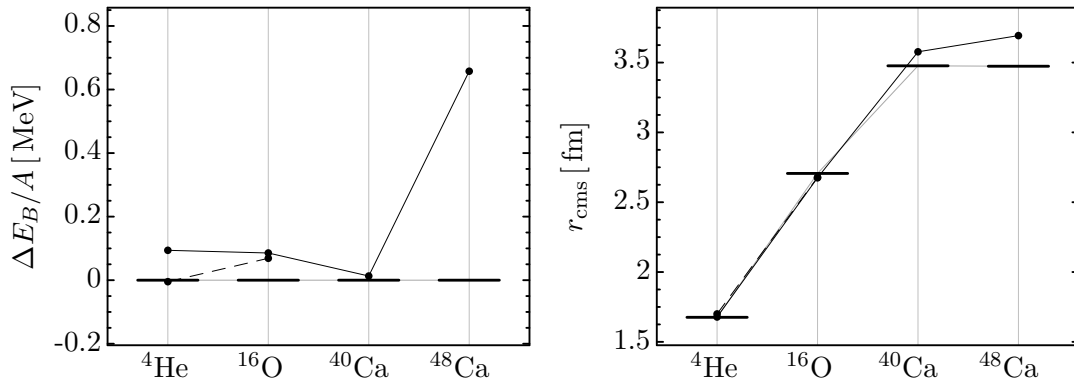
Figure 4.21: $\Delta E_B/A$ and r_cms for selected doubly magic nuclei, calculated for Bonn-Aα + w. Calculations were done using single-Gaussian trial states (———) and double-Gaussian states ($---$), respectively, with free spins.

fundament for our correction terms: the relative deviations in binding energy and charge radii are more uniform in magnitude than for Bonn-Aγ. The binding energies calculated for the latter are closer to experimental values, while both interactions were found to yield the same radii in Sect. 4.1.4. The type of modifications studied in the previous subsections increases both the radii and the binding energies, which quickly causes over-binding for Bonn-Aγ if the radii are close to experiment. Since the unmodified Bonn-Aα has smaller binding energies to begin with, the over-binding can be removed entirely.

Wigner corrections

While discussing the results for even-odd corrections with various shift parameters ε, we found that a correction with $\varepsilon = 0.5$ would actually give good results if it were not for the over-binding of ^{40}Ca and ^{48}Ca. We have argued that this can be cured by starting from the Bonn-Aα interaction. Since we have also shown that shifts among the even or the odd channels make no difference at all, we conclude that a simple Wigner correction to the Bonn-Aα interaction can reproduce experimental data well enough (see Fig. 4.21), while being structurally simple at the same time:

$$\widetilde{v}^c_{\mathrm{mod},ST}(r) = \widetilde{v}^c_{ST}(r) + \gamma^c \exp\left(-\frac{r^2}{2\kappa^c}\right), \tag{4.21}$$

$$\widetilde{v}^{p^2}_{\mathrm{mod},ST}(r) = \widetilde{v}^{p^2}_{ST}(r) + \gamma^{p^2} \exp\left(-\frac{r^2}{2\kappa^{p^2}}\right). \tag{4.22}$$

The parameters of the final Wigner-corrected interaction, denoted Bonn-Aα + w, are listed in Tab. 4.2.

4.2.2 Spin-Orbit Corrections

In the previous section, we have extensively studied ways to construct corrections using the first three operators of our proposed basic set

$$\{\mathrm{p}_r^2, \mathrm{l}^2, \mathbb{1}, \mathbf{l}\cdot\mathbf{s}\}, \tag{4.23}$$
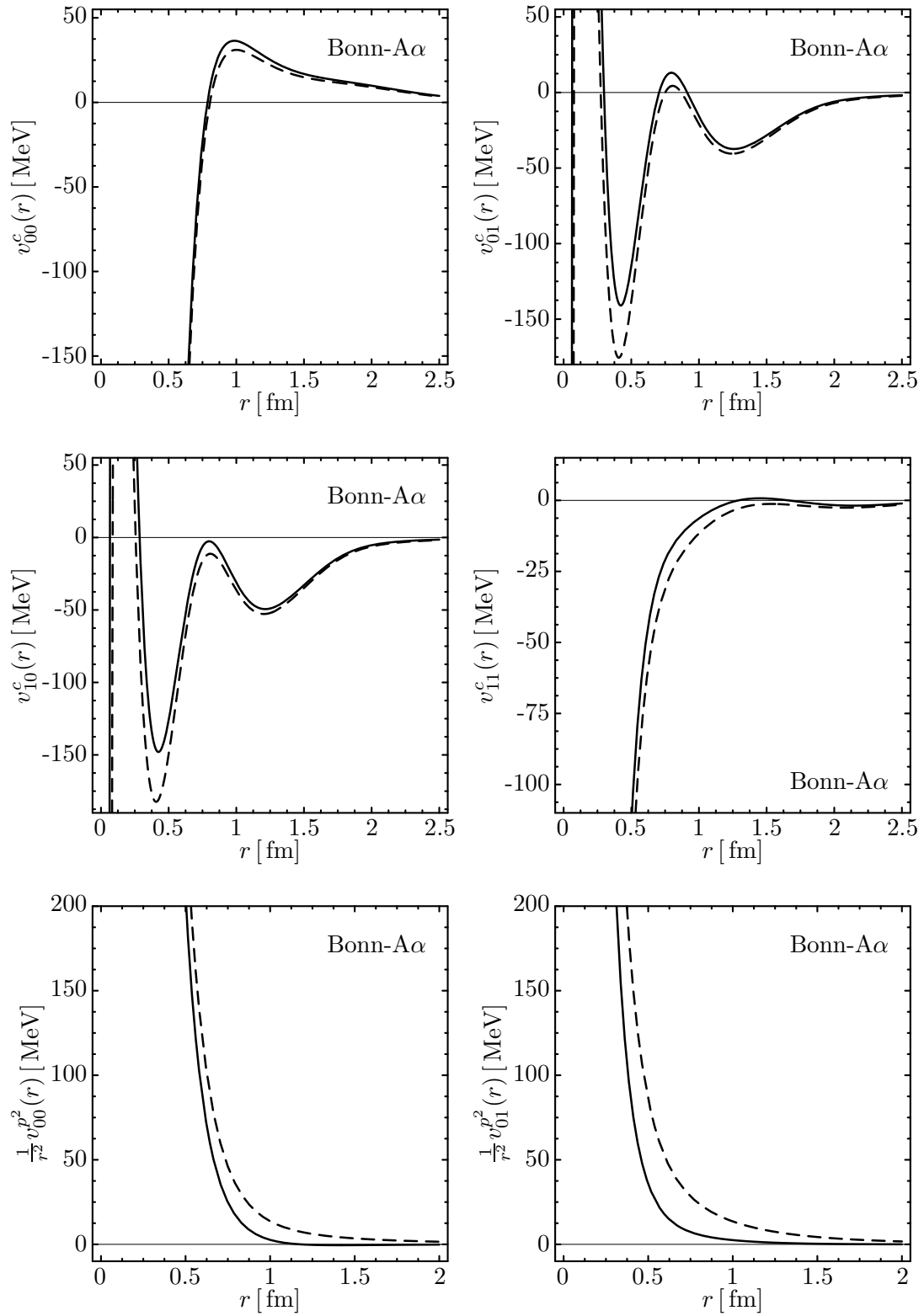
Figure 4.22: Modified radial dependencies of the Bonn-Aα + w interaction ($---$) , compared to the uncorrected Bonn-Aα ($\rule{1.5em}{0.4pt}$).
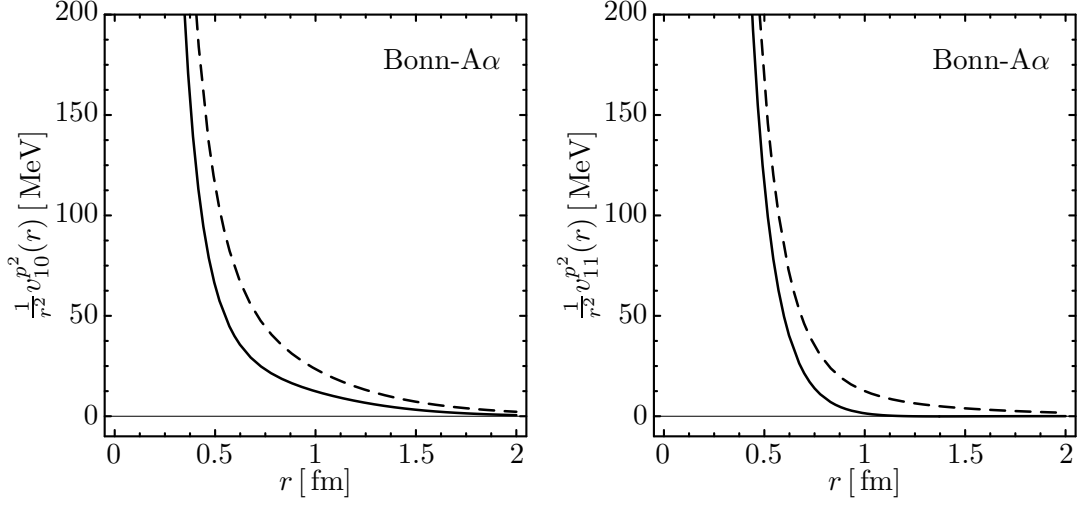
Figure 4.23: (cont.) Modified radial dependencies of the Bonn-Aα + w interaction ($---$) , compared to the uncorrected Bonn-Aα (———).

	γ^c [MeV]	κ^c [fm^2]	γ^{p^2} [MeV fm^2]	κ^{p^2} [fm^2]
Bonn-Aα + w (*)	-6.102	3.470	13.050	3.000
Bonn-Aγ + st10	-5.525	6.875	19.831	3.950
Bonn-Aγ + st10 + 11 ($\varepsilon = 0.2$)	-6.906	6.875	24.789	3.950
AV18α + w (*)	-7.261	2.750	14.050	2.500
AV18γ + st10	-5.529	6.350	20.450	4.000

Table 4.2: Local and momentum-dependent central corrections. Final parameters for the interactions marked with an (*) were adopted from R. Roth [54].

so we now focus on the remaining type, spin-orbit corrections. We add another Gaussian to the spin-orbit parts of the Bonn-Aα + w and AV18α + w interactions (cf. Tab. 4.2), respectively,

$$\widetilde{v}^{ls}_{\mathrm{mod}}(r) = \widetilde{v}^{ls}(r) + \gamma^{ls} \exp\left(-\frac{r^2}{2\kappa^{ls}}\right) , \qquad (4.24)$$

and determine its parameters by additionally fitting the properties of ^{24}O [2]. In this way, we obtain the interactions denoted Bonn-Aα + wls and AV18α + wls, whose parameters are listed in Tab. 4.3.

In Fig. 4.24, the binding energy deviations and charge radii are shown for selected

---

[2]Consider a Hartree-Fock Hamiltonian

$$H = T + U + V_r \simeq T + U, \quad V_r = \sum_{i,j} v_{ij} - U, \qquad (4.25)$$

where U denotes the mean-field potential, V_r the residual interaction, and v_{ij} a suitable NN-interaction (e.g., a free NN-interaction 'tamed' by a Brueckner-type partial summation of ladder diagrams, or a correlated interaction). The mean-field potential $U[\rho^{(1)}]$ depends on the single-particle densities in a self-consistent fashion, hence the single-particle energy levels and therefore the shell closures are subject to change over the whole nuclear chart. In particular, as the neutron dripline is approached, a new magic number $N = 16$ [55] appears for the neutrons, and ^{24}O is indeed doubly magic.
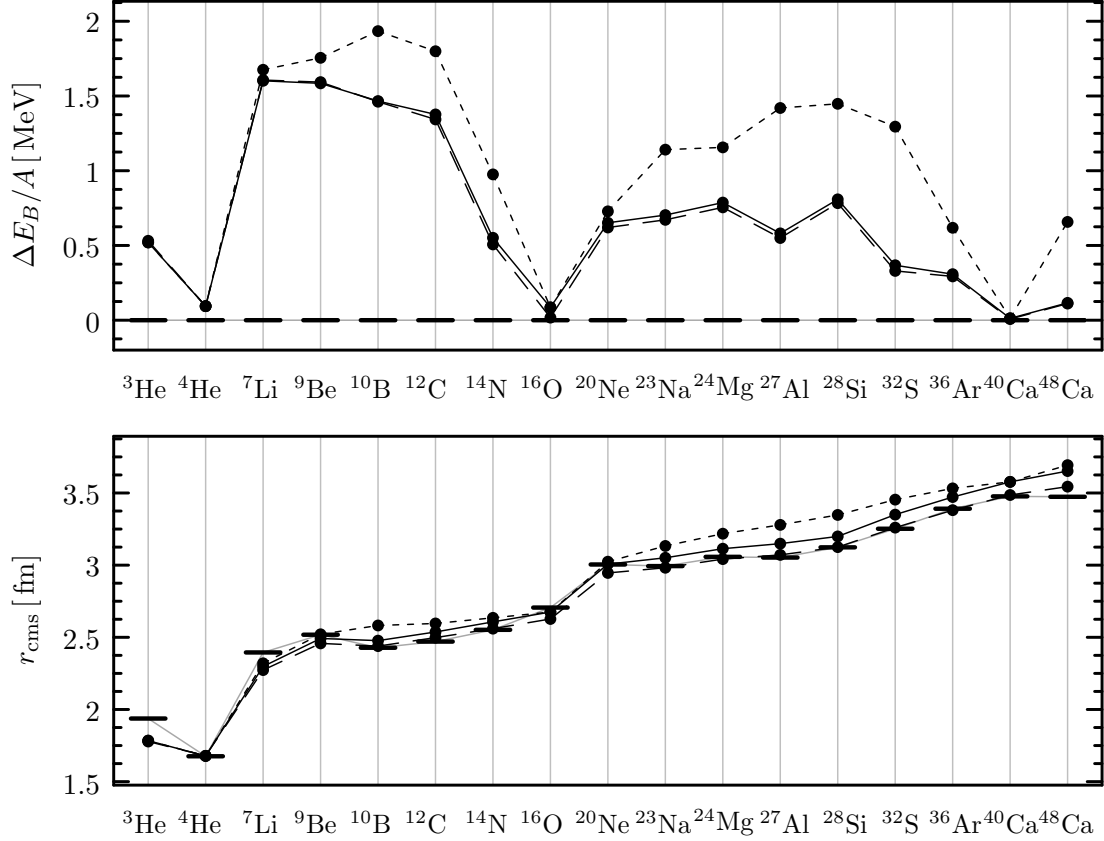
Figure 4.24: $\Delta E_B/A$ and r_{cms} of selected nuclei for the Bonn-Aα+wls (———) and AV18α+wls (— — —) interactions. Results for Bonn-Aα + w (-------) are shown for comparison.

stable nuclei. The spin-orbit modification improves the binding energies of the *sd*-shell isotopes considerably, since there are more nucleons with higher orbital angular momentum, while the effect is naturally less pronounced for the lighter *p*-shell nuclei. A remarkable feature is the excellent reproduction of the charge radii. While the increase of r_{cms} is approximately linear over the *p*- and *sd*-shells for Bonn-Aα + w, the spin-orbit modification produces just the right 'dents' in the r_{cms}-curves.

The differences between Bonn-Aα + wls and AV18α + wls can be traced back to the fit process — the former was tuned with emphasis on the charge radii of the *p*-shell nuclei and ^{16}O, while the parameters of the latter were adjusted with respect to the *sd*-shell nuclei. The strategy employed for the AV18α + wls interaction should actually be better, because the description of the *p*-shell nuclei improves if double-Gaussian trial states with free spin are used for the variational calculation. These are better suited to model slowly decaying density distributions, e.g., exponential tails for halo nuclei (see [6]), and therefore often produce slightly larger radii.

Figs. 4.25 and 4.26 display groundstate results for the Oxygen and Calcium isotopes, respectively. As for the stable nuclei, the binding energies improve significantly. Again, the *sd*-shell Calcium isotopes react stronger to the additional attraction, due to higher orbital angular momenta of their nucleons.
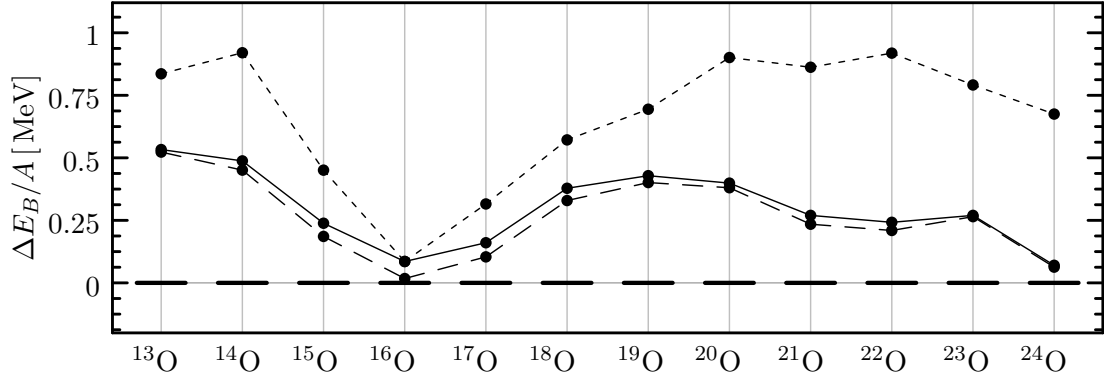
Figure 4.25: Binding energy deviations of the Oxygen isotopes, calculated using the Bonn-$A\alpha + \text{wls}$ (———) and $AV18\alpha + \text{wls}$ (— — —) interactions. Results for Bonn-$A\alpha + \text{w}$ (-------) are shown for comparison.
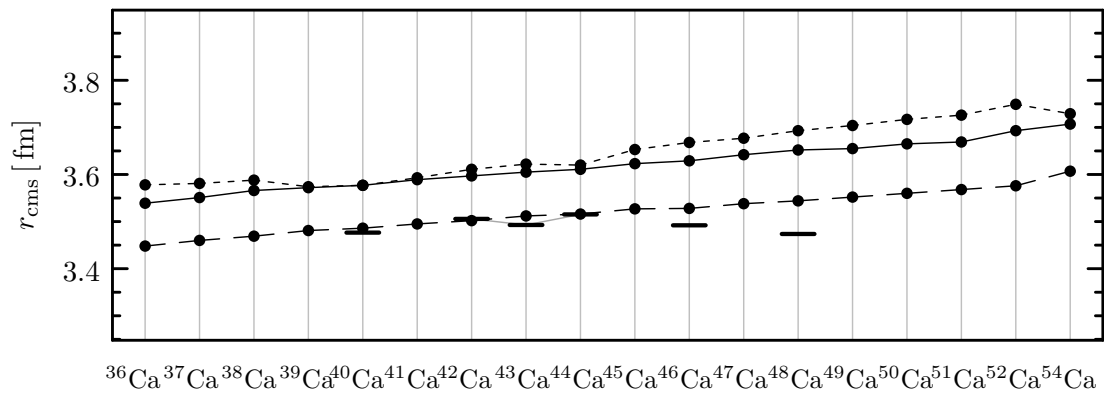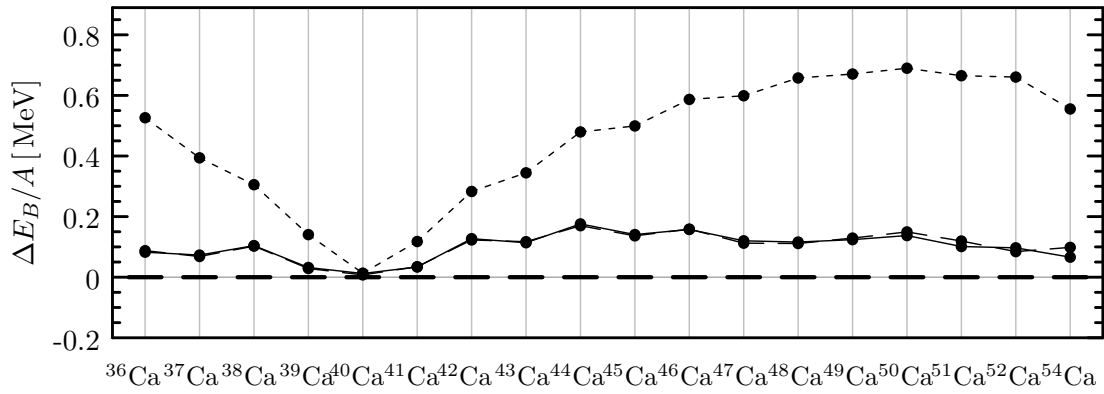
Figure 4.26: $\Delta E_B/A\,[\text{MeV}]$ and r_{cms} of the Calcium isotopes, calculated using the Bonn-$A\alpha + \text{wls}$ (———), $AV18\alpha + \text{wls}$ (— — —), and Bonn-$A\alpha + \text{w}$ (-------) interactions.

	$\gamma^c\,[\,\mathrm{MeV}\,]$	$\kappa^c\,[\,\mathrm{fm}^2\,]$	$\gamma^{p^2}\,[\,\mathrm{MeV}\,\mathrm{fm}^2\,]$	$\kappa^{p^2}\,[\,\mathrm{fm}^2\,]$	$\gamma^{ls}\,[\,\mathrm{MeV}\,]$	$\kappa^{ls}\,[\,\mathrm{fm}^2\,]$
AV18α + wls	-7.261	2.750	14.050	2.500	-2.700	3.000
Bonn-Aα + wls	-6.102	3.470	13.050	3.000	-3.000	3.000

Table 4.3: Parameters of the wls-Corrections, adopted from R. Roth [54].

Spin-Orbit Corrections and Three-Nucleon Forces

We introduced the spin-orbit correction in this section mainly for pragmatic reasons, since it is the only remaining term which can provide degrees of freedom for a tuning of the effective interactions. However, there might actually be a more fundamental motivation for the introduction of an effective spin-orbit correction.

Since the introduction of the second generation realistic NN-interactions — Bonn-A, AV18, etc., the so-called A_y *puzzle* has come under scrutiny. The vector analyzing power A_y is a polarization observable in elastic nucleon-deuteron scattering processes,

$$A_y = \frac{\sigma_\uparrow - \sigma_\downarrow}{\sigma_\uparrow + \sigma_\downarrow}\,, \tag{4.26}$$

where σ_i are the total cross sections for incoming nucleons with spin up or down perpendicular to the scattering plane [56]. All calculations using realistic NN-interactions as input under-predict the size of A_y by about 30%. In [57], Hüber and Friar have performed an extensive analysis of this problem, and shown that it is impossible to modify the NN-interaction to reproduce the experimentally observed A_y while preserving the correct description of scattering phase shifts. They conclude that the only consistent way to resolve this issue is the introduction of spin-dependent $3N$-forces — spin-orbit forces, in particular, since A_y is mainly sensitive to the ${}^3P_J$ phase shifts.

The idea that $3N$ forces are of spin-orbit type is supported by results of the Argonne group, too. In [52], results of Green's Function Monte Carlo calculations for ^{5}He are presented, which show that the AV18 potential under-predicts the $p_{3/2} - p_{1/2}$ level splitting by about 30 %, which is very close to the discrepancies quoted for A_y in the literature.

Preliminary studies of the question whether our NN spin-orbit modification can be understood as an effective approximation to more complicated $3N$ spin-orbit forces have not yielded conclusive results thus far.

4.3 Scaling

An alternative approach to the addition of correction terms to the correlated interactions discussed in the previous sections is the introduction of parameters into the correlated interaction or the complete Hamiltonian to provide a possibility to fit binding energies and charge radii on a nucleus-by-nucleus basis. Considering our experience with the previous modifications, it is to be expected that we need at least two such parameters, by which we can balance the repulsive and the attractive contributions to the nucleus' binding energy. A possible and quite natural choice is to introduce an effective mass
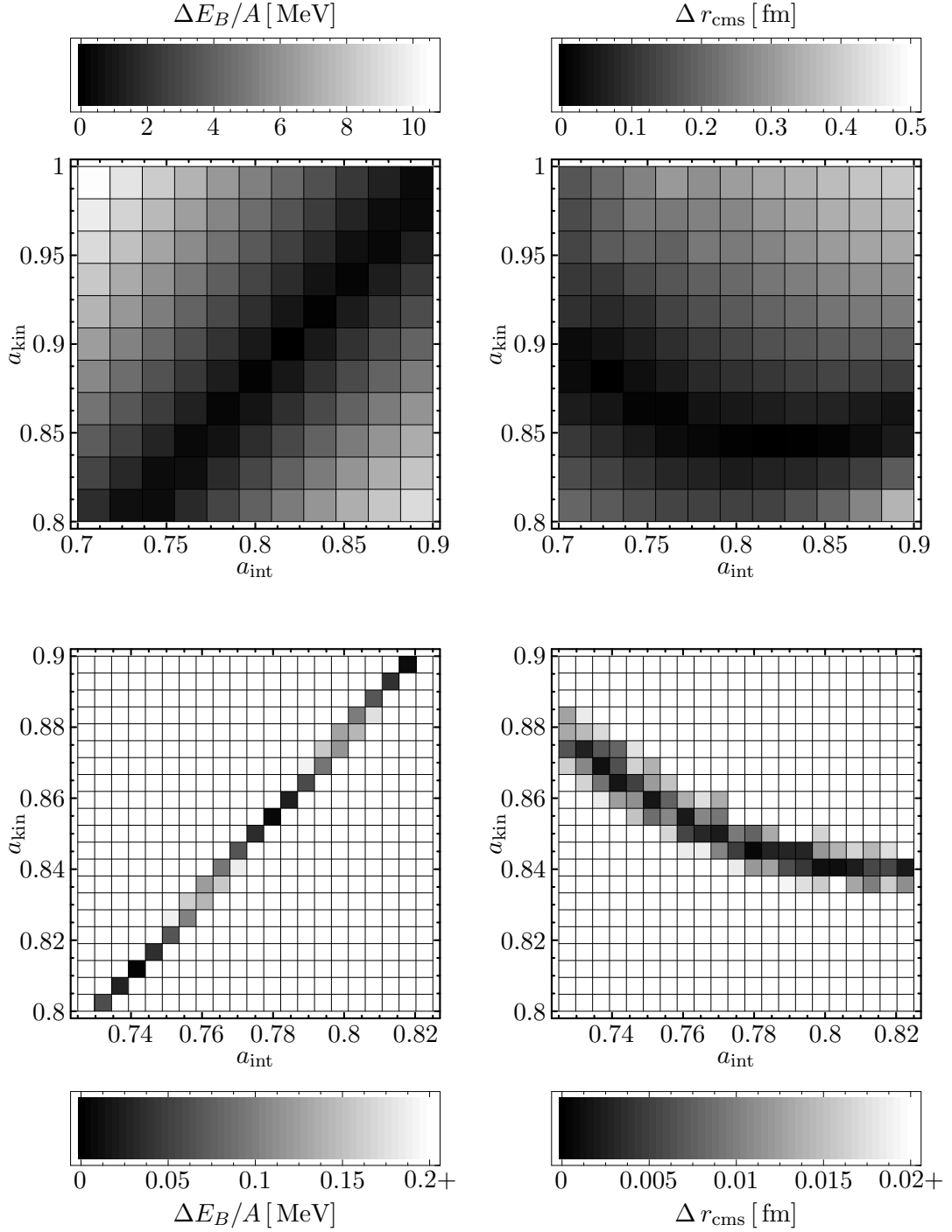
Figure 4.27: $\Delta E_B/A$ and Δr_{cms} of ^{20}Ne, calculated for raw (upper figure) and fine (lower picture) grids of the scale factors a_{kin} and a_{int}, using a scaled Bonn-Aα interaction and single-Gaussian trial states with fixed spin. The range of values was restricted in the lower density plots to provide a clearer picture. The $+$ symbols indicate values above $\Delta E_B/A = 0.2\,\mathrm{MeV}$ and $\Delta r_{\mathrm{cms}} = 0.02\,\mathrm{MeV}$.

into the kinetic energy by

$$m_N^* = a_{\text{kin}} m_N \,, \quad \text{T}, \text{T}_{\text{cm}} \longrightarrow \frac{\text{T}}{a_{\text{kin}}^2}, \frac{\text{T}_{\text{cm}}}{a_{\text{kin}}^2} \,, \tag{4.27}$$

and an 'effective range' of the potential by globally rescaling the length units of the correlated NN interaction[3]:

$$\mathbf{r} \longrightarrow a_{\text{int}} \mathbf{r} \,, \quad \Longrightarrow \quad \mathbf{p} \longrightarrow \frac{\mathbf{p}}{a_{\text{int}}} \,, \tag{4.28}$$

hence the name 'scaling'. In this context, a_{kin} and a_{int} will be referred to as scale factors. The modification can be interpreted as a many-body effect, i.e., the presence of other nucleons affects the interaction and the motion of a nucleon pair through screening (or anti-screening) effects. One may argue that the Coulomb interaction will undergo screening effects, too, and an effective charge should therefore be introduced. In this case, we would have to ask whether this effective charge is better obtained by including another scale factor, or if it should be connected to a_{kin} or a_{int}. Since we are going to use the scale factors to fit the binding energy and charge radius of selected nuclei, a third scale factor is clearly undesirable, since it would allow for an infinite degeneracy of the fit parameters and render the fit procedure useless. Thus, any rescaling of the Coulomb interaction needs to be done by either a_{kin} or a_{int}. We will discuss the effects of a scaled Coulomb interaction after outlining the general method and giving some results.

To determine optimal scale factors for a given nucleus, we proceed in a straightforward fashion. The groundstate of a given nucleus is calculated for all possible combinations of scale factors taken from a discrete grid in the space of a_{kin} and a_{int}; to reduce the computation time, these calculations were done using single-Gaussian trial states with fixed spin (cf. Sect. 3) for the first tests. The upper part of Fig. 4.27 displays density plots of the binding energy and charge radius deviations for ^{20}Ne obtained from this calculation. By choosing a rather large spacing of $\Delta a = 0.02$ for the first run, we can get an image of the $\Delta E_B/A$- and Δr_{cms}-planes over a 'wide' range. Each of them shows a distinct valley of small deviations, and these two valleys 'cross'. This behavior is common to all examined nuclei. Due to the crossing, we can find a set of parameters for which the sum of the relative deviations,

$$\chi \equiv \sqrt{\left(\frac{\Delta E_B}{E_B}\right)^2 + \left(\frac{\Delta r_{\text{cms}}}{r_{\text{cms}}}\right)^2} \tag{4.29}$$

becomes minimal. Before minimizing χ, however, we need to interpolate the values on the grid. This procedure is performed with *Mathematica*, using its built-in interpolation routines and interpolating functions of varying order. One recognizes quickly that the chosen resolution of the grid is insufficient, hence we perform a second minimization step: after determining the crossing region from the raw grid, we enhance the resolution and recalculate the groundstates for the corresponding smaller intervals of a_{kin} and a_{int}. A spacing of $\Delta a = 0.05$ has proven adequate for all examined nuclei. Density plots of

---

[3]The original idea was to consider a unitary scale transformation. This interpretation was ultimately dropped due to the need for different scale parameters for the kinetic energy and the interaction.
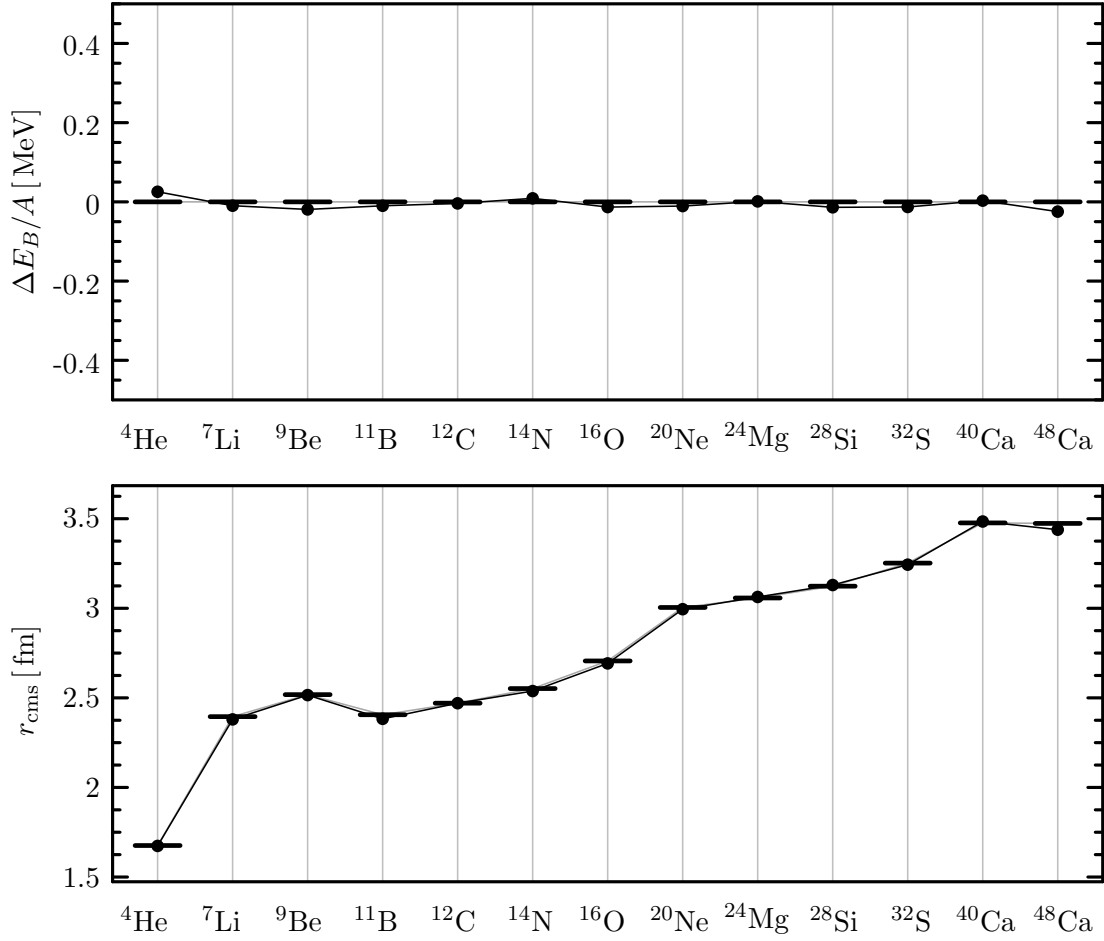
Figure 4.28: $\Delta E_B/A$ and r_{cms} for selected nuclei. The results were obtained using a scaled Bonn-Aα interaction (cf. Tab. 4.4) for each nucleus, and single-Gaussian states with fixed spin.

$\Delta E_B/A$ and Δr_{cms} for ^{20}Ne obtained with the enhanced grid are displayed in the lower half of Fig. 4.27. Due to the enhancement, a linear interpolation between neighboring data points is now sufficient to obtain scale factors which reproduce the binding energies and charge radii of the selected nuclei to accuracies of 0.5% and better (see Fig. 4.28).

Let us come back to the question of the effects of a scaled Coulomb interaction. The change in the energies for each point of the $(a_{\mathrm{kin}}, a_{\mathrm{int}})$ grid is

$$E'_B = E_B + V_{\mathrm{Coul}} \left(1 - \frac{1}{a} \right) , \tag{4.30}$$

where a is either a_{kin} or a_{int}, depending on our choice. This change would need to be compensated by a readjustment of a_{kin} and a_{int} in order to fit the experimental data. The valleys and cutting regions will simply be scaled in a hyperbolic fashion, similar to the scaling of intervals in special relativity, but without reaching extreme cases, since a is generally of order 1. The general features of the scaled interaction remain unchanged.

Tab. 4.4 lists scale factors for various nuclei, obtained using the outlined two-step

	^{4}He	^{7}Li	^{9}Be	^{11}B	^{12}C	^{13}C	^{14}C	^{14}N	^{16}O	^{17}O
a_kin	0.943	0.860	0.895	0.939	0.920	0.910	0.900	0.910	0.849	0.850
a_int	0.873	0.745	0.780	0.820	0.810	0.809	0.810	0.815	0.785	0.785

	^{18}O	^{20}Ne	^{24}Mg	^{28}Si	^{32}S	^{40}Ca	^{48}Ca
a_kin	0.839	0.849	0.870	0.905	0.854	0.820	0.850
a_int	0.770	0.775	0.790	0.825	0.785	0.775	0.790

Table 4.4: Scale factors a_kin and a_int for selected stable nuclei, obtained for single Gaussian trial states with fixed spin.
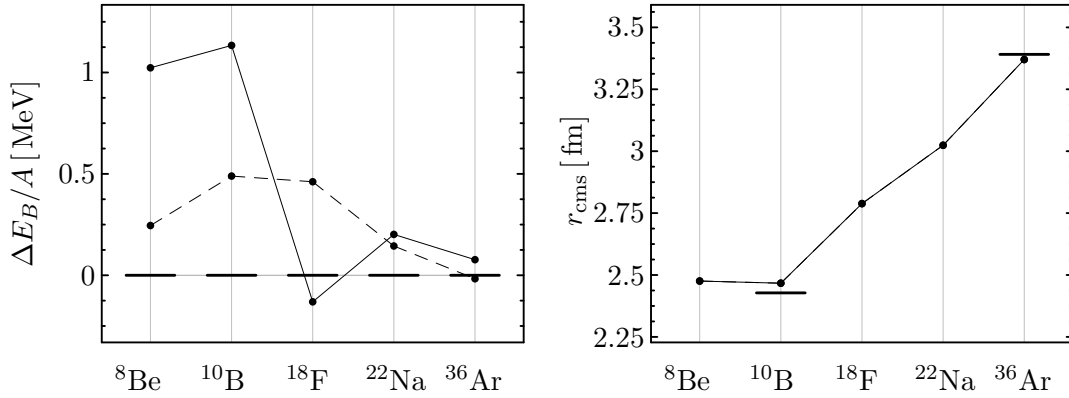
Figure 4.29: $\Delta E_B/A$ and r_cms for $N = Z$ nuclei. The scale factors were obtained by linear (———) and quadratic (———) interpolation of the optimal scale factors listed in Tab. 4.4. Single-Gaussian trial states with fixed spin were used for the calculation.

method. Using these, we can try to predict optimal scale factors by interpolation or extrapolation. In Fig. 4.29, groundstate results are shown for some $N = Z$ nuclei, whose scale factors were obtained by linear and quadratic interpolation. Interpolation functions of higher order have been tested, but they were found to give no improvement of the results — on the contrary, since higher orders allow steeper gradients between the data points, the interpolations actually became worse. A similarly unsatisfying picture emerges if one considers isotope chains, e.g., for Oxygen (Fig. 4.30). Using the scale factors of the stable isotopes ^{16}O to ^{18}O as a starting point, somewhat reasonable values for a_kin and a_int can be obtained for the neighboring isotopes ^{15}O and ^{19}O, but no further beyond these.

The main reason for the failure of the interpolation and extrapolation methods lies in their inability to deal with changes in the deformations of neighboring nuclei, because the scale factors can only concentrate or dilute existing density distributions. This is closely related to the problem of choosing the nuclei whose optimal scale factors are to be used as input data, which will obviously have considerable influence on the outcome of the inter- and extrapolations. Consider again the Oxygen isotopes. Whether we include ^{16}O or not, given the issue of the tetrahedron-admixture to its ground state (cf. sects. 4.1.4 and 4.2.1), will cause a prediction of $a_\text{kin} = 0.848$ or $a_\text{kin} = 0.872$ for ^{15}O, respectively, from a linear extrapolation. This inevitably leads to the conclusion that we have to perform the optimization procedure for each nucleus of interest.
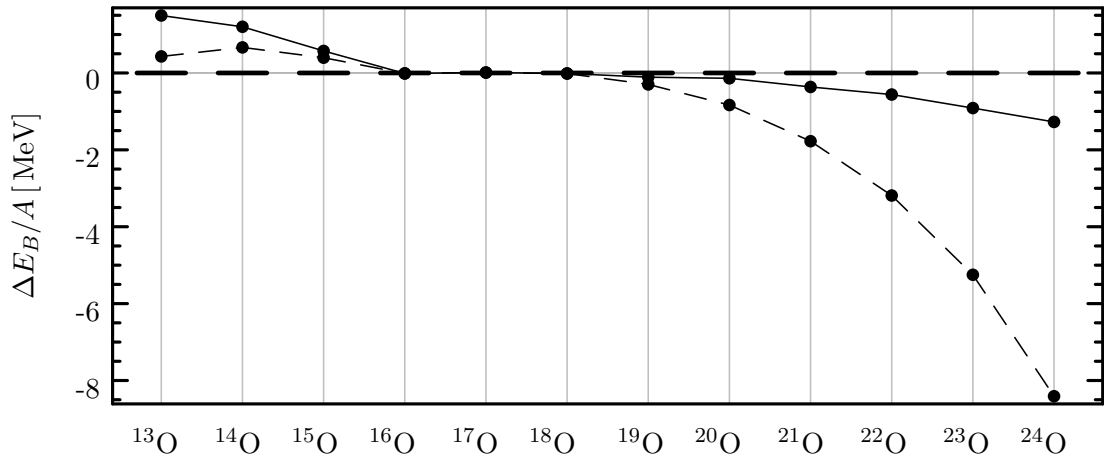
Figure 4.30: Oxygen isotopes. Scale factors were extrapolated from the optimal scale factors listed in Tab. 4.4, using linear (———) and quadratic (– – –) interpolating functions. $\Delta E_B/A$ were calculated using single-Gaussian trial states with fixed spin.

A further disadvantage of the outlined method is the high amount of computation time it requires, especially if we also vary the spin of the nuclei and move to larger mass numbers. The deviation measure χ (4.29) could in principle be used to determine the optimal scale factors in a variational scheme; however, since the calculation of each gradient in the parameter space of a_{kin} and a_{int} would involve two full minimizations, it is not clear by how much this would reduce the overall computation time (if anything at all). The brute-force two-step approach needed about 240 minimizations to obtain both grids, where the grid was chosen with rather conservative margins. Considering the general trend of the scale factors to move towards values smaller than 1 (see Tab. 4.4) to counteract the under-binding and too small radii of the unmodified correlated interactions, we are already able to reduce the grid size in eventually forthcoming calculations. This will most probably be sufficient to compete with an automated minimization of χ.

4.4 Conclusions

Over the course of this chapter, we have constructed several modifications of the correlated interactions used for FMD calculations. While all of them are able to improve the agreement between the FMD groundstate results and experimental data, the addition of phenomenological correction terms to the interaction is preferable: since their parameters are obtained by fitting the properties of a few nuclei, they have a high predictive power. The scaling method, on the other hand, needs to be redone for every nucleus, because the determination of scale factors by interpolation is very unreliable. Thus, the predictive power of this approach is limited to quantities beyond E_B and r_{cms} — spectra, density distributions, transition matrix elements, etc. In addition, the re-fitting of the scale factors for every nucleus requires a considerable computational effort.

Chapter 5

Nuclear Structure

5.1 The Nuclear Chart

The mean-field groundstate results agree best with experimental data if the Bonn-Aα + wls and AV18α + wls interactions are used (cf. Chapter 4). We therefore present groundstate results for the range of nuclei covered in FMD calculations to this point. Figs. 5.1 and 5.2 show the differences between calculated and experimental binding energies for AV18α + wls. The binding energies and charge radii are also listed in Tab. 5.1, alongside the results for Bonn-Aα + wls and the experimental values [47, 48].

	$E_B/A\,[\,\mathrm{MeV}]$			$r_{\mathrm{cms}}\,[\,\mathrm{fm}]$		
Nucleus	AV18α +wls	Bonn-Aα +wls	Exp	AV18α +wls	Bonn-Aα +wls	Exp
^{3}He	−2.041	−2.052	−2.573	1.778	1.784	1.937
^{4}He	−6.980	−6.980	−7.074	1.679	1.678	1.676
^{6}Li	−3.761	−3.778	−5.333	2.158	2.175	2.552
^{7}Li	−4.000	−4.005	−5.606	2.273	2.298	2.395
^{9}Be	−4.870	−4.878	−6.463	2.458	2.492	2.518
^{10}B	−5.013	−5.009	−6.475	2.439	2.477	2.428
^{11}B	−5.570	−5.555	−6.928	2.440	2.486	2.406
^{12}C	−6.337	−6.303	−7.680	2.498	2.537	2.470
^{13}C	−6.610	−6.574	−7.470	2.491	2.535	2.463
^{14}N	−6.969	−6.924	−7.476	2.560	2.607	2.552
^{15}N	−7.502	−7.444	−7.699	2.574	2.620	2.609
^{16}O	−7.959	−7.891	−7.976	2.627	2.675	2.706
^{17}O	−7.647	−7.590	−7.751	2.649	2.702	2.698
^{18}O	−7.438	−7.389	−7.767	2.676	2.727	2.760
^{19}F	−7.346	−7.304	−7.779	2.770	2.830	2.898
^{20}Ne	−7.412	−7.381	−8.032	2.946	3.007	3.005
^{21}Ne	−7.352	−7.322	−7.972	2.934	2.998	2.967
^{22}Ne	−7.379	−7.344	−8.081	2.925	2.993	2.954
^{23}Na	−7.440	−7.408	−8.112	2.982	3.051	2.994
^{24}Mg	−7.506	−7.474	−8.261	3.042	3.114	3.058

Table 5.1: FMD results for the groundstates of stable nuclei.

Nucleus	E_B/A [MeV]			r_{cms} [fm]		
	AV18α +wls	Bonn-Aα +wls	Exp	AV18α +wls	Bonn-Aα +wls	Exp
^{25}Mg	-7.510	-7.484	-8.223	3.081	3.157	3.027
^{26}Mg	-7.577	-7.562	-8.334	3.118	3.189	2.999
^{27}Al	-7.782	-7.751	-8.332	3.071	3.149	3.053
^{28}Si	-7.665	-7.639	-8.448	3.125	3.199	3.123
^{29}Si	-7.979	-7.932	-8.449	3.120	3.195	3.113
^{30}Si	-8.092	-8.054	-8.521	3.136	3.207	3.160
^{31}P	-8.072	-8.070	-8.481	3.234	3.283	3.189
^{32}S	-8.163	-8.126	-8.493	3.260	3.350	3.252
^{33}S	-8.213	-8.180	-8.498	3.269	3.358	$-$
^{34}S	-8.283	-8.255	-8.584	3.294	3.374	3.285
^{36}S	-8.439	-8.419	-8.576	3.322	3.410	3.298
^{35}Cl	-8.257	-8.229	-8.521	3.337	3.422	3.365
^{37}Cl	-8.458	-8.440	-8.571	3.369	3.462	3.384
^{36}Ar	-8.227	-8.212	-8.520	3.381	3.472	3.391
^{38}Ar	-8.490	-8.480	-8.614	3.411	3.504	3.404
^{40}Ar	-8.367	-8.352	-8.596	3.431	3.519	3.427
^{39}K	-8.513	-8.505	-8.557	3.451	3.545	3.435
^{41}K	-8.430	-8.421	-8.576	3.466	3.566	3.452
^{40}Ca	-8.544	-8.539	-8.551	3.486	3.577	3.477
^{42}Ca	-8.494	-8.489	-8.617	3.502	3.597	3.506
^{43}Ca	-8.484	-8.487	-8.601	3.512	3.605	3.493
^{44}Ca	-8.488	-8.482	-8.658	3.516	3.611	3.515
^{46}Ca	-8.510	-8.511	-8.669	3.528	3.629	3.492
^{48}Ca	-8.555	-8.551	-8.667	3.544	3.652	3.474
^{45}Sc	-8.435	-8.436	-8.619	3.561	3.664	3.546
^{46}Ti	-8.386	-8.382	-8.656	3.607	3.706	3.606
^{47}Ti	-8.414	-8.415	-8.661	3.611	3.713	3.596
^{48}Ti	-8.447	-8.448	-8.723	3.626	3.725	3.592
^{49}Ti	-8.482	-8.475	-8.711	3.626	3.730	3.574
^{50}Ti	-8.517	-8.520	-8.756	3.637	3.736	3.571
^{50}V	-8.454	-8.457	-8.696	3.684	3.785	$-$
^{51}V	-8.513	-8.509	-8.742	3.675	3.785	3.600
^{50}Cr	-8.278	-8.394	-8.700	3.716	3.814	3.660
^{52}Cr	-8.351	-8.355	-8.776	3.753	3.859	3.645
^{53}Cr	-8.395	-8.404	-8.760	3.733	3.839	3.659
^{54}Cr	-8.444	-8.366	-8.778	3.735	3.873	3.685
^{55}Mn	-8.269	-8.293	-8.765	3.818	3.927	$-$
^{54}Fe	-8.235	-8.192	-8.737	3.839	3.996	3.693
^{56}Fe	-8.356	-8.371	-8.790	3.827	3.935	3.738
^{57}Fe	-8.341	-8.362	-8.770	3.845	3.957	3.754
^{58}Fe	-8.424	-8.441	-8.792	3.841	3.953	3.774
^{59}Co	-8.359	-8.380	-8.768	3.901	4.010	3.788

Table 5.1: FMD results for the groundstates of stable nuclei.

Nucleus	E_B/A [MeV]			r_{cms} [fm]		
	AV18α +wls	Bonn-Aα +wls	Exp	AV18α +wls	Bonn-Aα +wls	Exp
^{58}Ni	-8.214	-8.208	-8.732	3.934	4.077	3.775
^{60}Ni	-8.312	-8.236	-8.781	3.950	4.107	3.812
^{61}Ni	-8.322	-8.346	-8.765	3.955	4.070	3.821

Table 5.1: FMD results for the groundstates of stable nuclei.

5.2   Spectra and Densities

Using the various corrections discussed in the previous chapter, we are able to reproduce experimental groundstate results with our FMD calculations rather well. Let us examine the spectra now, and see how well the modified interactions reproduce them. All data on experimental energy levels has been taken from [58].

The parameters of the scaled Bonn-Aα interactions used in this section are listed in Tab. 5.2. They have been redetermined for each nucleus using single-Gaussian trial states with free spin.

5.2.1 ^{6}Li

The lowest energy levels of ^{6}Li after angular momentum projection are shown in Fig. 5.4. In a mean-field picture, both a proton and a neutron occupy single particle energy levels in the $p_{3/2}$-shell. Since the tensor force favors the alignment of nucleon spins, one would expect that the angular momenta of the two p-shell nucleons couple to $J = 3$ in the groundstate to provide optimal binding. Quite to the contrary, the experimental groundstate is found to be $J^\pi = 1^+$, resulting from a distinct ^{4}He + d structure which can be understood by noting that the threshold for ^{4}He + d-decay lies at an excitation energy of just about 1.5 MeV [59].

The uncorrected Bonn-Aα and the Bonn-Aα+wls interaction both produce $J^\pi = 3^+$ groundstates, which is not surprising given the mean-field nature of the variation before the angular momentum projection. What is surprising, however, is that Bonn-Aα + w produces the correct groundstate, since the density distributions depicted in Fig. 5.5 become more dilute as a result of the Wigner correction. In the case of ^{6}Li, this effect seems to be beneficial to the formation of a cluster substructure, which is destroyed again by the additional attraction generated by the spin-orbit correction term of Bonn-

	^{7}Li	^{9}Be	^{12}C	^{17}O	^{20}Ne	^{24}Mg
a_{kin}	0.861	0.875	0.878	0.850	0.850	0.835
a_{int}	0.746	0.765	0.785	0.785	0.775	0.765

Table 5.2: Scale factors for the nuclei discussed in Sect. 5.2, determined using single Gaussian trial states with free spin.
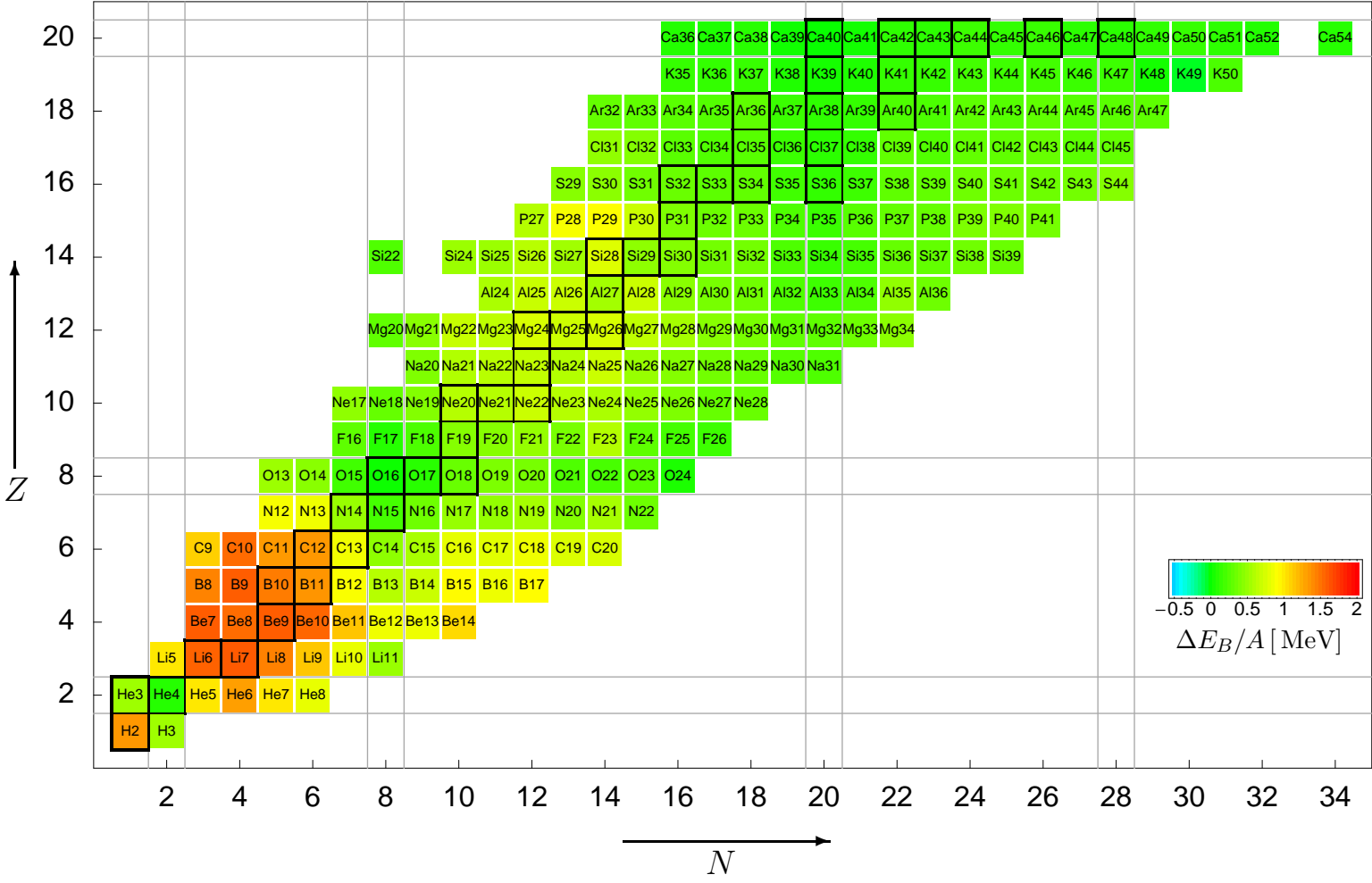
Figure 5.1: Nuclear chart up to $Z = 20$ for the AV18α-wls potential, calculated using single Gaussian states with free spin.
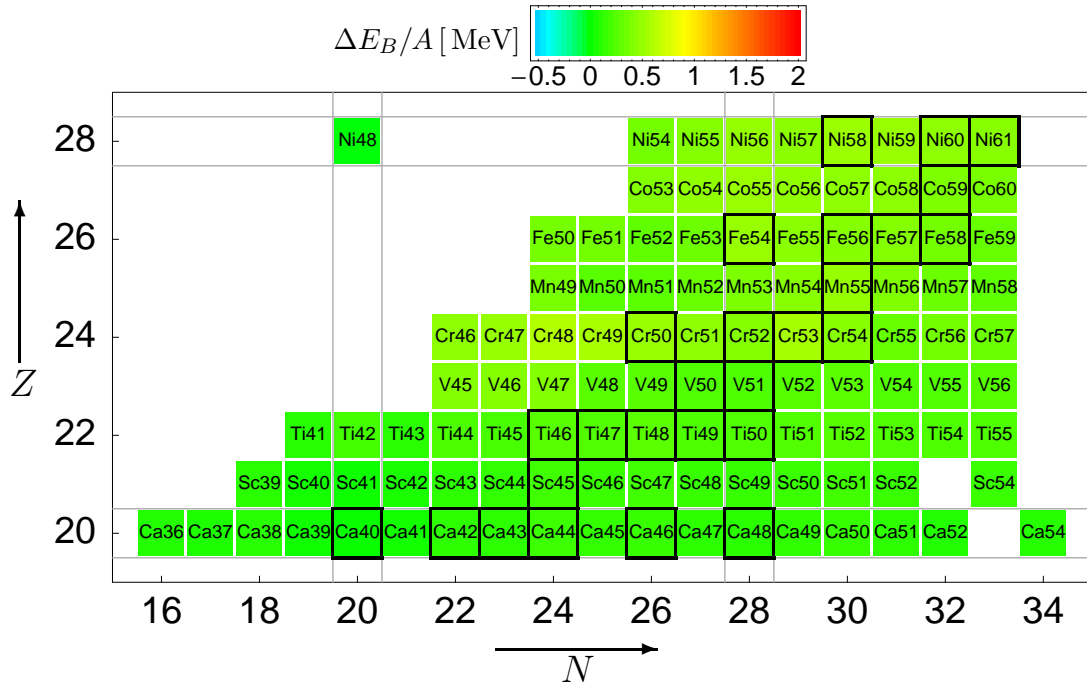
Figure 5.2: Nuclear chart beyond $Z = 20$ for the AV18α + wls potential, calculated using single Gaussian states with free spin.
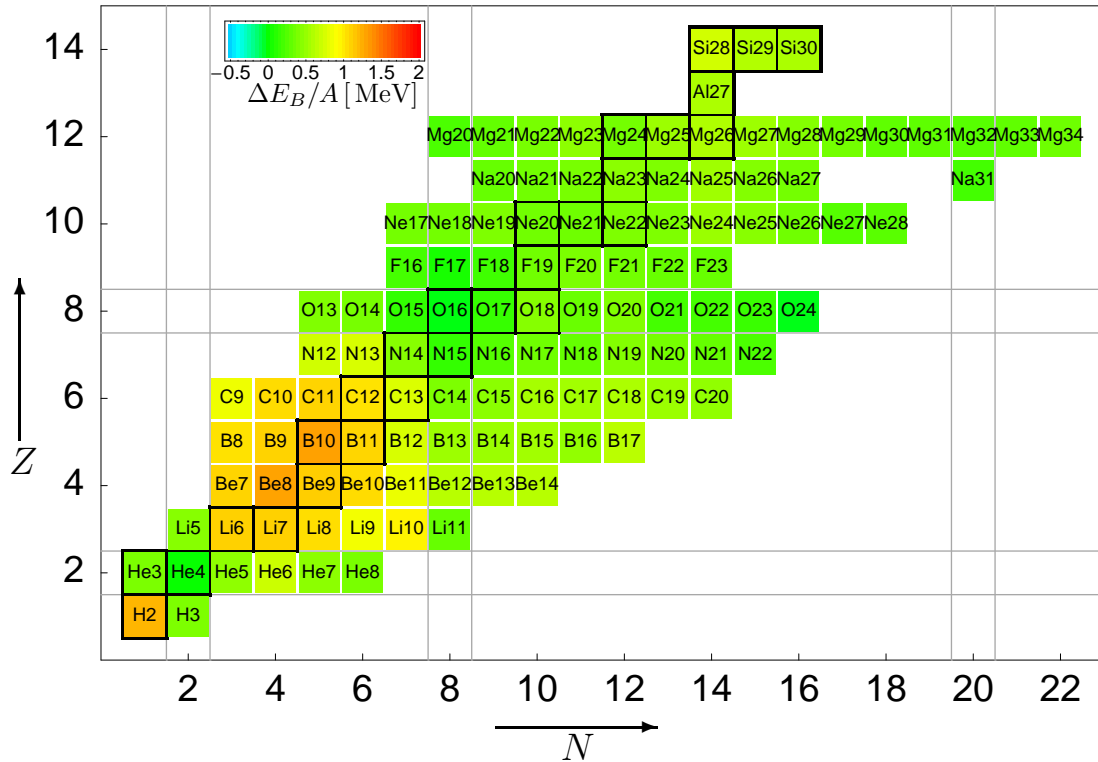
Figure 5.3: Chart of light isotopes for the AV18α + wls potential, calculated using double Gaussian states with free spin.
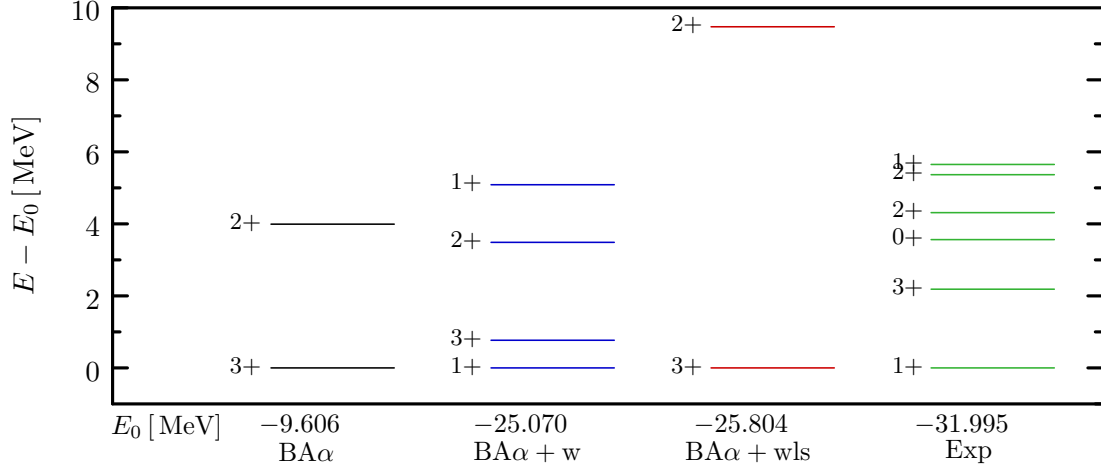
Figure 5.4: Energy levels of ^{6}Li.

	$E_0 \,[\text{MeV}]$	$E - E_0 \,[\text{MeV}]$	L^2	S^2	J^2	$r_{\text{mms}} \,[\text{fm}]$	$r_{\text{cms}} \,[\text{fm}]$
			Bonn-Aα				
3^+	-9.610		6.010	2.000	12.000	2.100	2.280
2^+		3.990	5.840	2.020	5.370	2.180	2.360
			Bonn-Aα + w				
1^+	-25.100		0.002	2.000	1.970	2.230	2.400
3^+		0.768	6.120	2.000	12.300	2.220	2.390
2^+		3.490	5.980	2.020	5.760	2.260	2.430
1^+		5.090	6.020	2.010	1.750	2.280	2.440
			Bonn-Aα + wls				
3^+	-25.800		6.000	2.000	12.000	2.140	2.320
2^+		9.470	5.650	2.100	4.090	2.210	2.370

Table 5.3: Calculated levels of ^{6}Li for Bonn-Aα and various modifications, using double Gaussian trial states.

Aα + wls. Bonn-Aα + w also reproduces the second 1^+ state rather well, although further experimental 0^+ and 2^+ states are missing.

The expectation values of the angular momentum observables

$$J^2 = \langle \mathbf{J}^2 \rangle, \quad L^2 = \langle \mathbf{L}^2 \rangle, \quad S^2 = \langle \mathbf{S}^2 \rangle, \tag{5.1}$$

listed in Tab. 5.3 agree well with the given explanation of the calculated spectrum. For the 3^+ groundstates of Bonn-Aα and Bonn-Aα + wls, $L^2 \approx 6$ and $S^2 \approx 2$ suggest that the valence nucleons are in a state with $L = 2$ and $S = 1$, as would be obtained by coupling two p-shell nucleons. The quantum numbers $L = 0$ and $S = 1$ of the Bonn-Aα + w groundstate, on the other hand, agree with the cluster picture, since ^{4}He and d have angular momenta $J^\pi = 0^+$ and $J^\pi = 1^+$, respectively.

To conclude the discussion, let us have a look at the intrinsic one-body densities of ^{6}Li displayed in Fig. 5.5. As mentioned above, the addition of the Wigner correction dilutes the density distribution, while the additional spin-orbit correction term concentrates it
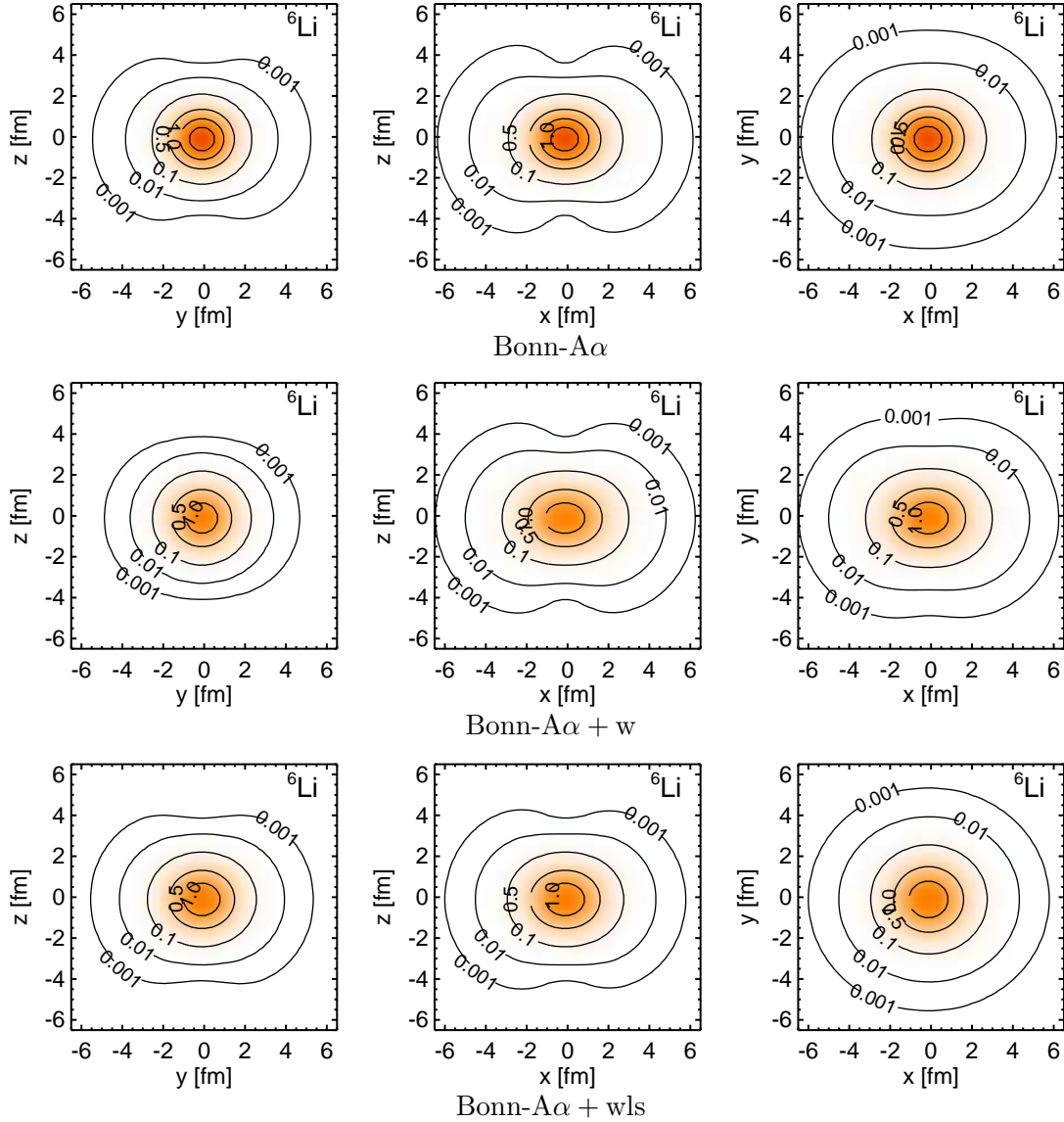
Figure 5.5: ^{6}Li intrinsic one-body densities, calculated for Bonn-Aα and various modifications using double Gaussian trial states. Values on the contours are densities in units of the nuclear matter density $\rho_0 = 0.17$ fm^{-3}.

again. Common to all three interactions is the oblate core region of the nucleus, and the slight hint of a dumb-bell or peanut shape of the densities, visible in the outermost contours. This may be taken as further evidence of the clustering in ^{6}Li, although the shape is quite symmetric and would therefore be more in line with, say, a ^{3}H + ^{3}He structure. ^{3}H + ^{3}He is indeed a decay channel for an excited ^{6}Li nucleus, but the threshold lies about 16 MeV above the groundstate, making it unlikely that this particular cluster structure should show more prominently in the intrinsic densities than ^{4}He + d.
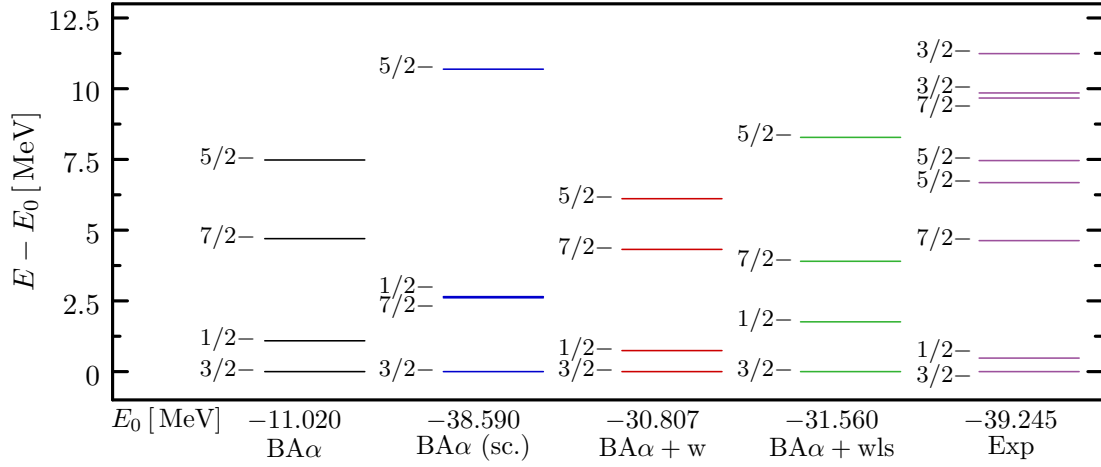
Figure 5.6: Rotational band of ^{7}Li.

5.2.2 ^{7}Li

Fig. 5.6 shows the relative spectra of ^{7}Li for Bonn-Aα and the various modified interactions, obtained by performing an angular momentum projection. The corresponding levels are listed in Tab. 5.4. We find that the order of the four lowest-lying states with negative parity is reproduced accurately. The density cuts displayed in Fig. 5.7 show that ^{7}Li is approximately an oblate ellipsoid, hence we can try to group these levels into a rotational band by comparing with a particle-plus-rotor model.

The rather large deformation suggests that the *strong coupling limit* is realized (cf. [41]), i.e., the odd nucleon is adiabatically following the rotation of an $A = 6$ core, either ^{6}He or ^{6}Li. The latter should be favored, because its binding energy is larger:

$$E_B(^6\mathrm{Li}) = -31.995\,\mathrm{MeV}, \quad E_B(^6\mathrm{He}) = -29.269\,\mathrm{MeV}\,. \tag{5.2}$$

In this case, a spectrum of levels

$$E_K(J) = \epsilon_K + \frac{1}{2\mathcal{J}}(J(J+1) - K^2) \tag{5.3}$$

with spacing $\Delta J = 1$ is expected, where ϵ_K is the single-particle energy of the band head, J denotes the total angular momentum, K the projection of J on the body-fixed 3-axis (the large axis of the ellipsoid), and $\mathcal{J}$ the moment of inertia. The reversed order of the levels can be explained if the Coriolis interaction is taken into account in first order perturbation theory. It contributes an additional term for $K = 1/2$ bands only,

$$E_K(J) = \epsilon_{1/2} + \frac{1}{2\mathcal{J}}\left(J(J+1) - \frac{1}{4} + a\left(J + \frac{1}{2}\right)(-1)^{J+1/2}\right)\,, \tag{5.4}$$

where a is the so-called *decoupling parameter*. This can be understood if one notes that K is also the projection of the valence particle's angular momentum on the symmetry axis of the rotor, because the angular momentum of the rotor has to be perpendicular to the symmetry axis. $K = 1/2$ corresponds to the minimal possible projection, and therefore to a maximal alignment between the angular momenta of rotor and valence

	E_0 [MeV]	$E - E_0$ [MeV]	L^2	S^2	J^2	r_{ms} [fm]	r_{cms} [fm]
			Bonn-Aα				
$3/2^-$	-11.020		2.010	0.770	3.730	2.040	2.150
$1/2^-$		1.090	1.990	0.770	0.720	2.040	2.140
$7/2^-$		4.700	12.070	0.770	15.860	2.050	2.150
$5/2^-$		7.480	12.000	0.770	8.770	2.050	2.150
			Bonn-Aα(sc.)				
$3/2^-$	-38.590		2.070	0.890	3.720	2.280	2.350
$7/2^-$		2.610	11.750	0.930	15.860	2.280	2.360
$1/2^-$		2.650	2.030	0.840	0.670	2.280	2.350
$5/2^-$		10.690	11.890	0.840	8.790	2.280	2.360
			Bonn-Aα + w				
$3/2^-$	-30.807		2.028	0.764	3.758	2.227	2.311
$1/2^-$		0.743	2.001	0.765	0.739	2.227	2.311
$7/2^-$		4.320	11.661	0.774	15.508	2.235	2.317
$5/2^-$		6.112	11.904	0.770	8.710	2.235	2.317
			Bonn-Aα + wls				
$3/2^-$	-31.560		2.060	0.810	3.760	2.200	2.290
$1/2^-$		1.760	2.040	0.790	0.770	2.200	2.290
$7/2^-$		3.900	11.900	0.810	15.710	2.210	2.300
$5/2^-$		8.280	11.820	0.780	8.740	2.210	2.300

Table 5.4: Calculated levels of ^{7}Li for Bonn-Aα and various modifications.

particle. Eq. 5.4 implies that all levels for which $J + \frac{1}{2}$ is even – $3/2^-, 7/2^-, \dots$ – are shifted downwards if a is negative[1].

Bonn-Aα and Bonn-Aα+w give the best reproduction of the first three states, aside from the splitting between the $1/2^-$ and $3/2^-$ states still being a bit too large. Bonn-Aα + wls drives these states as well as the $5/2^-$ and $7/2^-$ states further apart, which can be attributed to the additional attractive spin-orbit force. The results for the scaled Bonn-Aα are the continuation of this trend to the extreme – $7/2^-$ and $1/2^-$ overlap. This has to be attributed to the increased range of the interaction's rescaled spin-orbit part.

Examining the root-mean-square mass and charge radii listed in Tab. 5.4, we find confirmation for the ^{6}Li$+n$ picture. Extracting the rms radius of the proton distribution from the charge radius,

$$r_{p,\mathrm{ms}} = \sqrt{r_{\mathrm{cms}}^2 - r_p^2}, \quad r_p = 0.862 \,\mathrm{fm}, \tag{5.5}$$

---

[1]Depending on which of the two experimental $5/2^-$ levels one considers a member of the band, a simple least-squares fit to the experimental data yields the following values for a, $\mathcal{J}$ and $\epsilon_{1/2}$:

$$E_{\exp}\left(\frac{5}{2}^-\right) = 7.460 \,\mathrm{MeV}: \quad \epsilon_{1/2} = -0.449 \,\mathrm{MeV}, \; \frac{1}{2\mathcal{J}} = 0.581 \,\mathrm{MeV}, \; a = -1.631,$$

$$E_{\exp}\left(\frac{5}{2}^-\right) = 6.680 \,\mathrm{MeV}: \quad \epsilon_{1/2} = -0.437 \,\mathrm{MeV}, \; \frac{1}{2\mathcal{J}} = 0.542 \,\mathrm{MeV}, \; a = -1.502.$$

Bonn-Aα

Bonn-Aα (scaled)

Bonn-Aα + w

Bonn-Aα + wls
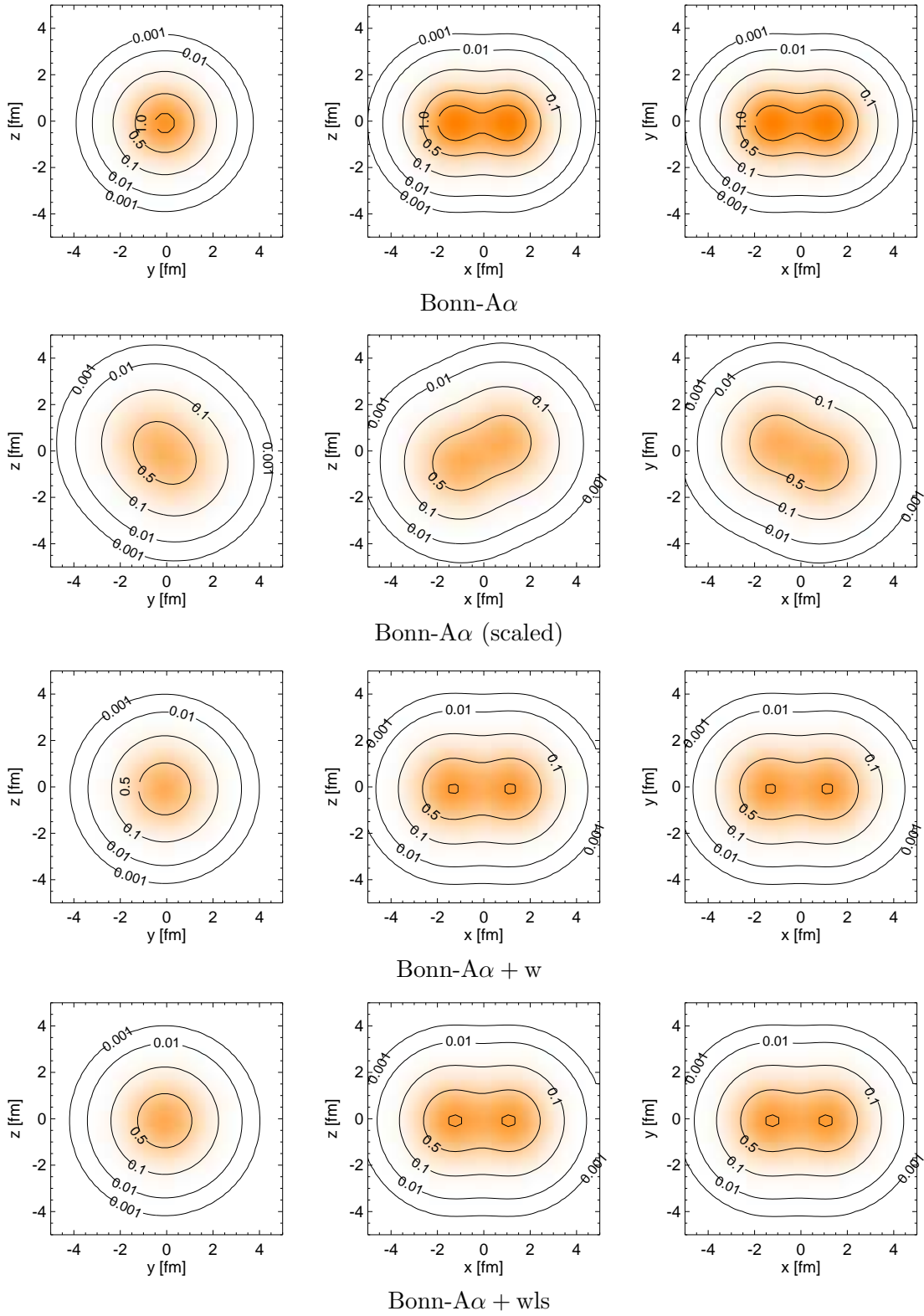
Figure 5.7: ^{7}Li intrinsic one-body densities, calculated for Bonn-Aα and various modifications. Values on the contours are densities in units of $\rho_0 = 0.17\,\mathrm{fm}^{-3}$.
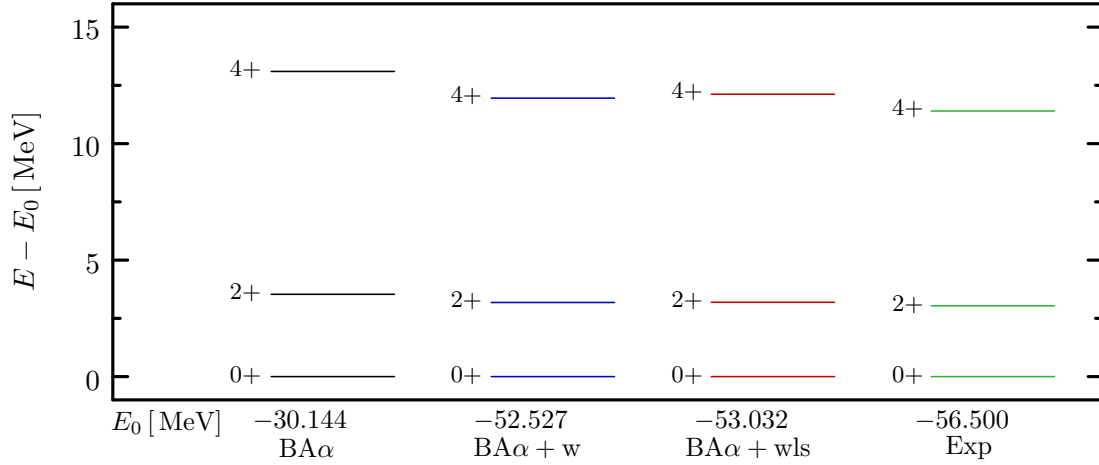
Figure 5.8: Lowest energy levels of ^{8}Be.

we find it to be usually about $0.2\,\mathrm{fm}$ smaller than r_{ms}, i.e., the neutron distribution is more extended. The results for the expectation values listed in Tab. 5.4 also agree with the $^6\mathrm{Li} + n$ model if we compare them with the ^{6}Li results given in Tab. 5.3. We found that the spins of the odd p-shell proton and neutron are coupled to $S = 1$ for all ^{6}Li states. With the addition of a further neutron, the spins are re-coupled to a total $S = 1/2$, which explains why S^2 is always close to $\frac{3}{4}$.

The orbital angular momentum of the $3/2^-$ and $1/2^-$ states is found to be dominated by a $L = 1$ component $(L^2 \approx 2)$, which corresponds to the orbital angular momentum of the odd neutron. For the $5/2^-$ and $7/2^-$ states, we find $L^2 \approx 12$, i.e., $L = 3$, and hence a $\Delta L = 2$ change of the core's orbital angular momentum, as was to be expected for an axially symmetric rotor.

Fig. 5.7 illustrates how the nucleon density distributions are affected by the modifications applied to Bonn-Aα. The net effect of all modifications is very similar for ^{7}Li: the densities are washed out over a larger spatial area, which was to be expected, since we used the corrections to increase the charge radii[2]. As a result, the cluster structure becomes less pronounced. For the scaled Bonn-Aα interaction, the cluster structure is almost completely dissolved.

5.2.3 ^{8}Be

For ^{8}Be, angular momentum projection of the double-Gaussian variational state yields the rotational spectrum displayed in Fig. 5.8, which agrees very well with experiment. The $0^+, 2^+, 4^+$ structure implies that ^{8}Be can be considered approximately axially symmetric for the groundstate rotational band, which is confirmed by the density cuts displayed in Fig. 5.9.

The intrinsic ^{8}Be state has a very pronounced 2α-structure, which is hardly surprising given that $\alpha + \alpha$ is the main decay channel of ^{8}Be ($\Gamma = 6.8\,\mathrm{eV}$ [58], corresponding to $T_{1/2} \approx 10^{-16}\,\mathrm{s}$). This structure is manifest in the S^2 values listed in Tab. 5.5: since

---

[2]The densities calculated with the scaled Bonn-Aα interactions are not properly rotated to their principal axes by the corresponding FMD program. However, this does not affect the results.
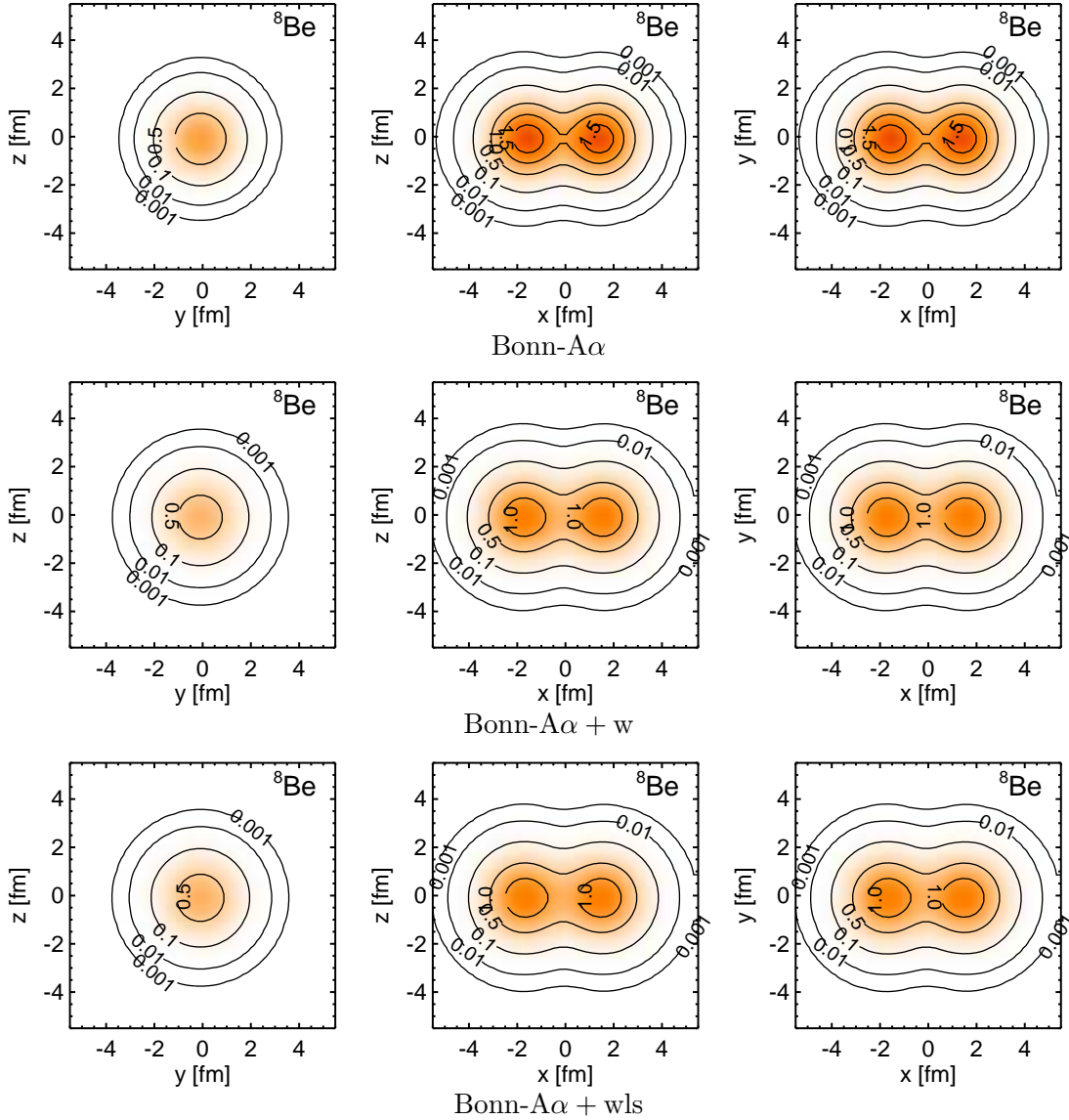
Figure 5.9: ^{8}Be intrinsic one-body densities, calculated for Bonn-Aα and various modifications using double-Gaussian trial states. Values on the contours are in units of $\rho_0 = 0.17\,\mathrm{fm}^{-3}$.

the groundstate of the α is $J^\pi = 0+$, all spins are coupled to zero in the respective subclusters of ^{8}Be, and correspondingly $S^2 \approx 0$.

The density cuts also show that the structure of the intrinsic state is practically the same for Bonn-Aα + w and Bonn-Aα + wls. Since the mean-field groundstate of ^{4}He has $L = 0$, spin-orbit forces do not contribute to its binding energy, and for nuclei with a multi-α structure, their effects are usually negligibly small, too. One noteworthy counter-example is ^{24}Mg, which will be discussed in Sect. 5.2.8.

	$E_0\,[\mathrm{MeV}]$	$E - E_0\,[\mathrm{MeV}]$	L^2	S^2	J^2	$r_{\mathrm{mms}}\,[\mathrm{fm}]$	$r_{\mathrm{cms}}\,[\mathrm{fm}]$
			Bonn-Aα				
0^+	-30.144		0.028	0.027	0.000	2.123	2.273
2^+		3.533	5.975	0.026	5.964	2.130	2.280
4^+		13.098	19.957	0.020	19.994	2.157	2.306
			Bonn-Aα + w				
0^+	-52.527		0.017	0.016	0.000	2.335	2.471
2^+		3.182	6.009	0.014	6.000	2.344	2.479
4^+		11.952	19.971	0.012	19.993	2.372	2.506
			Bonn-Aα + wls				
0^+	-53.032		0.080	0.080	0.000	2.303	2.442
2^+		3.191	5.986	0.078	5.986	2.314	2.453
4^+		12.120	19.889	0.058	19.999	2.339	2.476

Table 5.5: Calculated levels of ^{8}Be for Bonn-Aα and various modifications, using double Gaussian trial states.
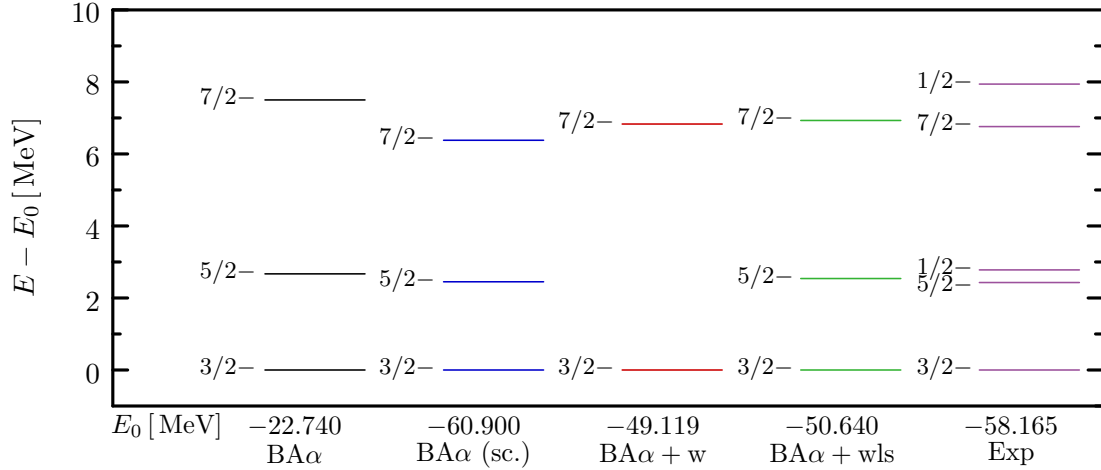
Figure 5.10: Groundstate rotational band of ^{9}Be.

5.2.4 ^{9}Be

^{9}Be is known to have one of the largest intrinsic deformations among the stable nuclei, which is evident from the density cuts displayed in Fig. 5.12. The nucleus has a very pronounced $\alpha + {}^5$He structure, hence we should compare with a two-center shell model to clarify the structure of the spectra displayed in Figs. 5.10 and 5.11 (see [60] and references therein).

Fig. 5.10 shows the groundstate rotational band [61], which is reproduced rather well by all versions of Bonn-Aα, aside from the missing $5/2^-$ state for the Bonn-Aα + w interaction. As mentioned in Sect. 5.2.2, the $\Delta J = 1$ spacing of the spectrum is indicative of a strong coupling between the motion of a ^{8}Be core (cf. Sect. 5.2.3) and an additional neutron. For the $3/2^-$ groundstate, the Coriolis force gives no contributions to the energy in first order perturbation theory, hence the ordering of the rotational

	$E_0\,[\text{MeV}]$	$E-E_0\,[\text{MeV}]$	L^2	S^2	J^2	$r_{\text{ms}}\,[\text{fm}]$	$r_{\text{cms}}\,[\text{fm}]$
			Bonn-Aα				
$3/2^-$	-22.740		2.780	0.760	3.710	2.160	2.290
$5/2^-$		2.670	7.130	0.760	8.720	2.170	2.290
$7/2^-$		7.500	14.200	0.760	15.780	2.180	2.310
			Bonn-Aα(sc.)				
$3/2^-$	-60.900		2.900	0.820	3.720	2.380	2.500
$5/2^-$		2.450	7.270	0.810	8.730	2.380	2.500
$7/2^-$		6.380	14.530	0.800	15.810	2.390	2.510
			Bonn-Aα + w				
$3/2^-$	-49.119		2.788	0.760	3.726	2.406	2.508
$7/2^-$		6.831	14.377	0.767	15.961	2.422	2.525
			Bonn-Aα + wls				
$3/2^-$	-50.640		2.830	0.780	3.730	2.370	2.480
$5/2^-$		2.540	7.180	0.770	8.750	2.380	2.480
$7/2^-$		6.930	14.310	0.770	15.800	2.390	2.500

Table 5.6: Calculated levels of ^{9}Be for Bonn-Aα and various modifications.

states is not interchanged. In the two-center shell model, the groundstate of ^{9}Be is correctly predicted to be $3/2^-$, which fixes the angular momentum of the valence neutron. Coupling of the orbital angular momenta of core and valence neutron, we obtain

$$0 \otimes 1 = 1 \tag{5.6}$$

$$2 \otimes 1 = 1 \oplus 2 \oplus 3 \tag{5.7}$$

$$4 \otimes 1 = 3 \oplus 4 \oplus 5\,, \tag{5.8}$$

and subsequent coupling with the total spin $S = 1/2$ of the system yields

$$(0^+ \otimes 1^-) \otimes \frac{1}{2} = \frac{1}{2}^- \oplus \frac{3}{2}^- \tag{5.9}$$

$$(2^+ \otimes 1^-) \otimes \frac{1}{2} = \frac{1}{2}^- \oplus \frac{3}{2}^- \oplus \frac{3}{2}^+ \oplus \frac{5}{2}^+ \oplus \frac{5}{2}^- \oplus \frac{7}{2}^- \tag{5.10}$$

$$(4^+ \otimes 1^-) \otimes \frac{1}{2} = \frac{5}{2}^- \oplus \frac{7}{2}^- \oplus \frac{7}{2}^+ \oplus \frac{9}{2}^+ \oplus \frac{9}{2}^- \oplus \frac{11}{2}^-\,. \tag{5.11}$$

The lowest states of the rotational spectrum appear twice in the coupling scheme, which can explain why the L^2 values listed in Tab. 5.6 correspond to mixtures of states with $\Delta L = 1$, e.g., for the $3/2^-$ state, we find $L^2 \approx 2.8$, which suggests a mixing between a strong $L = 1$ and a small $L = 2$ component.

In Fig. 5.11, we show the full projected spectrum of ^{9}Be. The unmodified Bonn-Aα reproduces the order of the $1/2^+, 5/2^+, 3/2^+$ triplet, but the splitting of the levels is smaller than for the experimental values. These states are, in fact, considered to be members of a further rotational band, starting from the band-head $K = 1/2$, which can be explained from the two-center shell model (cf. [60]). Bonn-Aα + wls and the scaled Bonn-Aα come close to reproducing these states, but the former reverses the order of
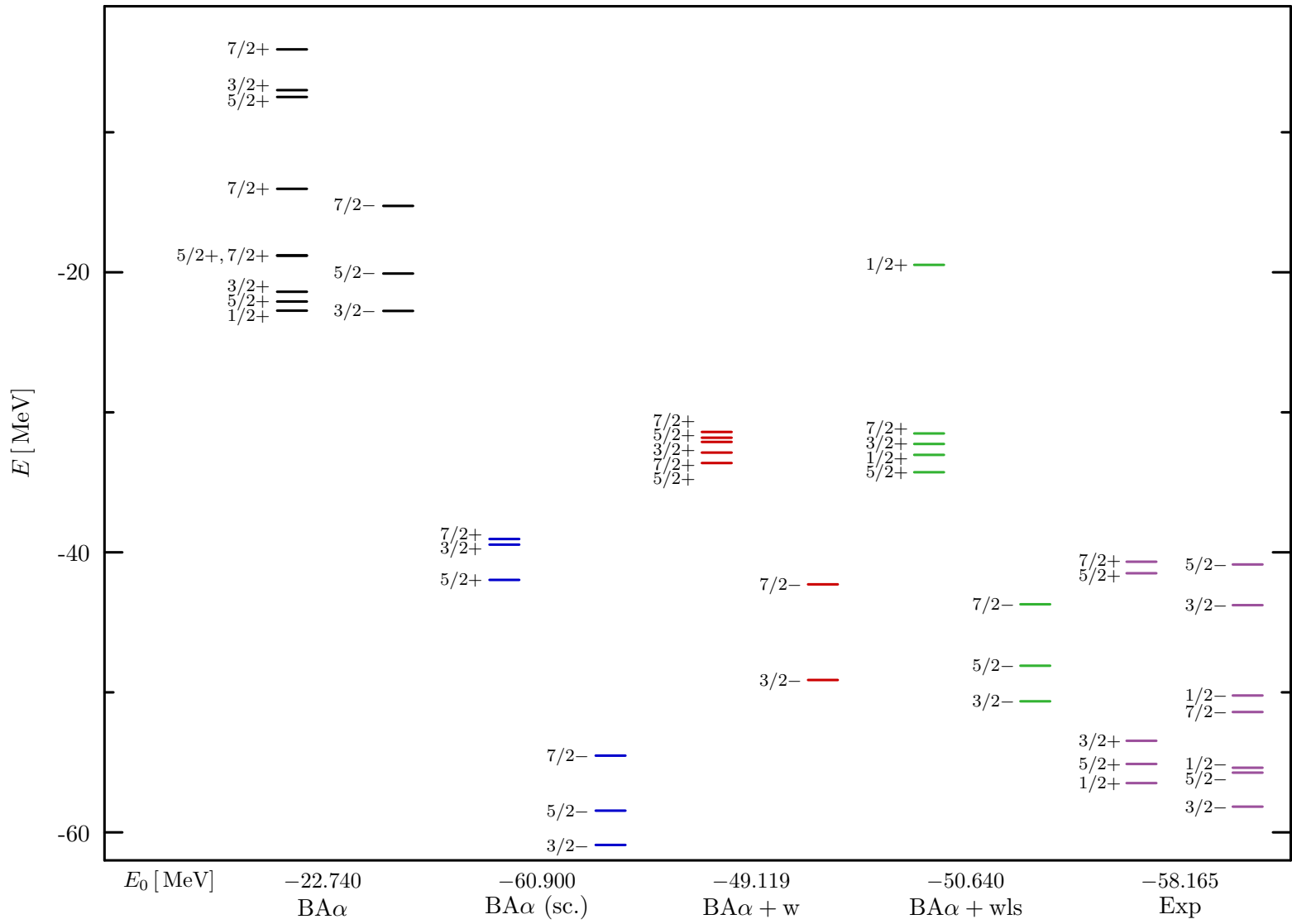
Figure 5.11: Spectrum of ⁹Be from angular momentum projection.

Bonn-Aα

Bonn-Aα (scaled)

Bonn-Aα + w

Bonn-Aα + wls
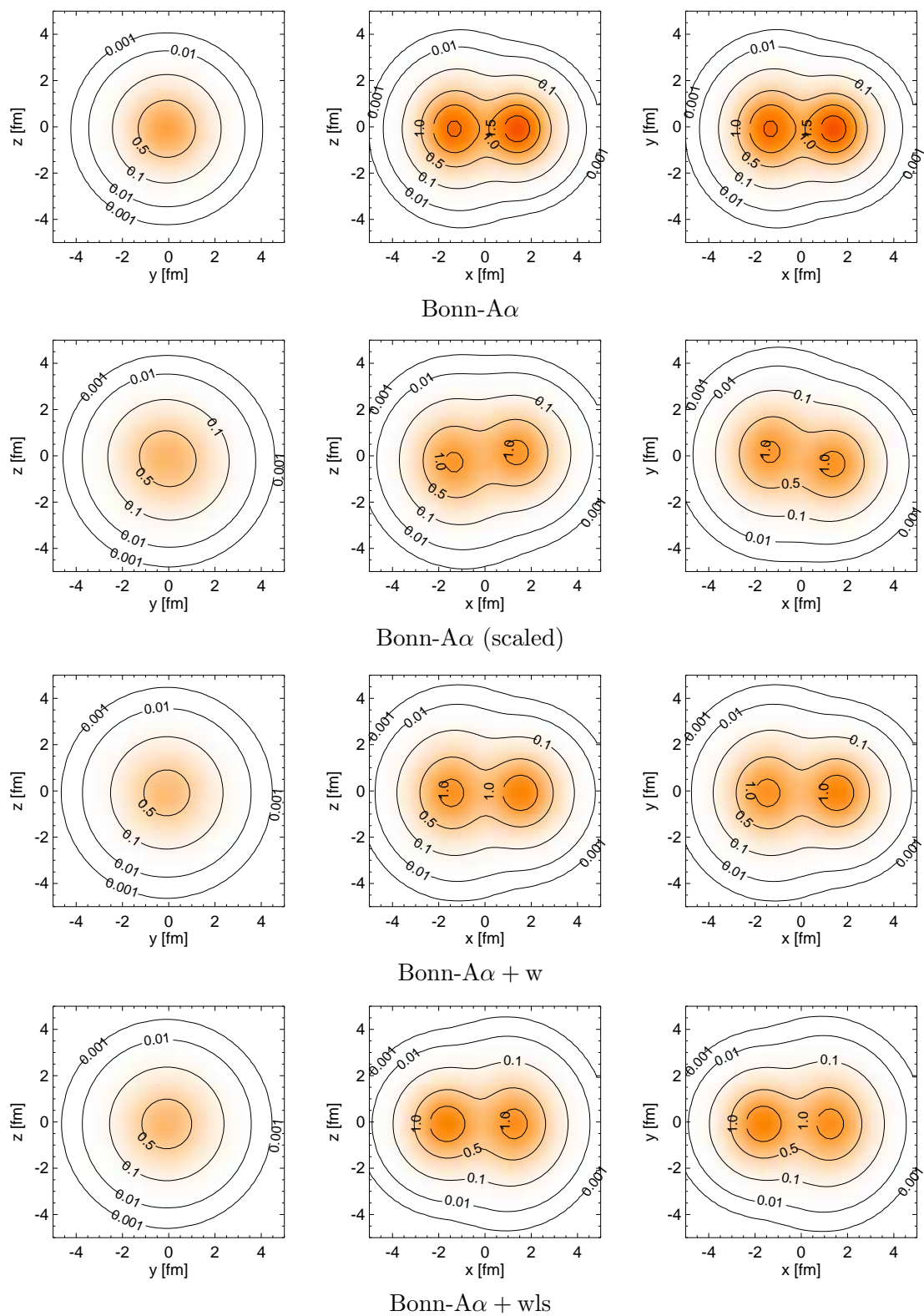
Figure 5.12: ^{9}Be intrinsic one-body densities. Values on the contours are in units of $\rho_0 = 0.17$ fm^{-3}.
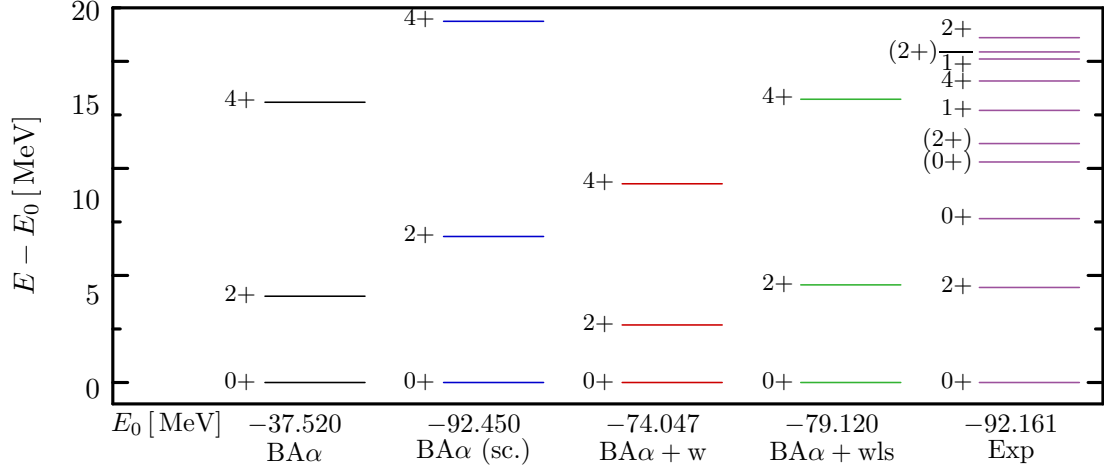
Figure 5.13: Groundstate rotational band of ^{12}C.

the $1/2^+$ and $5/2^+$ states, while the $1/2^+$ is missing from the spectrum for the latter interaction. The reversion of the order is most likely a result of an increase of the level splitting due to the enhanced spin orbit force, similar to what we found for ^{7}Li.

A more interesting finding is the way the modifications affect states of different parities although the added terms are parity-conserving. States whose parity corresponds to that of the groundstate gain a lot more binding energy than those with opposite parity. Furthermore, the density cuts of ^{7}Li and ^{9}Be in Figs. 5.7 and 5.12 show that the corrections wash out the cluster structure of the nuclei. The densities become smoother, more similar to rotational ellipsoids, i.e., their rotational symmetry is enhanced. At the same time, the binding energy gains achieved by angular momentum projection are reduced. One could say that the modified corrections already produce some of the effects of the angular momentum projection. Naturally, it then becomes harder to reproduce rotational states which are superimposed on clustered structures — the clusters would need to be reformed from the smooth state, which requires energy, hence the splitting between the rotational excitations of the groundstate and the clusters is increased. In comparison, the splitting between these kinds of excitations is small for the Bonn-Aα interaction, which has the strongest clustering. It is to be expected that the agreement with the experimental spectra will be much better if one performs the variation after the angular momentum projection and uses multi-configuration mixing. At the same time, these methods should reduce the size of the necessary correction terms notably.

5.2.5 ^{12}C

In Fig. 5.13, we show the groundstate rotational band of ^{12}C, calculated for Bonn-Aα and the various modifications. The expectation values listed in Tab. 5.7 are in good agreement with the picture of an axially deformed rotor. The unmodified Bonn-Aα-interactions reproduces the levels of the rotational band already almost perfectly. With the added Wigner correction, the density distributions are washed out (see Fig. 5.14), and the splitting of the levels is reduced. The additional spin-orbit correction restores the level splitting to roughly the correct size, while the even stronger spin-orbit force of
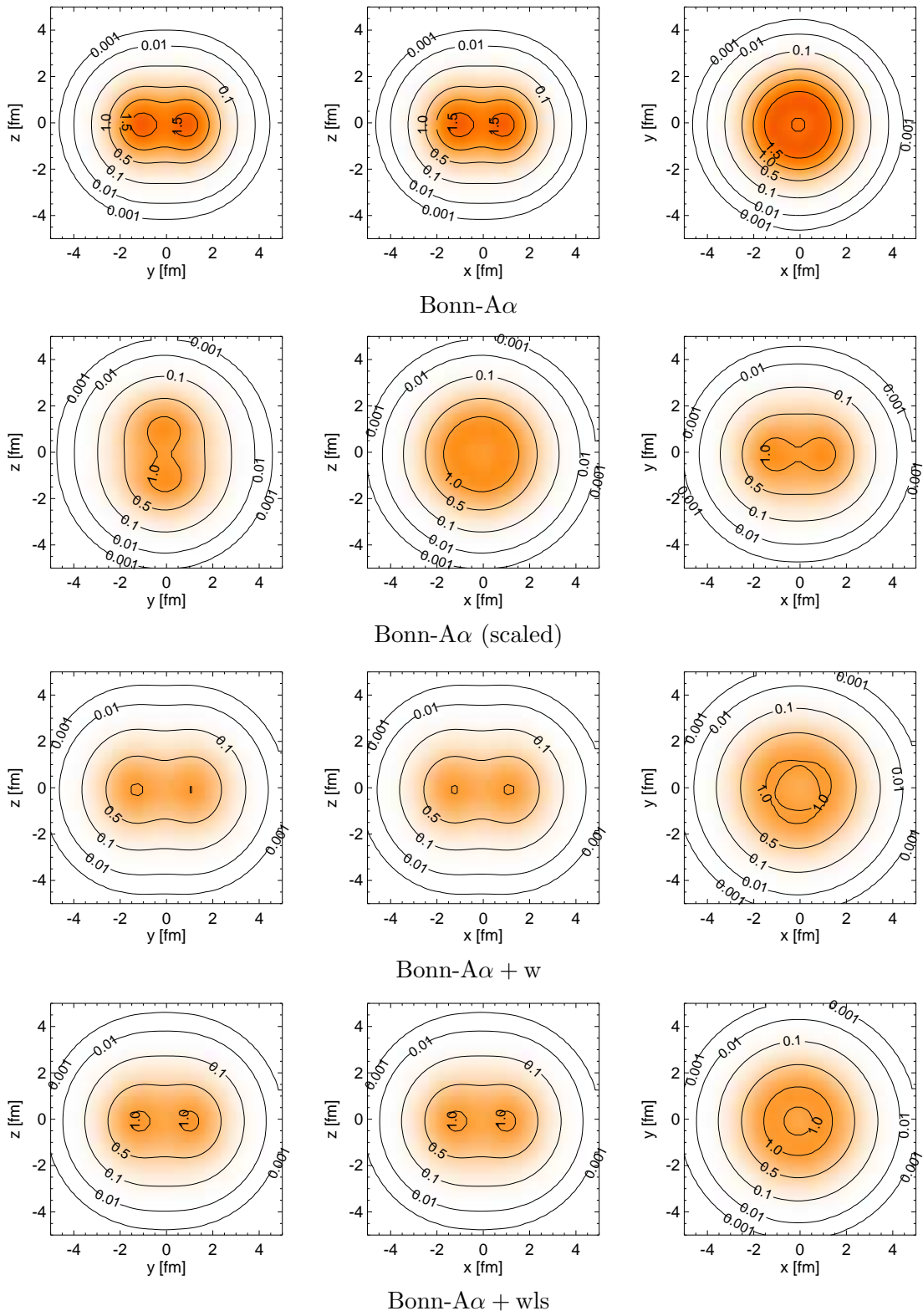
Figure 5.14: ^{12}C intrinsic one-body densities. Values on the contours are in units of $\rho_0 = 0.17$ fm^{-3}.

	$E_0\,[\mathrm{MeV}]$	$E - E_0\,[\mathrm{MeV}]$	L^2	S^2	J^2	$r_{\mathrm{ms}}\,[\mathrm{fm}]$	$r_{\mathrm{cms}}\,[\mathrm{fm}]$
		Bonn-Aα					
0^+	-37.520		1.130	1.150	0.020	2.040	2.220
2^+		4.030	6.310	0.740	6.000	2.040	2.220
4^+		13.090	19.440	0.280	20.670	2.040	2.220
		Bonn-Aα(sc.)					
0^+	-92.450		2.080	2.080	0.000	2.300	2.460
2^+		6.820	6.420	1.320	6.000	2.300	2.460
4^+		16.870	17.660	0.640	20.020	2.300	2.460
		Bonn-Aα + w					
0^+	-74.047		0.352	0.352	0.000	2.442	2.596
2^+		2.688	6.107	0.257	6.000	2.442	2.596
4^+		9.282	19.598	0.102	19.998	2.442	2.596
		Bonn-Aα + wls					
0^+	-79.120		1.650	1.660	0.010	2.380	2.540
2^+		4.560	6.390	1.040	6.010	2.380	2.540
4^+		13.230	18.870	0.430	20.700	2.380	2.540

Table 5.7: Calculated levels of ^{12}C.

the scaled Bonn-Aα drives the states even further apart.

A hint at the reason of the reduced level splitting produced by Bonn-Aα + w is provided by the triangular contour at the center of the xy-density cut depicted in Fig. 5.14. There is an experimental 0_2^+ state at $E - E_0 = 7.654\,\mathrm{MeV}$, which has been shown to have the structure of an oblate triangle of three α clusters (see [15, 62, 63]). The notable increase of the mass and charge radii for the Bonn-Aα + w interaction (cf. Tab. 5.7), which cannot be solely explained by the inflation of the nucleus due to the correction terms, can now be understood as the result of such a 3α-admixture to the mean-field state. Since the aforementioned 0_2^+ 'groundstate' of this configuration has the same quantum numbers as the oblate groundstate found for the other interactions, the two states can mix in the angular momentum projection. This mixing can also explain why the splitting between the 0^+ and 2^+ states is reduced — it is actually the 0^+ state which is 'lifted' energetically.

The additional spin-orbit correction term in Bonn-Aα+wls dissolves the 3α-structure again, which is evident from the density cuts and the decrease of the radii listed in Tab. 5.7.

5.2.6 ^{17}O

The results for ^{17}O are rather unspectacular. The groundstate corresponds to a neutron moving around a spherical ^{16}O core, hence the core cannot rotate. In a spherical shell model picture, the neutron is occupying the $2d_{5/2}$ level. The lowest experimental levels agree well with the shell model, including the gap between the two groups of positive parity states belonging to different main shells, and the placing of negative parity states in this gap.
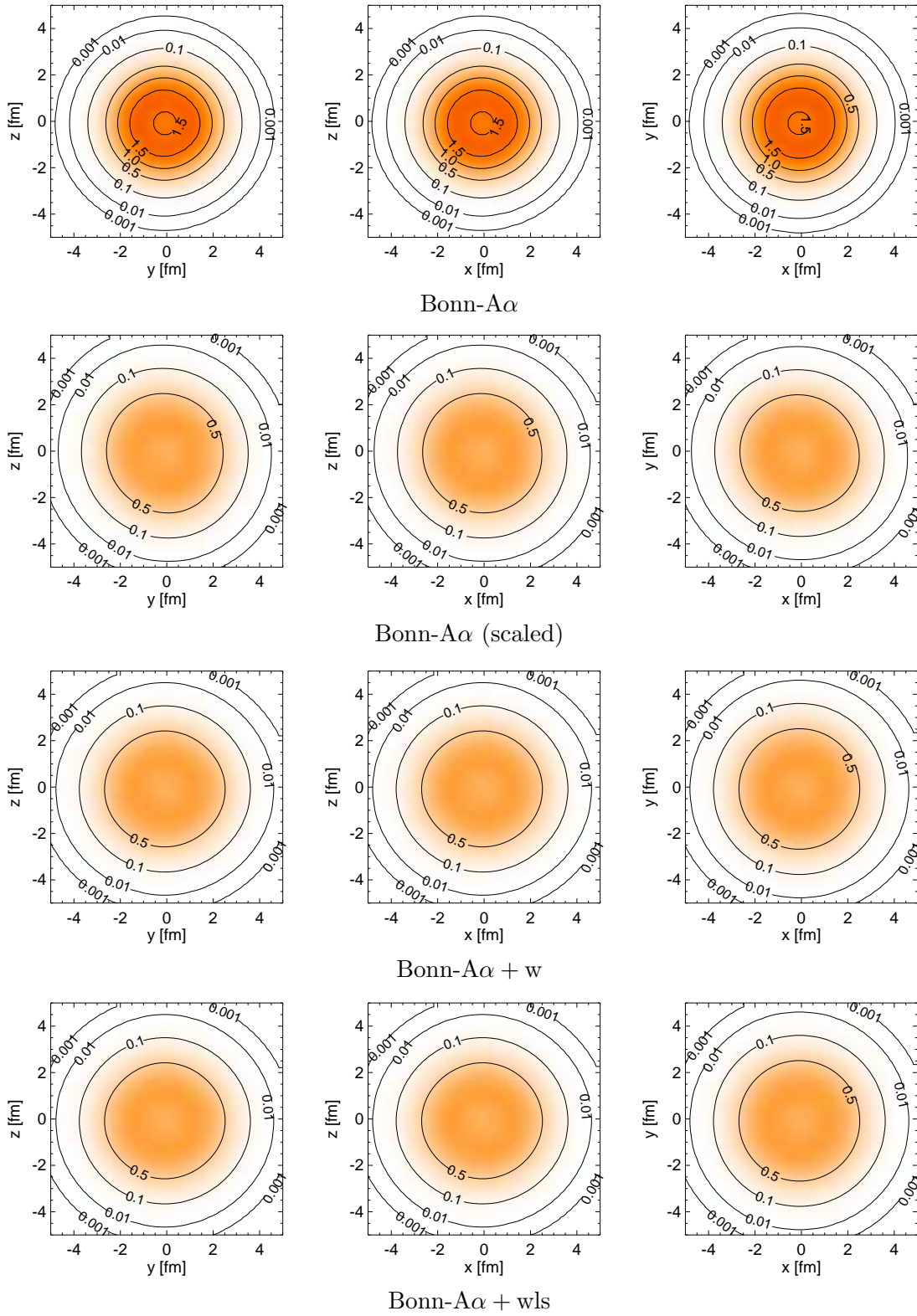
Figure 5.15: ^{17}O intrinsic one-body densities. Values on the contours are in units of $\rho_0 = 0.17$ fm^{-3}.

	$E_0\,[\,\text{MeV}]$	L^2	S^2	J^2	$r_{\text{ms}}\,[\,\text{fm}]$	$r_{\text{cms}}\,[\,\text{fm}]$
			Bonn-Aα			
$5/2^+$	-69.190	6.000	0.750	8.750	2.180	2.310
			Bonn-Aα(sc.)			
$5/2^+$	-127.670	6.000	0.750	8.750	2.600	2.700
			Bonn-Aα + w			
$5/2^+$	-126.428	6.000	0.750	8.750	2.603	2.702
			Bonn-Aα + wls			
$5/2^+$	-129.060	6.000	0.750	8.750	2.600	2.700

Table 5.8: Calculated levels of ^{17}O.
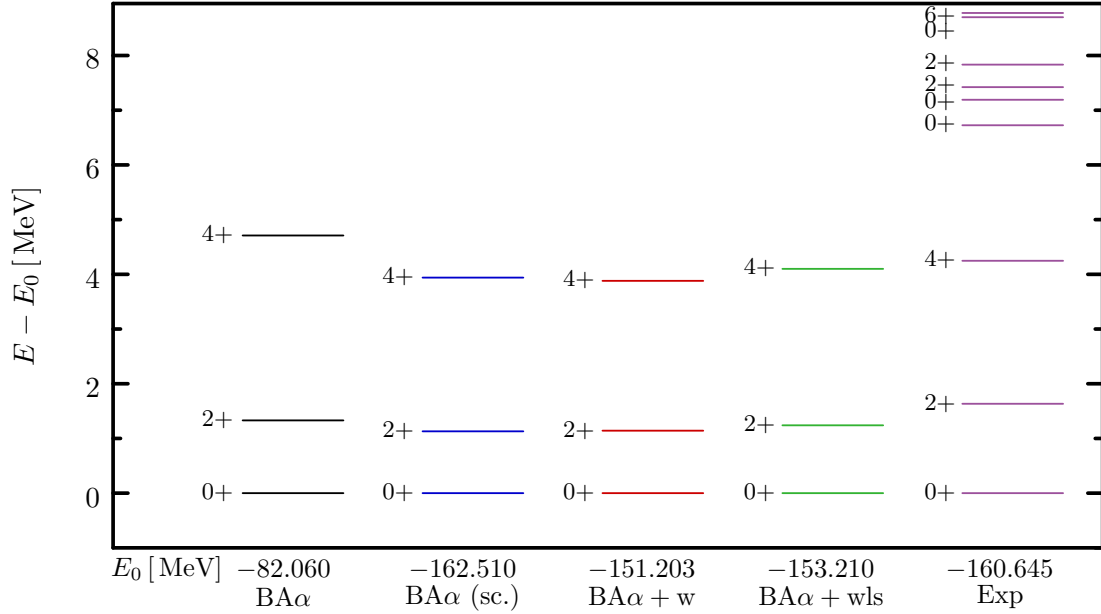
Figure 5.16: Groundstate rotational band of ^{20}Ne.

The expectation values for the $5/2^+$ ground state are listed in Tab. 5.8. The angular momenta correspond exactly to the quantum numbers of the odd neutron: $L = 2, S = 1/2, J = 5/2$. The density cuts are practically identical for all modified Bonn-Aα interactions, showing a perfect sphere. As for the other discussed nuclei, the densities are spread over a larger volume than for the unmodified Bonn-Aα interaction.

5.2.7 ^{20}Ne

Fig. 5.16 shows the groundstate rotational band of ^{20}Ne, and Tab. 5.9 lists the expectation values for the corresponding states. Again, the axially deformed rotor proves to be a valuable model for the rotational band.

The net effect of the spin-orbit correction is found to be rather small for the low levels, because their splitting is practically the same for Bonn-Aα+w and Bonn-Aα+wls. Moreover, the scaled Bonn-Aα interaction does not affect the level splitting much either,
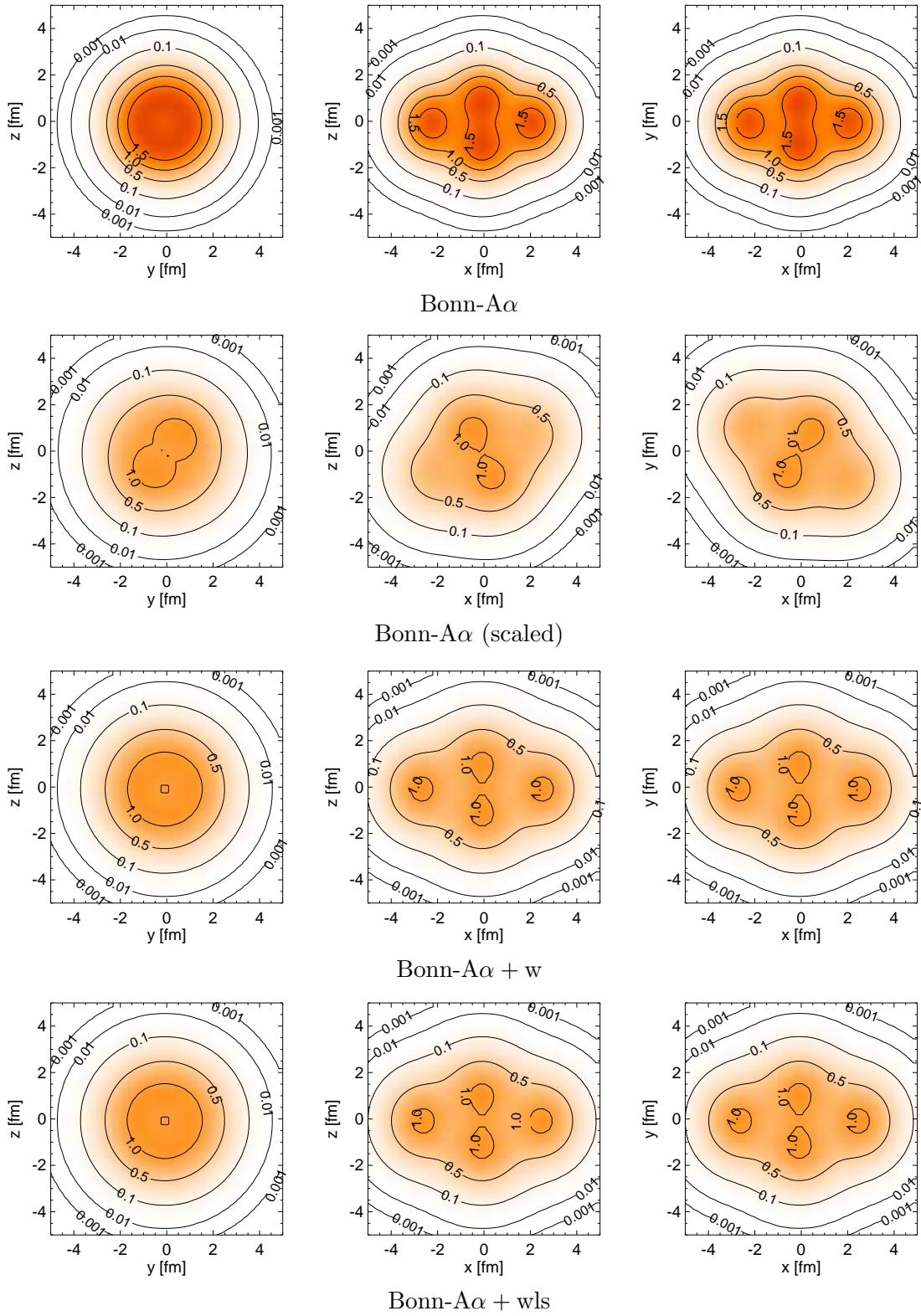
Figure 5.17: ^{20}Ne intrinsic one-body densities. Values on the contours are in units of $\rho_0 = 0.17$ fm^{-3}.

	E_0 [MeV]	$E - E_0$ [MeV]	L^2	S^2	J^2	r_{ms} [fm]	r_{cms} [fm]
Bonn-Aα							
0^+	-82.60		0.080	0.050	0.130	2.410	2.560
2^+		1.330	5.900	0.040	5.860	2.410	2.560
4^+		4.710	20.110	0.040	20.110	2.410	2.570
Bonn-Aα(sc.)							
0^+	-162.510		0.340	0.120	0.220	2.850	2.990
2^+		1.130	6.450	0.120	6.370	2.850	2.990
4^+		3.940	20.380	0.110	20.380	2.860	2.990
Bonn-Aα + w							
0^+	-151.203		0.051	0.014	0.037	2.882	3.018
2^+		1.142	6.067	0.013	6.057	2.883	3.019
4^+		3.881	20.027	0.013	20.026	2.887	3.022
Bonn-Aα + wls							
0^+	-153.210		0.270	0.110	0.160	2.870	3.000
2^+		1.240	6.360	0.110	6.280	2.870	3.000
4^+		4.100	20.530	0.110	20.520	2.870	3.010

Table 5.9: Calculated levels of ^{20}Ne.

	Bonn-Aα	Bonn-Aα (sc.)	Bonn-Aα + w	Bonn-Aα + wls
V^{ls} [MeV]	-2.496	-5.184	-0.495	-1.531
V^{ls}_{corr} [MeV]				-2.316
E_B [MeV]	-76.386	-160.857	-146.081	-147.610

Table 5.10: Contributions of the spin-orbit interaction to the binding energy of ^{20}Ne in FMD variational calculations.

although its scaled spin-orbit interaction has had rather dramatic effects in the nuclei discussed so far. Upon inspection of the mean-field groundstates, we find that the spin-orbit force contributes only about 3% of the final binding energy (see Tab. 5.10), with the notable exception of the Bonn-Aα + w interaction, for which the contribution is less than 1%. The reason for this is the multi-α-structure, because the spin-orbit force is zero for the s-wave ^{4}He. All spin-orbit effects in mean-field states with multi-α-structure are therefore a result of residual interactions like spin-polarization effects between the α-particles. This also explains why the spin-orbit forces are so weak for Bonn-Aα + w: the spreading of the density distributions (see Fig. 5.17) increases the size of the α particles, but it also increases their mean distance in the nucleus.

5.2.8 ^{24}Mg

We conclude our discussion of spectra and densities by presenting results for ^{24}Mg. As we see in Fig. 5.18, the groundstate rotational band is reproduced well by all interactions (with the possible exception of Bonn-Aα + w, see below). The situation is different in the case of the $K = 2$-band, whose band-head is the 2^+ state lying slightly above the 4^+ level of the experimental groundstate band. In a rotating-liquid-drop model, such
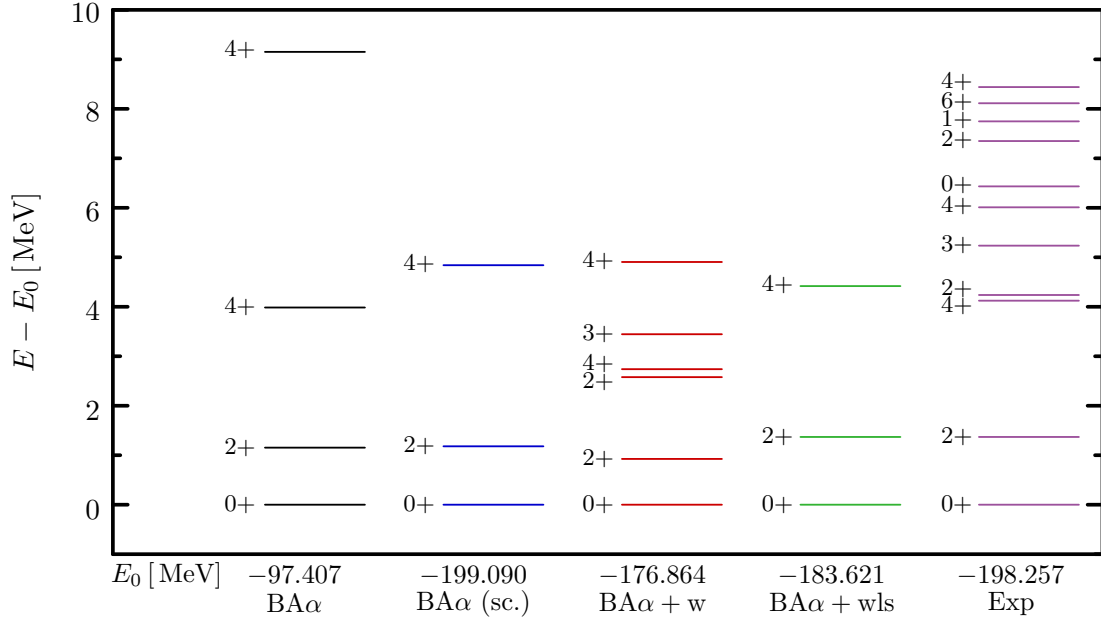
Figure 5.18: Groundstate rotational band of ^{24}Mg.

	E_0 [MeV]	$E - E_0$ [MeV]	L^2	S^2	J^2	r_{mms} [fm]	r_{cms} [fm]
			Bonn-Aα				
0^+	-97.418		1.937	1.936	0.001	2.462	2.598
2^+		1.153	7.865	1.923	5.997	2.462	2.598
4^+		3.985	21.703	1.884	20.205	2.464	2.599
4^+		9.151	20.254	1.497	19.595	2.466	2.602
			Bonn-Aα (sc.)				
0^+	-199.090		2.770	2.800	0.030	2.920	3.060
2^+		1.180	8.980	2.810	5.960	2.920	3.060
4^+		4.840	23.610	2.840	20.080	2.920	3.060
			Bonn-Aα + w				
0^+	-176.890		0.264	0.255	0.008	3.081	3.194
2^+		0.925	6.222	0.252	6.024	3.082	3.194
2^+		2.578	6.270	0.227	6.131	3.082	3.195
4^+		2.739	20.212	0.236	20.150	3.083	3.196
3^+		3.445	12.161	0.227	12.072	3.083	3.196
4^+		4.905	19.244	0.243	19.219	3.085	3.198
			Bonn-Aα + wls				
0^+	-183.620		2.799	2.796	0.003	2.977	3.092
2^+		1.369	8.828	2.801	5.723	2.978	3.093
4^+		4.418	22.996	2.870	20.099	2.980	3.095

Table 5.11: Calculated levels of ^{24}Mg.

		Bonn-Aα	Bonn-Aα (sc.)	Bonn-Aα + w	Bonn-Aα + wls
$\overline{V^{ls}}$	[MeV]	-21.647	-47.424	-2.444	-11.059
V_{corr}^{ls}	[MeV]				-15.086
E_B	[MeV]	-89.627	-198.840	-170.508	-179.371

Table 5.12: Contributions of the spin-orbit interaction to the binding energy of ^{24}Mg in FMD variational calculations.

bands are the result of collective roto-vibrational motion. However, we should note that this simple model predicts a quadratic J-dependence for the consecutive band members, i.e.,

$$E_{K=2}(J) = E_{K=2} + \frac{1}{2\mathcal{J}}(J(J+1) - K^2) \tag{5.12}$$

(cf. Sect. 5.2.2), which is clearly not the case for the $(2^+, 3^+, 4^+)$ triplet in the experimental spectrum. Aside from the overidealization of the nucleus as a liquid drop, this is due to the omission of non-collective excitations, which can have significant influence on the shape (and therefore the moment of inertia) of the nucleus, too.

While no trace of the $K = 2$ band can be found in the spectra of the scaled Bonn-Aα and Bonn-Aα + wls interactions, Bonn-Aw produces all experimental levels up to the second 4^+ state, although the ordering of the close-lying second 2^+ and first 4^+ state is interchanged. Regarding the structure of this spectrum, one cannot help but wonder if this first 4^+ is actually the member of the groundstate rotational band, because the splitting of the first 0^+ and 2^+ states is smaller than for the other interactions, probably as a result of a smaller moment of inertia. Grouping the levels in this fashion, we note that the spacings of the upper $(2^+, 3^+, 4^+)$ triplet indeed resemble those of a collective rotational band.

From the above discussion, it is obvious that a simple collective model would yield results which are similar to the ones obtained in our UCOM/FMD framework. However, the expectation values listed in Tab. 5.11 suggest that the situation is indeed more complex in a truly microscopic treatment. Especially the high values obtained for S^2 imply that many of the spins are not simply paired, as one conventionally assumes for inert rotating cores. This should also be the reason why the spin-orbit force gives larger relative contributions to the binding energy of ^{24}Mg than for ^{20}Ne (cf. Sect. 5.2.7), although ^{24}Mg's intrinsic state has a pronounced multi-α structure, too, as can be seen in Fig. 5.19.

Fig. 5.19 also illustrates that the 6α-structure of ^{24}Mg is dissolved very thoroughly by both Bonn-Aα + wls and the scaled Bonn-Aα interaction. This can be understood if one considers the 'evolution' of the interaction over the several modification steps. Bonn-Aα retains the α-cluster structure although the spin-orbit interaction contributes almost 25% percent of the binding energy (see Tab. 5.12), suggesting that the spin-orbit force primary adds binding between spin-polarized αs. With the addition of the Wigner correction, the contributions of the spin-orbit force are reduced for the same reason observed in the previous sections. However, now that the clusters have become more dilute, the addition of the spin-orbit correction causes an increased attraction primarily between nucleon-pairs, rather than α-clusters, which makes it energetically favorable to dissolve the α-clusters. The effect is taken to the extreme for the scaled
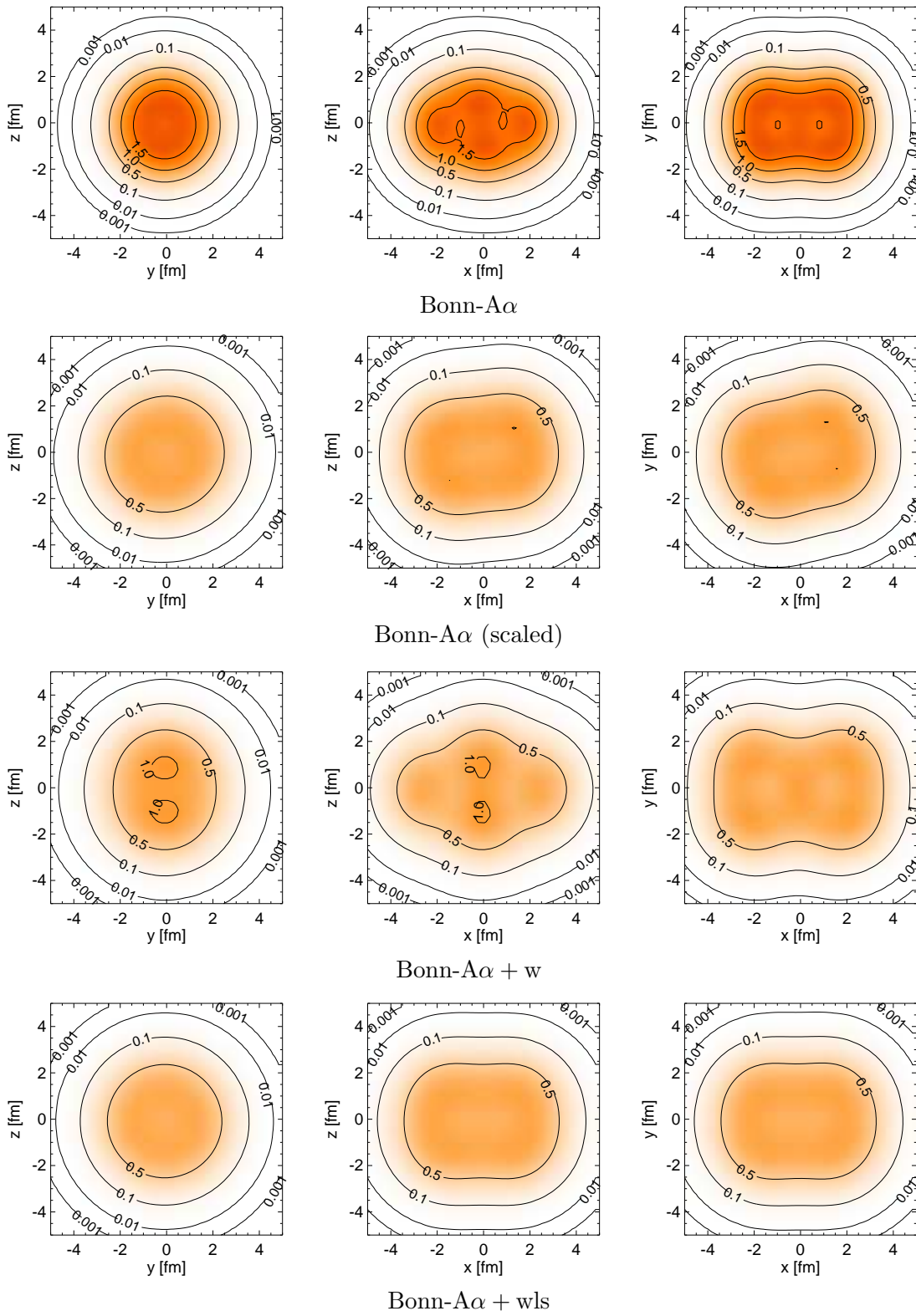
Figure 5.19: ^{24}Mg intrinsic one-body densities. Values on the contours are in units of $\rho_0 = 0.17$ fm^{-3}.

interaction, which combines the reduction of the density with an 'excessively' strong rescaled spin-orbit force.

5.3   Conclusions

While all modified correlated interactions constructed in Chapter 4 improve the agreement between the FMD groundstate results and experimental data, the studied spectra and densities provide further arguments in favor of the introduction of phenomenological correction terms.

When it comes to the spectra, they give more controlled results than the scaled interactions. The determination of the scale factors a_{kin} and a_{int}, as described in Sect. 4.3, ultimately yields a unique, ideal set, or at least one that is very close to it. Hence, there will always be cases where the rescaled spin-orbit force dramatically increases the level splitting, up to the point of reordering the level-sequence of studied spectra. This behavior is clearly undesirable.

In the studied cases, we have seen that both the Wigner and Wigner+LS corrections have their merits and drawbacks. Bonn-Aα + wls, while yielding the best results for the variational calculations, predicts the wrong groundstate for ^{6}Li and produces level-splittings which are too large in some cases. It also dissolves the cluster structure of ^{24}Mg, which we would like to retain due to experimental evidence of its presence. Bonn-Aα + w, on the other hand, fails to reproduce the $5/2^-$ state of the ^{9}Be spectrum and shows signs of mixing between 0^+ states of ^{12}C, but it retains the 6α structure of ^{24}Mg and apparently 'reproduces' this nucleus' $K = 2$ band. Under these aspects, it seems unwise to make a definite choice between the two modifications at this time.

As was discussed in Sect. 5.2.4, variation-after-projection and multi-configuration mixing are likely to improve the results for the unmodified Bonn-Aα interaction, making it possible to reduce the strength of the corrections. This would be very desirable, because although it underbinds the nuclei, Bonn-Aα gives the best reproduction of the structure of the experimental spectra in many cases.

Chapter 6

Summary and Outlook

The current status of realistic nucleon-nucleon interactions was reviewed in Chapter 1, with special emphasis on the Bonn-A and AV18 interactions used in our nuclear structure calculations. This review attempts to provide a condensed, but comprehensive overview of the theoretical considerations underlying the realistic models, and the methods which are used in their construction. Since the derivation of the NN interaction from chiral perturbation theory has produced a consistent potential of high accuracy, it was included in the review, in part for comparison to Bonn-A and AV18, but also with the prospect of a future use in calculations.

The Unitary Correlation Operator Method (UCOM) introduced in Chapter 2 combines the technical advantages of simple mean-field model spaces with the modern realistic nucleon-nucleon interactions. The importance of a proper treatment of central and tensor correlations in the many-nucleon system has been discussed, and the construction of the unitary central and tensor correlation operators was described in detail. The tensor correlator systematically induces the alignment of spin and relative distance vectors into simple mean-field states, and the central correlator provides the necessary degrees of freedom to model the correlation hole created by the repulsive short-range core common to all realistic NN interactions. Since this amounts to a decoupling of the short- and long-range behavior, or equivalently, the high- and low-momentum scales, the connection to the $V_{\text{low-k}}$ low-momentum interaction [8] was outlined.

The FMD mean-field model was summarized in Chapter 3, and ways to deal with the violation of the translational and rotational symmetries by the mean-field were discussed. The former was shown to primarily cause a shift of the system's energy by a spurious contribution from the nucleus' collective translational motion. The use of angular momentum projection to obtain the rotationally invariant physical groundstate was explained.

The correlated interactions obtained by applying the UCOM similarity transformation to the realistic Bonn-A and AV18 interactions, together with the global Wigner or Wigner+Spin-Orbit correction constructed in Chapter 4 of this work, enables us to describe the groundstate properties of more than 200 nuclei up to masses $A = 60$ in good agreement with experimental data. The correlated interaction and the 4 to 6 parameters of the correction are fixed *only once*, and *no further 'effective' parameters are introduced* and used to tune the results on a nucleus-by-nucleus basis. Thus we obtain a model with very high predictive power. With the additional use of angular momentum

projection after the variation, the agreement of binding energies, radii, and spectra with experimental data is surprisingly good, as we have seen in Chapter 5. Variation after projection and configuration mixing improve the FMD results even further [50].

The combined framework of the UCOM and FMD is all the more attractive for the relatively low numerical effort it requires, as opposed to, e.g., the quasi-exact Green's Function Monte Carlo technique employed by the Argonne group. It has enabled us to cover the nuclear chart up to masses $A = 60$ thus far. An FMD variational calculation of a heavy $A = 60$ nucleus takes roughly a day on a standard issue PC, so the mass range may be extended even further. In contrast, the GFMC calculations, which were performed with the Argonne supercomputer (although in various expansion stages) have reached $A = 12$ up to now.

The next steps are the application of correlated interactions in Hartree-Fock- and RPA-calculations in the intermediate and heavy mass region, and the inclusion of non-collective excitations. In addition, as indicated in Sect. 4.2.2, the examination and inclusion of three-nucleon contributions and genuine three-nucleon forces might provide a means to supersede the phenomenological modifications.

Appendix A

UCOM Formulas

This appendix collects UCOM formulas and operator relations from the original publications [4, 5, 6, 7] and provides some minor corrections.

A.1 Momentum Operators

A.1.1 Radial Momentum

The central correlator (Sect. 2.2) used to shift particles in their relative coordinate $\boldsymbol{r}$ is constructed from the *radial momentum operator* p_r

$$\mathrm{p}_r = \frac{1}{2}\left(\mathbf{p}\cdot\hat{\mathbf{r}} + \hat{\mathbf{r}}\cdot\mathbf{p}\right) . \tag{A.1}$$

Its coordinate space representation is

$$\left\langle\,\boldsymbol{r}\,\right|\mathrm{p}_r\left|\,\psi\,\right\rangle = -\left(\frac{i}{r} + \frac{\partial}{\partial r}\right)\left\langle\,\boldsymbol{r}|\psi\,\right\rangle = -i\frac{1}{r}\frac{\partial}{\partial r}r\left\langle\,\boldsymbol{r}|\psi\,\right\rangle, \tag{A.2}$$

yielding

$$\left\langle\,\boldsymbol{r}\,\right|\mathrm{p}_r^2\left|\,\psi\,\right\rangle = -\frac{1}{r}\frac{\partial}{\partial r}\left(r\frac{1}{r}\frac{\partial}{\partial r}r\left\langle\,\boldsymbol{r}|\psi\,\right\rangle\right) = -\frac{1}{r}\frac{\partial^2}{\partial r^2}r\left\langle\,\boldsymbol{r}|\psi\,\right\rangle . \tag{A.3}$$

When we switch to spherical coordinates in coordinate space, we have to carefully inspect how this affects the boundary conditions of the problem as well. From a mathematical point of view, it is sloppy to simply write down differential operators as coordinate space representations of an observable, because the boundary conditions are an important part of its definition — of particular interest to us is their impact on the operator's hermiticity (strictly: its *self-adjointness*). If the radial momentum operator

is to be hermitian on some Hilbert space $\mathcal{H}(\mathbb{R}^3)$ [1],

$$\langle\,\psi\,|\,\mathrm{p}_r\,|\,\phi\,\rangle = -i\int\limits_0^\infty dr\, r^2\psi^*(r)\frac{1}{r}\frac{\partial(r\phi(r))}{\partial r} = -ir^2\psi^*(r)\phi(r)\Big|_0^\infty + i\int\limits_0^\infty dr\,\frac{\partial(r\psi^*(r))}{\partial r}r\phi(r)$$

$$\overset{!}{=}\langle\,\phi\,|\,\mathrm{p}_r\,|\,\psi\,\rangle^* \tag{A.4}$$

has to be satisfied by making the surface term vanish at $r = 0$, thus the wavefunctions have to satisfy the following conditions:

$$r\psi(r)\xrightarrow{r\to 0} 0\,,\quad r\psi(r)\xrightarrow{r\to\infty} 0\,. \tag{A.5}$$

A.1.2   Orbital Momentum

The relative momentum operator $\mathbf{p}$ can be decomposed into a radial and an orbital part,

$$\mathbf{p} = \mathbf{p}_r + \mathbf{p}_\Omega\,. \tag{A.6}$$

The operators

$$\mathbf{p}_r \equiv \hat{\mathbf{r}}\,\mathrm{p}_r \quad\text{and}\quad \mathbf{p}_\Omega \equiv \frac{1}{2\mathrm{r}}(\mathbf{l}\times\hat{\mathbf{r}} - \hat{\mathbf{r}}\times\mathbf{l}) \tag{A.7}$$

do not commute; using the elementary commutation relation of position and momentum we find

$$\big[\mathrm{p}_r,\mathbf{p}_\Omega\big] = \frac{i}{\mathrm{r}}\mathbf{p}_\Omega \tag{A.8}$$

and

$$\mathbf{p}_r\cdot\mathbf{p}_\Omega - \mathbf{p}_\Omega\cdot\mathbf{p}_r = i\left(\mathrm{p}_r\frac{1}{\mathrm{r}} + \frac{1}{\mathrm{r}}\mathrm{p}_r\right) = -\frac{1}{\mathrm{r}^2} + \frac{2i}{\mathrm{r}}\mathrm{p}_r\,. \tag{A.9}$$

Definition (A.7) implies that $\mathbf{p}_\Omega$ commutes with (well-behaved) functions of the *relative distance* operator,

$$\big[\mathbf{p}_\Omega, f(\mathrm{r})\big] = 0\,, \tag{A.10}$$

but the orbital momentum operator does not commute with the relative position vector operator:

$$\big[\mathrm{p}_{\Omega k}, \mathrm{r}_l\big] = i\left(\frac{\mathrm{r}_k\mathrm{r}_l}{\mathrm{r}^2} - \delta_{kl}\right)\,. \tag{A.11}$$

By setting $k = l$ and summing in eq. (A.11), we obtain

$$\mathbf{r}\cdot\mathbf{p}_\Omega - \mathbf{p}_\Omega\cdot\mathbf{r} = 2i\,. \tag{A.12}$$

---

[1]Usually, one simply assumes $\mathcal{H} = \mathcal{L}^2(\mathbb{R}^3)$. In order to formally show that $\mathcal{L}^2(\mathbb{R}^3)$ is suitable for the spectral theory of the Hamiltonian and other observables, one has to do quite a deal of work. A free Hamiltonian, for instance, is not bounded, i.e., not continuous on $\mathcal{L}^2(\mathbb{R}^3)$, the space of square-integrable complex valued functions over three-dimensional space, and the addition of an interaction makes it semi-bounded at best. A possible solution to the problem comes with the introduction of weak derivatives, and Hilbert spaces of weakly derivable functions, the so-called *Sobolev spaces*. One can then define continuations of the Hamiltonian's expectation values to the space $\mathcal{L}^2(\mathbb{R}^3)$. Similar methods are used to extend the Fourier transformation from *Schwartz space* to $\mathcal{L}^2(\mathbb{R}^3)$, another property which is naively taken for granted. A good discussion of these topics can be found in [64].

Some additional helpful identities are

$$\mathbf{p}_r \cdot \mathbf{p}_\Omega + \mathbf{p}_\Omega \cdot \mathbf{p}_r = -\frac{1}{\mathrm{r}^2}\,, \tag{A.13}$$

$$\mathbf{p}_\Omega^2 = \frac{1}{\mathrm{r}^2}\left(\mathbf{l}^2 + 1\right)\,. \tag{A.14}$$

A.1.3 Representations of Momentum-Dependent Terms

Momentum-dependent interaction terms can be represented in several ways[2]:

$$\frac{1}{2}\left(\mathrm{p}_r^2 f(\mathrm{r}) + f(\mathrm{r})\mathrm{p}_r^2\right) = \mathrm{p}_r f(\mathrm{r})\mathrm{p}_r - \frac{1}{2}f''(\mathrm{r}) \tag{A.15}$$

$$= (\mathbf{p}\cdot\hat{\mathbf{r}})\,f(\mathrm{r})\,(\hat{\mathbf{r}}\cdot\mathbf{p}) - \frac{1}{2}f''(\mathrm{r}) - \frac{f'(\mathrm{r})}{\mathrm{r}} \tag{A.16}$$

$$= \mathbf{p}f(\mathrm{r})\mathbf{p} - f(\mathrm{r})\frac{\mathbf{l}^2}{\mathrm{r}^2} - \frac{1}{2}f''(\mathrm{r}) - \frac{f'(\mathrm{r})}{\mathrm{r}}\,, \tag{A.17}$$

where $f(\mathrm{r})$ is some well-behaved function of the relative distance operator r — in practice, this is either the radial dependency of a momentum-dependent potential, or an effective mass term. Of the above, we usually use the symmetric form, similar to the $\mathbf{p}^2$ terms in the definition of the Bonn-A OBEPR potential. The non-hermitian definition

$$\hat{\mathrm{p}}_r \equiv \mathbf{p}\cdot\hat{\mathbf{r}} \tag{A.18}$$

was used for the radial momentum operator in [4, 5], so eq. (A.16) provides the transformation rule for expressions appearing in these references, most notably the kinetic energy potential $\widetilde{\mathrm{w}}$ (cf. Sect. 2.4).

A.2 Relations for Correlated Operators

In order to calculate central- and tensor-correlated operators, algebraic relations for the correlation generators and the various operators of the uncorrelated interactions are required. These are used in the *Baker-Campbell-Hausdorff formula*

$$\exp\left(i\lambda\mathrm{A}\right)\,\mathrm{B}\,\exp\left(-i\lambda\mathrm{A}\right) = \sum_n \frac{1}{n!}(i\lambda)^n\left[\mathrm{A},\mathrm{B}\right]_{(n)}\,, \tag{A.19}$$

where

$$\left[\mathrm{A},\mathrm{B}\right]_{(0)} = \mathrm{B} \quad \text{and} \quad \left[\mathrm{A},\mathrm{B}\right]_{(n)} = \left[\mathrm{A},\left[\mathrm{A},\mathrm{B}\right]_{(n-1)}\right]\,. \tag{A.20}$$

While the operator transformations induced by the central correlator can be computed comparably simple, it is appropriate to perform the more complex calculations of algebraic relations involving the generator g_Ω in the irreducible spherical tensor representation of the operators (see Appendix B). The results obtained in [6] by using this approach are summarized below. Keep in mind that $\mathrm{s}_{12}(\mathbf{r}, \mathbf{p}_\Omega)$ is implicitly symmetrized in its arguments.

---

[2]These identities are misprinted in Refs. [6, 7].

A.2.1   Centrally Correlated Operators

In this section the centrally correlated versions of several basic operators are calculated. Recall the action of the central correlator and its adjoint on a relative wavefunction:

$$\langle \boldsymbol{r} | \, \mathrm{c} \, | \phi \rangle = \mathcal{R}_-(r) \langle R_-(r)\hat{\boldsymbol{r}} | \phi \rangle \tag{A.21}$$

and

$$\langle \boldsymbol{r} | \, \mathrm{c}^\dagger \, | \phi \rangle = \mathcal{R}_+(r) \langle R_+(r)\hat{\boldsymbol{r}} | \phi \rangle \,, \tag{A.22}$$

with

$$\mathcal{R}_\pm(r) = \frac{R_\pm(r)}{r} \sqrt{R'_\pm(r)} \,. \tag{A.23}$$

Angular Momentum Operators

Using spherical coordinates in the center-of-mass system, the components of the relative orbital angular momentum operator's coordinate space representation are given by

$$\langle \boldsymbol{r} | \, \mathrm{l}_x \, | \psi \rangle = -i \left(-\sin\phi \frac{\partial}{\partial \theta} - \cot\theta \cos\phi \frac{\partial}{\partial \phi} \right) \langle \boldsymbol{r} | \psi \rangle \,, \tag{A.24}$$

$$\langle \boldsymbol{r} | \, \mathrm{l}_y \, | \psi \rangle = -i \left(\cos\phi \frac{\partial}{\partial \theta} - \cot\theta \sin\phi \frac{\partial}{\partial \phi} \right) \langle \boldsymbol{r} | \psi \rangle \,, \tag{A.25}$$

$$\langle \boldsymbol{r} | \, \mathrm{l}_z \, | \psi \rangle = -i \frac{\partial}{\partial \phi} \langle \boldsymbol{r} | \psi \rangle \,. \tag{A.26}$$

This implies that

$$\left[\mathrm{l}_i, \mathrm{p}_r \right] = 0 \,, \tag{A.27}$$

and therefore

$$\mathrm{c}_r^\dagger \, \mathbf{l} \, \mathrm{c}_r = \mathbf{l} \,. \tag{A.28}$$

Since spin operators do not act in coordinate space at all, one obviously has

$$\left[\boldsymbol{\sigma}, \mathrm{p}_r \right] = 0 \,, \quad \text{i.e.,} \quad \mathrm{c}_r^\dagger \, \boldsymbol{\sigma} \, \mathrm{c}_r = \boldsymbol{\sigma} \,. \tag{A.29}$$

Position Operators

$$\begin{aligned} \langle \phi | \, \mathrm{c}_r^\dagger \mathbf{r} \, \mathrm{c}_r \, | \psi \rangle &= \int d^3r \, d^3r' \, \langle \phi | \, \mathrm{c}_r^\dagger \, | \boldsymbol{r} \rangle \langle \boldsymbol{r} | \, \mathbf{r} \, | \boldsymbol{r}' \rangle \langle \boldsymbol{r}' | \, \mathrm{c}_r \, | \psi \rangle \\ &= \int d^3r \, d^3r' \, \langle \phi | \, \mathrm{c}_r^\dagger \, | \boldsymbol{r} \rangle \, \boldsymbol{r} \delta^3(\boldsymbol{r}' - \boldsymbol{r}) \langle \boldsymbol{r}' | \, \mathrm{c}_r \, | \psi \rangle \\ &= \int dr \, d\Omega \, r^2 \, \langle \phi | \, \mathrm{c}_r^\dagger \, | \boldsymbol{r} \rangle \, r\hat{\boldsymbol{r}} \langle \boldsymbol{r}' | \, \mathrm{c}_r \, | \psi \rangle \\ &= \int dr \, d\Omega \, r^2 \left(\frac{R_-(r)}{r} \right)^2 R'_-(r) \langle \phi | R_-(r)\hat{\boldsymbol{r}} \rangle \, r\hat{\boldsymbol{r}} \langle R_-(r)\hat{\boldsymbol{r}} | \psi \rangle \\ &= \int dr_- \, d\Omega \, r_-^2 \, \langle \phi | \boldsymbol{r}_- \rangle \, R_+(r_-)\hat{\boldsymbol{r}}_- \langle \boldsymbol{r}_- | \psi \rangle \end{aligned} \tag{A.30}$$

Eqs. (A.21) and (A.22) were used in the third line, and in the last line coordinates were changed to

$$\boldsymbol{r}_- = R_-(r)\hat{\boldsymbol{r}}\,, \quad d^3r_- = r_-^2\, dr_- d\Omega = (R_-(r))^2\, R'_-(r)\, drd\Omega\,. \tag{A.31}$$

Since the $R_\pm(r)$ are mutually inverse, the remaining r-dependences can be replaced by

$$r = R_+(r_-)\,. \tag{A.32}$$

Owing to unitarity, the transformation behaviour of **r** carries over to all functions of this operator which can be expanded into a well-defined Taylor series.

Momentum Operators

The matrix element of the centrally correlated radial momentum operator is

$$
\begin{aligned}
\langle\,\phi\,|\,c_r^\dagger p_r c_r\,|\,\psi\,\rangle &= \int d^3r\, d^3r'\, \langle\,\phi\,|\,c_r^\dagger\,|\,\boldsymbol{r}\,\rangle\,\langle\,\boldsymbol{r}\,|\,p_r\,|\,\boldsymbol{r}'\,\rangle\,\langle\,\boldsymbol{r}'\,|\,c_r\,|\,\psi\,\rangle \\
&= -i\int d^3r\, d^3r'\, \langle\,\phi\,|\,c_r^\dagger\,|\,\boldsymbol{r}\,\rangle\, \frac{1}{r}\frac{\partial}{\partial r} r\delta^3(\boldsymbol{r}' - \boldsymbol{r})\,\langle\,\boldsymbol{r}\,|\,c_r\,|\,\psi\,\rangle \\
&= -i\int drd\Omega\, R_-(r)\sqrt{R'_-(r)}\,\langle\,\phi\,|\,R_-(r)\hat{\boldsymbol{r}}\,\rangle\, \frac{\partial}{\partial r} R_-(r)\sqrt{R'_-(r)}\,\langle\,R_-(r)\hat{\boldsymbol{r}}\,|\,\psi\,\rangle \\
&= -i\int \frac{dr_-}{R'_-(r)}d\Omega\, r_-\sqrt{R'_-(r)}\,\langle\,\phi\,|\,\boldsymbol{r}_-\,\rangle\, R'_-(r)\frac{\partial}{\partial r_-} r_-\sqrt{R'_-(r)}\,\langle\,\boldsymbol{r}_-\,|\,\psi\,\rangle \\
&= -i\int dr_-\, d\Omega\, r_-^2\,\langle\,\phi\,|\,\boldsymbol{r}_-\,\rangle\, \frac{1}{\sqrt{R'_+(r_-)}}\frac{1}{r_-}\frac{\partial}{\partial r_-} r_-\frac{1}{\sqrt{R'_+(r_-)}}\,\langle\,\boldsymbol{r}_-\,|\,\psi\,\rangle\,, \quad \text{(A.33)}
\end{aligned}
$$

where the coordinate transformation (A.31) and the relation

$$R'_\pm(r) = \left[R'_\mp(R_\pm(r))\right]^{-1} \tag{A.34}$$

for the derivatives of the central correlation functions were used. The latter is an immediate consequence of them being mutually inverse. Thus, one has

$$c_r^\dagger p_r c_r = \frac{1}{\sqrt{R_+(r)}} p_r \frac{1}{\sqrt{R_+(r)}}\,. \tag{A.35}$$

Using the previous results, the centrally correlated orbital momentum operator is found to be[3]

$$
\begin{aligned}
c_r^\dagger p_{\Omega k} c_r &= c_r^\dagger \frac{1}{2r} \left[\varepsilon_{klm}\left(l_l\hat{r}_m - \hat{r}_l l_m\right)\right] c_r = c_r^\dagger \frac{1}{2r} c_r \left[\varepsilon_{klm}\left(l_l\hat{r}_m - \hat{r}_l l_m\right)\right] \\
&= \frac{1}{2R_+(r)} \left[\varepsilon_{klm}\left(l_l\hat{r}_m - \hat{r}_l l_m\right)\right] = \frac{r}{R_+(r)} p_{\Omega k}\,. \tag{A.36}
\end{aligned}
$$

---

[3]This relation is misprinted in Ref. [4].

Summary

$$c_r^\dagger \, \mathbf{r} \, c_r = R_+(\mathrm{r}) \hat{\mathbf{r}} \qquad\qquad\qquad c_r^\dagger \, \mathrm{r} \, c_r = R_+(\mathrm{r}) \tag{A.37a}$$

$$c_r^\dagger \, \hat{\mathbf{r}} \, c_r = \hat{\mathbf{r}} \tag{A.37b}$$

$$c_r^\dagger \mathrm{p}_r c_r = \frac{1}{\sqrt{R_+(\mathrm{r})}} \mathrm{p}_r \frac{1}{\sqrt{R_+(\mathrm{r})}} \qquad\qquad c_r^\dagger \mathrm{p}_{\Omega k} c_r = \frac{\mathrm{r}}{R_+(\mathrm{r})} \mathrm{p}_{\Omega k} \tag{A.37c}$$

$$c_r^\dagger \, \mathbf{l} \, c_r = \mathbf{l} \qquad\qquad\qquad c_r^\dagger \, \boldsymbol{\sigma} \, c_r = \boldsymbol{\sigma} \tag{A.37d}$$

Appendix B

Partial Wave Analysis of Tensor Operators

In this appendix, the calculation of interaction operator matrix elements in partial wave states is outlined. After introducing irreducible spherical tensors and partial wave states, the matrix elements of some basic operators are summarized, which can then be used to derive the reduced matrix elements of the various complex interaction operators which are present in the uncorrelated and correlated interactions. Tables of these matrix elements in the lowest partial waves are given for convenience. Throughout the present work, the conventions of the Particle Data Group [24] for the Wigner-Eckart theorem and the Clebsch-Gordan coefficients are used.

B.1   Plane and Partial Wave States

Consider the eigenstates of the relative momentum and orbital angular momentum operators, $\left| klm \right\rangle$, which satisfy the orthogonality and completeness relations

$$\left\langle k'l'm' | klm \right\rangle = \frac{\delta(k - k')}{kk'} \delta_{ll'} \delta_{mm'} \tag{B.1}$$

$$\sum_{l,m} \int dk\, k^2 \left| klm \right\rangle\!\left\langle klm \right| = \mathbb{1} \,. \tag{B.2}$$

Their momentum space representation is

$$\left\langle \boldsymbol{k}' | klm \right\rangle = \frac{\delta(k' - k)}{kk'} Y_{lm}(\hat{\boldsymbol{k}}) \,. \tag{B.3}$$

Using the expansion

$$\left\langle \boldsymbol{r} | \boldsymbol{k} \right\rangle = \frac{1}{(2\pi)^{3/2}} e^{i\boldsymbol{k}\cdot\boldsymbol{r}} = \sqrt{\frac{2}{\pi}} \sum_{l=0}^{\infty} \sum_{m=-l}^{l} i^l j_l(kr) Y_{lm}^*(\hat{\boldsymbol{k}}) Y_{lm}(\hat{\boldsymbol{r}}) \,, \tag{B.4}$$

we find the coordinate space representation with the correct normalization factors in scattering units ($\hbar = c = \hbar^2/m_N = 1$):

$$
\begin{aligned}
\langle \boldsymbol{r}|klm \rangle &= \int d^3k' \langle \boldsymbol{r}|\boldsymbol{k}' \rangle \langle \boldsymbol{k}'|klm \rangle \\
&= \sqrt{\frac{2}{\pi}} \sum_{l',m'} i^{l'} \int d^3k' \, j_{l'}(k'r) Y^*_{l'm'}(\hat{\boldsymbol{k}}') Y_{lm}(\hat{\boldsymbol{r}}) \frac{\delta(k'-k)}{k'k} Y_{lm}(\hat{\boldsymbol{k}}) \\
&= \sqrt{\frac{2}{\pi}} \sum_{l',m'} i^{l'} j_{l'}(kr) Y_{l'm'}(\hat{\boldsymbol{r}}) \int d\Omega_{\boldsymbol{k}} Y^*_{l'm'}(\Omega_{\boldsymbol{k}}) Y_{lm}(\Omega_{\boldsymbol{k}}) \\
&= \sqrt{\frac{2}{\pi}} i^l j_l(kr) Y_{lm}(\hat{\boldsymbol{r}}) \,,
\end{aligned}
\tag{B.5}
$$

where the orthogonality relation of the spherical harmonics was used in the third line.

Analogously to $|klm \rangle$ we can define a set of states $|rlm \rangle$,

$$
\langle \boldsymbol{r}'|rlm \rangle = \frac{\delta(r-r')}{rr'} Y_{lm}(\hat{\boldsymbol{r}}') \,,
\tag{B.6}
$$

which satisfy the completeness and orthogonality relations

$$
\langle r'l'm'|rlm \rangle = \frac{\delta(r-r')}{rr'} \delta_{ll'} \delta_{mm'}
\tag{B.7}
$$

and

$$
\sum_{l,m} \int dr\, r^2 \, |rlm \rangle \langle rlm| = \mathbb{1} \,.
\tag{B.8}
$$

Their projections on general momentum and plane wave states are given by

$$
\langle \boldsymbol{k}|rlm \rangle = \sqrt{\frac{2}{\pi}} i^{-l} j_l(kr) Y_{lm}(\hat{\boldsymbol{k}})
\tag{B.9}
$$

and

$$
\langle kl'm'|rlm \rangle = \sqrt{\frac{2}{\pi}} i^{-l} j_l(kr) \delta_{ll'} \delta_{mm'} \,,
\tag{B.10}
$$

respectively. Starting from (B.7), we arrive at a useful relation for the delta function:

$$
\begin{aligned}
\langle r'l'm'|rlm \rangle &= \sum_{l'',m''} \int dk''\, k''^2 \langle r'l'm'|k''l''m'' \rangle \langle k''l''m''|rlm \rangle \\
&= i^{l'-l} \frac{2}{\pi} \int dk''\, k''^2 j_l(k''r') j_l(k''r) \delta_{ll'} \delta_{mm'} \\
&= \frac{2}{\pi} \int dk''\, k''^2 j_l(k''r') j_l(k''r) \delta_{ll'} \delta_{mm'} \,,
\end{aligned}
\tag{B.11}
$$

i.e.,

$$
\int dk\, k^2 j_l(kr') j_l(kr) = \frac{\pi}{2} \frac{\delta(r-r')}{rr'} \,.
\tag{B.12}
$$

The $^{2s+1}l_j$ partial wave states can now be defined by

$$\left|k(ls)jm\right\rangle = \sum_{m_l,m_s} \left\langle lm_lsm_s\middle|jm\right\rangle \left|klm_l\right\rangle \otimes \left|sm_s\right\rangle, \tag{B.13}$$

with the new completeness relation

$$\sum_{l,s} \sum_{j=|l-s|}^{|l+s|} \sum_{m} \int dk\, k^2 \left|k(ls)jm\right\rangle\left\langle k(ls)jm\right| = \mathbb{1}. \tag{B.14}$$

B.2 Irreducible Spherical Tensor Operators

In classical theoretical physics, a (Cartesian) tensor $T_{i_1,\ldots,i_n}$ of rank n is defined via its transformation behavior under the matrix representation of the orthogonal group $O(3)$, which describes the action of rotations and reflections on the real three-dimensional vector space $\mathbb{R}^3$:

$$T'_{i_1,\ldots,i_n} = \sum_{k_1,\ldots,k_n} R_{i_1k_1}\ldots R_{i_nk_n}T_{k_1,\ldots,k_n}, \quad R \in O(3). \tag{B.15}$$

As it turns out in (relativistic) quantum mechanics, we need to describe rotations by $SU(2)$, the covering group of $O(3)$, due to the non-classical spin degree of freedom, which introduces fermions into the particle spectrum as $SU(2)$'s half-integer representations.

On the abstract Hilbert space of quantum mechanics, the rotation group is represented by unitary operators. In the classical limit, the transformation behaviour of the classical tensor has to be reproduced by the expectation value of the corresponding tensor operator, and since this has to be true for arbitrary states, we find, e.g., for a vector operator

$$\mathrm{U}^\dagger(R)\mathrm{v}_i\mathrm{U}(R) = \sum_j R_{ij}\mathrm{v}_j. \tag{B.16}$$

By looking at an infinitesimal rotation, one finds the commutator

$$\left[\mathrm{v}_k,\mathrm{j}_l\right] = i\varepsilon_{klm}\mathrm{v}_k \tag{B.17}$$

(see, e.g., [65]), which is now understood as the *defining property* of a quantum-mechanical vector operator. For a scalar operator, one obviously has

$$\mathrm{U}^\dagger(R)\,\mathrm{s}\,\mathrm{U}(R) = \mathrm{s} \quad \Longrightarrow \quad \left[\mathrm{s},\mathbf{j}\right] = 0, \tag{B.18}$$

and in the case of higher tensor operators, the commutators can be found by looking at corresponding dyadic products of vector operators, e.g.,

$$\left[\mathrm{t}_{ik},\mathrm{j}_l\right] = i\varepsilon_{klm}\mathrm{t}_{im} + i\varepsilon_{iln}\mathrm{t}_{nk}. \tag{B.19}$$

This provides us with a consistent prescription to define tensor operators of arbitrary rank. However, as one already notices in classical physics, Cartesian coordinates are not always the ideal choice for calculations. Objects like the quadrupole tensor of electrodynamics, for example, can be represented more economically in a spherical basis,

where it is manifest that it only has five independent components, a fact that is obscured at first by writing it as a general 3×3-matrix in a Cartesian basis. The choice of spherical coordinates particularly facilitates calculations for systems with rotational symmetries, so a closer look at the rotation group is in order.

One of the most important properties of $SU(2)$ is its compactness, which can easily be deduced from the fact that the Euler angles parametrizing an arbitrary rotation are elements of finite intervals. A theorem of group theory [44] states that finite-dimensional unitary representations exist for any compact group, which implies that we can decompose any (reducible) infinite-dimensional representation of $\mathcal{H}$ into a direct sum of irreducible representations. The latter are characterized by the eigenvalues of the group's Casimir operators, i.e., its invariants. $SU(2)$'s basic Casimir operator is $\mathbf{j}^2$, thus the decomposition can be done by using a complete set of angular momentum eigenstates as a basis for $\mathcal{H}$. This is essentially a *Clebsch-Gordan decomposition*, which is familiar from angular momentum coupling. In general terms, a tensor product of irreducible representations is usually reducible, so it can be decomposed into irreducible representations by switching to an appropriate new basis, e.g., a basis of coupled states in angular momentum theory.

The decomposition of $\mathcal{H}$ has consequences for the operators defined on it, too. Since any non-singular operator t maps the Hilbert space onto itself, we can conclude that it is possible to decompose t's representation as an infinite-dimensional matrix acting on $\mathcal{H}$. In the case of the rotation group, we arrive at the notion of an *irreducible spherical tensor operators of rank k*

$$\mathrm{t}_q^{(k)}, \quad q = -k, \ldots, k, \tag{B.20}$$

where q, commonly referred to as the magnetic quantum number, is the generalization of m for angular momentum operators. When represented as matrices in a basis of angular momentum eigenstates, these operators show block structures due to the fact that a rank-k operator can at most connect states with $\Delta j \leq k$. In practice, one usually has additional selection rules due to parity and other internal symmetries, which restrict the operators and depopulate their matrix representations even further, and therefore calculations are greatly facilitated.

In general, two irreducible spherical tensor operators of ranks k_1 and k_2 which act on the same Hilbert space can be coupled to an irreducible tensor operator of rank k by using the Clebsch-Gordan coefficients:

$$\left\{ \mathrm{a}^{(k_1)}\mathrm{b}^{(k_2)} \right\}_q^{(k)} = \sum_{q_1,q_2} \left\langle\, k_1 q_1, k_2 q_2 \big| kq \,\right\rangle \mathrm{a}_{q_1}^{(k_1)} \mathrm{b}_{q_2}^{(k_2)} . \tag{B.21}$$

In some cases, we need a hermitized coupled product of tensor operators acting on the same Hilbert space. It will be denoted by the shorthand expression

$$(\mathrm{ab})_q^{(k)} = \frac{1}{2} \left(\left\{ \mathrm{a}^{(k_1)}\mathrm{b}^{(k_2)} \right\}_q^{(k)} + \left\{ \mathrm{b}^{(k_2)}\mathrm{a}^{(k_1)} \right\}_q^{(k)} \right) \tag{B.22}$$

For two spherical tensor operators of rank 1 which act on different Hilbert spaces, Eq. (B.21) defines a scalar product by

$$\mathrm{a}^{(1)} \cdot \mathrm{t}^{(1)} = -\sqrt{3} \left\{ \mathrm{a}^{(1)} \otimes \mathrm{t}^1 \right\}^{(0)} , \tag{B.23}$$

and for rank 2 tensor operators one finds

$$\mathrm{a}^{(2)} \cdot \mathrm{t}^{(2)} = -\sqrt{5} \left\{ \mathrm{a}^{(2)} \otimes \mathrm{t}^2 \right\}^{(0)} . \tag{B.24}$$

Here, we indicate that the operators act on different spaces by explicitly writing out the tensor product sign $\otimes$. Concrete examples are the spin-orbit and tensor operators. For the former, the scalar product reads

$$\mathbf{l} \cdot \mathbf{s} = \mathrm{l}^{(1)} \cdot \mathrm{s}^{(1)} = -\sqrt{3} \left\{ \mathrm{l}^{(1)} \otimes \mathrm{s}^{(1)} \right\}^{(0)} , \tag{B.25}$$

and the latter is given by

$$\begin{aligned} \mathrm{s}_{12}(\mathbf{a}, \mathbf{b}) &= \frac{3}{2} \left[(\boldsymbol{\sigma}_1 \cdot \mathbf{a})(\boldsymbol{\sigma}_2 \cdot \mathbf{b}) - (\boldsymbol{\sigma}_1 \cdot \boldsymbol{\sigma}_2)(\mathbf{a} \cdot \mathbf{b}) + \mathbf{a} \leftrightarrow \mathbf{b} \right] \\ &= 3 \left\{ \mathrm{a}^{(1)} \mathrm{b}^{(1)} \right\}^{(2)} \cdot \mathrm{s}^{(2)} = 3\sqrt{5} \left\{ (\mathrm{ab})^{(2)} \otimes \mathrm{s}^{(2)} \right\}^{(0)} , \end{aligned} \tag{B.26}$$

where the operators $\mathrm{s}^{(1)}$ and $\mathrm{s}^{(2)}$ act on spin space.

B.3 Decomposition of Reducible Tensor Operators

In this section we list decomposition formulas for reducible tensor operators occuring in the correlated and uncorrelated NN interactions. The derivation was performed in [6], using the irreducible spherical tensor representation of the operators.

$$(\mathbf{l} \cdot \mathbf{s})^2 = \frac{2}{3} \mathrm{l}^2 \Pi_{S=1} - \frac{1}{2} \mathbf{l} \cdot \mathbf{s} + \frac{1}{6} \mathrm{s}_{12}(\mathbf{l}, \mathbf{l}) \tag{B.27}$$

$$\bar{\mathrm{s}}_{12}(\mathbf{p}_\Omega, \mathbf{p}_\Omega) = 2\mathrm{r}^2 \mathrm{s}_{12}(\mathbf{p}_\Omega, \mathbf{p}_\Omega) + \mathrm{s}_{12}(\mathbf{l}, \mathbf{l}) - \frac{1}{2} \mathrm{s}_{12}(\hat{\mathbf{r}}, \hat{\mathbf{r}}) \tag{B.28}$$

$$\bar{\mathrm{s}}_{12}(\mathbf{r}, \mathbf{p}_\Omega)^2 = 6(\mathrm{l}^2 + 3)\Pi_{S=1} + \frac{45}{2} \mathbf{l} \cdot \mathbf{s} + \frac{3}{2} \mathrm{s}_{12}(\mathbf{l}, \mathbf{l}) \tag{B.29}$$

The explicit dependencies of the tensor operators on the *radial coordinate* are cancelled by corresponding factors of $\mathbf{p}_\Omega$ (see (A.7) or (B.40)), hence they only act on directional variables in coordinate space.

B.4 Algebra of Cartesian Tensor Operators

This section lists the algebraic relations needed to calculate tensor-correlated interactions up to next-to-next-to-leading order in angular momentum, as derived in Ref. [6]. Recall

$$\bar{\mathrm{s}}_{12}(\mathbf{p}_\Omega, \mathbf{p}_\Omega) = 2\mathrm{r}^2 \mathrm{s}_{12}(\mathbf{p}_\Omega, \mathbf{p}_\Omega) + \mathrm{s}_{12}(\mathbf{l}, \mathbf{l}) - \frac{1}{2} \mathrm{s}_{12}(\hat{\mathbf{r}}, \hat{\mathbf{r}}) . \tag{B.30}$$

$$\left[\mathrm{s}_{12}(\mathbf{r},\mathbf{p}_\Omega),\mathrm{s}_{12}\right] = -24i\,\Pi_{S=1} - 18i\,\mathbf{l}\cdot\mathbf{s} + 3i\,\mathrm{s}_{12} \tag{B.31}$$

$$\left[\mathrm{s}_{12}(\mathbf{r},\mathbf{p}_\Omega),\mathbf{l}\cdot\mathbf{s}\right] = -i\,\bar{\mathrm{s}}_{12}(\mathbf{p}_\Omega,\mathbf{p}_\Omega) \tag{B.32}$$

$$\left[\mathrm{s}_{12}(\mathbf{r},\mathbf{p}_\Omega),\mathbf{l}^2\right] = 2i\,\bar{\mathrm{s}}_{12}(\mathbf{p}_\Omega,\mathbf{p}_\Omega) \tag{B.33}$$

$$\left[\mathrm{s}_{12}(\mathbf{r},\mathbf{p}_\Omega),\mathrm{s}_{12}(\mathbf{l},\mathbf{l})\right] = 7i\,\bar{\mathrm{s}}_{12}(\mathbf{p}_\Omega,\mathbf{p}_\Omega) \tag{B.34}$$

$$\left[\mathrm{s}_{12}(\mathbf{r},\mathbf{p}_\Omega),\bar{\mathrm{s}}_{12}(\mathbf{p}_\Omega,\mathbf{p}_\Omega)\right] = i(96\,\mathbf{l}^2 + 108)\Pi_{S=1} + i(36\,\mathbf{l}^2 + 153)\mathbf{l}\cdot\mathbf{s}$$
$$+ 15i\,\mathrm{s}_{12}(\mathbf{l},\mathbf{l}) \tag{B.35}$$

$$\left[\mathrm{s}_{12}(\mathbf{r},\mathbf{p}_\Omega),\mathbf{l}^2\mathbf{l}\cdot\mathbf{s}\right] = -3i\bar{\mathrm{s}}_{12}(\mathbf{p}_\Omega,\mathbf{p}_\Omega)$$
$$-\frac{i}{2}\left(\mathbf{l}^2\bar{\mathrm{s}}_{12}(\mathbf{p}_\Omega,\mathbf{p}_\Omega) + \bar{\mathrm{s}}_{12}(\mathbf{p}_\Omega,\mathbf{p}_\Omega)\mathbf{l}^2\right) \tag{B.36}$$

$$\left[\mathrm{s}_{12}(\mathbf{r},\mathbf{p}_\Omega),\mathbf{l}^2\bar{\mathrm{s}}_{12}(\mathbf{p}_\Omega,\mathbf{p}_\Omega)\right] = i(144\,\mathbf{l}^4 + 600\,\mathbf{l}^2 + 324)\Pi_{S=1}$$
$$+ i(36\,\mathbf{l}^4 + 477\,\mathbf{l}^2 + 477)\mathbf{l}\cdot\mathbf{s} + i(27\,\mathbf{l}^2 + 51)\mathrm{s}_{12}(\mathbf{l},\mathbf{l}) \tag{B.37}$$

B.5   Reduced Matrix Elements of Tensor Operators

B.5.1   The Wigner-Eckart Theorem

The significance of the *Wigner-Eckart theorem*

$$\left\langle n'j'm'\right|\mathrm{t}_q^{(k)}\left|njm\right\rangle = (-1)^{2k}\left\langle jmkq|j'm'\right\rangle\frac{\left\langle n'j'\right|\!\left|\,\mathrm{t}^{(k)}\,\right|\!\left|nj\right\rangle}{\sqrt{2j+1}} \tag{B.38}$$

lies in the way it separates the geometrical and dynamical parts of an expectation value. The Clebsch-Gordan coefficient reflects the orientation of the system with respect to a chosen quantization axis (usually the z-axis), which is completely specified by the quantum numbers m, m', and q; the reduced matrix element, on the other hand, contains the information about the dynamics of the tensor operator, and is completely independent of the magnetic quantum numbers.

B.5.2   Reduced Matrix Elements of Basic Operators

Coordinate Space Operators

The reduced matrix elements of the basic operators $\mathbf{r}$, $\mathbf{p}_\Omega$, and $\mathbf{l}$ in angular momentum eigenstates are needed to calculate the matrix elements of the various tensor operators (see tables B.1 and B.2). Since all of the above operators are vector operators, they can only connect states with $\Delta l = \pm 1$, while all other matrix elements vanish. It should be noted that a slightly different prescription for the reduced matrix elements is used in Ref. [6, 7].

$$\left\langle l'\right|\!\left|\,\mathrm{r}_q^{(1)}\,\right|\!\left|l\right\rangle = (\sqrt{l+1}\,\delta_{l',l+1} - \sqrt{l}\,\delta_{l',l-1})r\,, \tag{B.39}$$

$$\left\langle l'\right|\!\left|\,\mathrm{p}_{\Omega,q}^{(1)}\,\right|\!\left|l\right\rangle = \left((l+1)^{3/2}\delta_{l',l+1} + l^{3/2}\delta_{l',l-1}\right)\frac{i}{r} \tag{B.40}$$

and

$$\langle\, l'\,||\, \mathrm{l}_q^{(1)}\, ||l\,\rangle = \sqrt{l(l+1)(2l+1)}\delta_{ll'}\,. \tag{B.41}$$

Spin Operators

In spin space, we need the matrix elements of the total spin operator

$$\mathrm{s}^{(1)} = \frac{1}{2}\left(\sigma^{(1)}\otimes\mathbb{1} + \mathbb{1}\otimes\sigma^{(1)}\right)\,, \tag{B.42}$$

and the rank 2 tensor operator which is needed to construct the cartesian tensor operators s_{12}:

$$\mathrm{s}^{(2)} = \left\{\mathrm{s}^{(1)}\mathrm{s}^{(1)}\right\}^{(2)}\,. \tag{B.43}$$

The only non-vanishing matrix elements are between $s=1$ states:

$$\langle\, 1\,||\, \mathrm{s}^{(1)}\, ||1\,\rangle = \sqrt{6} \tag{B.44}$$

and

$$\langle\, 1\,||\, \mathrm{s}^{(2)}\, ||1\,\rangle = 2\sqrt{5}\,. \tag{B.45}$$

B.5.3 Reduced Matrix Elements of Cartesian Tensor Operators

The reduced matrix element of a general product like (B.21) can be calculated with the help of the Wigner $6j$-symbols [66]:

$$\langle\, l'\,||\, \{\mathrm{a}^{(k_1)}\mathrm{b}^{(k_2)}\}^{(k)}\, ||l\,\rangle =$$
$$(-1)^{l'+l-k}\sqrt{2k+1}\sum_{l''}\begin{Bmatrix} k_1 & k_2 & k \\ l & l' & l \end{Bmatrix}\langle\, l'\,||\, \mathrm{a}^{(k_1)}\, ||l''\,\rangle\langle\, l''\,||\, \mathrm{b}^{(k_2)}\, ||l\,\rangle\,. \tag{B.46}$$

As an example, we derive the matrix elements of $\mathrm{s}_{12}(\mathbf{r},\mathbf{p}_\Omega)$, which is used to construct the generator of tensor correlations g_Ω. In coordinate space, the matrix elements of $(\mathrm{rp}_\Omega)^{(2)}$ need to be evaluated:

$$\langle\, l'\,||\, \{\mathrm{rp}_\Omega\}^{(2)}\, ||l\,\rangle =(-1)^{l'+l-2}\sqrt{5}\sum_{l''}\begin{Bmatrix} 1 & 1 & 2 \\ l & l' & l'' \end{Bmatrix}\langle\, l'\,||\, \mathrm{r}^{(1)}\, ||l''\,\rangle\langle\, l''\,||\, \mathrm{p}_\Omega^{(1)}\, ||l\,\rangle$$

$$=(-1)^{l'+l-2}\sqrt{5}\sum_{l''}\begin{Bmatrix} 1 & 1 & 2 \\ l & l' & l'' \end{Bmatrix}\left(\sqrt{l''+1}\delta_{l',l''+1}-\sqrt{l''}\delta_{l',l''-1}\right)r$$

$$\times\frac{i}{r}\left((l+1)^{3/2}\delta_{l'',l+1}-(l)^{3/2}\delta_{l'',l-1}\right)$$

$$=i\sqrt{5}\left(\begin{Bmatrix} 1 & 1 & 2 \\ l & l' & l+1 \end{Bmatrix}\left(\sqrt{l+2}(l+1)^{3/2}\delta_{l',l+2}-(l+1)^2\delta_{ll'}\right)\right.$$

$$\left.+\begin{Bmatrix} 1 & 1 & 2 \\ l & l' & l-1 \end{Bmatrix}\left(l^2\delta_{ll'}-\sqrt{l-1}l^{3/2}\delta_{l',l-2}\right)\right)\,, \tag{B.47}$$

where the exponent $(-1)^{l'+l-2}$ is always even due to the Kronecker deltas, i.e., the factor is always 1. A similar calculation yields

$$\left\langle l'\middle|\middle| \{p_\Omega r\}^{(2)} \middle|\middle| l \right\rangle = i\sqrt{5}\left(\begin{Bmatrix} 1 & 1 & 2 \\ l & l' & l+1 \end{Bmatrix} \left(\sqrt{l+1}(l+2)^{3/2}\delta_{l',l+2} + (l+1)^2\delta_{ll'} \right) \right.$$
$$\left. - \begin{Bmatrix} 1 & 1 & 2 \\ l & l' & l-1 \end{Bmatrix} \left(l^2\delta_{ll'} + \sqrt{l}(l-1)^{3/2}\delta_{l',l-2} \right) \right), \quad \text{(B.48)}$$

hence

$$\left\langle l'\middle|\middle| (rp_\Omega)^{(2)} \middle|\middle| l \right\rangle = \frac{i}{2}\sqrt{5}\left(\begin{Bmatrix} 1 & 1 & 2 \\ l & l' & l+1 \end{Bmatrix} (2l+3)\sqrt{(l+1)(l+2)}\delta_{l',l+2} \right.$$
$$\left. - \begin{Bmatrix} 1 & 1 & 2 \\ l & l' & l-1 \end{Bmatrix} (2l-1)\sqrt{(l-1)l}\delta_{l',l-2} \right). \quad \text{(B.49)}$$

Using

$$\begin{Bmatrix} 1 & 1 & 2 \\ l & l+2 & l+1 \end{Bmatrix} = \frac{1}{\sqrt{5}}\frac{1}{\sqrt{2l+3}} \quad \text{and} \quad \begin{Bmatrix} 1 & 1 & 2 \\ l & l-2 & l+1 \end{Bmatrix} = \frac{1}{\sqrt{5}}\frac{1}{\sqrt{2l-1}}, \quad \text{(B.50)}$$

one finally has

$$\left\langle l'\middle|\middle| (rp_\Omega)^{(2)} \middle|\middle| l \right\rangle$$
$$= \frac{i}{2}\left(\sqrt{(l+1)(l+2)(2l+3)}\delta_{l',l+2} - \sqrt{(l-1)l(2l-1)}\delta_{l',l-2} \right). \quad \text{(B.51)}$$

The reduced matrix element of a scalar product between two rank-k tensor operators $a^{(k)}$ in coordinate and $s^{(k)}$ in spin space can be calculated with [66]

$$\left\langle (l'1)j\middle|\middle| r^{(k)} \cdot s^{(k)} \middle|\middle| (l1)j \right\rangle = (-1)^{j+l+1}\sqrt{2j+1}\begin{Bmatrix} l' & l & k \\ 1 & 1 & j \end{Bmatrix}\left\langle l'\middle|\middle| r^{(k)} \middle|\middle| l \right\rangle\left\langle 1\middle|\middle| s^{(k)} \middle|\middle| 1 \right\rangle. \quad \text{(B.52)}$$

Note that the formulae given for the 'basic' reduced matrix elements are specified in an uncoupled basis, so the $6j$-symbol is needed to switch to the $(ls)j$-coupling, i.e., the appropriate irreducible representation for such scalar products. With

$$\begin{Bmatrix} j+1 & j-1 & 2 \\ 1 & 1 & j \end{Bmatrix} = \begin{Bmatrix} j-1 & j+1 & 2 \\ 1 & 1 & j \end{Bmatrix} = \frac{1}{\sqrt{5}}\frac{(-1)^{2j}}{\sqrt{2j+1}} \quad \text{(B.53)}$$

one obtains

$$\left\langle (j\pm 1,1)j\middle|\middle| s_{12}(\mathbf{r},\mathbf{p}_\Omega) \middle|\middle| (j\mp 1,1)j \right\rangle = \pm 3i\sqrt{j(j+1)(2j+1)}, \quad \text{(B.54)}$$

for the only nonzero matrix elements.

For convenience, the non-vanishing reduced matrix elements of $s_{12}(\mathbf{r},\mathbf{p}_\Omega)$ in the lowest partial waves are listed together with those of the various interaction operators in tables B.1 and B.2. In the tables, the shorthand notation

$$((l's)j\middle|\middle| o \middle|\middle| (ls)j) \equiv \frac{\left\langle (l's)j\middle|\middle| o \middle|\middle| (ls)j \right\rangle}{\sqrt{2j+1}} \quad \text{(B.55)}$$

partial wave	$\big((ls)j\big\|\circ\big\|(ls)j\big)$	$\mathbf{l}^2$	$\mathbf{l}\cdot\mathbf{s}$	$\mathbf{l}^2\mathbf{l}\cdot\mathbf{s}$	s_{12}	$\mathrm{s}_{12}(\mathbf{l},\mathbf{l})$
$^1P_1$	$\big((10)1\big\|\circ\big\|(10)1\big)$	2	0	0	0	0
$^3P_0$	$\big((11)0\big\|\circ\big\|(11)0\big)$	2	-2	-4	-4	10
$^3P_1$	$\big((11)1\big\|\circ\big\|(11)1\big)$	2	-1	-2	2	-5
$^3P_2$	$\big((11)2\big\|\circ\big\|(11)2\big)$	2	1	2	$-\frac{2}{5}$	1
$^1D_2$	$\big((20)2\big\|\circ\big\|(20)2\big)$	6	0	0	0	0
$^3D_1$	$\big((21)1\big\|\circ\big\|(21)1\big)$	6	-3	-18	-2	21
$^3D_2$	$\big((21)2\big\|\circ\big\|(21)2\big)$	6	-1	-6	2	-21
$^3D_3$	$\big((21)3\big\|\circ\big\|(21)3\big)$	6	2	12	$-\frac{4}{7}$	6
$^1F_3$	$\big((30)3\big\|\circ\big\|(30)3\big)$	12	0	0	0	0
$^3F_2$	$\big((31)2\big\|\circ\big\|(31)2\big)$	12	-4	-48	$-\frac{8}{5}$	36
$^3F_3$	$\big((31)3\big\|\circ\big\|(31)3\big)$	12	-1	-12	2	-45
$^3F_4$	$\big((31)4\big\|\circ\big\|(31)4\big)$	12	3	36	$-\frac{2}{3}$	15
$^1G_4$	$\big((40)4\big\|\circ\big\|(40)4\big)$	20	0	0	0	0
$^3G_3$	$\big((41)3\big\|\circ\big\|(41)3\big)$	20	-5	-100	$-\frac{10}{7}$	55
$^3G_4$	$\big((41)4\big\|\circ\big\|(41)4\big)$	20	-1	-20	2	-77
$^3G_5$	$\big((41)5\big\|\circ\big\|(41)5\big)$	20	4	80	$-\frac{8}{11}$	28
$^1H_5$	$\big((50)5\big\|\circ\big\|(50)5\big)$	30	0	0	0	0
$^3H_4$	$\big((51)4\big\|\circ\big\|(51)4\big)$	30	-6	-180	$-\frac{4}{3}$	78
$^3H_5$	$\big((51)5\big\|\circ\big\|(51)5\big)$	30	-1	-30	2	-117
$^3H_6$	$\big((51)6\big\|\circ\big\|(51)6\big)$	30	5	150	$-\frac{10}{13}$	45
$^1I_6$	$\big((60)6\big\|\circ\big\|(60)6\big)$	42	0	0	0	0
$^3I_5$	$\big((61)5\big\|\circ\big\|(61)5\big)$	42	-7	-294	$-\frac{14}{11}$	105
$^3I_6$	$\big((61)6\big\|\circ\big\|(61)6\big)$	42	-1	-42	2	-165
$^3I_7$	$\big((61)7\big\|\circ\big\|(61)7\big)$	42	6	252	$-\frac{4}{5}$	66
$^1J_7$	$\big((70)7\big\|\circ\big\|(70)7\big)$	56	0	0	0	0
$^3J_6$	$\big((71)6\big\|\circ\big\|(71)6\big)$	56	-8	-448	$-\frac{16}{13}$	136
$^3J_7$	$\big((71)7\big\|\circ\big\|(71)7\big)$	56	-1	-56	2	-221
$^3J_8$	$\big((71)8\big\|\circ\big\|(71)8\big)$	56	7	392	$-\frac{14}{17}$	91

Table B.1: Non-vanishing diagonal reduced matrix elements. The matrix elements of s_{12} are misprinted in Tab. B.4 of Ref. [6].

partial wave	$\big((l's')j'\big\|\circ\big\|(ls)j\big)$	s_{12}	$\bar{\mathrm{s}}_{12}(\mathbf{p}_\Omega,\mathbf{p}_\Omega)$	$\mathbf{l}^2\,\bar{\mathrm{s}}_{12}(\mathbf{p}_\Omega,\mathbf{p}_\Omega)$	$\mathrm{s}_{12}(\mathbf{r},\mathbf{p}_\Omega)$
$^3S_1-{}^3D_1$	$\big((01)1\big\|\circ\big\|(21)1\big)$	$2\sqrt{2}$	$-9\sqrt{2}$	$-27\sqrt{2}$	$-3\,i\,\sqrt{2}$
$^3P_2-{}^3F_2$	$\big((11)2\big\|\circ\big\|(31)2\big)$	$\frac{6\sqrt{6}}{5}$	$-15\sqrt{6}$	$-105\sqrt{6}$	$-3\,i\,\sqrt{6}$
$^3D_3-{}^3G_3$	$\big((21)3\big\|\circ\big\|(41)3\big)$	$\frac{12\sqrt{3}}{7}$	$-42\sqrt{3}$	$-546\sqrt{3}$	$-6\,i\,\sqrt{3}$
$^3F_4-{}^3H_4$	$\big((31)4\big\|\circ\big\|(51)4\big)$	$\frac{4\sqrt{5}}{3}$	$-54\sqrt{5}$	$-1134\sqrt{5}$	$-6\,i\,\sqrt{5}$
$^3G_5-{}^3I_5$	$\big((41)5\big\|\circ\big\|(61)5\big)$	$\frac{6\sqrt{30}}{11}$	$-33\sqrt{30}$	$-1023\sqrt{30}$	$-3\,i\,\sqrt{30}$
$^3H_6-{}^3J_6$	$\big((51)6\big\|\circ\big\|(71)6\big)$	$\frac{6\sqrt{42}}{13}$	$-39\sqrt{42}$	$-1677\sqrt{42}$	$-3\,i\,\sqrt{42}$

Table B.2: Non-vanishing off-diagonal reduced matrix elements.

is used (cf. Sect. 2.3), which allows for a direct comparison with Ref. [6]. The subscript h indicates that the operator

$$\left(\mathbf{l}^2\,\bar{\mathrm{s}}_{12}(\mathbf{p}_\Omega, \mathbf{p}_\Omega)\right)_h \equiv \frac{1}{2}(\mathbf{l}^2\,\bar{\mathrm{s}}_{12}(\mathbf{p}_\Omega, \mathbf{p}_\Omega) + \bar{\mathrm{s}}_{12}(\mathbf{p}_\Omega, \mathbf{p}_\Omega)\,\mathbf{l}^2)\,, \qquad (\text{B.56})$$

is hermitized, which is necessary since $\mathbf{l}^2$ and $\bar{\mathrm{s}}_{12}(\mathbf{p}_\Omega, \mathbf{p}_\Omega)$ do not commute.

Appendix C

Correlators

In this appendix, the parameters of the correlators used in this work are presented for reference. They were determined by T. Neff in Refs. [6, 7].

C.1 Parametrizations

The central correlation functions $R_+(r)$ will be given in terms of the parametrizations

$$R_+(r) = r + \alpha \left(\frac{r}{\beta} \right)^\eta \exp\left(- \exp \frac{r}{\beta} \right), \tag{C.1}$$

and

$$R_+(r) = r + \alpha \gamma^\eta \left(1 - \exp\left\{ - \left(\frac{r}{\gamma} \right)^\eta \right\} \right) \exp\left(- \exp \frac{r}{\beta} \right). \tag{C.2}$$

The tensor correlation functions are parametrized by

$$\vartheta(r) = \alpha \gamma^\eta \left(1 - \exp\left\{ - \left(\frac{r}{\beta} \right)^\eta \right\} \right) \exp\left(- \frac{r}{\beta} \right) \tag{C.3}$$

and

$$\vartheta(r) = \alpha \gamma^\eta \left(1 - \exp\left\{ - \left(\frac{r}{\beta} \right)^\eta \right\} \right) \exp\left(- \exp \frac{r}{\beta} \right). \tag{C.4}$$

As outlined in sect. 2.5, parameter sets are obtained by

   (i) minimizing the energy in the two-nucleon system (min) and

   (ii) minimizing the ^{4}He binding energy (min-^{4}He),

where greek letters in the tables indicate different constraints on the correlation range via the following measures:

$$\int dr\, r^2 \left(R_+(r) - r \right) \stackrel{!}{=} \begin{cases} 0.1 \text{ fm}^4 & \alpha \\ 0.2 \text{ fm}^4 & \beta \end{cases}, \quad \int dr\, r^2\, \vartheta(r) \stackrel{!}{=} \begin{cases} 0.1 \text{ fm}^3 & \alpha \\ 0.2 \text{ fm}^3 & \beta \\ 0.5 \text{ fm}^3 & \gamma \end{cases}. \tag{C.5}$$

C.2   Argonne-V18 Potential

Correlator	ST	Type	$\alpha\,[\,\mathrm{fm}]$	$\beta\,[\,\mathrm{fm}]$	$\gamma\,[\,\mathrm{fm}]$	η
min^{α}	00	C.2	1.804	1.272	0.424	1
min^{β}	00	C.2	2.306	1.603	0.307	1
min	01	C.1	1.379	0.885		0.372
min	10	C.1	1.296	0.849		0.419
min	11	C.2	3.102	1.374	0.187	1
min–^{4}He	01	C.1	1.380	0.981		0.336
min–^{4}He	10	C.1	1.372	0.907		0.419

Table C.1: Parameters of the central correlation functions $R_{+}(r)$ for the Argonne V18 potential.

Correlator	ST	Type	α	$\beta\,[\,\mathrm{fm}]$	$\gamma\,[\,\mathrm{fm}]$	η
min^{α}	10	C.4	0.530	1.298	1000	1
min^{β}	10	C.4	0.579	1.717	1.590	1
min^{γ}	10	C.4	0.786	2.665	0.488	1
min	10	C.3	0.341	2.153	0.407	1
min^{α}	11	C.4	-0.081	3.477	0.420	1
min	11	C.3	-0.027	1.685	0.864	1
min^{α}–^{4}He	10	C.4	0.590	1.266	100	1
min^{β}–^{4}He	10	C.4	0.520	1.554	100	1
min^{γ}–^{4}He	10	C.4	0.621	2.446	0.883	1
min–^{4}He	10	C.3	0.361	4.017	0.303	1

Table C.2: Parameters of the tensor correlation functions $\vartheta(r)$ for the Argonne V18 potential.

C.3   Bonn-A Potential

Correlator	ST	Type	$\alpha\,[\,\mathrm{fm}]$	$\beta\,[\,\mathrm{fm}]$	$\gamma\,[\,\mathrm{fm}]$	η
min^{α}	00	C.2	0.250	1.406	1000	2
min^{β}	00	C.2	0.348	1.797	1.449	2
min	01	C.1	1.199	0.808		0.734
min	10	C.1	1.132	0.779		0.848
min	11	C.1	0.658	1.198		0.798
min–^{4}He	01	C.1	1.344	0.899		0.699
min–^{4}He	10	C.1	1.256	0.853		0.811

Table C.3: Parameters of the central correlation functions $R_{+}(r)$ for the Bonn-A OBEPR potential.

Correlator	ST	Type	α	$\beta\,[\,\mathrm{fm}]$	$\gamma\,[\,\mathrm{fm}]$	η
min^α	10	C.4	0.412	1.287	4.994	2
min^β	10	C.4	0.408	1.834	1.215	2
min^γ	10	C.4	0.420	2.745	0.925	2
min	10	C.3	0.170	2.372	0.863	2
min^α	11	C.4	-0.032	3.353	1.106	3
min	11	C.3	-0.014	1.699	1.197	3
min^α–^{4}He	10	C.4	0.468	1.241	100	2
min^β–^{4}He	10	C.4	0.398	1.472	100	2
min^γ–^{4}He	10	C.4	0.383	2.551	1.109	2
min–^{4}He	10	C.3	0.152	7.201	0.741	2

Table C.4: Parameters of the tensor correlation functions $\vartheta(r)$ for the Bonn-A OBEPR potential.

Appendix D

FMD Interactions

In this appendix we provide the parameters of the fitted interactions used for calculations in the FMD basis as a reference. The Coulomb interaction is hard-coded in the FMD code and therefore *not* contained in the parameter sets. Details on the implementation of interaction matrix elements can be found in [40].

D.1 Fit Model

The radial dependencies of the interaction terms are parametrized by Gaussians

$$G_\kappa(x) = \exp\left(-\frac{x^2}{2\kappa}\right) \tag{D.1}$$

of range $\sqrt{\kappa}$. The subscripts σ, τ and $\sigma\tau$ indicate the spin and isospin parts of the different operators, where

$$
\begin{aligned}
\sigma : & \quad \boldsymbol{\sigma}_1 \cdot \boldsymbol{\sigma}_2 \\
\tau : & \quad \boldsymbol{\tau}_1 \cdot \boldsymbol{\tau}_2 \\
\sigma\tau : & \quad (\boldsymbol{\sigma}_1 \cdot \boldsymbol{\sigma}_2)(\boldsymbol{\tau}_1 \cdot \boldsymbol{\tau}_2) \,.
\end{aligned}
$$

Central Interactions

Central potentials in the FMD interaction file include both the correlated central interaction and the local potential part of the correlated kinetic energy.

$$v : \quad \widetilde{v}(r) + \widetilde{w}(r) \simeq \gamma G_\kappa(r) \tag{D.2}$$

Tensor Interactions

$$v^t : \quad \widetilde{v}^t(r) \simeq \gamma r^2 G_\kappa(r) \tag{D.3}$$

Spin-Orbit Interactions

$$v^{ls} : \quad \widetilde{v}_{ls}(r) \simeq \gamma G_\kappa(r) \tag{D.4}$$

Momentum-Dependent Interactions

Momentum-dependent potential terms are fits of the correlated radial and gradient masses $\widetilde{\mu}_{r*}(r)$ and $\widetilde{\mu}_{\boldsymbol{\nabla}}(r)$ introduced for the FMD representation of the interactions. Additional terms of this type are due to the 'FMD-transformed' correlated $\mathbf{p}^2$ or $\mathbf{l}^2$ parts (see section 4.1).

$$v^{p_r^2}: \quad \frac{1}{2\widetilde{\mu}_{r*}} \simeq \gamma r^2 G_\kappa(r) \tag{D.5}$$

$$v^{p^2}: \quad \frac{1}{2\widetilde{\mu}_{\boldsymbol{\nabla}}} \simeq \gamma G_\kappa(r) \tag{D.6}$$

D.2 Fitted Interactions

The fit of Argonne V18α was performed for this work, while the parameter files for Bonn-Aα and Bonn-Aγ were kindly provided by T. Neff [45].

D.2.1 Argonne V18α

	$\gamma[fm^{-1}]$	$\kappa[fm^2]$		$\gamma[fm^{-1}]$	$\kappa[fm^2]$
v^{p^2}	-0.204797700	0.010000000	v^{p^2}	-0.261667850	0.040000000
v^{p^2}	0.248098720	0.016000000	v^{p^2}	0.156125400	0.064000000
v^{p^2}	-0.523286180	0.128000000	v^{p^2}	0.325362330	0.256000000
v^{p^2}	0.106209950	0.512000000	v^{p^2}	-0.088362290	1.024000000
v^{p^2}	0.063260170	1.560000000	v^{p^2}	-0.029023420	2.048000000
v^{p^2}	0.004890130	3.072000000	v^{p^2}	0.000077710	4.096000000
$v_\sigma^{p^2}$	-0.041267760	0.010000000	$v_\sigma^{p^2}$	-0.048356290	0.040000000
$v_\sigma^{p^2}$	0.053805780	0.016000000	$v_\sigma^{p^2}$	0.030266680	0.064000000
$v_\sigma^{p^2}$	-0.147652330	0.128000000	$v_\sigma^{p^2}$	0.150501960	0.256000000
$v_\sigma^{p^2}$	0.014311810	0.512000000	$v_\sigma^{p^2}$	-0.025512440	1.024000000
$v_\sigma^{p^2}$	0.015994610	1.560000000	$v_\sigma^{p^2}$	-0.006575260	2.048000000
$v_\sigma^{p^2}$	0.000893480	3.072000000	$v_\sigma^{p^2}$	0.000168180	4.096000000
$v_\tau^{p^2}$	-0.031206960	0.010000000	$v_\tau^{p^2}$	-0.030863030	0.040000000
$v_\tau^{p^2}$	0.043155570	0.016000000	$v_\tau^{p^2}$	0.022282290	0.064000000
$v_\tau^{p^2}$	-0.179060090	0.128000000	$v_\tau^{p^2}$	0.268850530	0.256000000
$v_\tau^{p^2}$	-0.079585070	0.512000000	$v_\tau^{p^2}$	-0.036911880	1.024000000
$v_\tau^{p^2}$	0.034863090	1.560000000	$v_\tau^{p^2}$	-0.018463000	2.048000000
$v_\tau^{p^2}$	0.003880770	3.072000000	$v_\tau^{p^2}$	-0.000398520	4.096000000

Table D.1: Correlated AV18 potential, using central correlators min$^\alpha(ST = 00)$, min $(ST = 01, 10, 11)$ and tensor correlators min $^\alpha(ST = 10)$, min $(ST = 11)$ (cf. tables C.1 and C.2).

	$\gamma[fm^{-1}]$	$\kappa[fm^2]$		$\gamma[fm^{-1}]$	$\kappa[fm^2]$
$v_{\sigma\tau}^{p^2}$	-0.005572680	0.010000000	$v_{\sigma\tau}^{p^2}$	-0.003583380	0.040000000
$v_{\sigma\tau}^{p^2}$	0.008080280	0.016000000	$v_{\sigma\tau}^{p^2}$	-0.007648060	0.064000000
$v_{\sigma\tau}^{p^2}$	-0.054349650	0.128000000	$v_{\sigma\tau}^{p^2}$	0.103940600	0.256000000
$v_{\sigma\tau}^{p^2}$	-0.028623070	0.512000000	$v_{\sigma\tau}^{p^2}$	-0.013022990	1.024000000
$v_{\sigma\tau}^{p^2}$	0.011408640	1.560000000	$v_{\sigma\tau}^{p^2}$	-0.006349010	2.048000000
$v_{\sigma\tau}^{p^2}$	0.001299670	3.072000000	$v_{\sigma\tau}^{p^2}$	-0.000156710	4.096000000
$v^{p_r^2}$	1.440618900	0.010000000	$v^{p_r^2}$	0.638814520	0.040000000
$v^{p_r^2}$	0.707699380	0.016000000	$v^{p_r^2}$	0.118425390	0.064000000
$v^{p_r^2}$	-0.002340050	0.128000000	$v^{p_r^2}$	-0.019883660	0.256000000
$v^{p_r^2}$	0.070290750	0.512000000	$v^{p_r^2}$	0.013073400	1.024000000
$v^{p_r^2}$	-0.008385870	1.560000000	$v^{p_r^2}$	0.003371700	2.048000000
$v^{p_r^2}$	-0.000532390	3.072000000	$v^{p_r^2}$	0.000055950	4.096000000
$v_{\sigma}^{p_r^2}$	-1.114853970	0.010000000	$v_{\sigma}^{p_r^2}$	-0.368056240	0.040000000
$v_{\sigma}^{p_r^2}$	0.481761040	0.016000000	$v_{\sigma}^{p_r^2}$	0.287613090	0.064000000
$v_{\sigma}^{p_r^2}$	-0.321512420	0.128000000	$v_{\sigma}^{p_r^2}$	-0.199781720	0.256000000
$v_{\sigma}^{p_r^2}$	0.022729100	0.512000000	$v_{\sigma}^{p_r^2}$	0.003058130	1.024000000
$v_{\sigma}^{p_r^2}$	-0.001781940	1.560000000	$v_{\sigma}^{p_r^2}$	0.000638690	2.048000000
$v_{\sigma}^{p_r^2}$	-0.000094690	3.072000000	$v_{\sigma}^{p_r^2}$	0.000005370	4.096000000
$v_{\tau}^{p_r^2}$	-3.596230380	0.010000000	$v_{\tau}^{p_r^2}$	-1.026676180	0.040000000
$v_{\tau}^{p_r^2}$	2.422157780	0.016000000	$v_{\tau}^{p_r^2}$	0.813676140	0.064000000
$v_{\tau}^{p_r^2}$	-0.480467890	0.128000000	$v_{\tau}^{p_r^2}$	-0.098169560	0.256000000
$v_{\tau}^{p_r^2}$	0.063452220	0.512000000	$v_{\tau}^{p_r^2}$	-0.004162230	1.024000000
$v_{\tau}^{p_r^2}$	0.002505740	1.560000000	$v_{\tau}^{p_r^2}$	-0.001349670	2.048000000
$v_{\tau}^{p_r^2}$	0.000225900	3.072000000	$v_{\tau}^{p_r^2}$	-0.000046160	4.096000000
$v_{\sigma\tau}^{p_r^2}$	-1.312220130	0.010000000	$v_{\sigma\tau}^{p_r^2}$	-0.423072110	0.040000000
$v_{\sigma\tau}^{p_r^2}$	0.636624410	0.016000000	$v_{\sigma\tau}^{p_r^2}$	0.266226600	0.064000000
$v_{\sigma\tau}^{p_r^2}$	-0.271126300	0.128000000	$v_{\sigma\tau}^{p_r^2}$	-0.096026770	0.256000000
$v_{\sigma\tau}^{p_r^2}$	0.035195000	0.512000000	$v_{\sigma\tau}^{p_r^2}$	-0.001512510	1.024000000
$v_{\sigma\tau}^{p_r^2}$	0.000953160	1.560000000	$v_{\sigma\tau}^{p_r^2}$	-0.000467030	2.048000000
$v_{\sigma\tau}^{p_r^2}$	0.000078090	3.072000000	$v_{\sigma\tau}^{p_r^2}$	-0.000015170	4.096000000
v	-3.580775810	0.010000000	v	1.516114490	0.040000000
v	3.096871070	0.016000000	v	0.685958350	0.064000000

Table D.1: Correlated AV18 potential, using central correlators $\min^{\alpha}(ST = 00)$, $\min (ST = 01, 10, 11)$ and tensor correlators $\min{}^{\alpha}(ST = 10)$, $\min (ST = 11)$ (cf. tables C.1 and C.2).

	$\gamma[fm^{-1}]$	$\kappa[fm^2]$		$\gamma[fm^{-1}]$	$\kappa[fm^2]$
v	-0.745238900	0.128000000	v	0.321870820	0.256000000
v	-0.309266370	0.512000000	v	0.185505570	1.024000000
v	-0.299240760	1.560000000	v	0.168604330	2.048000000
v	-0.037206770	3.072000000	v	0.006824810	4.096000000
v_σ	0.057668100	0.010000000	v_σ	-1.453794170	0.040000000
v_σ	0.390036770	0.016000000	v_σ	1.320639150	0.064000000
v_σ	0.306871020	0.128000000	v_σ	-0.670471650	0.256000000
v_σ	0.104854490	0.512000000	v_σ	0.108789840	1.024000000
v_σ	-0.135477370	1.560000000	v_σ	0.083096380	2.048000000
v_σ	-0.019380430	3.072000000	v_σ	0.003786560	4.096000000
v_τ	-0.621547020	0.010000000	v_τ	-2.426321990	0.040000000
v_τ	1.381312840	0.016000000	v_τ	2.320184870	0.064000000
v_τ	-0.100413860	0.128000000	v_τ	-0.772757310	0.256000000
v_τ	0.362654460	0.512000000	v_τ	-0.094086350	1.024000000
v_τ	0.078761290	1.560000000	v_τ	-0.048586920	2.048000000
v_τ	0.011612680	3.072000000	v_τ	-0.002344940	4.096000000
$v_{\sigma\tau}$	-0.087987430	0.010000000	$v_{\sigma\tau}$	-1.451478690	0.040000000
$v_{\sigma\tau}$	0.397913900	0.016000000	$v_{\sigma\tau}$	1.311978010	0.064000000
$v_{\sigma\tau}$	0.239361790	0.128000000	$v_{\sigma\tau}$	-0.513554000	0.256000000
$v_{\sigma\tau}$	0.249734700	0.512000000	$v_{\sigma\tau}$	0.044631600	1.024000000
$v_{\sigma\tau}$	-0.112352070	1.560000000	$v_{\sigma\tau}$	0.102143520	2.048000000
$v_{\sigma\tau}$	-0.039722400	3.072000000	$v_{\sigma\tau}$	0.013454710	4.096000000
v^{ls}	0.195587890	0.010000000	v^{ls}	0.122919950	0.040000000
v^{ls}	0.233614120	0.016000000	v^{ls}	0.239968120	0.064000000
v^{ls}	-1.419286310	0.128000000	v^{ls}	-0.949923280	0.256000000
v^{ls}	-0.028819120	0.512000000	v^{ls}	0.009346350	1.024000000
v^{ls}	-0.017686780	1.560000000	v^{ls}	0.010158210	2.048000000
v^{ls}	-0.002645560	3.072000000	v^{ls}	0.000518590	4.096000000
v_σ^{ls}	-0.589433560	0.010000000	v_σ^{ls}	-0.668921190	0.040000000
v_σ^{ls}	0.622642980	0.016000000	v_σ^{ls}	0.577874250	0.064000000
v_σ^{ls}	-0.810313230	0.128000000	v_σ^{ls}	-0.390511960	0.256000000
v_σ^{ls}	0.114773340	0.512000000	v_σ^{ls}	-0.066438240	1.024000000
v_σ^{ls}	0.072826570	1.560000000	v_σ^{ls}	-0.045690160	2.048000000
v_σ^{ls}	0.010871570	3.072000000	v_σ^{ls}	-0.002166400	4.096000000

Table D.1: Correlated AV18 potential, using central correlators $\min^\alpha(ST = 00)$, min $(ST = 01, 10, 11)$ and tensor correlators min $^\alpha(ST = 10)$, min $(ST = 11)$ (cf. tables C.1 and C.2).

D.2.2 Bonn-Aα

	$\gamma[fm^{-1}]$	$\kappa[fm^2]$		$\gamma[fm^{-1}]$	$\kappa[fm^2]$
v^{p^2}	-0.011989400	0.010000000	v^{p^2}	0.179003070	0.040000000
v^{p^2}	0.153402990	0.016000000	v^{p^2}	0.141178880	0.064000000
v^{p^2}	0.172823350	0.128000000	v^{p^2}	0.020798310	0.256000000
v^{p^2}	-0.016915190	0.512000000	v^{p^2}	0.073986920	1.024000000
v^{p^2}	-0.077440740	1.536000000	v^{p^2}	0.048021690	2.048000000
v^{p^2}	-0.013223290	3.072000000	v^{p^2}	0.003518150	4.096000000
$v_\sigma^{p^2}$	0.018835730	0.010000000	$v_\sigma^{p^2}$	0.033920040	0.040000000
$v_\sigma^{p^2}$	-0.016646930	0.016000000	$v_\sigma^{p^2}$	-0.018734360	0.064000000
$v_\sigma^{p^2}$	0.023003580	0.128000000	$v_\sigma^{p^2}$	0.004748490	0.256000000
$v_\sigma^{p^2}$	-0.022072480	0.512000000	$v_\sigma^{p^2}$	0.035023890	1.024000000
$v_\sigma^{p^2}$	-0.034662600	1.536000000	$v_\sigma^{p^2}$	0.020719310	2.048000000
$v_\sigma^{p^2}$	-0.005474890	3.072000000	$v_\sigma^{p^2}$	0.001378240	4.096000000
$v_\tau^{p^2}$	-0.087248210	0.010000000	$v_\tau^{p^2}$	-0.090773900	0.040000000
$v_\tau^{p^2}$	0.098408890	0.016000000	$v_\tau^{p^2}$	0.095085930	0.064000000
$v_\tau^{p^2}$	-0.051226420	0.128000000	$v_\tau^{p^2}$	0.068274420	0.256000000
$v_\tau^{p^2}$	-0.012920870	0.512000000	$v_\tau^{p^2}$	-0.063412310	1.024000000
$v_\tau^{p^2}$	0.066106680	1.536000000	$v_\tau^{p^2}$	-0.036823270	2.048000000
$v_\tau^{p^2}$	0.008242770	3.072000000	$v_\tau^{p^2}$	-0.001318930	4.096000000
$v_{\sigma\tau}^{p^2}$	-0.018120730	0.010000000	$v_{\sigma\tau}^{p^2}$	-0.001916640	0.040000000
$v_{\sigma\tau}^{p^2}$	0.047908220	0.016000000	$v_{\sigma\tau}^{p^2}$	0.055498500	0.064000000
$v_{\sigma\tau}^{p^2}$	0.009680040	0.128000000	$v_{\sigma\tau}^{p^2}$	0.032997690	0.256000000
$v_{\sigma\tau}^{p^2}$	-0.004532550	0.512000000	$v_{\sigma\tau}^{p^2}$	-0.026609950	1.024000000
$v_{\sigma\tau}^{p^2}$	0.025651250	1.536000000	$v_{\sigma\tau}^{p^2}$	-0.013996840	2.048000000
$v_{\sigma\tau}^{p^2}$	0.003095270	3.072000000	$v_{\sigma\tau}^{p^2}$	-0.000502930	4.096000000
$v^{p_r^2}$	13.996259930	0.010000000	$v^{p_r^2}$	3.328033340	0.040000000
$v^{p_r^2}$	-1.507563040	0.016000000	$v^{p_r^2}$	-0.858087600	0.064000000
$v^{p_r^2}$	0.857723370	0.128000000	$v^{p_r^2}$	0.245546020	0.256000000
$v^{p_r^2}$	0.029240680	0.512000000	$v^{p_r^2}$	0.006624110	1.024000000
$v^{p_r^2}$	-0.004483010	1.536000000	$v^{p_r^2}$	0.001739180	2.048000000
$v^{p_r^2}$	-0.000277740	3.072000000	$v^{p_r^2}$	0.000018330	4.096000000
$v_\sigma^{p_r^2}$	-1.705146490	0.010000000	$v_\sigma^{p_r^2}$	-0.530747720	0.040000000

Table D.2: Correlated Bonn-A potential, using central correlators $\min^\alpha(ST = 00)$, $\min(ST = 01, 10, 11)$ and tensor correlators $\min^\alpha(ST = 10)$, $\min(ST = 11)$ (cf. tables C.3 and C.4).

	$\gamma[fm^{-1}]$	$\kappa[fm^2]$		$\gamma[fm^{-1}]$	$\kappa[fm^2]$
$v_\sigma^{p_r^2}$	1.208952750	0.016000000	$v_\sigma^{p_r^2}$	0.348990740	0.064000000
$v_\sigma^{p_r^2}$	-0.179172680	0.128000000	$v_\sigma^{p_r^2}$	-0.088826290	0.256000000
$v_\sigma^{p_r^2}$	0.027982950	0.512000000	$v_\sigma^{p_r^2}$	-0.008552710	1.024000000
$v_\sigma^{p_r^2}$	0.004703330	1.536000000	$v_\sigma^{p_r^2}$	-0.002014030	2.048000000
$v_\sigma^{p_r^2}$	0.000338700	3.072000000	$v_\sigma^{p_r^2}$	-0.000062420	4.096000000
$v_\tau^{p_r^2}$	-0.011954490	0.010000000	$v_\tau^{p_r^2}$	-0.277367840	0.040000000
$v_\tau^{p_r^2}$	0.970240190	0.016000000	$v_\tau^{p_r^2}$	0.359716130	0.064000000
$v_\tau^{p_r^2}$	-0.102066590	0.128000000	$v_\tau^{p_r^2}$	-0.080606210	0.256000000
$v_\tau^{p_r^2}$	0.069078020	0.512000000	$v_\tau^{p_r^2}$	-0.010517200	1.024000000
$v_\tau^{p_r^2}$	0.005125700	1.536000000	$v_\tau^{p_r^2}$	-0.002051530	2.048000000
$v_\tau^{p_r^2}$	0.000323570	3.072000000	$v_\tau^{p_r^2}$	-0.000058450	4.096000000
$v_{\sigma\tau}^{p_r^2}$	-1.751613740	0.010000000	$v_{\sigma\tau}^{p_r^2}$	-0.561803750	0.040000000
$v_{\sigma\tau}^{p_r^2}$	0.439042240	0.016000000	$v_{\sigma\tau}^{p_r^2}$	0.248843300	0.064000000
$v_{\sigma\tau}^{p_r^2}$	-0.177210620	0.128000000	$v_{\sigma\tau}^{p_r^2}$	-0.087388690	0.256000000
$v_{\sigma\tau}^{p_r^2}$	0.022478910	0.512000000	$v_{\sigma\tau}^{p_r^2}$	0.002120650	1.024000000
$v_{\sigma\tau}^{p_r^2}$	-0.000966090	1.536000000	$v_{\sigma\tau}^{p_r^2}$	0.000331160	2.048000000
$v_{\sigma\tau}^{p_r^2}$	-0.000045500	3.072000000	$v_{\sigma\tau}^{p_r^2}$	0.000003780	4.096000000
v	-20.453574810	0.010000000	v	-0.410591800	0.040000000
v	2.251952100	0.016000000	v	-4.704468050	0.064000000
v	-1.831477170	0.128000000	v	2.152963270	0.256000000
v	-1.310669650	0.512000000	v	0.919449830	1.024000000
v	-1.097564980	1.536000000	v	0.652269350	2.048000000
v	-0.161669080	3.072000000	v	0.032296780	4.096000000
v_σ	-5.876027080	0.010000000	v_σ	-1.745570720	0.040000000
v_σ	2.410505980	0.016000000	v_σ	1.410109220	0.064000000
v_σ	1.307923450	0.128000000	v_σ	-1.206104290	0.256000000
v_σ	0.521746140	0.512000000	v_σ	-0.181214680	1.024000000
v_σ	0.094663240	1.536000000	v_σ	-0.031819950	2.048000000
v_σ	0.002942200	3.072000000	v_σ	-0.000198040	4.096000000
v_τ	-6.506861010	0.010000000	v_τ	-2.375955180	0.040000000
v_τ	4.096523020	0.016000000	v_τ	1.731517310	0.064000000
v_τ	1.344593100	0.128000000	v_τ	-1.457000890	0.256000000
v_τ	0.800538330	0.512000000	v_τ	-0.375874610	1.024000000
v_τ	0.288286460	1.536000000	v_τ	-0.145314690	2.048000000

Table D.2: Correlated Bonn-A potential, using central correlators $\min^\alpha(ST = 00)$, min $(ST = 01, 10, 11)$ and tensor correlators $\min^\alpha(ST = 10)$, min $(ST = 11)$ (cf. tables C.3 and C.4).

	$\gamma[fm^{-1}]$	$\kappa[fm^2]$		$\gamma[fm^{-1}]$	$\kappa[fm^2]$
v_τ	0.030739340	3.072000000	v_τ	-0.005746300	4.096000000
$v_{\sigma\tau}$	-5.027466370	0.010000000	$v_{\sigma\tau}$	-4.907261310	0.040000000
$v_{\sigma\tau}$	0.197595800	0.016000000	$v_{\sigma\tau}$	0.963735560	0.064000000
$v_{\sigma\tau}$	0.174901770	0.128000000	$v_{\sigma\tau}$	-0.673543190	0.256000000
$v_{\sigma\tau}$	0.348851760	0.512000000	$v_{\sigma\tau}$	-0.056078400	1.024000000
$v_{\sigma\tau}$	0.023522390	1.536000000	$v_{\sigma\tau}$	0.012027300	2.048000000
$v_{\sigma\tau}$	-0.017777810	3.072000000	$v_{\sigma\tau}$	0.009468500	4.096000000
v^{ls}	-23.378608440	0.010000000	v^{ls}	-10.913388700	0.040000000
v^{ls}	-1.375718570	0.016000000	v^{ls}	-0.781809590	0.064000000
v^{ls}	-2.667546660	0.128000000	v^{ls}	-0.058147420	0.256000000
v^{ls}	-0.208192290	0.512000000	v^{ls}	0.111380860	1.024000000
v^{ls}	-0.125525460	1.536000000	v^{ls}	0.074117220	2.048000000
v^{ls}	-0.018594610	3.072000000	v^{ls}	0.003734850	4.096000000
v_σ^{ls}	-2.017380260	0.010000000	v_σ^{ls}	-1.699444480	0.040000000
v_σ^{ls}	-1.215418650	0.016000000	v_σ^{ls}	-0.729095950	0.064000000
v_σ^{ls}	-0.539664260	0.128000000	v_σ^{ls}	-0.202176220	0.256000000
v_σ^{ls}	0.019098180	0.512000000	v_σ^{ls}	-0.024957230	1.024000000
v_σ^{ls}	0.025307020	1.536000000	v_σ^{ls}	-0.014855290	2.048000000
v_σ^{ls}	0.003526040	3.072000000	v_σ^{ls}	-0.000695730	4.096000000

Table D.2: Correlated Bonn-A potential, using central correlators $\min^\alpha(ST = 00)$, $\min (ST = 01, 10, 11)$ and tensor correlators $\min^\alpha(ST = 10)$, $\min (ST = 11)$ (cf. tables C.3 and C.4).

D.2.3   Bonn-Aγ

	$\gamma[fm^{-1}]$	$\kappa[fm^2]$		$\gamma[fm^{-1}]$	$\kappa[fm^2]$
v^{p^2}	-0.030633680	0.010000000	v^{p^2}	0.166639390	0.040000000
v^{p^2}	0.175807190	0.016000000	v^{p^2}	0.143011490	0.064000000
v^{p^2}	0.180020470	0.128000000	v^{p^2}	0.016092510	0.256000000
v^{p^2}	-0.027051130	0.512000000	v^{p^2}	0.042666270	1.024000000
v^{p^2}	-0.036969410	1.536000000	v^{p^2}	0.047406960	2.048000000
v^{p^2}	-0.010126440	3.072000000	v^{p^2}	0.002671410	4.096000000
$v_\sigma^{p^2}$	0.012620970	0.010000000	$v_\sigma^{p^2}$	0.029798810	0.040000000
$v_\sigma^{p^2}$	-0.009178870	0.016000000	$v_\sigma^{p^2}$	-0.018123490	0.064000000
$v_\sigma^{p^2}$	0.025402630	0.128000000	$v_\sigma^{p^2}$	0.003179890	0.256000000
$v_\sigma^{p^2}$	-0.025451130	0.512000000	$v_\sigma^{p^2}$	0.024583670	1.024000000

Table D.3: Correlated Bonn-A potential, using central correlators $\min^\alpha(ST = 00)$, $\min (ST = 01, 10, 11)$ and tensor correlators $\min^\alpha(ST = 10)$, $\min (ST = 11)$ (cf. tables C.3 and C.4).

	$\gamma[fm^{-1}]$	$\kappa[fm^2]$		$\gamma[fm^{-1}]$	$\kappa[fm^2]$
$v_\sigma^{p^2}$	-0.021172150	1.536000000	$v_\sigma^{p^2}$	0.020514400	2.048000000
$v_\sigma^{p^2}$	-0.004442610	3.072000000	$v_\sigma^{p^2}$	0.001096000	4.096000000
$v_\tau^{p^2}$	-0.068603930	0.010000000	$v_\tau^{p^2}$	-0.078410220	0.040000000
$v_\tau^{p^2}$	0.076004690	0.016000000	$v_\tau^{p^2}$	0.093253310	0.064000000
$v_\tau^{p^2}$	-0.058423540	0.128000000	$v_\tau^{p^2}$	0.072980220	0.256000000
$v_\tau^{p^2}$	-0.002784930	0.512000000	$v_\tau^{p^2}$	-0.032091660	1.024000000
$v_\tau^{p^2}$	0.025635350	1.536000000	$v_\tau^{p^2}$	-0.036208550	2.048000000
$v_\tau^{p^2}$	0.005145920	3.072000000	$v_\tau^{p^2}$	-0.000472200	4.096000000
$v_{\sigma\tau}^{p^2}$	-0.011905970	0.010000000	$v_{\sigma\tau}^{p^2}$	0.002204580	0.040000000
$v_{\sigma\tau}^{p^2}$	0.040440160	0.016000000	$v_{\sigma\tau}^{p^2}$	0.054887630	0.064000000
$v_{\sigma\tau}^{p^2}$	0.007281000	0.128000000	$v_{\sigma\tau}^{p^2}$	0.034566290	0.256000000
$v_{\sigma\tau}^{p^2}$	-0.001153910	0.512000000	$v_{\sigma\tau}^{p^2}$	-0.016169730	1.024000000
$v_{\sigma\tau}^{p^2}$	0.012160800	1.536000000	$v_{\sigma\tau}^{p^2}$	-0.013791930	2.048000000
$v_{\sigma\tau}^{p^2}$	0.002062990	3.072000000	$v_{\sigma\tau}^{p^2}$	-0.000220680	4.096000000
$v^{p_r^2}$	15.324151010	0.010000000	$v^{p_r^2}$	3.662108070	0.040000000
$v^{p_r^2}$	-2.449254360	0.016000000	$v^{p_r^2}$	-1.043334050	0.064000000
$v^{p_r^2}$	0.895580910	0.128000000	$v^{p_r^2}$	0.239420330	0.256000000
$v^{p_r^2}$	0.028721550	0.512000000	$v^{p_r^2}$	-0.002214700	1.024000000
$v^{p_r^2}$	-0.005351400	1.536000000	$v^{p_r^2}$	0.000727260	2.048000000
$v^{p_r^2}$	-0.000104410	3.072000000	$v^{p_r^2}$	-0.000006950	4.096000000
$v_\sigma^{p_r^2}$	-1.262516130	0.010000000	$v_\sigma^{p_r^2}$	-0.419389480	0.040000000
$v_\sigma^{p_r^2}$	0.895055640	0.016000000	$v_\sigma^{p_r^2}$	0.287241920	0.064000000
$v_\sigma^{p_r^2}$	-0.166553490	0.128000000	$v_\sigma^{p_r^2}$	-0.090868190	0.256000000
$v_\sigma^{p_r^2}$	0.027809910	0.512000000	$v_\sigma^{p_r^2}$	-0.011498980	1.024000000
$v_\sigma^{p_r^2}$	0.004413870	1.536000000	$v_\sigma^{p_r^2}$	-0.002351340	2.048000000
$v_\sigma^{p_r^2}$	0.000396470	3.072000000	$v_\sigma^{p_r^2}$	-0.000070850	4.096000000
$v_\tau^{p_r^2}$	-1.339845580	0.010000000	$v_\tau^{p_r^2}$	-0.611442570	0.040000000
$v_\tau^{p_r^2}$	1.911931510	0.016000000	$v_\tau^{p_r^2}$	0.544962570	0.064000000
$v_\tau^{p_r^2}$	-0.139924140	0.128000000	$v_\tau^{p_r^2}$	-0.074480510	0.256000000
$v_\tau^{p_r^2}$	0.069597150	0.512000000	$v_\tau^{p_r^2}$	-0.001678390	1.024000000
$v_\tau^{p_r^2}$	0.005994090	1.536000000	$v_\tau^{p_r^2}$	-0.001039610	2.048000000
$v_\tau^{p_r^2}$	0.000150250	3.072000000	$v_\tau^{p_r^2}$	-0.000033170	4.096000000

Table D.3: Correlated Bonn-A potential, using central correlators $\min^\alpha(ST = 00)$, min $(ST = 01, 10, 11)$ and tensor correlators $\min^\alpha(ST = 10)$, min $(ST = 11)$ (cf. tables C.3 and C.4).

	$\gamma[fm^{-1}]$	$\kappa[fm^2]$		$\gamma[fm^{-1}]$	$\kappa[fm^2]$
$v_{\sigma\tau}^{p_r^2}$	-2.194244100	0.010000000	$v_{\sigma\tau}^{p_r^2}$	-0.673161990	0.040000000
$v_{\sigma\tau}^{p_r^2}$	0.752939350	0.016000000	$v_{\sigma\tau}^{p_r^2}$	0.310592120	0.064000000
$v_{\sigma\tau}^{p_r^2}$	-0.189829800	0.128000000	$v_{\sigma\tau}^{p_r^2}$	-0.085346790	0.256000000
$v_{\sigma\tau}^{p_r^2}$	0.022651950	0.512000000	$v_{\sigma\tau}^{p_r^2}$	0.005066920	1.024000000
$v_{\sigma\tau}^{p_r^2}$	-0.000676620	1.536000000	$v_{\sigma\tau}^{p_r^2}$	0.000668460	2.048000000
$v_{\sigma\tau}^{p_r^2}$	-0.000103280	3.072000000	$v_{\sigma\tau}^{p_r^2}$	0.000012210	4.096000000
v	-20.474598490	0.010000000	v	-0.417964390	0.040000000
v	2.262382860	0.016000000	v	-4.715754160	0.064000000
v	-1.776428100	0.128000000	v	2.077466200	0.256000000
v	-1.211264210	0.512000000	v	0.838438280	1.024000000
v	-1.045901420	1.536000000	v	0.622971680	2.048000000
v	-0.154830920	3.072000000	v	0.030949060	4.096000000
v_σ	-5.883034980	0.010000000	v_σ	-1.748028250	0.040000000
v_σ	2.413982900	0.016000000	v_σ	1.406347180	0.064000000
v_σ	1.326273140	0.128000000	v_σ	-1.231269980	0.256000000
v_σ	0.554881290	0.512000000	v_σ	-0.208218530	1.024000000
v_σ	0.111884420	1.536000000	v_σ	-0.041585840	2.048000000
v_σ	0.005221590	3.072000000	v_σ	-0.000647280	4.096000000
v_τ	-6.485837330	0.010000000	v_τ	-2.368582590	0.040000000
v_τ	4.086092260	0.016000000	v_τ	1.742803430	0.064000000
v_τ	1.289544030	0.128000000	v_τ	-1.381503820	0.256000000
v_τ	0.701132880	0.512000000	v_τ	-0.294863070	1.024000000
v_τ	0.236622900	1.536000000	v_τ	-0.116017010	2.048000000
v_τ	0.023901180	3.072000000	v_τ	-0.004398580	4.096000000
$v_{\sigma\tau}$	-5.020458470	0.010000000	$v_{\sigma\tau}$	-4.904803780	0.040000000
$v_{\sigma\tau}$	0.194118880	0.016000000	$v_{\sigma\tau}$	0.967497600	0.064000000
$v_{\sigma\tau}$	0.156552080	0.128000000	$v_{\sigma\tau}$	-0.648377500	0.256000000
$v_{\sigma\tau}$	0.315716610	0.512000000	$v_{\sigma\tau}$	-0.029074550	1.024000000
$v_{\sigma\tau}$	0.006301200	1.536000000	$v_{\sigma\tau}$	0.021793190	2.048000000
$v_{\sigma\tau}$	-0.020057200	3.072000000	$v_{\sigma\tau}$	0.009917740	4.096000000
v^{ls}	-23.332946770	0.010000000	v^{ls}	-10.858671580	0.040000000
v^{ls}	-1.484701070	0.016000000	v^{ls}	-0.875446090	0.064000000
v^{ls}	-2.546259550	0.128000000	v^{ls}	-0.155836790	0.256000000
v^{ls}	-0.122052350	0.512000000	v^{ls}	0.092440500	1.024000000
v^{ls}	-0.094485090	1.536000000	v^{ls}	0.059533480	2.048000000

Table D.3: Correlated Bonn-A potential, using central correlators $\min^\alpha(ST = 00)$, $\min (ST = 01, 10, 11)$ and tensor correlators $\min^\alpha(ST = 10)$, $\min (ST = 11)$ (cf. tables C.3 and C.4).

	$\gamma[fm^{-1}]$	$\kappa[fm^2]$		$\gamma[fm^{-1}]$	$\kappa[fm^2]$
v^{ls}	-0.015030760	3.072000000	v^{ls}	0.003002370	4.096000000
v^{ls}_σ	-2.063041940	0.010000000	v^{ls}_σ	-1.754161600	0.040000000
v^{ls}_σ	-1.106436140	0.016000000	v^{ls}_σ	-0.635459450	0.064000000
v^{ls}_σ	-0.660951370	0.128000000	v^{ls}_σ	-0.104486850	0.256000000
v^{ls}_σ	-0.067041760	0.512000000	v^{ls}_σ	-0.006016870	1.024000000
v^{ls}_σ	-0.005733360	1.536000000	v^{ls}_σ	-0.000271550	2.048000000
v^{ls}_σ	-0.000037800	3.072000000	v^{ls}_σ	0.000036750	4.096000000

Table D.3: Correlated Bonn-A potential, using central correlators $\min^\alpha(ST = 00)$, $\min (ST = 01, 10, 11)$ and tensor correlators $\min^\alpha(ST = 10)$, $\min (ST = 11)$ (cf. tables C.3 and C.4).

Appendix E

Notation and Conventions

E.1 Units and Constants

Throughout this work, we primarily use

$$\hbar = c = 1 \,.$$

The value of the conversion factor is

$$\hbar c = 197.327053 \text{ MeV fm} \,. \tag{E.1}$$

Nucleon Properties			
$m_p\,[\text{MeV}]$	938.27231	proton mass	[24]
$m_n\,[\text{MeV}]$	939.56563	neutron mass	[24]
$m_N\,[\text{MeV}]$	938.91897	average nucleon mass	[24]
$r_p\,[\text{fm}]$	0.862	proton charge radius	[49]

E.2 Common Functions

$j_l(kr)$	spherical Bessel function
$P_l(cos\theta)$	Legendre polynomial
$W(r)$	Woods-Saxon function (see eq. (1.21)
$Y_l^m(\Omega)$	spherical harmonic
$\mathcal{Y}(x)$	Yukawa function (see eq. (1.14))
$\mathcal{Z}(x)$	derived Yukawava function (see eq. (1.14))

E.3 Operators and Vectors

Vectors are denoted by bold-face letters, i.e. $\boldsymbol{x}$. For operators, a font of the Roman family is used: O. Vector operators are therefore written in bold-face Roman style: $\mathbf{L}$. Several common vectors and operators are listed below. Note that although the relative momentum *vector* will be denoted $\boldsymbol{k}$, the more common notation $\mathbf{p}$ is used for the relative momentum *operator*.

Symbol Conventions		
Vector	Operator	
$\hat{\boldsymbol{a}}$		general unit vector
$\boldsymbol{x}_i$	$\mathbf{x}_i$	single particle position
$\boldsymbol{p}_i$	$\mathbf{p}_i$	single particle momentum
$\boldsymbol{r} = \boldsymbol{x}_1 - \boldsymbol{x}_2$	$\mathbf{r}$	relative position of two particles
$\boldsymbol{k} = \frac{1}{2}(\boldsymbol{p}_1 - \boldsymbol{p}_2)$	$\mathbf{p}$	relative momentum of two particles
$\boldsymbol{q}$	$\mathbf{q}$	momentum transfer
$\boldsymbol{x}_{\mathrm{cm}}$	$\mathbf{x}_{\mathrm{cm}}$	center-of-mass position
$\boldsymbol{p}_{\mathrm{cm}}$	$\mathbf{p}_{\mathrm{cm}}$	center-of-mass position

Operator Conventions	
o	k-body operator in k-body space
O	operator in many-body space
$\mathrm{O}^{[k]}$	irreducible k-body part of an operator in many-body space
$\mathrm{o}_{i_1 \ldots i_k}$	k-body operator in many-body space with respect to the subspace of particles $i_1, \ldots, i_k$
C	correlation operator in many-body space
$\mathrm{c} = \mathrm{C}_2$	correlation operator in two-body space
$\widetilde{\mathrm{O}} = \mathrm{C}^\dagger \mathrm{O} \mathrm{C}$	correlated operator in many-body space
$\widetilde{\mathrm{O}}^{C2}$	correlated operator in two-body approximation
$\mathrm{t}_q^{(k)}$	irreducible spherical tensor operator of rank k

E.4 Pauli Matrices

The Pauli matrices, denoted σ in spin and τ in isospin space, are

$$\sigma_1 = \tau_1 = \begin{pmatrix} 0 & 1 \\ 1 & 0 \end{pmatrix}, \quad \sigma_2 = \tau_2 = \begin{pmatrix} 0 & -i \\ i & 0 \end{pmatrix}, \quad \sigma_3 = \tau_3 = \begin{pmatrix} 1 & 0 \\ 0 & -1 \end{pmatrix}.$$

The projection operators on spin singlet and triplet spaces read

$$\Pi_0 = \frac{1}{4}(1 - \boldsymbol{\sigma}_1 \cdot \boldsymbol{\sigma}_2) \quad \text{and} \quad \Pi_1 = \frac{3}{4}(1 + \boldsymbol{\sigma}_1 \cdot \boldsymbol{\sigma}_2).$$

The isospin projectors are given by the same relations with $\boldsymbol{\sigma}$ replaced by $\boldsymbol{\tau}$.

E.5 Clebsch-Gordan Coefficients

The notation

$$\left\langle j_1 m_1 j_2 m_2 \middle| JM \right\rangle$$

is used for *Clebsch-Gordan coefficients*, since it better reflects the underlying unitary transformation between different bases.

Bibliography

[1] R. Brockmann and R. Machleidt, nucl-th/9612004 v1.

[2] D. R. Entem and R. Machleidt, nucl-th/0304018 v1, and references therein.

[3] S. C. Pieper, K. Varga, and R. B. Wiringa, Phys. Rev. **C66**, 044310 (2002).

[4] H. Feldmeier, T. Neff, R. Roth, and J. Schnack, Nucl. Phys. **A632**, 61 (1998).

[5] R. Roth, *Effektive Wechselwirkungen für Quantenflüssigkeiten und Quantengase: Kernmaterie. flüssiges Helium und ultrakalte atomare Fermigase*, PhD thesis, TU Darmstadt, 2000.

[6] T. Neff, *Short-Ranged Central and Tensor Correlations in Nuclear Many-Body Systems*, PhD thesis, TU Darmstadt, 2002.

[7] T. Neff and H. Feldmeier, Nucl. Phys. **A713**, 311 (2003).

[8] S. K. Bogner, T. T. S. Kuo, and A. Schwenk, nucl-th/0305035 v1.

[9] R. B. Wiringa, V. Stoks, and R. Schiavilla, Phys. Rev. **C51**, 38 (1995).

[10] R. Machleidt, Phys. Rep. **149**, 1 (1987).

[11] R. Machleidt, Adv. Nucl. Phys. **19**, 189 (1989).

[12] R. Machleidt, Phys. Rev. **C63**, 024001 (2001).

[13] H. Feldmeier and J. Schnack, Progr. Part. Nucl. Phys. **39**, 393 (1997).

[14] H. Feldmeier and J. Schnack, Rev. Mod. Phys. **72**, 655 (2000).

[15] T. Neff and H. Feldmeier, nucl-th/0312130.

[16] R. Machleidt, Adv. Nucl. Phys. **19**, 189 (1989), and references therein for a comprehensive review.

[17] M. Lacombe et al., Phys. Rev. **C21**, 861 (1980).

[18] R. Blankenbecler and R. Sugar, Phys. Rev. **142**, 1051 (1966).

[19] V. G. J. Stoks, R. A. M. Klomp, M. C. M. Rentmeester, and J. J. de Swart, Phys. Rev. **C48**, 792 (1993).

[20] F. Schwabl, *Quantenmechanik*, Springer Verlag, 5th edition, 1997.

[21] R. B. Wiringa, R. Smith, and T. Ainsworth, Phys. Rev. **C29**, 1207 (1984).

[22] S. Weinberg, Physica **A96**, 327 (1979).

[23] S. Weinberg, *The Quantum Theory of Fields*, Cambridge University Press, 2nd. edition, 1996.

[24] K. Hagiwara et al., Phys. Rev. **D66**, 010001 (2002).

[25] V. Bernard, N. Kaiser, and U.-G. Meißner, Int. J. Mod. Phys. **E4**, 193 (1995).

[26] N. Fettes, U.-G. Meißner, M. Mojžiš, and S. Steininger, hep-ph/0001308v3.

[27] D. R. Entem and R. Machleidt, Phys. Rev. **C66**, 014002 (2002).

[28] M. Walzl, U. G. Meißner, and E. Epelbaum, Nucl. Phys. **A693**, 663 (2001).

[29] S. Weinberg, *The Quantum Theory of Fields*, volume I: Foundations, Cambridge University Press, 2nd. edition, 1996.

[30] M. E. Peskin and D. V. Schroeder, *An Introduction to Quantum Field Theory*, Perseus Books, 1997.

[31] G. P. Lepage, nucl-th/9706029 v1.

[32] J. F. Donoghue, hep-ph/9607351 v1.

[33] R. Machleidt and G. Q. Li, nucl-th/9301019 v1, talk presented at 'Realistic Nuclear Structure' conference, Stony Brook, 05/1992.

[34] W. N. Cottingham, M. Lacombe, B. Loiseau, J. M. Richard, and R. V. Mau, Phys. Rev. **D8**, 800 (1973).

[35] V. G. J. Stoks, R. A. M. Klomp, C. P. F. Terheggen, and J. J. de Swart, Phys. Rev. **C49**, 2950 (1994).

[36] R. G. Newton, *Scattering Theory of Waves and Particles*, Springer Verlag, 2nd edition, 1982.

[37] R. V. Reid, Ann. Phys. (N.Y.) **50**, 411 (1968).

[38] A. Sitenko and V. Tartakovskii, *Lectures on the Theory of the Nucleus*, Pergamon Press, 1975.

[39] S. K. Bogner, T. T. S. Kuo, A. Schwenk, and G. E. Brown, nucl-th/0111042 v1.

[40] T. Neff, Fermionische Molekulardynamik mit Konfigurationsmischungen und realistischen Wechselwirkungen, diploma thesis, TU Darmstadt, 1998.

[41] P. Ring and P. Schuck, *The Nuclear Many-Body Problem*, Springer Verlag, 1st edition, 2000 (2nd printing).

[42] F. M. H. Villars and G. Cooper, Ann. Phys. (N. Y.) **56**, 224 (1970).

[43] C. W. Wong, Phys. Rep. **15**, 285 (1975).

[44] S. Hassani, *Mathematical Physics*, Springer Verlag, 1999.

[45] T. Neff, personal communication.

[46] V. B. Cheng, J. H. H. Suzukawa, and M. Wolfsberg, J. Chem. Phys. **59**, 3992 (1973).

[47] G. Audi and A. H. Wapstra, Nucl. Phys. **A595**, 409 (1995), binding energies taken from table of recommended masses.

[48] I. Angeli, Table of Nuclear Root-Mean-Square Charge Radii, Technical Report INDC(HUN)-033, International Nuclear Data Commitee (INDC), 1999, online: http://iaeand.iaea.or.at/indc_sel.html.

[49] G. G. Simon, C. Schmitt, F. Borkowski, and V. H. Walther, Nucl. Phys. **A333**, 381 (1980).

[50] T. Neff, Nuclear Structure Within FMD: From α-Nuclei to Exotics, talk presented at the KPII seminar at GSI, 11/2003, http://theory.gsi.de/ tneff.

[51] B. S. Pudliner, V. R. Pandharipande, J. Carlson, and R. B. Wiringa, Phys. Rev. Lett. **74**, 4396 (1995).

[52] B. S. Pudliner, V. R. Pandharipande, J. Carlson, S. C. Pieper, and R. B. Wiringa, Phys. Rev. **C56**, 1720 (1997).

[53] R. B. Wiringa, S. C. Pieper, J. Carlson, and V. R. Pandharipande, Phys. Rev. **C62**, 014001 (2000).

[54] R. Roth, personal communication.

[55] A. Ozawa et al., Phys. Rev. Lett. **84**, 5493 (2000).

[56] G. G. Ohlsen, Rep. Prog. Phys. **35**, 717 (1972).

[57] D. Hüber and J. L. Friar, Phys. Rev. **C58**, 674 (1998).

[58] R. R. Kingsley et al., The NUDAT/PCNUDAT Program for Nuclear Data, paper submitted to the 9th International Symposium of Capture Gamma-Ray Spectroscopy and Related Topics, Budapest, Hungary, October 1996. Data extracted from the NUDAT online database, version 12 Aug 03, http://www.nndc.bnl.gov/nndc/nudat.

[59] D. R. Tilley et al., Nucl. Phys. **A708**, 3 (2002).

[60] A. Doté, H. Horiuchi, and Y. Kanada-En'yo, nucl-th/9705050 v1.

[61] N. Soić et al., nucl-ex/9801009 v1.

[62] M. Milin and W. von Oertzen, Fizika **B12**, 61 (2003).

[63] A. Cribeiro, Response of Nuclei to Quadrupole Constraints in the Framework of Fermionic Molecular Dynamics, diploma thesis, TU Darmstadt, 2003.

[64] D. Werner, *Funktionalanalysis*, Springer Verlag, 3rd. edition, 2000.

[65] J. J. Sakurai, *Modern Quantum Mechanics*, Addison-Wesley, 1st edition, 1985.

[66] D. A. Varshalovich, A. N. Moskalev, and V. K. Khersonskii, *Quantum Theory of Angular Momentum*, World Scientific, 1988.

Danksagung

An erster Stelle möchte ich Prof. Dr. Robert Roth für die Gelegenheit danken, diese Arbeit zu verfassen, ebenso für sein anhaltendes Interesse und die sehr angenehme Zusammenarbeit während der Anfertigung.

Ohne die Mitwirkung von Dr. Thomas Neff, mit dessen FMD-Programmen der Großteil der Rechnungen durchgeführt wurde, wäre diese Arbeit ebenfalls nicht denkbar gewesen. Bei Fragen zum FMD-Code oder seinem Fundus an *Mathematica*-Notebooks war er stets schnell und gerne bereit, zu helfen.

Prof. Dr. H. Feldmeier danke ich für die Übernahme des Zweitgutachtens und die daraus resultierenden Verbesserungsvorschläge, die in dieser überarbeiteten Fassung umgesetzt wurden.

Den Mitgliedern der Theorie-Abteilung des Instituts für Kernphysik danke ich für die freundliche Aufnahme und die durchweg kollegiale Atmosphäre. Meinem Kommilitonen Dominik Nickel gebührt Dank für interessante Diskussionen über fachliche und außerfachliche Themen.

Dr. Bernd-Jochen Schäfer danke ich für einige wertvolle Hinweise, die mir sehr beim Verständnis von Renormierungsgruppen-Methoden und $V_{\text{low-k}}$ geholfen haben.

Prof. Dr. Ruprecht Machleidt, University of Idaho, Moscow (USA), sei gedankt für die Übermittlung des Computer-Codes für das chirale Potential und dessen ausgezeichnete Dokumentation.

Der Deutschen Forschungsgesellschaft danke ich für die Unterstützung im Rahmen des Sonderforschungsbereiches 634.

Meinem Vater Heinrich, sowie meinem Bruder Stefan und seiner Familie danke ich für die anhaltende seelische und moralische Unterstützung während des Studiums, wo keine andere möglich war. Auch meiner umfangreichen Verwandtschaft bin ich dankbar für die materielle und immaterielle Unterstützung während meines Studiums, insbesondere nach den privaten Rückschlägen der letzten beiden Jahre. Besonderer Dank gebührt M. und J. Brüske, E. Piltz-Hergert und E. Hergert, M. und W. Wendel, sowie B. Zwirner und R. Reidel.